

---

**Experimental and Numerical Investigation of the Influence  
of Multiple-Burner Arrangements on Combustion  
Instabilities in Turbulent Swirl-Stabilized Flames**

Christian Kraus

---

Dissertation, Karlsruher Institut für Technologie, 2014

**Experimental and Numerical Investigation of the Influence of  
Multiple-Burner Arrangements on Combustion Instabilities in  
Turbulent Swirl-Stabilized Flames**

zur Erlangung des akademischen Grades eines  
DOKTORS DER INGENIEURWISSENSCHAFTEN (Dr.-Ing.)

der Fakultät für Chemieingenieurwesen und Verfahrenstechnik des  
Karlsruher Instituts für Technologie (KIT)

genehmigte  
DISSERTATION

von  
Dipl.-Ing. Christian Kraus  
aus Erlenbach am Main

Referent: Prof. Dr.-Ing. Henning Bockhorn

Korreferent: Prof. Dr. rer. nat. habil. Ulrich Maas

Tag der mündlichen Prüfung: 10.09.2014

*Meinen Freunden und  
meiner Familie gewidmet*

## **Danksagung**

Die vorliegende Arbeit entstand während meiner Zeit als wissenschaftlicher Mitarbeiter am Engler-Bunte-Institut, Bereich Verbrennungstechnik am KIT Karlsruhe. Sie wäre nicht möglich gewesen ohne die tatkräftige Unterstützung zahlreicher Personen, die mich in dieser Zeit fachlich und persönlich begleitet und bereichert haben.

Mein besonderer Dank gilt meinem Doktorvater Prof. Dr.-Ing. Henning Bockhorn. Sein entgegengebrachtes Vertrauen, seine kontinuierliche Unterstützung und die gewährte große wissenschaftliche Freiheit haben maßgeblich zu dem Gelingen dieser Arbeit beigetragen.

Herrn Prof. Dr. rer. nat. habil. Ulrich Maas danke ich für die Übernahme des Korreferats, die hilfreichen Kommentare zu meiner Arbeit und der schnellen Bearbeitung der Begutachtung meiner Dissertation.

Bei Prof. Dr.-Ing. Matthias Kind und bei Herrn Prof. Dr. rer. nat. Harald Horn möchte ich mich für die Übernahme des Prüfungsbeisitzes bzw. des Vorsitzes bei meiner mündlichen Doktorprüfung und für das Interesse an meiner Arbeit bedanken.

Die offene und angenehme Atmosphäre am Institut ließen einen manchen Rückschlag besser wegstecken und waren zwischenmenschlich und fachlich sehr bereichernd. Die dadurch stets vorhandene emotionale und fachliche Unterstützung war von enormem Wert für mich. Stellvertretend sollen dafür Peter Habisreuther, Stefan Harth, Julia Sedlmaier, Helmut Pabel, Meinrad Berg, Walter Pfeffinger, Feichi Zhang und Manuel Gruber genannt werden.

Weiterhin möchte ich meinen Eltern und meiner Familie danken, die mir durch ihre Unterstützung das Studium ermöglicht haben. Den weitaus größten Dank schulde ich Fionna, die mich während des Schreibens der Arbeit kontinuierlich begleitete und unterstützte, und damit der notwendige große Rückhalt war, um die Arbeit fertigzustellen.

Christian Kraus

Karlsruhe, im September 2014

# Table of Contents

<b>Nomenclature</b> .....	<b>V</b>
<b>1. Introduction</b> .....	<b>1</b>
1.1 Motivation .....	2
1.2 Objective .....	3
1.3 Thesis Outline.....	4
<b>2. Theoretical Background</b> .....	<b>5</b>
2.1 Governing Equations of Reactive Flows.....	5
2.1.1 Conservation of Momentum.....	5
2.1.2 Conservation of Mass .....	6
2.1.3 Conservation of Energy .....	6
2.1.4 Equation of State .....	7
2.2 Turbulence.....	8
2.2.1 Time and Length Scales in Turbulent Flows.....	8
2.2.2 Statistical Description of Turbulence.....	9
2.2.3 Turbulence Modelling.....	11
2.2.3.1 RANS-Models.....	11
2.2.3.2 Large-Eddy-Simulation .....	13
2.3 Fundamentals of Combustion.....	15
2.3.1 Reaction Kinetics of Combustion Processes.....	15
2.3.2 Modelling of Combustion Processes.....	16
2.3.2.1 Laminar Premixed Flame.....	17
2.3.2.2 Laminar Non-Premixed Flame.....	19
2.3.3 Turbulent Combustion.....	20
2.3.3.1 Borghi Diagram for Premixed Turbulent Flames.....	21
2.3.3.2 Non-Premixed, Turbulent Flames in the Borghi Diagram.....	23
2.3.4 Flame Stabilization in Swirl Flames.....	23
2.3.5 Turbulent Combustion Modelling.....	26
2.3.5.1 Simplification of Reaction Mechanisms.....	27
2.3.5.2 Unified-Turbulent-Flame-Speed-Closure Model (UTFC-Model) .....	28
<b>3. Combustion Instabilities</b> .....	<b>35</b>
3.1 Driving Mechanisms for Combustion Instabilities .....	36
3.2 Acoustic Resonances in Combustion Systems.....	37
3.3 Damping processes .....	40
3.4 Control and Modelling Approaches for Combustion Instabilities .....	40
3.4.1 1D-Network Models and Flame Response Modelling.....	41
3.4.2 3D-Methods: Helmholtz-Solvers and Large-Eddy-Simulation.....	43

3.4.3	Acoustic Impedance and Acoustic Boundaries .....	44
<b>4.</b>	<b>Experimental Investigations .....</b>	<b>47</b>
4.1	Design Concept of the Modular Combustor .....	47
4.1.1	Design of the Burner Nozzle .....	47
4.1.2	Design of the Single-Burner .....	47
4.1.3	Multiple-Burner Setups .....	49
4.2	Test Rig and Diagnostic Methods .....	51
4.2.1	Setup for the Measurement of Pressure Oscillations .....	51
4.2.2	High-Speed Measurements of OH*-Chemiluminescence .....	51
4.2.3	Recording and Analysis of the OH*-Intensity Signal .....	52
4.3	Investigated Operating Points .....	53
4.4	Experimental Results .....	55
4.4.1	Overall Sound Pressure Levels and Lean Stability Limit .....	55
4.4.2	Typical Combustor Modes in the Different Combustor Setups .....	56
4.4.2.1	Low-Frequency Modes in the Frequency Range of 100-300 Hz .....	57
4.4.2.2	Unstable Mode in the Frequency Range of 400 Hz .....	58
4.4.2.3	Unstable Mode in the SBS in the Frequency Range of 750 Hz .....	58
4.4.3	Summary of the Combustor Modes .....	60
4.4.4	Definition of the Designations for the Different Combustor Modes .....	60
4.5	Detailed Analysis of the Combustor Modes .....	61
4.5.1	Low-Frequency Modes .....	61
4.5.1.1	Low-Frequency Mode1 and the 190-Hz Mode at $L = 1.6$ .....	61
4.5.1.2	Influence of the Swirler Mass Flow Ratio on LF-Mode1 and the 190-Hz Mode .....	64
4.5.1.3	Low-Frequency Mode2 and Low-Frequency Mode3 at $L = 1.6$ .....	67
4.5.1.4	Influence of the Swirler Mass Flow Ratio on LF-Mode2 and LF-Mode3 .....	70
4.5.1.5	OH*-Intensity Responses to the Low-Frequency Pressure Oscillations .....	73
4.5.1.6	Summary and Discussion of the Results for the LF-Modes .....	83
4.5.2	400-Hz Mode .....	86
4.5.2.1	Influence of the Swirler Mass Flow Ratio on 400-Hz Mode .....	90
4.5.2.2	OH*-Intensity Responses to the 400-Hz Mode .....	93
4.5.2.3	Summary and Discussion of the Results for the 400-Hz Mode .....	100
4.5.3	750-Hz Mode .....	101
4.5.3.1	OH*-Intensity Responses to the 750-Hz Mode and Estimation of the Helmholtz-Resonator Frequency of the Combustion Chamber .....	104
4.5.4	Pressure Oscillations in the Non-Reactive Flow .....	107
4.5.4.1	Pressure Oscillations in the Non-Reactive Flow in the SBS .....	107
4.5.4.2	Pressure Oscillations in the Non-Reactive Flow in the MBS2 .....	110
4.5.5	Discussion of the Stability Charts of the Combustor Setups .....	112
<b>5.</b>	<b>Numerical Investigations .....</b>	<b>115</b>
5.1	Numerical Setup .....	115
5.1.1	Flow Solver .....	115
5.1.2	Geometric Model and Computational Grid .....	116
5.1.3	Boundary Conditions .....	119

5.2	Investigated Operating Points.....	121
5.3	Numerical Results .....	121
5.3.1	Non-Reactive Flow.....	122
5.3.1.1	LES Single-Burner Setup, $P_{th} = 25 \text{ kW}$ , $\phi = 0.7$ , $L = 1.6$ .....	122
5.3.1.2	LES Single-Burner Setup, $P_{th} = 30 \text{ kW}$ , $\phi = 0.85$ , $L = 1.6$ .....	129
5.3.1.3	LES Multiple-Burner Setup 2, $P_{th} = 30 \text{ kW/burner}$ , $\phi = 0.85$ , $L = 1.6$ .....	134
5.3.2	Reactive Flow .....	142
5.3.2.1	LES Single-Burner Setup, $P_{th} = 25 \text{ kW}$ , $\phi = 0.7$ , $L = 1.6$ .....	142
5.3.2.2	LES Single-Burner Setup, $P_{th} = 30 \text{ kW}$ , $\phi = 0.85$ , $L = 1.6$ .....	151
5.3.2.3	LES Multiple-Burner Setup 2, $P_{th} = 30 \text{ kW/burner}$ , $\phi = 0.85$ , $L = 1.6$ ,.....	159
5.3.2.4	Estimation of the Convective Time Delay in the LES.....	170
5.4	Concluding Remarks for the Discussion of the Numerical Results .....	172
<b>6.</b>	<b>Summary and Conclusions.....</b>	<b>175</b>
	<b>Bibliography .....</b>	<b>179</b>



## Nomenclature

### *Latin*

$a$	Thermal diffusivity
$a_x$	Axial
$A^+, A^-$	Pressure amplitude of an acoustic wave
$A_n$	Surface area of the outlet neck
$A_{SD}$	Flow cross-section of the swirl duct
$A_i$	Pre-exponential factor for reaction $i$
$A$	Cross-section
$b$	Relaxation coefficient
$B$	Burner transfer matrix
$c_0$	Speed of sound
$c_w$	Specific constant
$c_p$	Specific heat capacity at constant pressure
$c_x$	Constant
$C_s$	Smagorinsky constant
$Co$	Courant number
$\dot{D}$	Angular momentum flux
$D_k$	Diffusion coefficient of species $k$
$D_t$	Turbulent diffusivity
$Da$	Damköhler Number
$E_i$	Activation energy of reaction $i$
$E$	Activation energy for the reaction of fuel to products
$f_{HR}$	Helmholtz resonator frequency
$f_i$	Volumetric force in direction $i$
$f$	Frequency
$G$	Gain
$h_k$	Total enthalpy of species $k$
$h$	Total enthalpy
$\dot{i}$	Axial momentum flux
$I$	(Mean) OH*-intensity
$I'$	OH*-intensity fluctuation
$j_i^{d,k}$	Diffusive flux
$j_i^q$	Flux of energy
$k_i^{f,b}$	Reaction rate for the forward/backward reaction of reaction $i$
$k$	Turbulent kinetic energy

$Ka$	Karlovitz Number
$l_{n, \text{equ}}$	Equivalent length of the neck
$l_F$	Flame thickness
$l_\delta$	Thickness of the consumption layer
$l$	Characteristic length scale
$L_i$	$i$ -th energy loss process
$L$	Swirler mass flow ratio
$Le$	Lewis Number
$\dot{m}$	Mass flow
$p'$	Pressure oscillation
$p_\infty$	Ambient pressure
$p$	Static pressure
$Pr$	Prandtl Number
$\dot{q}$	Heat release rate
$q'$	Heat release oscillation
$\dot{Q}$	Volumetric heat release rate
$r_i$	Reaction velocity
$R$	Gas constant, reflection coefficient of an acoustic boundary
$Re$	Reynolds Number
$r$	Radial coordinate
$R_1 \sin \alpha$	Eccentricity of the swirl duct
$R_n$	Radius of the neck
$R_{\text{spec}}$	Specific gas constant
$R_o$	Characteristic Radius
$S_{\text{th}}$	Theoretical swirl number
$S_{ij}$	Strain rate tensor
$s_L$	Laminar burning velocity
$s_t$	Turbulent burning velocity
$S$	Swirl number
$Sc$	Schmidt Number
$St$	Strouhal number
$t$	Time
$T$	Temperature
$\mathbf{T}$	Transfer matrix
$u_i$	Velocity component in direction $i$
$u'_t$	Velocity of the energy-containing turbulent eddies
$V_{\text{HR}}$	Helmholtz resonator volume
$V$	Volume

$V_k$	Diffusion velocity of species $k$
$x_i$	Cartesian coordinate in direction $i$
$x, y, z$	Cartesian coordinates
$X_k$	Mole fraction of species $k$
$Y_i$	Mass fraction of species $i$
$z_0$	Specific acoustic impedance of a gas/fluid
$z_B$	Specific acoustic impedance of an acoustic boundary
$Z_i$	Element mass fraction of element $i$
$Z$	Pre-exponential factor for the reaction velocity, reduced specific acoustic impedance

### *Greek*

$\alpha$	Thermal diffusivity, pressure wave coefficient, factor for dependency of $I'$ on $Y'_{\text{Fuel}}$
$\beta$	Temperature exponent
$\gamma$	Ratio of specific heats
$\delta_{ij}$	Kronecker Symbol
$\Delta$	LES filter width, difference
$\Delta t$	Time step
$\delta$	Cell-face distance coefficient
$\epsilon$	Turbulent dissipation rate
$\eta$	Kolmogorov length scale
$\theta$	Reaction progress variable
$\lambda$	Thermal conductivity, wave length of an acoustic wave
$\mu$	Dynamic viscosity
$\nu_{ki}$	Stoichiometric coefficient of species $k$ in reaction $i$
$\nu$	Kinematic viscosity
$\Xi$	Relaxation factor
$\xi$	Mixture fraction
$\rho$	Density
$\tau_{ij}$	Viscous stress tensor
$\tau$	Time scale, time delay
$\varphi$	Phase
$\phi$	(Fuel-air) equivalence ratio
$\chi$	Scalar dissipation rate
$\psi$	Compressibility of the fluid
$\dot{\omega}_k$	Reaction rate of species $k$
$\omega$	Velocity of the outgoing pressure wave, angular frequency

## *Acronyms*

BC	Boundary condition
CC	Combustion chamber
CFD	Computational Fluid Dynamics
DNS	Direct Numerical Simulation
FFT	Fast Fourier Transformation
FGM	Flamelet Generated Manifold
GRI	Gas Research Institute
HR	Helmholtz resonator
ILDM	Intrinsic Low Dimensional Manifold
IP	Inner plenum
IRZ	Inner recirculation zone
IS	Inner swirler
LES	Large-Eddy Simulation
LF-Mode	Low-frequency mode
MBS	Multiple-burner setup
MBS1	Multiple-burner setup1
MBS2	Multiple-burner setup2
OP	Operating point
ORZ	Outer recirculation zone
OTP	Outer plenum
OTS	Outer swirler
ox	Oxidizer
PISO	Pressure-Implicit Split-Operator
PIV	Particle Image Velocimetry
PVC	Precessing Vortex Core
RANS	Reynolds Averaged Navier Stokes
rec	Recirculated
RMS	Root mean square
SBS	Single-burner setup
SGS	Subgrid Scale
STP	Standard pressure and temperature ( $T_n = 273$ K, $p_n = 1013$ mbar)
th	Theoretical, Thermal
UTFC	Unified Turbulent Flame Speed Closure

## *Superscripts*

$\vec{\cdot}$	Vectorial value
$\bar{\cdot}$	Time mean/ensemble averaged/spatially averaged value

$\tilde{\cdot}$	Favre-averaged/Favre-filtered value; averaged value over PDF
$\cdot'/'$	Fluctuating/unresolved component

## *Subscripts*

$\infty$	Values at far field conditions
ax	Axial
$c$	Chemical
$d$	Downstream
eff	effective
$i, j, k, n$	Indexes
IP	Inner plenum
IRZ	Inner recirculation zone
IS	Inner swirler
L	Laminar
mix	Mixture
ORZ	Outer recirculation zone
OTP	Outer plenum
OTS	Outer swirler
ox	Oxidizer
r	Radial
rec	Recirculated
RMS	Root mean square
SGS	Subgrid Scale
t	Turbulent, tangential
th	Theoretical, Thermal
$u$	Unburned, upstream
$\eta$	Kolmogorov scale



# 1. Introduction

Current predictions estimate the energy consumption in 2040 at 86500 PJ [1], thus a continuous growth of the world's energy consumption is expected (Figure 1.1). In order to cope with this development, it will be inevitable to provide energy from sustainable sources while simultaneously minimizing environmental impact.

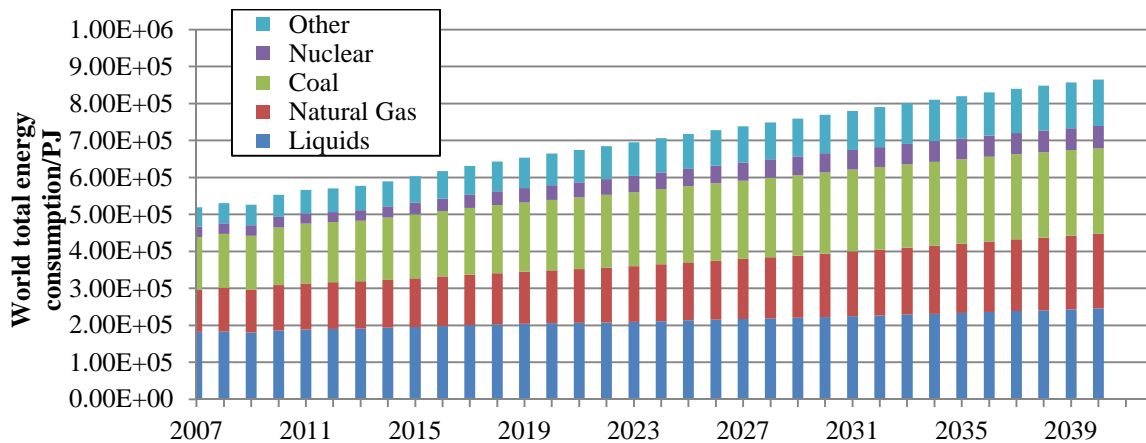


**Figure 1.1. Projection of the world energy consumption (reference case) [1]**

The major part of the energy demand is covered by conventional energy sources. Most conventional energy sources, except e.g. nuclear power, convert the chemical energy stored in fossil fuels into electrical power or heat. However, conventional energy sources can cause pollutant emissions which result in serious ecological damage. In addition, conventional energy sources that involve combustion processes lead to emission of greenhouse gases which are suspected to change the world's climate. One way to cope with this problem is to provide a significant amount of the demanded energy from renewable energy sources, such as wind power, solar power and hydropower. Unfortunately, the potential of renewable energy sources to provide energy with the necessary efficiency and reliability is highly location-dependant. Additionally, adequate technologies are needed, which provide the possibility to store large amounts of energy, since wind and sun radiation are subject to high fluctuations. However, such technologies are not yet available and alternative strategies are necessary.

Increasing the efficiency of conventional energy sources also holds the possibility to reduce their environmental impact. Today, combustion is the major process in the field of conventional/fossil power generation. Hence, the optimization of combustion processes in terms of efficiency and pollutant emissions provides a high potential for increasing the environmental compatibility of conventional power generation. Furthermore, modern gas turbines installed in gas-fired power plants are capable of compensating for power fluctuations from renewable energy sources, as they combine high efficiency with high flexibility regarding start-up time.

Combustion processes are highly complex and improvements in efficiency and emissions are not easily achieved. As an example, the reduction of thermal  $\text{NO}_x$ -emissions can be accomplished by reducing the temperature in the combustion chamber. This is realised by operating combustors with lean (partially) premixed flames, which unfortunately are prone to flame instabilities. As a consequence, acoustic velocity and pressure perturbations can lead to flame and heat release fluctuations. Such flame-acoustics interactions, also known as “thermoacoustics”, can result in broadband combustion noise and/or combustion instabilities. In contrast to the generation of broadband combustion noise, where the flame mainly amplifies turbulence-induced noise, combustion instabilities are only generated when a strong coupling between the flame and the acoustic oscillations is present. Combustion instabilities lead to pressure oscillations with very high amplitudes and may result in damage to the combustor or complete engine failure. They are often associated with acoustic resonances in combustor components which induce periodic fluctuations of the air and/or fuel flow rate which result in oscillations of the heat release.

### **1.1 Motivation**

The sensitivity of flames to acoustic excitations has been known for long time. In 1858 Le Conte reported his observation of singing flames, which interacted with the music played during a concert [2]. This observation was of great interest in the science community and was also discussed by other scientists [3, 4]. While singing flames may represent a fascinating phenomenon, the interaction of flames with acoustic oscillations represents an ongoing challenge in the design and operation of combustion systems. Therefore solutions for the avoidance of instabilities in modern low- $\text{NO}_x$  combustors are necessary, since efficiency and low pollutant emissions become more and more important, as stated in the previous section.

Rayleigh formulated a criterion [5] which describes under what conditions a flame adds energy to the acoustic field. It states, that combustion chamber pressure and heat release must oscillate in phase in order to generate unstable modes. However, the satisfaction of the Rayleigh-criterion does not necessarily imply that a combustor becomes unstable. Combustion instabilities with high pressure amplitudes are only excited, if the amount of energy transferred to the unstable mode exceeds the losses due to viscous effects and sound radiation [6, 7].

One way to cope with combustion instabilities is to apply active [8–12] or passive [13, 14] damping methods. However, applying these methods to different combustors usually requires specific adjustments. Alternatively, it is possible to only operate the combustor in its stable regime. However, this limits its operating range and flexibility, which are important features of modern combustors. As a consequence, the most favourable approach is to prevent the occurrence of combustion instabilities by an adequate combustor design. In order to evaluate the stable regime of a combustion system, it is common to measure and determine combustor

transfer matrices and Flame Transfer Functions (FTFs) [15–23] or to perform acoustic analysis [24–26].

Detailed stability analysis is mostly performed with single-burner flames. However, modern combustors often operate with multiple-burner arrangements, as the combustion chamber design is simpler in comparison to multiple single-burner combustion chambers. Most modelling approaches assume that no interactions take place between neighbouring flames. As a consequence, they are not able to take account for nonlinear effects induced by flame-flame interactions in multiple-burner systems.

Recent studies have shown that flow fields and thermoacoustic flame response characteristics in multiple-burner arrangements can differ considerably from single-burner combustors. Hirsch et al. found significant differences in the flow fields of swirl jets in an annular combustion chamber compared to the single-burner combustion chamber [27]. Worth and Dawson investigated the influence of the distance between the single-burners on the flame-flame interaction and the FTF [28, 29]. They demonstrated that reducing the distance between the single-burners can result in large-scale flame-flame interactions, which show a strong impact on the thermoacoustic flame response. Staffelbach et al. performed an LES of an annular combustor and concluded that the FTF of the single-burner flame reproduces the FTFs of the multiple-burner flames reasonably well. However, the distance between the single-burners in their simulations constituted several nozzle diameters, which may prevent large-scale flame interactions.

As a result, it is an ongoing discussion about whether or not or to what extent FTFs of single-burner flames are representative for the flame dynamics in multiple-burner arrangements and how model approaches can be extended in order to reliably predict combustion instabilities in multiple-burner arrangements.

## 1.2 Objective

The first objective of the investigations and discussions shown in this thesis is to analyse the influence of multiple-burner setups on combustion instabilities in comparison to the corresponding single-burner setup. The second objective is to examine the influence of different arrangements of the multiple burners.

In order to achieve the named objectives, experimental and numerical studies were performed. Measurements of pressure oscillations were conducted in a modular combustor, which was operated in single-burner and two multiple-burner setups. The swirl-stabilized flame was operated under atmospheric conditions in partially-premixed mode, using natural gas as fuel.

The purpose of these experiments was the global characterization of the thermoacoustic stability of the modular combustor in dependency on the combustor setup. In addition, mechanisms should be identified which result in different thermoacoustic responses of the

single-burner and the multiple-burner setups. This was done by using high-speed OH\*-chemiluminescence imaging and numerical studies. Large-Eddy simulations (LESs) of the non-reactive and reactive flow were carried out for the single-burner setup and one multiple-burner setup. The objective of the LESs was to identify possible feedback mechanisms of unstable modes and to investigate the influence of the multiple-burner setup on the flow conditions in the combustor.

### **1.3 Thesis Outline**

After the introduction in Chapter 1, the theoretical basics are discussed in Chapter 2. In the first part, the governing equations of reactive flows are introduced. The phenomena of turbulence and common approaches for modelling turbulence are discussed. The second part of Chapter 2 focuses on the fundamentals of combustion. Reaction kinetics of combustion processes are briefly discussed. Idealized systems are introduced, which are commonly used to study combustion processes. The complex interaction of turbulence and combustion is described, as well as several model approaches for turbulent combustion. Chapter 2 ends with the introduction of the Unified-Turbulent-Flame-Speed-Closure-Model (UTFC), which was used to perform the simulations of the turbulent flames in the scope of this thesis.

Chapter 3 is devoted to combustion instabilities. The basic driving mechanisms and damping processes are explained. Subsequently, frequently applied control and model approaches are discussed. The quantities used to define acoustic boundaries and the problems that occur when dealing with realistic acoustic boundaries are described in the last part of Chapter 3.

Chapter 4 starts with descriptions of the modular combustor, the used double-concentric swirl nozzle and the experimental setup. Before the experimental results are discussed, a summary of the investigated operating points is given. The typical combustor modes are presented followed up by a detailed analysis of the observed instabilities at selected operating points. Chapter 4 closes with the discussion of the global stability chart of all combustor setups and some concluding thoughts on the experimental results.

In Chapter 5, the numerical investigations are discussed. The numerical setup and the used computational grids are presented. The discussion of the results starts with the analysis of the non-reactive flows and concludes with the results for the simulations of the reactive flows. Chapter 5 ends with a summary of the numerical results and their conclusive discussion.

Chapter 6 concludes the thesis with a summary and some concluding remarks.

## 2. Theoretical Background

This chapter addresses the theoretical background of the investigations presented in this thesis. The governing equations of reactive flows, the characteristics and the modelling of turbulent flows, the fundamentals of combustion and the topic of turbulent combustion modelling are briefly discussed.

### 2.1 Governing Equations of Reactive Flows

The governing equations that describe the motion of reactive flows are

- the conservation equation of momentum,
- the conservation equation of mass,
- the conservation equation of energy.

These equations are derived from balance equations applied to an infinitesimal control volume and describe the fluid motions of reacting and non-reacting flows. Derivations and detailed explanations of these equations can be found in literature [30–33]. The following explanations are based on the named references.

#### 2.1.1 Conservation of Momentum

The conservation equations of momentum are also called the Navier-Stokes-Equations. They may be written in the following way using Einstein's index notation:

$$\frac{\partial}{\partial t}(\rho u_i) + \frac{\partial}{\partial x_j}(\rho u_i u_j) = -\frac{\partial p}{\partial x_i} + \frac{\partial \tau_{ij}}{\partial x_j} + \rho \sum_{k=1}^N Y_k f_{k,i}. \quad (2.1)$$

In Equation (2.1),  $u_i$  denotes the  $i$ -th component of the velocity,  $\rho$  is the density of the fluid and  $p$  stands for the static pressure.  $Y_k$  is the mass fraction of the  $k$ -th species and  $f_{k,i}$  represents a volumetric force (e.g. gravity, buoyancy) acting in direction  $i$  on the species  $k$ . The term  $\rho \sum_{k=1}^N Y_k f_{k,i}$  is often negligible and is neglected in the following discussion. The viscous stress-tensor  $\tau_{ij}$  is defined according to the linear Newtonian viscous-stress law:

$$\tau_{ij} = \mu \left( 2S_{ij} - \frac{2}{3} \delta_{ij} \frac{\partial u_i}{\partial x_j} \right), \text{ where } S_{ij} = \left( \frac{\partial u_i}{\partial x_j} + \frac{\partial u_j}{\partial x_i} \right). \quad (2.2)$$

In Equation (2.2),  $S_{ij}$  is the strain rate tensor and  $\mu$  is the dynamic viscosity. Combustion processes lead to very high temperature gradients and strong changes in the viscosity  $\mu$  and the density  $\rho$ . In this way, the influence of combustion on the fluid motion is included in Equation (2.1).

### 2.1.2 Conservation of Mass

The conservation equation of mass is also called the continuity equation. It is defined in the following way:

$$\frac{\partial \rho}{\partial t} + \frac{\partial(\rho u_i)}{\partial x_i} = 0. \quad (2.3)$$

The mass conservation equation for a species  $k$  reads:

$$\frac{\partial(\rho Y_k)}{\partial t} + \frac{\partial(\rho u_i Y_k)}{\partial x_i} = -\frac{\partial j_i^{d,k}}{\partial x_i} + \dot{\omega}_k \quad \text{for } k = 1, \dots, N, \quad (2.4)$$

with the diffusive flux  $j_i^{d,k}$  for the species  $k$ . The term  $\dot{\omega}_k$  represents the corresponding reaction rate of a species  $k$ . The diffusive fluxes are usually calculated according to Ficks' law:

$$j_i^{d,k} = -\rho D_k \frac{\partial Y_k}{\partial x_i} \quad \text{for } k = 1, \dots, N, \quad (2.5)$$

with the diffusion coefficient  $D_k$  of the species  $k$ . Using the dimensionless Schmidt-Number

$$Sc_k = \frac{\mu}{\rho D_k}, \quad (2.6)$$

which is defined as the ratio of momentum and mass diffusivity, Equation (2.6) can be formed to

$$j_i^{d,k} = -\frac{\mu}{Sc_k} \frac{\partial Y_k}{\partial x_i}. \quad (2.7)$$

For a system of  $N$  species it holds:

$$\sum_{k=1}^N Y_k = 1, \quad \sum_{k=1}^N Y_k j_i^{d,k} = 0 \implies \sum_{k=1}^N \dot{\omega}_k = 0. \quad (2.8)$$

### 2.1.3 Conservation of Energy

The equation for the conservation of energy can be defined for different quantities, such as total energy or enthalpy. The balance equation for the total enthalpy  $h$  reads:

$$\frac{\partial(\rho h)}{\partial t} + \frac{\partial}{\partial x_i}(\rho u_i h) = \frac{Dp}{Dt} - \frac{\partial j_i^q}{\partial x_i} + \tau_{ij} \frac{\partial u_i}{\partial x_j} + q_s + \rho \sum_{k=1}^N Y_k f_{k,i} V_{k,i}. \quad (2.9)$$

The term  $\rho \sum_{k=1}^N Y_k f_{k,i} V_{k,i}$  stands for the power produced by a volumetric force on the species  $k$  in the direction  $i$ , where  $V_{k,i}$  is the corresponding diffusion velocity. It is neglected in the following, since in most applications it is small compared to the other terms. The term  $\tau_{ij}(\partial u_i/\partial x_j)$  represents the source term for viscous heating and  $q_s$  represents heat sources such as radiation or an electrical spark. The flux of energy  $j_i^q$  may be calculated by:

$$j_i^q = -\lambda \frac{\partial T}{\partial x_i} + \rho \sum_{k=1}^N h_k j_i^{d,k}. \quad (2.10)$$

The first term on the right hand side is the heat diffusion term according to Fourier with the thermal conductivity  $\lambda$ . The second term represents the diffusion of species with different enthalpies, which is a typical process in combustion. Equation (2.10) can be rewritten as

$$j_i^q = -\frac{\mu}{Pr} \left[ \frac{\partial h}{\partial x_i} + \sum_{k=1}^N \left( \frac{Pr}{Sc_k} - 1 \right) h_k \frac{\partial Y_k}{\partial x_i} \right], \quad (2.11)$$

where  $Pr$  denotes the dimensionless Prandtl-Number, which is defined as the ratio of the kinematic viscosity and the thermal diffusivity  $\alpha$ :

$$Pr = \frac{\nu}{\alpha}. \quad (2.12)$$

The thermal diffusivity is defined by  $\alpha = \lambda/c_p$ , where  $c_p$  stands for the specific heat capacity of the mixture. The Lewis-Number  $Le_k$  is defined as the ratio of  $Pr$  to  $Sc_k$

$$Le_k = \frac{Pr}{Sc_k}, \quad (2.13)$$

and describes the ratio of thermal and mass diffusivity for the species  $k$ .

#### 2.1.4 Equation of State

The balance equations discussed in 2.1.1-2.1.3 are not mathematically closed, since changes in both pressure and temperature cause variations in the density. If the density changes, then the pressure is unknown and has to be determined using an additional equation which describes the relationship between pressure and density. For gaseous flows, this is usually done using the ideal gas law:

$$p = \rho R_{\text{spec}} T, \quad (2.14)$$

with  $R_{\text{spec}}$  being the specific gas constant of the mixture.

## 2.2 Turbulence

In fluid mechanics, it is common to make a distinction between laminar and turbulent flows. In technical combustion chambers, flows are turbulent in most cases. In laminar flows, the fluid flows in parallel streamlines, whereas turbulent flows are characterised by chaotic and three-dimensional fluid motions. The Reynolds-Number  $Re$  is commonly used to assess the flow state. It describes the ratio of the destabilizing, inertial forces to the stabilizing, viscous forces in a fluid motion and is defined by:

$$Re = \frac{u \cdot l_{\text{char}}}{\nu}. \quad (2.15)$$

In Equation (2.15)  $u$  denotes the mean velocity of the flow,  $l_{\text{char}}$  stands for the characteristic length scale of the flow and  $\nu$  is the kinematic viscosity of the fluid. At high Reynolds-Numbers, flows tend to be unstable and show turbulent fluid motions. At low Reynolds-Numbers flows are laminar, as the viscous forces dominate the fluid motion. The critical Reynolds-Number at which a flow becomes unstable depends on the application. Flows in pipes typically become turbulent at Reynolds-Numbers above  $Re \approx 2300$ . Due to the chaotic flow patterns in turbulent flows, transport processes of momentum, heat or species are significantly increased compared to laminar flows. Turbulent structures are generated in and derive their energy out of high velocity gradients in the normal direction of the flow streamlines.

### 2.2.1 Time and Length Scales in Turbulent Flows

In turbulent flows eddies with different time and length scales are present. The large turbulent structures carry most of the turbulent kinetic energy. The characteristic turbulent length scale  $l_t$  of the largest eddies is in most cases determined by geometrical parameters. Inside the turbulent flow, turbulent kinetic energy is transferred from the large eddies to smaller eddies. The large eddies are unstable and break up into smaller eddies which contain the energy of the original eddies. The smaller turbulent structures also break up into even smaller structures. This process continues until eddies are formed, whose length scales are so small that they are dissipated due to the viscous forces inside the fluid. The transfer process of turbulent kinetic energy from larger scales to smaller scales is known as the energy cascade, which is based on the notion of Richardson [34]. The energy cascade describes the distribution of kinetic energy in reference to the turbulent length scale. The range with the largest eddies is called the

energy-containing range. The dissipation range denotes the range with the smallest turbulent structures and the inertial subrange refers to the range between the largest and the smallest turbulent structures. In the inertial subrange, mainly turbulent kinetic energy is transported from larger to smaller scales. Inertial effects are dominating and viscous effects are negligible [35].

Kolmogorov [36, 37] postulated that in a turbulent flow with a sufficiently high Reynolds-Number the smallest structures are universal and isotropic, i.e. in contrast to the largest eddies in the flow fields, they do not contain any directional or geometrical information. The length scale of these universal turbulent structures is known as the Kolmogorov length scale. The Kolmogorov length scale  $\eta$  is only a function of the kinematic viscosity  $\nu$  and the turbulent dissipation rate  $\epsilon$ . The Kolmogorov length scale  $\eta$ , the Kolmogorov velocity scale  $u_\eta$  and the Kolmogorov time scale  $\tau_\eta$  represent the Kolmogorov scales:

$$\eta = \left(\frac{\nu^3}{\epsilon}\right)^{1/4}, \quad u_\eta = \left(\frac{\nu}{\epsilon}\right)^{1/2}, \quad \tau_\eta = (\nu\epsilon)^{1/4}. \quad (2.16)$$

It can be shown by dimensional analysis that the ratio of the Kolmogorov length scale to the characteristic length scale depends on the Reynolds-Number [35]:

$$\frac{\eta}{l_t} \propto Re^{-\frac{3}{4}}. \quad (2.17)$$

Therefore, the difference between the Kolmogorov scale  $\eta$  and the characteristic length scale  $l_t$  increases with increasing Reynolds-Number. In technical flows, the characteristic length scale of the turbulent eddies are often determined by geometrical parameters. Hence, an increase in the Reynolds-Number leads to a significantly smaller value of the Kolmogorov length scale. As a consequence, the necessary computational resources for direct numerical simulations (DNSs) of turbulent flows with high Reynolds-Numbers (e.g. in technical combustion chambers) are not available in most cases, since performing a DNS requires resolving all turbulent time and length scales. In order to simulate turbulent flows with acceptable computational effort using CFD-Methods (Computational Fluid Dynamics), it is necessary to apply alternative approaches. One possibility is to introduce statistical methods to describe turbulent flow motions. These are discussed in the subsequent section.

### 2.2.2 Statistical Description of Turbulence

Due to the chaotic fluid motions in turbulent flows, it is convenient to describe the turbulent fluctuations in a statistical manner and split any quantity  $g$  into its mean value  $\bar{g}$  and its fluctuation  $g'$ :

$$g = \bar{g} + g' \quad \text{with} \quad \bar{g}(x_i, t) = \lim_{N \rightarrow \infty} \frac{1}{N} \sum_N^{n=1} g(x_i, t). \quad (2.18)$$

The mean value of the fluctuating component is defined as equal to zero, i.e.  $\bar{g}' = 0$ . This statistical approach is called Reynolds averaging. Applying Reynolds averaging to the governing equations for variable density flows (2.1), (2.3) and (2.9) leads to several unclosed correlations with density fluctuations  $\overline{\rho'g'}$  for any quantity. Therefore, it is common to introduce mass-weighted averages, which are called Favre averages:

$$\tilde{g} = \frac{\overline{\rho g}}{\bar{\rho}}. \quad (2.19)$$

Similar to Reynolds averaging, any quantity is divided into a mean and a fluctuating component:

$$g = \tilde{g} + g'' \quad (2.20)$$

and the mean value of the fluctuating component is equal to zero:

$$\overline{\tilde{g}''} = 0. \quad (2.21)$$

As a result, one obtains the averaged balance equations:

$$\frac{\partial \bar{\rho}}{\partial t} + \frac{\partial(\bar{\rho}\tilde{u}_i)}{\partial x_i} = 0, \quad (2.22)$$

$$\frac{\partial(\bar{\rho}\tilde{u}_i)}{\partial t} + \frac{\partial(\bar{\rho}\tilde{u}_i\tilde{u}_j)}{\partial x_i} + \frac{\partial \bar{p}}{\partial x_i} = \frac{\partial}{\partial x_i} (\bar{\tau}_{ij} - \overline{\rho u_i'' u_j''}), \quad (2.23)$$

$$\frac{\partial(\bar{\rho}\tilde{Y}_k)}{\partial t} + \frac{\partial(\bar{\rho}\tilde{u}_i\tilde{Y}_k)}{\partial x_i} = -\frac{\partial}{\partial x_i} (\bar{j}_i^{d,k} + \overline{\rho u_i'' Y_k''}) + \bar{\omega}_k \quad \text{for} \quad k = 1, \dots, N \quad (2.24)$$

$$\frac{\partial(\bar{\rho}\tilde{h})}{\partial t} + \frac{\partial(\bar{\rho}u_i\tilde{h})}{\partial x_i} = \frac{D\bar{p}}{Dt} - \frac{\partial}{\partial x_i} (\bar{j}_i^q - \overline{\rho u_i'' h''}) + \overline{\tau_{ij} \frac{\partial u_i}{\partial x_j}}. \quad (2.25)$$

In Equation (2.25), the heat source term  $\bar{q}_s$  is neglected. In addition to the unclosed terms of the laminar diffusion fluxes of species and enthalpy, the Favre-averaged balance equations

contain unclosed correlations  $\overline{u_i'' u_j''}$ ,  $\overline{u_i'' Y_k''}$  and  $\overline{u_i'' h_i''}$ , which are unknown and have to be modelled. The tensor  $\overline{u_i'' u_j''}$  is also known as the Reynolds-Stress tensor. The diagonal sum of the Reynolds-Stress tensor is used to calculate the turbulent kinetic energy  $k$ , whose value can be used to assess the turbulent intensity. The definition of  $k$  reads as follows:

$$k = \frac{1}{2} \sum_{k=1}^3 \overline{u_i'' u_j''}. \quad (2.26)$$

### 2.2.3 Turbulence Modelling

Turbulence Models can be differentiated by their requirements for the spatial resolution of the computational grid. In RANS-Models (Reynolds-Averaged-Navier-Stokes) all turbulent scales are modelled and only the mean flow has to be resolved by the computational grid, which leads to comparably low computational costs. The Large-Eddy-Simulation (LES) only models the small turbulent structures, whereas the large, energy containing eddies are resolved. This requires finer grid resolutions and leads to significantly increased simulation times.

#### 2.2.3.1 RANS-Models

In general, in RANS-Models the turbulent viscosity assumption made by Boussinesq in [38] is applied to model the Reynolds-Stress tensor [33]:

$$\overline{\rho u_i'' u_j''} = -\mu_t \left( \frac{\partial \tilde{u}_i}{\partial x_j} + \frac{\partial \tilde{u}_j}{\partial x_i} - 2\delta_{ij} \frac{\partial \tilde{u}_k}{\partial x_k} \right) + \frac{2}{3} \bar{\rho} k. \quad (2.27)$$

In Equation (2.27)  $\mu_t$  stands for the turbulent dynamic viscosity and  $\delta$  is the Kronecker Symbol. Various approaches exist to calculate the turbulent viscosity  $\mu_t$ , involving algebraic models (for example the Prandtl mixing length model), one-equation models (Prandtl-Kolmogorov model) and numerous two-equation models. One of the most commonly used two-equation models is the  $k$ - $\epsilon$ -Model, which was proposed by Jones and Launder [39].

In the  $k$ - $\epsilon$ -Model the turbulent viscosity is calculated by:

$$\mu_t = \bar{\rho} C_\mu \frac{k^2}{\epsilon}. \quad (2.28)$$

The turbulent kinetic energy and its dissipation rate are modelled by two additional balance equations:

$$\frac{\partial(\bar{\rho}k)}{\partial t} + \frac{\partial(\rho\tilde{u}_i k)}{\partial x_i} = \frac{\partial}{\partial x_i} \left[ \left( \mu + \frac{\mu_t}{\sigma_k} \right) \frac{\partial k}{\partial x_i} \right] + P_k - \bar{\rho}\epsilon, \quad (2.29)$$

$$\frac{\partial(\bar{\rho}\epsilon)}{\partial t} + \frac{\partial(\rho\tilde{u}_i \epsilon)}{\partial x_i} = \frac{\partial}{\partial x_i} \left[ \left( \mu + \frac{\mu_t}{\sigma_\epsilon} \right) \frac{\partial \epsilon}{\partial x_i} \right] + C_{\epsilon 1} \frac{\epsilon}{k} P_k - C_{\epsilon 2} \bar{\rho} \frac{\epsilon^2}{k}, \quad (2.30)$$

$$\text{where } P_k = -\bar{\rho} \widetilde{u_i'' u_j''} \frac{\partial \tilde{u}_i}{\partial x_j}. \quad (2.31)$$

$C_\mu$ ,  $\sigma_k$ ,  $\sigma_\epsilon$ ,  $C_{\epsilon 1}$  and  $C_{\epsilon 2}$  are model constants with standard values of

$$C_\mu = 0.09, \sigma_k = 1.0, \sigma_\epsilon = 1.3, C_{\epsilon 1} = 1.44, C_{\epsilon 2} = 1.92, \quad (2.32)$$

as proposed by Launder and Sharma [40]. The balance equations for  $k$  and  $\epsilon$  are formulated for high Reynolds-Numbers, assuming homogenous, isotropic turbulence. However, as discussed in 2.2.1, this is only valid for the smallest turbulent structures. Extensions for the  $k$ - $\epsilon$ -Model have been formulated [41, 42] and two-equation-models with different approaches exist, as for example the  $k$ - $\omega$ -Model [43]. There are also approaches, where balance equations for the Reynolds-Stress tensor are derived and closed, which leads to the Reynolds-Stresses-Models (RSMs). Further details about the RSMs and all named models with additional references can be found in [35].

The unclosed terms  $\widetilde{u_i'' Y_k''}$  and  $\widetilde{u_i'' h''}$  in the balance equations are usually modelled by applying the Boussinesq assumption for the transport of mass and energy:

$$\widetilde{\rho u_i'' Y_k''} = -\frac{\mu_t}{Sc_t} \frac{\partial \bar{Y}_k}{\partial x_i}, \quad (2.33)$$

$$\widetilde{\rho u_i'' h''} = -\frac{\mu_t}{Pr_t} \frac{\partial \bar{h}}{\partial x_i}, \quad (2.34)$$

where  $Sc_t$  is the corresponding turbulent Schmidt-Number and  $Pr_t$  the turbulent Prandtl-Number.

The laminar diffusive fluxes of species and enthalpy are often neglected in turbulent flows. They can also be taken into account by adding a laminar diffusivity to the turbulent viscosity  $\mu_t$  in the Equations (2.33) and (2.34) or be modelled by other expressions. As an example, the species laminar diffusion fluxes are generally modelled by [33]:

$$\overline{j_i^{d,k}} = -\overline{\rho D_k \frac{\partial Y_k}{\partial x_i}} \approx -\bar{\rho} \bar{D}_k \frac{\partial \tilde{Y}_k}{\partial x_i}, \quad (2.35)$$

with  $\bar{D}_k$  being the mean species molecular diffusion coefficient. The laminar heat diffusion flux is generally calculated by:

$$\overline{\lambda \frac{\partial T}{\partial x_i}} \approx \bar{\lambda} \frac{\partial \tilde{T}}{\partial x_i}, \quad (2.36)$$

with  $\bar{\lambda}$  representing the mean thermal diffusivity.

### 2.2.3.2 Large-Eddy-Simulation

The LES resolves the large turbulent eddies, whereas the smaller turbulent scales are modelled by a turbulence model. The large turbulent structures strongly depend on geometrical parameters of the system and are considered to be anisotropic and non-universal. The small turbulent scales are assumed to be more universal and isotropic. Hence, turbulence models are more suited to describe the smallest turbulent structures. In addition, in contrast to RANS-Methods, the LES captures large coherent flow structures and unsteady features of the flow, which may influence the characteristics of the mean flow field. As a consequence, the LES often provides more precise predictions of turbulent flows. However, it requires higher grid resolutions than RANS-Methods and the turbulent flow is resolved in time. These aspects of the LES lead to a significant increase in the necessary computational effort compared to RANS-Methods.

#### *Filtering of the balance equations*

The separation of the turbulent scales in the LES is performed by a spatial filtering of any quantity:

$$g = \bar{g} + g'. \quad (2.37)$$

For flows with variable density, a mass-weighted Favre-filtering operation is also applied:

$$g = \tilde{g} + g''. \quad (2.38)$$

The most common approach is to use the computational grid as an implicit filter. In this case, the filtered quantity ( $g', \tilde{g}$ ) equals the numerically resolved quantity. The unresolved component ( $g', g''$ ) is often named as the subgrid scale (SGS) part. Different approaches for LES-Filters have been developed, which are not discussed here. Details about these filters can be found for example in [35, 44].

Applying the filtering operations to the balance equations leads to the filtered balance equations for variable density flows:

$$\frac{\partial \bar{\rho}}{\partial t} + \frac{\partial(\bar{\rho}\tilde{u}_i)}{\partial x_i} = 0, \quad (2.39)$$

$$\frac{\partial(\bar{\rho}\tilde{u}_i)}{\partial t} + \frac{\partial(\bar{\rho}\tilde{u}_i\tilde{u}_j)}{\partial x_i} + \frac{\partial \bar{p}}{\partial x_i} = \frac{\partial}{\partial x_i} [\bar{\tau}_{ij} - \bar{\rho}(u_i\tilde{u}_j - \tilde{u}_i\tilde{u}_j)], \quad (2.40)$$

$$\frac{\partial(\bar{\rho}\tilde{Y}_k)}{\partial t} + \frac{\partial(\bar{\rho}\tilde{u}_i\tilde{Y}_k)}{\partial x_i} = -\frac{\partial}{\partial x_i} [j_i^{d,k} + \bar{\rho}(u_i\tilde{Y}_k - \tilde{u}_i\tilde{Y}_k)] + \bar{\omega}_k \quad \text{for } k = 1, \dots, N, \quad (2.41)$$

$$\frac{\partial(\bar{\rho}\tilde{h})}{\partial t} + \frac{\partial}{\partial x_i} (\rho u_i \tilde{h}) = \frac{D\bar{p}}{Dt} - \frac{\partial}{\partial x_i} [j_i^q - \bar{\rho}(u_i\tilde{h} - \tilde{u}_i\tilde{h})] + \tau_{ij} \frac{\partial u_i}{\partial x_j}. \quad (2.42)$$

Similar to the averaged balance equations discussed in 2.2.2, the filtered balance equations contain unknown correlations which have to be modelled. Besides the laminar diffusion fluxes of species and enthalpy, these are the unresolved Reynolds stresses  $(u_i\tilde{u}_j - \tilde{u}_i\tilde{u}_j)$ , the unresolved species  $(u_i\tilde{Y}_k - \tilde{u}_i\tilde{Y}_k)$  and the unresolved enthalpy fluxes  $(u_i\tilde{h} - \tilde{u}_i\tilde{h})$ .

### *Smagorinsky subgrid scale model*

The first subgrid scale model was proposed by Smagorinsky [45]. Due to its simplicity and robustness, it is a frequently applied subgrid scale model. The unresolved Reynolds stresses  $\tau_{ij}^{sgs} = (u_i\tilde{u}_j - \tilde{u}_i\tilde{u}_j)$  are modelled according to the Boussinesq assumption. For variable density flows, using Favre filtered quantities, the model for  $\tau_{ij}^{sgs}$  reads:

$$\tau_{ij}^{sgs} - \frac{1}{3}\tau_{kk}^{sgs}\delta_{ij} = -2\nu_t \left( \tilde{S}_{ij} - \frac{\delta_{ij}}{3}\tilde{S}_{kk} \right), \quad (2.43)$$

with the resolved part of the strain rate tensor  $\tilde{S}_{ij}$

$$\tilde{S}_{ij} = \frac{1}{2} \left( \frac{\partial \tilde{u}_i}{\partial x_j} + \frac{\partial \tilde{u}_j}{\partial x_i} \right). \quad (2.44)$$

The turbulent subgrid scale viscosity is modelled by:

$$\nu_t = (C_s\Delta)^2 |\tilde{S}| \quad \text{with } |\tilde{S}| = \sqrt{2\tilde{S}_{ij}\tilde{S}_{ij}}. \quad (2.45)$$

$C_s$  represents the Smagorinsky constant and is typically set to a value of  $C_s = 0.2$ . The unknown term  $\tau_{kk}^{sgs}$  is commonly modelled according to the expression proposed by Yoshizawa [46]:

$$\tau_{kk}^{sgs} = 2c_I \bar{\rho} \Delta^2 |\bar{S}|, \quad (2.46)$$

where  $c_I$  is a model constant. Since  $C_s$  depends on the flow configuration [44], Germano et al. [47] formulated an approach to automatically determine the adequate value of  $C_s$ . Further information and details about alternative subgrid scale models can be found in [35, 44].

The subgrid scale species and enthalpy fluxes are generally modelled similar to RANS:

$$\widetilde{u_i Y_k} - \tilde{u}_i \tilde{Y}_k = -\frac{\nu_t}{Sc_t} \frac{\partial \bar{Y}_k}{\partial x_i}, \quad (2.47)$$

$$\widetilde{u_i h_k} - \tilde{u}_i \tilde{h}_k = -\frac{\nu_t}{Pr_t} \frac{\partial \bar{h}}{\partial x_i}, \quad (2.48)$$

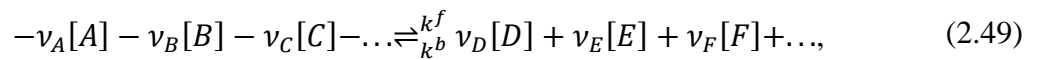
where  $Sc_t$  and  $Pr_t$  denote the subgrid scale Schmidt- and Prandtl-Number, respectively. The laminar diffusion fluxes of species and enthalpy are either neglected or also modelled similar to RANS approximations.

## 2.3 Fundamentals of Combustion

In this section, some of the fundamentals of combustion are briefly introduced. After some basics, the influence of turbulence on combustion is discussed, since reactive flows in technical combustion chambers are in turbulent most cases. Subsequently, the UTFC-Model (Unified-Turbulent-Flame-Speed-Closure) is described, which was used to perform the turbulent flame simulations.

### 2.3.1 Reaction Kinetics of Combustion Processes

In general, combustion is a chemical reaction where fuel is mixed with an oxidizer (in most cases air) and burned. Chemical reactions, and therefore also combustion processes, are described by chemical equations:



where  $\nu_{A\dots F}$  are the stoichiometric coefficients of the species  $A\dots F$ ,  $k^f$  is the reaction rate coefficient for the forward reaction and  $k^b$  the reaction rate coefficient for the backward

reaction. In general, chemical equations only describe the global reaction of reactants into products. However, a chemical reaction, as for example the combustion of methane with oxygen:



consists of numerous elementary reactions. For elementary reactions, the corresponding chemical equation represents the actual reaction taking place. The system of elementary reactions that describes a global reaction is usually called a reaction mechanism. A reaction mechanism which consists of  $N_r$  chemical reactions can be described by

$$\sum_{k=1}^{N_k} v_{ki}^f X_k \rightleftharpoons \sum_{k=1}^{N_k} v_{ki}^b X_k \quad i = 1 - N_r, \quad (2.51)$$

where  $v_{ki}^f$  and  $v_{ki}^b$  are the stoichiometric coefficients of the species  $k$  for the forward and backward reactions of the elementary reaction  $i$ .  $X_k$  represents the mole fraction of the species  $k$ . Thus the production rate  $\dot{\omega}_k$  of a species  $k$  can be determined by

$$\dot{\omega}_k = \sum_{i=1}^{N_r} v_{ki} r_i \quad \text{with } v_{ki} = (v_{ki}^f - v_{ki}^b) \quad i = 1, \dots, N_r, \quad (2.52)$$

with  $r_i$  being the reaction velocity of the elementary reaction  $i$  which is given by

$$r_i = k_i^f \prod_{k=1}^{N_k} [X_k]^{v_{ki}^f} - k_i^b \prod_{k=1}^{N_k} [X_k]^{v_{ki}^b}. \quad (2.53)$$

The respective reaction rate coefficient  $k_i$  may be calculated using the approach by Arrhenius [48] in its extended formulation [49]:

$$k_i = A_i T_i^\beta e^{-\frac{E_i}{RT}}. \quad (2.54)$$

$A_i$  is the pre-exponential factor,  $\beta$  stands for the temperature exponent,  $R$  denotes the gas constant and  $E_i$  represents the activation energy.

### 2.3.2 Modelling of Combustion Processes

Combustion processes can be found in all kinds of technical systems. Depending on the application, the reactive flow may be laminar or turbulent and reacts under premixed or non-premixed conditions. In premixed combustion, the fuel and the oxidizer are perfectly mixed

before they enter the combustion chamber. In non-premixed combustion, the mixing of the fuel and the oxidizer takes place simultaneously with the chemical reaction.

Laminar premixed combustion can be found in gas stoves, heaters and Bunsen burners. Turbulent premixed combustion is frequently applied in stationary gas turbines and internal combustion engines. A well-known example for laminar non-premixed combustion is a candle, whereas turbulent non-premixed combustion is found in aero-engines and diesel engines.

In addition, combustion processes can be subdivided into lean and fuel rich combustion. This is usually described by the (fuel-air) equivalence ratio  $\phi$ . In the case where air is used as oxidizer, it is defined in the following way:

$$\phi = \frac{X_{\text{fuel,u}}/X_{\text{air,u}}}{X_{\text{fuel,st}}/X_{\text{air,st}}}, \quad (2.55)$$

where  $X_{\text{air,u}}$  and  $X_{\text{fuel,u}}$  are the mole fractions of air and fuel in the unburnt mixture and  $X_{\text{air,st}}$  and  $X_{\text{fuel,st}}$  the corresponding stoichiometric mole fractions. In premixed combustion  $\phi$  is constant in the unburnt mixture, whereas in non-premixed combustion the local values for  $\phi$  vary from 0 to  $\infty$ . As a consequence, for non-premixed combustion,  $\phi$  can only be determined globally, using the mole fractions in the fuel and oxidizer streams at the inlets.

In order to assess specific quantities of a combustion process, for example the burning velocity, the reaction kinetics have to be considered in combination with the balance equations. However, the underlying physics of combustion processes in technical applications are very complex. Therefore, as a first step, often idealized systems are used in order to study combustion processes, since they allow for determining all significant quantities, like the variation of temperature or species concentration.

### 2.3.2.1 Laminar Premixed Flame

One example of such an idealized system is the laminar steady-state one-dimensional premixed flame. From the balance equations discussed in 2.1.1-2.1.3, the one-dimensional balance equations for total mass, species and energy for the planar steady-state premixed flame can be derived [49]:

$$\frac{\partial(\rho u)}{\partial x} = 0. \quad (2.56)$$

$$\rho u \frac{\partial Y_k}{\partial x} = -\frac{\partial j_k^d}{\partial x} + \dot{\omega}_k \quad \text{for } k = 1, \dots, N, \quad (2.57)$$

$$c_p \rho u \frac{\partial T}{\partial x} = \frac{\partial}{\partial x} \left( \lambda \frac{\partial T}{\partial x} \right) - \sum_{i=1}^n c_{p,i} j_i \frac{\partial T}{\partial x} - \sum_{k=1}^N h_k \dot{\omega}_k. \quad (2.58)$$

The heat transfer due to radiation is neglected in Equation (2.58). A typical structure of a laminar premixed methane-air flame is shown in Figure 2.1. The flame features a preheat zone for the fuel/air-mixture, an inner layer with the temperature  $T_0$ , where the main part of the fuel consumption takes place, and an oxidation layer. The thickness of the inner layer  $l_\delta$  is a fraction of the flame thickness  $l_F$

$$l_\delta = \delta l_F, \quad (2.59)$$

with a value of  $\delta \approx 0.1$  at atmospheric pressure. Under elevated pressure conditions,  $\delta$  decreases down to a value of  $\delta \approx 0.03$  at 30 bar [50, 51]. The flame thickness may be determined by [51, 52]:

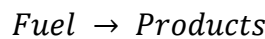
$$l_F = \frac{\lambda_0 / c_{p,0}}{\rho_u s_L}, \quad (2.60)$$

where  $\rho_u$  is the density of the unburnt mixture at the beginning of the preheat zone. The flame propagates with the laminar burning velocity  $s_L$ . Integrating Equation (2.56) leads to [51]:

$$\rho_\infty u_\infty = \dot{m} = \rho_u s_L, \quad (2.61)$$

where  $\rho_\infty$  and  $u_\infty$  are the density and the velocity of the unburnt mixture far away from the flame. The laminar burning velocity represents an eigenvalue of the equations (2.56)-(2.58) and can be interpreted as a thermo-chemical property, primarily depending on equivalence ratio, temperature and pressure in the unburnt state.

Based on the simplified model of Zeldovich [53], one can derive an analytical expression for  $s_L$ , assuming a one-step reaction of fuel into products [49]



with a given reaction velocity  $r_{\text{Fuel}} = -\rho Y_{\text{Fuel}} Z e^{-\frac{E}{RT}}$ , where  $Z$  represents the pre-exponential factor for the reaction velocity.  $Y_{\text{Fuel}}$  is the fuel mass fraction and  $E$  denotes the activation energy of the reaction of fuel to products. The derived equation for  $s_L$  then reads:

$$s_L = \sqrt{\frac{a}{\tau_{\text{Fuel}}}}, \quad (2.62)$$

where  $\tau_{\text{Fuel}}$  represents a characteristic time scale of the reaction with

$$\tau_{\text{Fuel}} = \left( Z e^{-\frac{E}{RT}} \right)^{-1}. \quad (2.63)$$

The dependence of the laminar burning velocity on the thermal diffusivity and the chemical time scale according Equation (2.62) reflects the mechanism of flame propagation by diffusive processes, which is driven by gradients generated by the chemical reaction.

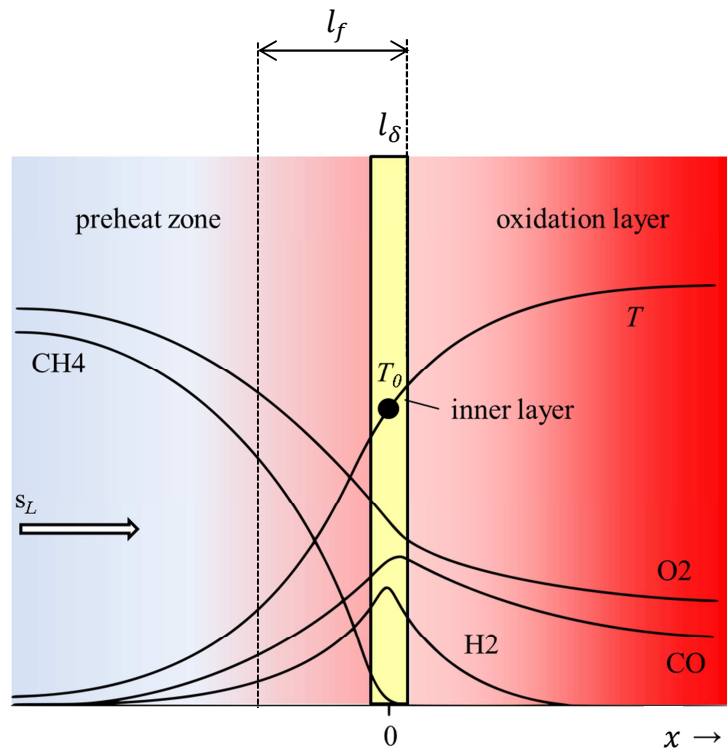


**Figure 2.1. Schematic diagram of the structure of a laminar premixed flame (adapted from [51, 54])**

### 2.3.2.2 Laminar Non-Premixed Flame

Laminar non-premixed flames are idealized systems which are used to study non-premixed combustion. Often non-premixed flames are called “diffusion” flames, since unlike premixed flames they are mainly dominated by the mixing of the fuel and the oxidizer.

One example of a laminar non-premixed flame is the “counterflow diffusion flame”. It is frequently used in experimental and numerical studies, since its flame structure can be treated as a one-dimensional problem.

Figure 2.2 shows a schematic of a counterflow diffusion flame, with the fuel stream originating from the left hand side and the oxidizer stream originating from the right hand side. The fuel and the oxidizer diffuse towards the reaction zone, where heat is released due to the combustion process. In the reaction zone, the temperature reaches its maximum. Heat is transported by diffusion towards the fuel and oxidizer streams.

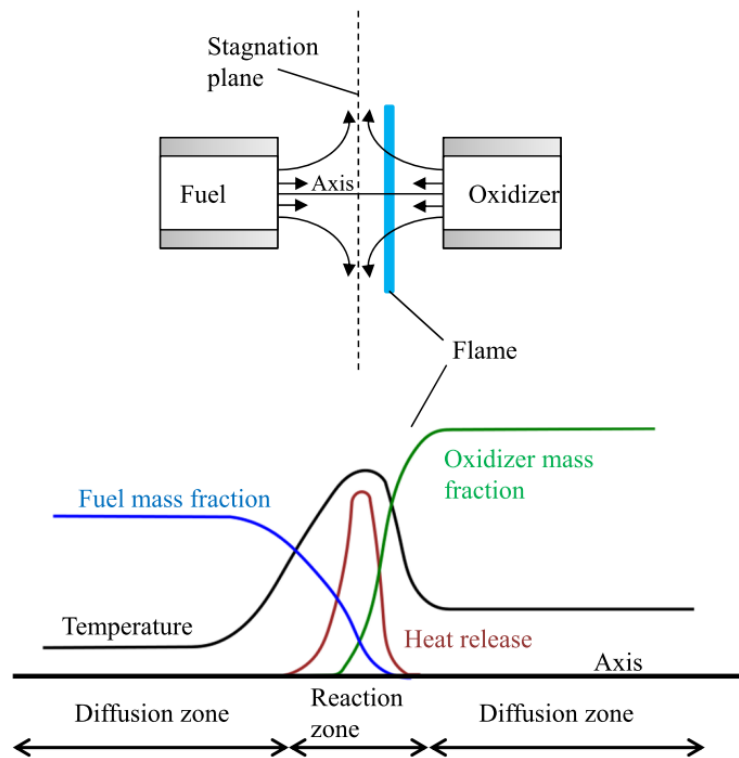


**Figure 2.2. Structure of a non-premixed flame (Adapted from [33, 51])**

Far from the reaction zone, the mixture is either too rich or too lean to burn. In general, it can be expected that the reaction takes place at the location of the stoichiometric mixture. As a consequence, non-premixed flames do not propagate like premixed flames and it is not possible to define a characteristic burning velocity and flame thickness. The thickness of a non-premixed flame is mainly determined by the stretch. Due to the high influence of the mixing, non-premixed flames are more sensitive to the flow than premixed flames.

In turbulent combustion modelling, it is often assumed that the flame front is stretched due to turbulent flow structures. The Flamelet-Model by Peters [55, 56] is based on the assumption that a turbulent non-premixed flame represents an ensemble of flamelets, which are “thin reactive-diffusive layers embedded within an otherwise non-reacting turbulent flow field” [51]. In this context, the counterflow diffusion flame is often applied to model such flamelets.

### 2.3.3 Turbulent Combustion

In a certain range of turbulence intensity, a significant increase of the burning velocity can be observed in turbulent flows. According to Damköhler [57], turbulent eddies can penetrate the

inner layer of a premixed flame and increase the surface area of the flame front. Damköhler proposed that the turbulent burning velocity  $s_t$  can then simply be determined by [33]

$$s_t = s_L \frac{A_t}{A_L}. \quad (2.64)$$

Beyond a certain turbulence level, the turbulent burning velocity shows no further increase with increasing turbulence (Figure 2.3). Increasing the turbulence even further eventually results in local flame extinction. Experimental results also showed a decrease of the turbulent burning velocity before the occurrence of local flame extinction [49, 58].

For a better understanding of turbulent combustion processes, turbulent flames are classified into different regimes. Classifications have been proposed by many authors [33, 51, 59]. In the following, the classification proposed by Borghi [59] is briefly discussed.

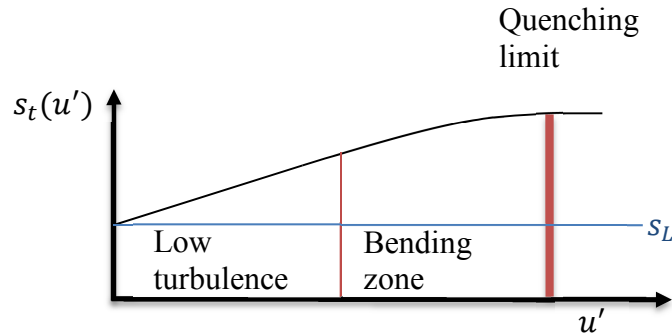


**Figure 2.3. Influence of the turbulence level on the turbulent burning velocity (adapted from [33])**

### 2.3.3.1 Borghi Diagram for Premixed Turbulent Flames

Based on the assumption that the turbulent Prandtl-Number constitutes unity, the turbulent Reynolds-Number  $Re_t = Re(l_t)$  can be determined by:

$$Re_t = \frac{u'_t}{s_L} \cdot \frac{l_t}{l_F} \Rightarrow \frac{u'_t}{s_L} = Re_t \cdot \left(\frac{l_t}{l_F}\right)^{-1}, \quad (2.65)$$

where  $u'_t$  represents the velocity of the energy-containing eddies in the turbulent flow. As a consequence, the characteristic time scale of the energy-containing eddies is given by  $\tau_t = l_t/u'_t$ . The turbulent Damköhler-Number  $Da_t$  reflects the ratio of the turbulent time scale  $l_t$  to the time scale of the flame or the chemical time scale  $\tau_c = l_F/s_L$ :

$$Da_t = \frac{\tau_t}{\tau_c} = \frac{l_t/u'_t}{l_F/s_L} \Rightarrow \frac{u'_t}{s_L} = Da_t^{-1} \cdot \left(\frac{l_t}{l_F}\right)^{-1}, \quad (2.66)$$

The turbulent Karlovitz-Number  $Ka_t$  is used to assess effects due to flame stretching.  $Ka_t$  is calculated by the ratio of the time scale of the flame  $\tau_c$  and the respective characteristic time scale of the turbulent eddies interacting with the flame. As a consequence,  $Ka_t$  reaches its maximum value  $Ka_{t,\max}$  for the smallest turbulent scales with the Kolmogorov length scale  $\eta$ . Therefore it is possible to derive an equation for  $Ka_{t,\max}$  dependent on the turbulent scales  $\tau_t$ ,  $l_t$  and  $u'_t$ :

$$Ka_{t,\max} = \frac{\tau_c}{\tau_\eta} \approx \left(\frac{u'_t}{s_L}\right)^{3/2} \cdot \left(\frac{l_t}{l_F}\right)^{-1/2} \Rightarrow \frac{u'_t}{s_L} = Ka_{t,\max}^{2/3} \cdot \left(\frac{l_t}{l_F}\right)^{-1/2}. \quad (2.67)$$

Based on the dimensionless numbers  $Re_t$ ,  $Da_t$  and  $Ka_{t,\max}$ , Borghi defined different regimes for turbulent flames (Figure 2.4):

- $Re_t < 1$ : The flame basically features the characteristics of a laminar flame, similar to the schematic shown in Figure 2.1
- $Re_t > 1 / u'_t < s_L$ : The flame is only slightly disturbed by turbulent structures, since the turbulent velocity fluctuations are small compared to the burning velocity. The flame thickness is not increased, but the mean structure of the flame front may appear thicker due to the turbulent fluctuations. The burning velocity is augmented compared to the laminar flame, since the flame is wrinkled and the flame surface area is increased.
- $Re_t > 1 / u'_t > s_L / Ka_{t,\max} < 1$ : The augmented velocity fluctuations lead to an increased bending of the flame. The flame thickness can still be considered as thin in comparison to the turbulent eddies; the flame front is convoluted and convectively transported by the turbulent motions. Local quenching and reigniting processes are possible and pockets can separate from the wrinkled flame front.
- $Re_t > 1 / Ka_{t,\max} < 1 / Da_t \geq 1$ : The smallest turbulent structures can penetrate the flame front and intensify diffusion processes. This leads to an augmentation of the flame thickness, which enables eddies with a bigger length scale than  $\eta$  to penetrate the flame front. As a result, the flame thickness is significantly increased and the flame front cannot be considered as laminar. Local quenching takes place due to flame stretching which leads to distributed reaction zones. An increase of the turbulent velocity fluctuations combined with a constant value of the turbulent length scale results in a decrease of  $Da_t$ , down to a level where  $Da_t = 1$  is reached. At this point, eddies with length scales up to the turbulent time scale can enter the flame front.
- $Re_t > 1 / Da_t < 1$ : In this regime, even the turbulent time scale  $\tau_t$  is smaller than the chemical time scale  $\tau_c$  and all turbulent structures are contained inside the flame front. The conditions in such flames are similar to the conditions inside well stirred reactors.

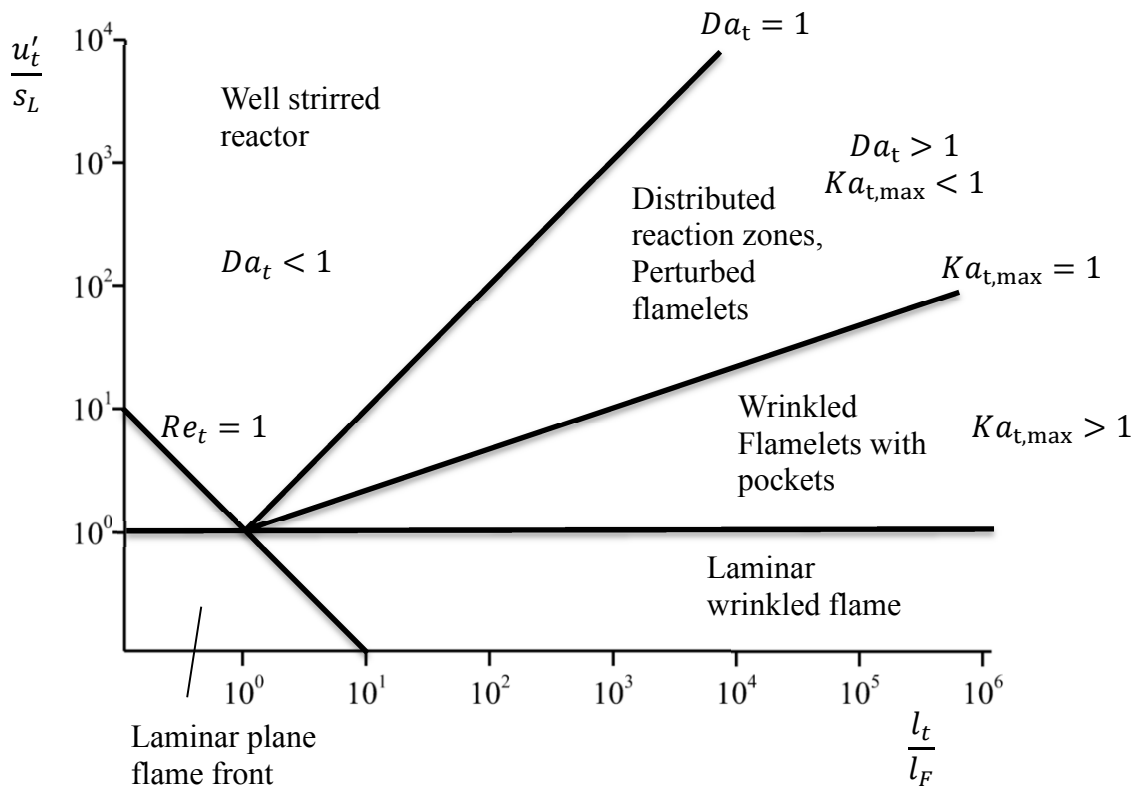


**Figure 2.4. Classification of turbulent premixed combustion according to Borghi**

### 2.3.3.2 Non-Premixed, Turbulent Flames in the Borghi Diagram

According to Borghi, the classification of the turbulent premixed combustion in Figure 2.4 can be transferred to non-premixed turbulent flames. This is based on the assumption that the main reaction zone is located on the isosurface of stoichiometric mixtures. As a consequence, the laminar burning velocity and the flame thickness of laminar premixed flames at stoichiometric mixtures are used for the classification of turbulent non-premixed flames. The classification of non-premixed turbulent flames in the Borghi diagram is similar to that of premixed turbulent flames. When the Karlovitz-Number exceeds a certain value, high strain rates of the smallest turbulent structures can cause local extinction of flamelets. After the decay of the high strain rates by the short-lived Kolmogorov eddies, local extinction may be followed by local premixing and reignition. Further increase of the turbulent intensity results in enhanced local premixing, leading to a more premixed character of the flame.

### 2.3.4 Flame Stabilization in Swirl Flames

Technical combustion chambers are operated with power densities of up to 20 MW/m<sup>3</sup> [21]. In order to reach the necessary reaction rates, it is common to apply swirl nozzles or bluff-bodies to create an inner recirculation zone (IRZ). The high turbulence intensity in the shear layers between the downstream flow and the reverse flow and the mixing of hot burnt gases results in an increase of the local burning velocity. This ensures high reactions rates and a

high flexibility in terms of operating range. The advantage of swirl nozzles is that the stabilization is purely aerodynamic and no bluff-body is present inside the combustion chamber which has to withstand high temperatures. Unfortunately, swirl stabilized flames are prone to combustion instabilities, such as in the very complex flow field of swirl flows often coherent vortex structures are present which can interact with the flame. Flame vortex interactions are typical driving mechanisms for combustion instabilities (see 3.1).

Figure 2.5 shows a schematic of a swirl stabilized flame. Depending on the nozzle and the combustion chamber design, the inner recirculation zone (IRZ) and the outer recirculation zones (ORZs) can change size and shape.

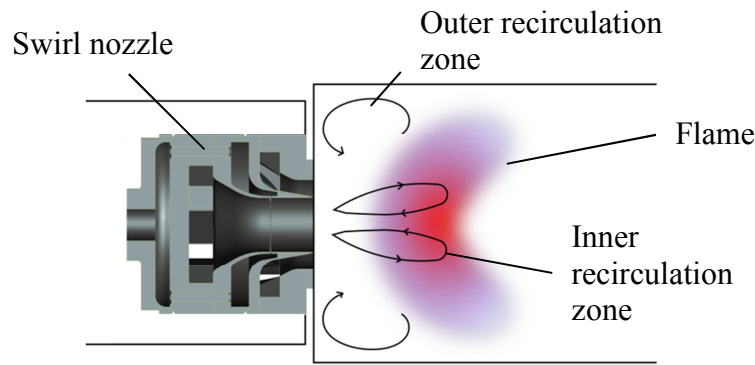


**Figure 2.5. Typical recirculation zones in swirl flows which stabilize the flame**

In order to create an IRZ, the swirl intensity has to reach a certain, critical value at which the so-called vortex breakdown occurs. The vortex breakdown can be explained by a positive pressure gradient along the central axis of the swirl flow. The pressure gradient is induced by the transport of angular momentum to higher radii. The typical shape of the axial velocity profile is shown in Figure 2.6.  $S$  denotes the swirl number, which expresses the swirl intensity in a swirl flow. The most common formulation reads:

$$S = \frac{\bar{D}}{\bar{I} \cdot R_0}, \quad (2.68)$$

where  $\bar{D}$  denotes the angular momentum flux

$$\bar{D} = 2\pi \int_0^{\infty} \left( \rho (\bar{u}_{ax} \bar{u}_t + \overline{u'_{ax} u'_t}) \right) r^2 dr, \quad (2.69)$$

and  $\bar{I}$  the axial momentum flux

$$\bar{I} = 2\pi \int_0^{\infty} \left( \rho (\bar{u}_{ax}^2 + \overline{u'_{ax}{}^2}) + (p - p_{\infty}) \right) r dr, \quad (2.70)$$

where  $\bar{u}_{ax}$ ,  $\bar{u}_t$  are the mean axial and tangential velocity components,  $u'_{ax}$ ,  $u'_t$  the corresponding fluctuation components and  $p_\infty$  represents the ambient pressure. In order to obtain a dimensionless number, the axial momentum flux is usually multiplied with a characteristic radius  $R_0$ , which in many cases is the radius of the nozzle outlet.

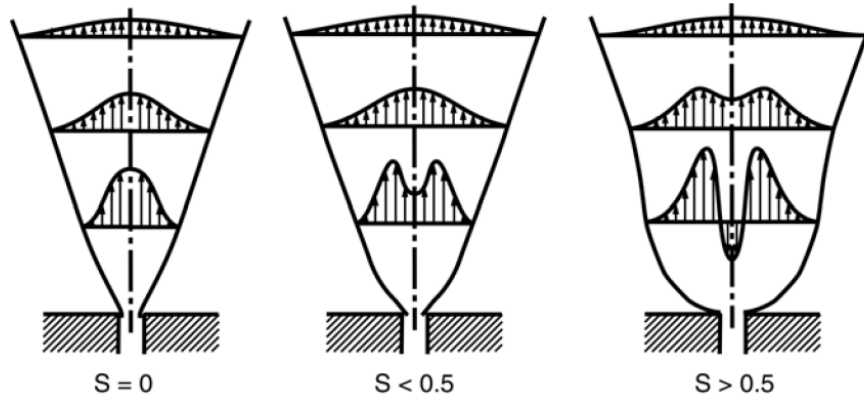


**Figure 2.6. Axial velocity profile in a jet at different swirl numbers [60]**

The determination of the quantities needed to evaluate the swirl number according to Equation (2.68) is usually a difficult task and requires complex field measurements. Therefore it is common to calculate a theoretical swirl number with the geometric parameters of the nozzle. According to Leuckel [61], this can be done by neglecting the turbulent fluctuation terms and the influence of the static pressure, and assuming a homogeneous block profile of the velocity. The theoretical swirl number  $S_{th}$  is then calculated by:

$$S_{th} = \frac{1}{nA_{SD}} R_1 \sin \alpha \pi \frac{R_{ot}^2}{R_0} \left( 1 - \left( \frac{R_i}{R_0} \right)^2 \right), \quad (2.71)$$

where  $n$  is the number of swirl ducts,  $A_{SD}$  denotes the flow cross-section of a single swirl duct and the term  $R_1 \sin \alpha$  describes the eccentricity of the swirl ducts (Figure 2.7).  $R_i$  and  $R_{ot}$  are the inner and the outer radius of the nozzle outlet, respectively.

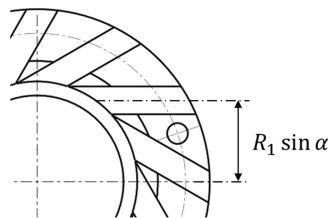


**Figure 2.7. Eccentricity  $R_1 \sin \alpha$  used for the calculation of  $S_{th}$**

For the case when the nozzle consists of two swirlers, the theoretical swirl number of the nozzle can be determined according to the proposal by Kerr and Fraser [62]:

$$S_{th} = \frac{S_{th,IS}}{1+C} + \frac{S_{th,OTS}}{1+C^{-1}}, \quad (2.72)$$

$$\text{with } C = \frac{A_{IS}}{A_{OTS}} \left( \frac{1-x_{IS}}{x_{OTS}} \right) \text{ and } x_{IS} = \frac{\dot{m}_{IS}}{\dot{m}_{OTS} + \dot{m}_{IS}}.$$

$S_{th,IS}$  and  $S_{th,OTS}$  are the theoretical swirl numbers of the outer and the inner swirler, respectively.  $A_{IS}$  stands for the smallest flow cross-section in the inner swirler and  $A_{OTS}$  for the smallest flow cross-section in the outer swirler.  $\dot{m}_{IS}$  and  $\dot{m}_{OTS}$  denote the corresponding swirler mass flows. The nozzle that is installed in the investigated modular combustor consists of two swirlers with different theoretical swirl numbers. The ratio of the mass flows through each swirler was varied, which results in different global theoretical swirl numbers and affects the flame characteristics. This is discussed in detail in the description of the nozzle design in 4.1.1 and the discussion of the investigated operating points in 4.3.

### 2.3.5 Turbulent Combustion Modelling

In order to perform numerical simulations of turbulent combustion processes with acceptable computational effort, it is generally necessary to use a model for the turbulent flame in addition to the model for the turbulent flow. In most cases, the flame front is too thin to be resolved by the highest acceptable grid resolution, as the flame thickness and the time scale of the chemical reaction can be on the order of magnitude of the time and the length scales of the smallest turbulent structures. In addition, without the use of a flame model, it would be necessary to solve a balance equation for each individual species participating in the chemical reaction of the combustion process. The GRI3.0-Mechanism for the combustion of methane and air, provided by the Gas Research Institute [63], consists of 325 elementary reactions with 53 different species. As a result, the computational effort for a direct simulation of a turbulent flame exceeds acceptable limits in most cases.

A variety of model approaches for turbulent combustion exist; a few of them are listed here:

- **Models based on correlations for the turbulent burning velocity**

The reaction rate is modelled in dependency on the turbulent burning velocity, which is calculated by correlations for asymptotic time and length scales. Similar to the description of laminar combustion, in many cases only one characteristic chemical time scale and turbulent time scale is used to model the flame-turbulence interaction. Correlations for the turbulent burning velocity were formulated for example by Zimont [64] and Schmid et al. [65, 66].

- **Models based on the scalar dissipation rate**

These models are based on the assumption that the chemical time scale is very small compared to the turbulent time scale. The scalar dissipation rate describes the relaxation of fluctuations due to molecular mixing. The reaction rate is assumed to

only depend on turbulent mixture processes. A well-known category of such models are represented by the already mentioned Flamelet-Models for non-premixed combustion, where the reactive-diffusive structure of the flame is described by the scalar dissipation rate and the position of the flame front is defined by the zone of stoichiometric mixture.

- **PDF-Models**

The turbulent fluctuations of the main quantities of the combustion process are modelled by the usage of probability density functions (PDF). It is assumed that the turbulent and the chemical time and length scales are reflected by the shape of the pdf. No restrictions are made beforehand concerning the kinetics of the chemical reaction and the turbulent transport processes [67].

Further models for turbulent combustion processes and more detailed discussions about the named model approaches may be found in [33, 49, 51, 68].

### 2.3.5.1 Simplification of Reaction Mechanisms

As stated in the beginning of this section, using detailed chemical mechanisms in simulations of turbulent flames would require solving a balance equation for each chemical species included in the reaction mechanism. Since this is usually beyond computational capacities, it is necessary to use methods that simplify the reaction system. Simplifications of reaction mechanisms based on assumptions of quasi-steady state and partial equilibrium are often limited to certain conditions, for example to certain temperature ranges or mixture compositions [49].

One method to circumvent this problem is given by the intrinsic low-dimensional manifold method (ILDM) by Maas and Pope [69]. In the ILDM, the reduction of the reaction system is based on an eigenvector analysis, in order to only take into account the chemical reactions with the largest time scales. It is then possible to describe the reaction system by a reduced set of variables. A progress variable can be used to describe the reaction progress and the mixing of the fuel and the oxidizer can be described by a mixture fraction. Possible formulations for these quantities are introduced in the next section. In a next step, a look-up table is generated. It provides species mass fractions and reaction rates in dependence on progress variable and mixture fraction and is searched by the usage of multi-linear interpolations [33].

Another possibility is represented by the Flamelet-Generated-Manifolds (FGM). Similar to the ILDM formalism, a progress variable is used to monitor the chemical reaction progress and the mixing of the fuel and the oxidizer is described by a mixture fraction. Look-up tables, also providing reaction rates and species mass fractions, are derived from calculations of idealized systems (e.g. the laminar premixed flame described in section 2.3.2.1) with complex chemical mechanisms.

### 2.3.5.2 Unified-Turbulent-Flame-Speed-Closure Model (UTFC-Model)

In the simulations discussed in the present work the Unified-Turbulent-Flame-Speed-Closure Model was used to perform LESs of the reactive flow in the investigated modular combustor. The model describes premixed combustion and non-premixed combustion. It was established at the Engler-Bunte-Institute, Combustion Technology at KIT Karlsruhe and is described in detail in [70]. In the following, the model will be discussed briefly.

#### *Basic Concept*

Similar to the popular Flamelet-Model, the basic idea of the UTFC-Model is that a turbulent flame can be described by an ensemble of laminar reactions zones with different equivalence ratios. The UTFC-Model employs a progress variable that describes the reaction and the propagation of the flame from burnt to fresh gases. Balance equations for a mixture fraction and its variance are solved in order to account for the turbulent mixing process in turbulent non-premixed combustion. Tabulated chemistry based on simulations of laminar premixed 1D-flames is used to determine species mass fractions and laminar burning velocities. A correlation for the turbulent burning velocity is applied in order to model the influence of turbulence on the reaction rate.

#### *Progress Variable and Mean Reaction Rate*

In the UTFC-Model the progress variable is defined by the consumption of oxygen, following the suggestion by Habisreuther [67]:

$$\theta = \frac{Y_{O_2, \text{bound}}}{\min(Y_{O_2, \text{needed}}, Y_{O_2, \text{present}})}, \quad (2.73)$$

where  $Y_{O_2, \text{bound}}$  is the chemically bounded concentration of  $O_2$  in the products.  $Y_{O_2, \text{needed}}$  constitutes the concentration of  $O_2$  necessary for a complete combustion of all species in the local mixture.  $Y_{O_2, \text{present}}$  is the locally present concentration of  $O_2$ . The denominator switches between  $Y_{O_2, \text{needed}}$  and  $Y_{O_2, \text{present}}$ , depending on whether the reaction takes place under lean or fuel rich conditions.

Like several other combustion models, the UTFC-Model is based on solving a balance equation for the progress variable:

$$\frac{\partial(\bar{\rho}\tilde{\theta})}{\partial t} + \frac{\partial(\bar{\rho}\tilde{u}_i\tilde{\theta})}{\partial x_i} = \frac{\partial}{\partial x_i} \left( \frac{\mu_L + \mu_t}{Sc_t} \frac{\partial \tilde{\theta}}{\partial x_i} \right) + \bar{\omega}_\theta, \quad (2.74)$$

where  $\bar{\omega}_\theta$  represents the mean reaction rate that has to be modelled. As indicated by its name, the UTFC-Model applies a correlation for the turbulent burning velocity to model turbulent combustion. The implemented correlation for the turbulent burning velocity is the one proposed by Schmid et al. [65, 71]:

$$\frac{s_t}{s_L} = 1 + \frac{u'_t}{s_L} \cdot (1 + Da^{-2})^{-1/4}, \quad Da = \frac{\tau_t}{\tau_c} = \frac{l_t}{u'_t} / \left( \frac{C_W^2 a}{0.09 s_L^2} \right). \quad (2.75)$$

$C_W$  represents a specific constant which may be adapted to the chosen fuel. As proposed by Schmid, the mean reaction rate is calculated by:

$$\bar{\omega}_\theta = \frac{1}{4} \rho_u \frac{s_t^2}{D_t} \cdot 4\tilde{\theta} (1 - \tilde{\theta}) = \rho_u \frac{s_t^2}{u'_t l_t} \cdot \tilde{\theta} (1 - \tilde{\theta}), \quad (2.76)$$

where  $D_t$  is the turbulent diffusivity modelled by  $D_t \approx u'_t l_t$ . The correlation for the turbulent burning velocity and the equation for the mean reaction rate were originally intended to be used in RANS models. In order to use the Schmid-Model in LES, the turbulent velocity, time and length scale were substituted with the subgrid velocity, time and length scale. They are calculated using the filter width  $\Delta$ , the Smagorinsky constant  $C_s$  and  $|\tilde{S}|$ :

$$u'_t = C_s \Delta |S|, \quad l_t = C_s \Delta, \quad \tau_t = u'_t / l_t = |\tilde{S}|. \quad (2.77)$$

The value of  $l_t$  tends to be zero at  $\Delta \rightarrow 0$ , which would result in an infinitely high reaction rate. Hence, the laminar diffusivity is added to the turbulent diffusivity  $D_t$  in equation (2.76):

$$\bar{\omega}_\theta = \rho_u \frac{s_t^2}{D_L + u'_t l_t} \cdot \tilde{\theta} (1 - \tilde{\theta}). \quad (2.78)$$

This leads to a consistent transfer from LES to DNS, as the DNS resolves the laminar flame front. For  $\Delta \rightarrow 0$  or  $s_t \rightarrow s_l$  the mean reaction rate tends to:

$$\bar{\omega}_\theta = \rho_u \frac{s_L^2}{D_L} \cdot \tilde{\theta} (1 - \tilde{\theta}). \quad (2.79)$$

### *Mixture fraction and mixture fraction variance*

In order to simulate non-premixed combustion, the TFC-model of Schmid has to be extended, since it was formulated for premixed turbulent combustion. Hence, a mixture fraction is introduced which describes the fuel concentration in the turbulent flow field. For two-stream flows with pure streams of the fuel and the oxidizer, the mixture fraction can be expressed using the element mass fractions [49]:

$$\xi = \frac{Z_i - Z_{i,\text{ox}}}{Z_{i,\text{fuel}} - Z_{i,\text{ox}}}, \quad (2.80)$$

where  $Z_i$  denotes the element mass fraction of the  $i$ -th element. The subscripts “fuel” and “ox” indicate that  $Z_{i,\text{fuel}}$  and  $Z_{i,\text{ox}}$  are the initial element mass fractions at the fuel stream inlet and the oxidizer stream inlet, respectively. For equal diffusion coefficients of chemical species, the mixture fraction can be expressed as the ratio of the fuel mass flow to the total mass flow in unburnt state [51]:

$$\xi = \frac{\dot{m}_{\text{fuel}}}{\dot{m}_{\text{fuel}} + \dot{m}_{\text{ox}}}. \quad (2.81)$$

In general,  $\xi$  takes the value  $\xi = 1$  in the fuel stream and  $\xi = 0$  in the oxidizer stream. Based on this definition, various formulations for the mixture fraction can be derived, as discussed in [51].

Under the assumption of equal species diffusivities, the transport of all chemical species can be described by a single transport equation for the mixture fraction. The implemented mixture fraction transport equation reads:

$$\frac{\partial(\bar{\rho}\tilde{\xi})}{\partial t} + \frac{\partial(\bar{\rho}\tilde{u}_i\tilde{\xi})}{\partial x_i} = \frac{\partial}{\partial x_i} \left( \frac{\mu_L + \mu_t}{Sc_t} \frac{\partial \tilde{\xi}}{\partial x_i} \right). \quad (2.82)$$

Equation (2.82) does not show a source term for the mixture fraction and is therefore valid for definitions of the mixture fraction using element mass fractions. In the UTFC-Model, the mixture fraction serves as a passive scalar which does not participate in the chemical reaction. It provides the local fuel concentration in the unburnt state.

In order to account for the influence of the unresolved turbulent scales on the mixing process, a balance equation for the mixture fraction variance  $\xi''^2$  is solved:

$$\frac{\partial(\bar{\rho}\tilde{\xi}''^2)}{\partial t} + \frac{\partial(\bar{\rho}\tilde{u}_i\tilde{\xi}''^2)}{\partial x_i} = \frac{\partial}{\partial x_i} \left( \frac{\mu_L + \mu_t}{Sc_t} \frac{\partial \tilde{\xi}''^2}{\partial x_i} \right) + \bar{\omega}_{\xi''^2}. \quad (2.83)$$

The source term for the mixture fraction variance  $\bar{\omega}_{\xi''^2}$  is given by [51]:

$$\bar{\omega}_{\xi''^2} = 2\rho D_t |\nabla \tilde{\xi}|^2 - 2\bar{\rho}\tilde{\chi}, \quad (2.84)$$

where  $\tilde{\chi}$  denotes the Favre-filtered scalar dissipation rate, which is assumed to be proportional to the inverse of the turbulent time scale and  $\tilde{\xi}''^2$ :

$$\tilde{\chi} = 2D_t \left( \frac{\partial \tilde{\xi}}{\partial x_i} \frac{\partial \tilde{\xi}}{\partial x_i} \right) \propto \frac{1}{\tau_t} \tilde{\xi}''^2. \quad (2.85)$$

This leads to the used expression for the subgrid scale scalar dissipation rate:

$$\tilde{\chi} = c_\chi |\mathcal{S}| \tilde{\xi}''^2, \quad (2.86)$$

where the value for  $c_\chi$  is set to  $c_\chi = 2$ .

### *Pre-Processing and Coupling of the LES with the Chemistry Table*

In order to perform an LES of a turbulent flame with the UTFC-Model, some pre-processing is required to build the chemistry table used for modelling the chemical reaction.

As mentioned in the beginning of this section, the UTFC-Model is based on the assumptions that mixing of the fuel and the oxidizer takes place before the chemical reaction and that a turbulent flame can be described by an ensemble of diffusive-reactive flame sheets with different equivalence ratios. The influence of the turbulence on the burning velocity on those flame sheets is modelled by calculating the turbulent burning velocity and the reaction rate according to the Schmid-Model. The mixture fraction describes the mixture field in the turbulent flame and the reaction progress variable is used to model the chemical reaction. As a consequence, the density of the unburned mixture  $\rho_u$ , the laminar burning velocity  $s_l$  and the thermal diffusivity  $a_u$  in the unburnt state directly depend on the mixture fraction, whereas the species mass fractions  $Y_k$  depend on the mixture fraction and the progress variable. The corresponding values for these quantities can be determined experimentally or alternatively by the calculation of laminar 1D premixed flames. For the latter method, 1D-laminar premixed flames are computed for different mixture fractions. The computations can be carried out, for example, by using the PREMIX code of the CHEMKIN program package [72]. This was also done in the pre-processing of the LESs performed in the scope of this work.

As discussed, a transport equation for the mixture fraction variance  $\tilde{\xi}''^2$  is solved in order to account for the influence of the turbulence on the mixing process. The quantities derived from the calculation of the 1D-flames are statistically averaged by using a PDF which features the shape of a beta function determined by  $\tilde{\xi}$  and  $\tilde{\xi}''^2$ :

$$\tilde{g}_i(\tilde{\xi}, \tilde{\xi}''^2) = \int_0^1 g_i(\xi) P(\xi) d\xi, \quad g_i = s_L, \rho_u, Y_k(\tilde{\theta}), a_u. \quad (2.87)$$

The statistically averaged quantities  $\tilde{s}_L$ ,  $\tilde{\rho}_u$ ,  $\tilde{Y}_k(\tilde{\theta})$  and  $\tilde{a}_u$  are tabulated as a function of the control parameters  $\tilde{\xi}$ ,  $\tilde{\xi}''^2$  and  $\tilde{\theta}$  (Figure 2.8). Intermediate values are calculated using

multidimensional interpolation. During the calculation, the CFD-Solver provides the values for  $\tilde{\xi}$ ,  $\tilde{\xi}''^2$  and  $\tilde{\theta}$ . The species mass fractions are used to solve the balance equations of mass, momentum and enthalpy. The values for  $l_t$ ,  $u_t$  and  $\tau_t$  are provided by the turbulence model. The tabulated values for  $\tilde{s}_L$ ,  $\tilde{\rho}_u$  and  $\tilde{a}_u$  and the values of the turbulent scales are utilized to compute the mean reaction rate  $\bar{\omega}_\theta$  according to the Schmid-Model.

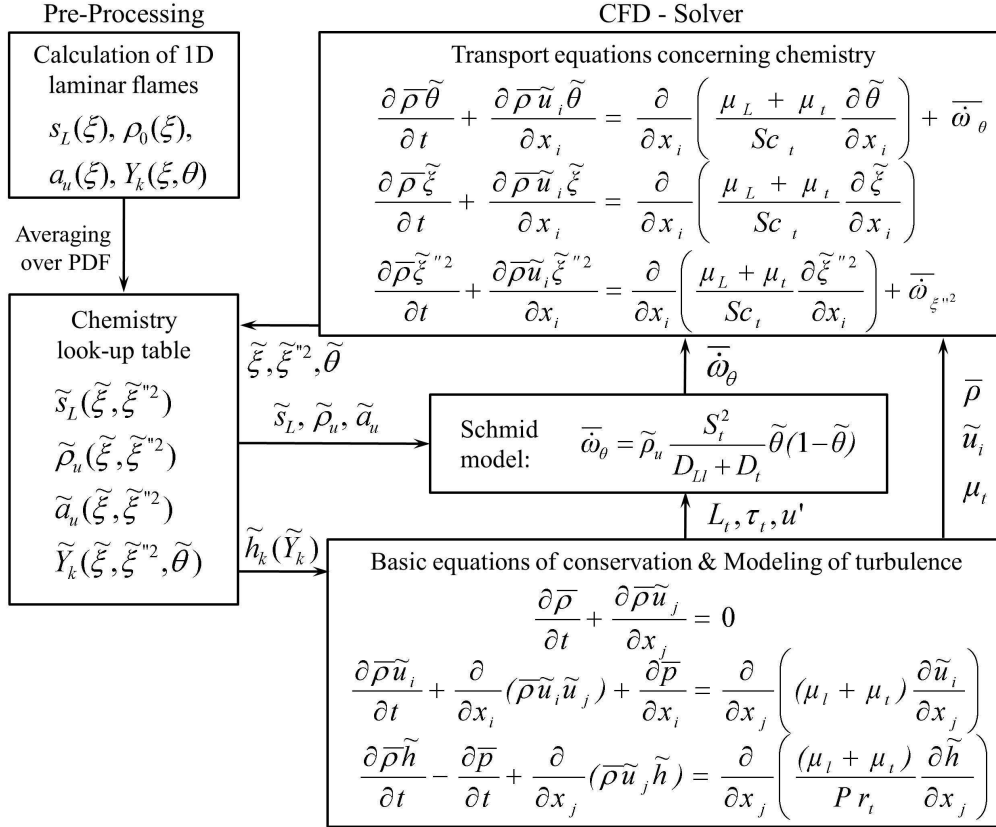


**Figure 2.8. Process chart for the coupling of the chemistry look-up table and the CFD Solver [70]**

### Calculation of the Heat Release Rate

In the UTF-C-Model, an equation for the heat release is also implemented. Theoretically, the heat release is given by the specific enthalpies of the species and their reaction rates:

$$\bar{q} = - \sum_1^{N_k} h_k \bar{\omega}_k. \quad (2.88)$$

Determining the reaction rates would require solving a balance equation for each species, which often leads to unacceptable computation times. Since the mixture fraction, the mixture fraction variance and the progress variable describe the simplified reaction mechanism, an equation can be derived which models the heat release in dependence on the control moments  $\tilde{\xi}$ ,  $\tilde{\xi}''^2$  and  $\tilde{\theta}$  [70]:

$$\bar{\omega}_k = \frac{D\tilde{Y}_k}{D\tilde{\xi}''^2} \bar{\omega}_{\xi''^2} + \frac{D\tilde{Y}_k}{D\tilde{\theta}} \bar{\omega}_{\theta}. \quad (2.89)$$

### *Applicability of the UTFC-Model*

As discussed in [70], the UTFC-Model is essentially only applicable for the combustion regime with thin reaction zones for  $Da > 1$  and  $Ka < 1$ , since laminar flamelets are used to describe the turbulent flame structure. The effect of turbulent eddies penetrating the flamelet is not included in the model. In addition, the laminar flame sheets do not affect each other, which implies that the UTFC-model is only valid in the fast chemistry limit with  $Da > 1$ .

Nevertheless, the UTFC-Model has proven to be effective in the LES of premixed and non-premixed combustion, as well as in the simulation of combustion noise and combustion instabilities [70, 73–78].



### 3. Combustion Instabilities

Flames and acoustics can interact in different ways. One possibility is that the flame generates broadband noise and the feedback of the acoustic pressure oscillations on the flame is either non-existent or negligible. Lighthill's acoustic analogy [79] is recognized as the first approach to assess aero-acoustic noise, whereas Strahle [80] was the first to apply Lighthill's method to turbulent combustion. Broadband noise emissions of turbulent flames are still an important subject and therefore numerous investigations [70, 73–75, 81–84] can be found in literature. The aim is to develop methods which identify and/or predict the most important sources of combustion noise.

Another possibility for flame-acoustics interaction is that a strong coupling between the flame and the acoustic oscillations is present. This may result in a feedback loop, which causes a massive pressure-heat release pulsation known as combustion instability. Combustion instabilities can result in damage to the combustor components or complete engine failure [85, 86]. The interaction between pressure and heat release oscillation was first reported by Rayleigh [5, 87]. Based on his observations, Putnam defined the well-known Rayleigh-Criterion [88]:

$$\int_T p'(t)q'(t) > 0, \quad (3.1)$$

where  $p'(t)$  represents the pressure oscillation and  $q'(t)$  is the heat release oscillation in the reaction zone. The integral over the periodic time  $T$  of the instability mode in Equation (3.1) is positive when the phase angle between pressure and heat release oscillation is  $\leq 90^\circ$ . Under these conditions, the flame adds energy to the acoustic field. However, a positive value of the integral does not necessarily mean that a combustor will become unstable. The acoustic energy dissipated inside the combustor and/or transmitted through the combustor boundaries damps the thermoacoustic oscillation. Therefore the energy transferred from the flame to the acoustic field must exceed the loss of acoustic energy in order to generate an unstable combustor mode. This can be expressed mathematically by [89]:

$$\iint_{V_T} p'(x, t)q'(x, t) dt dV \geq \iint_{V_T} \sum_i L_i(x, t) dt dV. \quad (3.2)$$

where  $p'(x, t)$  and  $q'(x, t)$  represent the combustor pressure oscillations and heat-addition oscillations, respectively.  $V$  denotes the combustor volume and  $L_i(x, t)$  is the  $i$ -th energy loss process. While the Rayleigh-Criterion is still the most commonly used criterion to assess the stability of a combustor, alternatives and extended formulations are discussed in literature [7].

Combustion instabilities have been observed in all kinds of combustion systems, such as in rocket motors [90, 91], aero engines [92, 93] and gas turbines [85, 94]. This indicates that numerous different excitation mechanisms exist and many may still be unknown. Some of them are briefly discussed in the next section. Additional, more detailed discussions of driving mechanisms can be found in literature. For example, a review of different excitation mechanisms in gas turbine combustion chambers is given by Keller in [95], whereas Ducroix et al. discuss excitation mechanisms of premixed flames in [96].

### 3.1 Driving Mechanisms for Combustion Instabilities

The schematic in Figure 3.1 shows processes which can drive combustion instabilities in gas turbines. However, the basic principles can be transferred to all kinds of combustion systems. According to Lieuwen and Zinn [6] driving mechanisms can be classified into:

- **Coupling of the fuel feed line with acoustic oscillations**

Pressure oscillations in the combustion chamber lead to oscillations of the pressure drop over the fuel nozzle. Since the pressure drop modulates the fuel flow rate into the combustion chamber or the combustion system, an oscillating pressure drop leads to an oscillation of the fuel flow rate and in turn results in an oscillating heat release. An example is given by [97].

- **Oscillations of the equivalence ratio**

Pressure oscillations in the combustor lead to unsteady mixing processes in the premixing process or modulate the oxidizer and/or the fuel flow rate. This leads to oscillations of the equivalence ratio of the mixture entering the combustion chamber, resulting in periodic variations of the heat release [98–100].

- **Periodic variations of atomization, vaporization and mixing**

Pressure oscillations in the combustor lead to perturbations of the fuel spray which may result in periodic changes in droplet sizes, evaporation rates and mixing rates of the vaporized fuel with surrounding gases. As a result, oscillations of the fuel supply rate and equivalence ratio are possible, leading to heat release oscillations which excite acoustic oscillations [101].

- **Oscillations of the flame area**

Acoustic velocity oscillations result in periodic variations of the flame area that lead to a periodic increase in the overall heat release rate which causes intensified acoustic oscillations [102].

- **Flame/vortex interactions**

Large coherent vortex structures, which initially consist of combustible gases, form inside the combustion chamber. During the formation of the vortex structures they entrain hot gases, leading to an impulsive combustion of the reactive mixture inside the vortex. The vortex then breaks down into small scale turbulent structures. Vortex structures can also lead to distortions of the flame surface, which results in periodic variations of the flame surface area. The heat release oscillates with the oscillating flame surface area which leads to massive pulsations when the heat release oscillates in phase with the pressure oscillation. Examples are the ring-vortex structures in lean-premixed swirl flames observed by Büchner et al. [15, 16, 103] and precessing vortex structures [104–107].

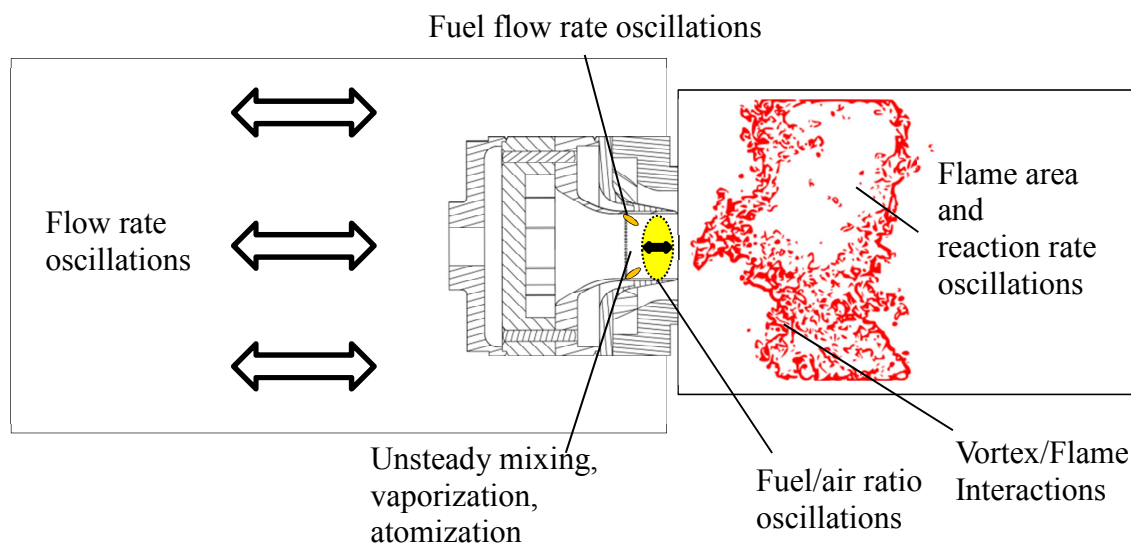


**Figure 3.1. Driving mechanisms for combustion instabilities. Adapted from [6].**

In general, combustion instabilities are found at frequencies that can be associated with acoustic eigenmodes of combustor components (e.g. the air supply pipes or the combustion chamber). In the range of their eigenfrequencies, they show increased acoustic responses to acoustic excitations and thus may amplify pressure and heat release disturbances. The formation of acoustic resonances is briefly discussed in the next section.

On occasion, oscillations are observed in combustors which are not purely associated with acoustic modes. One example is an oscillation triggered by entropy waves [100, 108]. Hot-gas packets (entropy waves), e.g. caused by equivalence ratio oscillations, are convectively transported towards the combustion chamber outlet, where they induce acoustic waves that travel back to the flame.

### 3.2 Acoustic Resonances in Combustion Systems

In the previous section it was stated that unstable modes are frequently caused by the excitation of acoustic eigenmodes of the combustion chamber or other combustor

components. In many cases, acoustic eigenmodes are related to Helmholtz-type oscillations and standing waves in cavities (Figure 3.2).

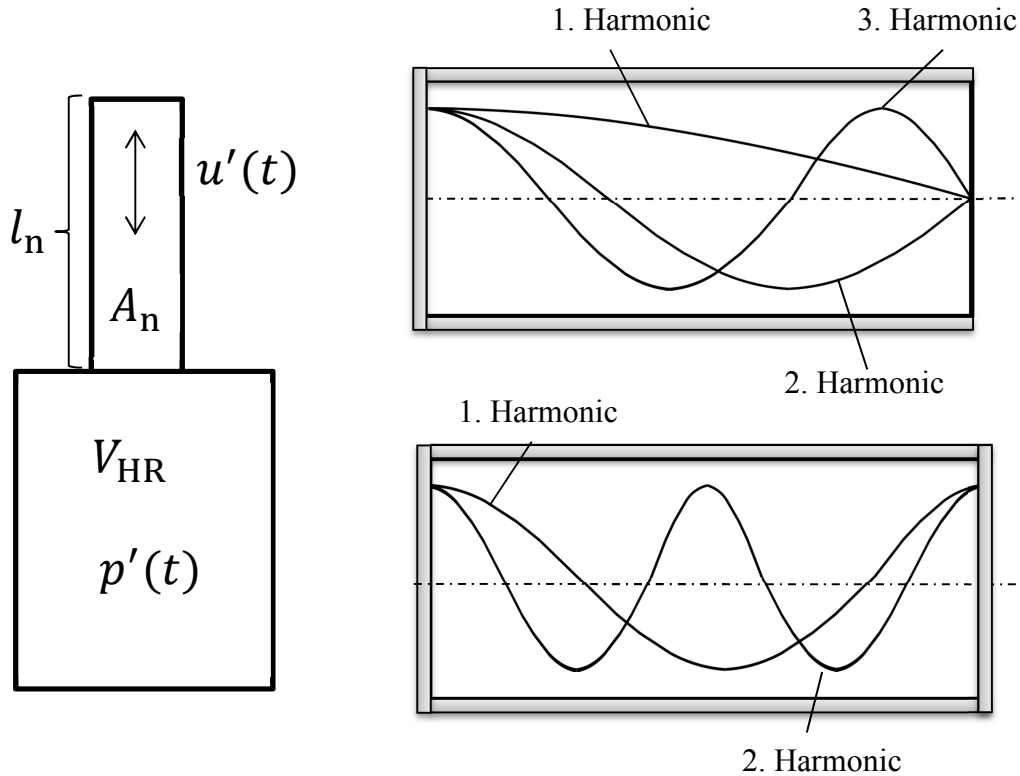


**Figure 3.2. l.h.s.: Acoustic oscillations in Helmholtz resonators; r.h.s.: Standing waves in pipes with one open end and two closed ends**

The basic principle of a Helmholtz-Resonator can be seen in analogy to a spring-mass system. The enclosed air is compressible and serves as the spring, whereas the air in the open neck corresponds to the oscillating mass. The pressure distribution inside the cavity is typically uniform and fluctuates periodically, resulting in a velocity oscillation at the outlet. The frequency of the Helmholtz-oscillation can be estimated by:

$$f_{HR} = \frac{c_0}{2} \sqrt{\frac{A_n}{V_{HR} l_{n,eq}}}, \quad (3.3)$$

where  $c_0$  corresponds to the speed of sound.  $A_n$  denotes the surface area of the outlet and  $l_{n,eq}$  the equivalent length of the neck, which is equal to its physical length plus an end correction. A common approach to calculate the equivalent neck length is given by:

$$l_{n,eq} = l_n + 2\Delta l_n \text{ with } \Delta l_n = \frac{\pi}{4} R_n, \quad (3.4)$$

where  $R_n$  represents the radius of the neck. The actual value of  $\Delta l_n$  depends on the geometry of the resonator neck. In order to account for a different inlet and outlet radius of the resonator neck, one can calculate  $l_{n,eq}$  by

$$l_{n,eq} = l_n + \Delta l_{n,i} + \Delta l_{n,o} \quad (3.5)$$

with  $\Delta l_{n,i} = \pi/4 \cdot R_{n,i}$  and  $\Delta l_{n,o} = \pi/4 \cdot R_{n,o}$ .

$R_{n,i}$  and  $R_{n,o}$  denote the inner and the outer radius of the resonator neck, respectively. Often Helmholtz modes are present in combustors which are associated with the burner nozzle or the combustion chamber exit, which have small diameters and serve as resonator necks for the large volumes of the combustor plenum (see e.g. [109]) or the combustion chamber.

Standing waves are caused by interference of acoustic waves travelling in opposite directions and can be found in pipes, for example. Assuming a constant speed of sound, frequencies of standing waves in pipes can be calculated with the wave length  $\lambda$ . In pipes with one acoustically closed end and one acoustically open end, the frequencies of the standing waves can be calculated by

$$f = \frac{2 \cdot n - 1}{4} \cdot \lambda, \quad (3.6)$$

whereas in pipes with two acoustically closed ends the frequencies attain values of

$$f = \frac{n}{2} \cdot \lambda. \quad (3.7)$$

At an acoustically closed end, the incoming wave is reflected with a phase-shift of  $\pi$  ( $180^\circ$ ), whereas the phase-shift for the reflection at an acoustically open end constitutes  $\pi/2$ . This leads to differences between the frequencies of standing waves in pipes with two acoustically closed ends and pipes with one acoustically closed and one acoustically open end.

The accuracy of the approximation of frequencies of acoustic resonances using equations (3.3)-(3.7) depends on to what extent the acoustic characteristics of combustor components and their acoustic boundaries correspond to Helmholtz resonators or pipes with ideal acoustic boundaries. In most cases, they do not comply with such idealized systems. Additionally, large temperature gradients in combustors result in different sound speeds. Therefore, more sophisticated strategies are necessary to model the acoustic behaviour of combustion systems (see 3.4.1 and 3.4.2).

### 3.3 Damping processes

As previously discussed, in order to assess the stability of a combustor one has to account for the losses of acoustic energy and damping mechanisms. According to [6], there are three mechanisms which remove energy from unstable modes or lead to dissipation processes.

- Transfer of acoustic energy to turbulence (viscous processes) or entropy disturbances (heat transfer processes)
- Transport of acoustic energy out of the combustor by convection and/or sound radiation
- Energy transfer between different acoustic modes

These processes are based on complex physical mechanisms and are not discussed in detail. Further and more detailed explanations can be found in [6]. Based on these damping processes, methods have been developed which allow for damping of unstable combustor modes. These are discussed briefly in the next section.

### 3.4 Control and Modelling Approaches for Combustion Instabilities

Combustion instabilities represent a major risk for combustor components as well as for the combustor itself. If a combustor becomes unstable and the amplitude of the unstable mode exceeds acceptable limits, one possibility to prevent damage to the combustion system is to change the operating parameters into a stable regime. However, this limits the operating range and the combustor flexibility, which represent important features of modern combustors.

Another possibility is to damp unstable modes by passive or active damping methods. Passive methods usually employ baffles, resonators and acoustic liners, which are effective in damping high-frequency oscillations [110]. Examples are given in [13, 14, 93, 111]. It is also possible to modify the fuel injection geometry in order to change the flame characteristics. Active control methods employ actuators to perturb the instability cycle. In order to decouple the heat release from the acoustic field, the fuel flow rate or mixing process can be modulated [12, 112]. Also, secondary fuel injection can be applied to damp combustion instabilities [9]. All methods are usually based on the perturbation of one or more of the discussed driving mechanisms. Further approaches for the active control of combustion instabilities are given in [10, 94, 113, 114].

In order to effectively apply passive and active control methods, it is necessary to model the thermoacoustic stability of the combustor. Modelling approaches that are able to predict the stability of the combustor in the test phase or even in the design phase would be of great advantage. In this case, the combustor design could be modified (if necessary) to ensure stable operating conditions in the desired range of operation. Some commonly used modelling approaches used to assess the thermoacoustic stability of a combustion system are discussed briefly in the following sections.

### 3.4.1 1D-Network Models and Flame Response Modelling

Figure 3.3 shows typical feedback mechanisms in technical combustion chambers with the corresponding input and output parameters of the combustor components. The feedback loop is closed by the flame, since it responds with heat release oscillations to mass flow or equivalence ratio oscillations. It modulates the oscillation of the combustion chamber pressure which in turn modulates mass flow and/or fuel flow rate.

Based on the idea that a combustion system can be described as a network of combustor components, network model approaches have been developed with the aim to describe and predict the thermoacoustic stability of the combustor.

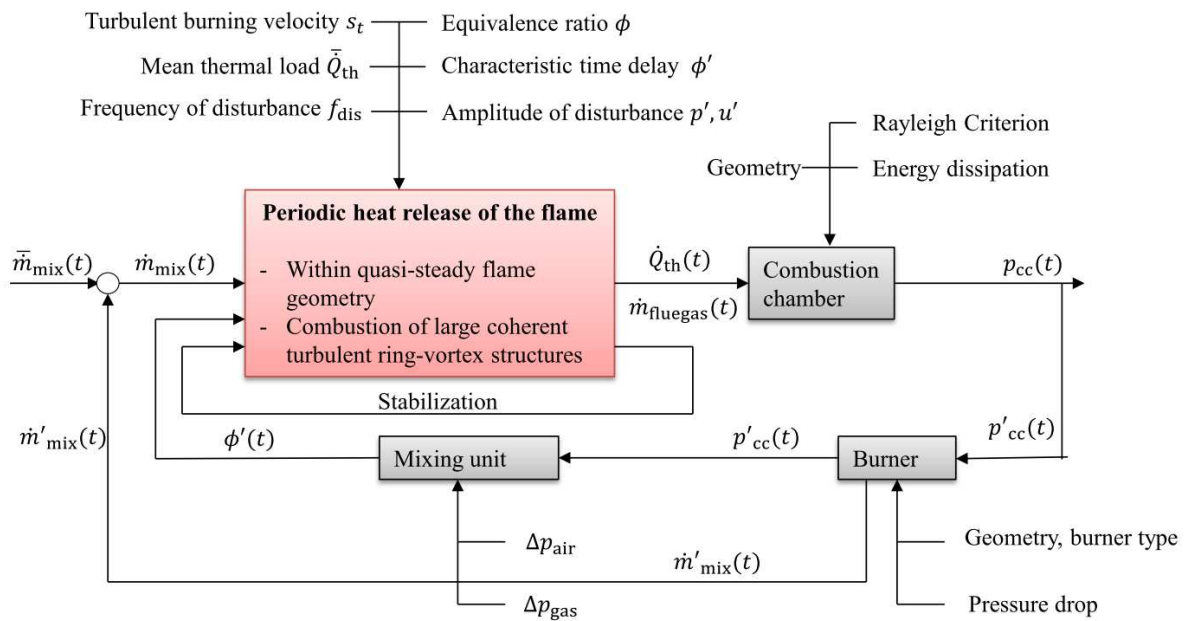


**Figure 3.3. Feedback mechanisms in technical combustion systems (adapted from [15])**

One common approach is the transfer-matrix approach, where the acoustic response characteristics of burner components are described by an acoustic element with a specific transfer function. Figure 3.4 shows an acoustic element modelled as an acoustic two-port.

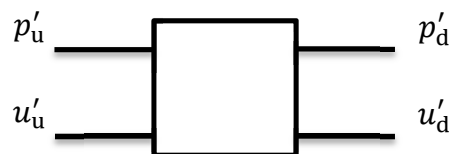


**Figure 3.4. Acoustic elements relating pressure and velocity fluctuations on both sides of the element (u  $\rightarrow$  upstream, d  $\rightarrow$  downstream)**

In the frequency domain the acoustic two-port can be described by the equation [115]

$$\begin{pmatrix} p'_d \\ u'_d \end{pmatrix} = \begin{pmatrix} T_{11} & T_{12} \\ T_{21} & T_{22} \end{pmatrix} \begin{pmatrix} p'_u \\ u'_u \end{pmatrix}, \quad (3.8)$$

where  $T_{11}$ - $T_{22}$  represent the elements of the transfer matrix  $\mathbf{T}$  which has to be determined for every element. This can be achieved experimentally by acoustic forcing and must be carried out for two independent test cases. While analytical expressions may be derived for acoustic elements other than the flame (see for example [33]), the modelling of the flame and the oscillations triggered by its unsteady heat release pose a great challenge. In the transfer matrix approach, the flame can be included as a source term [115], which has to be determined by an additional test case. Under the assumption that the burner transfer matrix  $\mathbf{B}$  does not change with combustion, the Flame Transfer Function  $FTF$  can be determined by:

$$FTF = \mathbf{T}\mathbf{B}^{-1}, \quad (3.9)$$

where  $\mathbf{T}$  represents the measured transfer matrix. For further details see [11, 115].

Another commonly used approach to describe the flame transfer function is given by:

$$F(\omega) = \frac{\dot{Q}'/\bar{Q}}{u'/\bar{u}}, \quad (3.10)$$

where  $\bar{Q}$  corresponds to the mean volumetric heat release rate and  $\bar{u}$  is the mean value of a velocity, which is usually the axial velocity near the outlet of the burner nozzle.  $\dot{Q}'$  and  $u'$  are the Fourier components of the measured signals at the driving angular frequency  $\omega$ . The FTF may be written in complex form in terms of gain  $G$  and phase  $\varphi$ :

$$F(\omega) = G(\omega)e^{i\varphi(\omega)}. \quad (3.11)$$

The FTF describes the flame response to a velocity perturbation at the combustion chamber inlet. The sensitivity of the flame's heat release on the perturbation is expressed by the gain  $G$ . The frequency-dependent phase  $\varphi$  describes the time delay between the entering of the perturbation into the combustion chamber and the heat release response. Therefore all characteristic time scales are included in the phase, including the time delays induced by mixing, convection of fuel into the flame front, ignition and reaction rate. In many cases, the convective time delay is dominant. At unstable conditions, the total time delay  $\tau$  often approximately corresponds to an odd multiple of the half-period  $\pi/2$  of the frequency of the unstable mode [102, 109, 116]. The mass flow and therefore the velocity oscillation at the combustion chamber inlet are modulated by the combustion chamber pressure which in turn has to be in phase with the heat release oscillations.

The FTF can be dependent on the magnitude of the perturbation  $|u'|$ . One possible reason for this nonlinearity of the flame response is a similar magnitude of the mean velocity  $\bar{u}$  and the

velocity oscillation  $|u'|$ . A common non-linear model approach is to extend the FTF to the Flame Describing Function (FDF) [117]:

$$F(\omega, |u'|) = \frac{\dot{Q}'/\bar{Q}}{u'/\bar{u}}. \quad (3.12)$$

The FTF may be determined analytically, for example by the  $n - \tau$  time lag model [118]. However, FTFs and FDFs are generally determined experimentally [16, 18, 19, 22, 26, 116, 119] or by CFD methods [120, 121]. The resulting FTF or FDF can then be integrated in a network model [23, 26].

### 3.4.2 3D-Methods: Helmholtz-Solvers and Large-Eddy-Simulation

It is also common to apply 3D-methods in order to study and model combustion instabilities, since they usually provide a higher level of accuracy. The downside of 3D-methods is that they usually require an increased computational effort. This is especially true for the LES, as it requires long computation times. Therefore, in most cases it is not possible to perform parameter studies with the LES when investigating the stability a combustor. However, the LES is capable of reproducing a large number of instability mechanisms when an adequate flame model is applied. It is also useful for general studies of combustion instabilities, as a large number of quantities is available, which cannot be accessed by experimental methods.

In general, the LES of combustion instabilities can be performed with or without acoustic forcing. The “forced response” method has some advantages, as it usually requires smaller computational domains than the “self-excited” method. In addition, the computational time which is needed for the system to reach limit cycle pressure amplitude may be shorter for the forced LES. The self-excited method may be more accurate, since it only models the “natural” instability of the combustion system. However, all combustor components that may be relevant for the excitation of the unstable mode have to be modelled. Additionally, it is possible that a significantly longer time period is required for the unstable mode to develop, which can result in unacceptable computation times. Discussions of the topic of forced LES vs. self-excited LES can be found in [33, 122]. References which discuss the LES of combustion instabilities are [121, 123–129].

Acoustic analysis using Helmholtz-solvers requires less computation time than the LES. Helmholtz-solvers solve the inhomogeneous Helmholtz-equation in the frequency domain. They rely on the assumption that the mean flow velocity is slow compared to the speed of sound. The Helmholtz-equation for reactive flows can be derived from the wave equation, assuming harmonic waves  $p(x, y, z) = p' e^{-i\omega t}$  and harmonic oscillations of the heat release  $\dot{q} = q' e^{-i\omega t}$ :

$$\nabla \cdot c_0^2 \nabla p' + \omega^2 p' = i\omega(\gamma - 1)q', \quad (3.13)$$

where  $c_0$  is the local speed of sound [33] and  $\gamma$  the ratio of the specific heats. Solving equation (3.13) leads to the harmonic acoustic eigenfrequencies of the modelled system. In a first step, it is possible to calculate the eigenfrequencies of a combustor by neglecting the oscillations of the heat release and assuming a constant temperature field inside the combustion chamber. For example, the heat release rate can be modelled using the  $n - \tau$  time lag model [118]. Examples for the acoustic analysis of combustion systems with Helmholtz-solvers are given in [130] and [25].

### 3.4.3 Acoustic Impedance and Acoustic Boundaries

The thermoacoustic stability of a combustor is strongly influenced by acoustic transmission properties of the reactive flow and the acoustic boundaries of the combustor components. The acoustic transmission properties of a medium are described by its specific acoustic impedance  $z_0$ . It represents the ratio of the sound pressure  $p'$  and the particle velocity  $u'$ . For planar waves, it holds

$$z_0 = \frac{p'}{u'} = \rho c_0, \quad (3.14)$$

where  $\rho$  denotes the density of the gas or fluid. Accordingly, for a one-dimensional planar acoustic wave propagating in a constant cross section duct [33]

$$p'_1 = A^+ \left( t - \frac{x}{c_0} \right) + A^- \left( t + \frac{x}{c_0} \right), \quad (3.15)$$

the velocity perturbation yields

$$u'_1 = \frac{1}{z_0} \left( A^+ \left( t - \frac{x}{c_0} \right) - A^- \left( t + \frac{x}{c_0} \right) \right). \quad (3.16)$$

$A^+$  is the amplitude of the wave propagating in the positive  $x$ -direction and  $A^-$  denotes the amplitude of the wave propagating in the opposite direction. The acoustic transmission properties of an acoustic boundary are dependent on the ratio of its specific acoustic impedance  $z_B$  and the specific acoustic impedance of the gas/fluid in which the acoustic waves propagate. This may be described by a reduced specific acoustic impedance

$$Z = \frac{z_B}{z_0} = \frac{1}{\rho c_0} \frac{p'_1}{u'_1}. \quad (3.17)$$

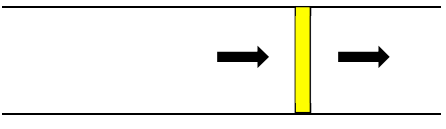
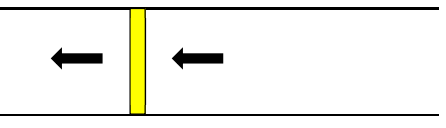
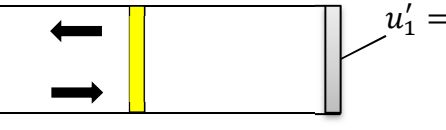
The reflection coefficient  $R$  of an acoustic boundary at a location  $x = x_p$  is defined as the amplitude ratio of the acoustic waves:

$$R = \frac{A^+(t - x_p/c_0)}{A^-(t + x_p/c_0)}. \quad (3.18)$$

Thus it can also be defined using the reduced specific acoustic impedance  $Z$ :

$$R = \frac{Z + 1}{Z - 1}. \quad (3.19)$$

Table 3.1 shows the reduced specific acoustic impedances and reflection coefficients for the acoustic boundaries of an ideal one-dimensional duct. If the duct is infinitely long in the positive  $x$ -direction, all acoustic waves propagate in the positive  $x$ -direction. As a consequence  $A^-$  is zero and  $R$  is infinite. When the duct is infinite in the negative  $x$ -direction,  $A^+$  and therefore also  $R$  are zero. In both cases  $Z$  equals unity.

Configuration	Boundary condition	$R$	$Z$
 Infinite duct on the right side	Non-reflecting	$\infty$	1
 Infinite duct on the left side	Non-reflecting	0	-1
 Duct terminating in large vessel	$p'_1 = 0$	-1	0
 Duct terminating on rigid wall	$u'_1 = 0$	1	$\infty$

**Table 3.1. Reflection coefficients and specific acoustic impedances in ideal one-dimensional ducts (adapted from [33])**

At closed ends, for example walls, all incoming waves are reflected and the velocity perturbations vanish ( $u_1 = 0$ ). The acoustic boundary is “sound hard” and features infinite specific acoustic impedance, which results in a reflection coefficient of  $R = 1$ . When the duct leads into a large cavity, where the pressure can be considered constant and the pressure perturbations are zero ( $p_1 = 0$ ), the acoustic boundary is considered to be “sound soft”. The specific acoustic impedance is zero and the reflection coefficient constitutes  $R = -1$ .

Real acoustic boundaries of combustor components or combustion chambers do not feature reflection coefficients or specific acoustic impedances which correspond to the discussed ideal acoustic boundaries, since their reflection coefficients are influenced by area and temperature variations as well as mean flow effects (see [131]). The modelling of the acoustic transmission characteristics with complex geometries is even more involved. Perforated plates, for example, show a frequency-dependent reflection coefficient which is also influenced by the presence of mean flow [132]. In general, specific acoustic impedances of combustor components and their boundaries have to be determined experimentally or predicted by adequate models.

## 4. Experimental Investigations

In this chapter, first the modular combustor is described that was used to perform the experimental investigations. In the subsequent text, the test facility, the diagnostic tools and the operating conditions under which the measurements were performed are explained. Afterwards, the results of the measurements are discussed in detail.

### 4.1 Design Concept of the Modular Combustor

The aim of the design process of the modular combustor was to construct a burner system which can be operated in single- and multiple-burner configuration. Additionally, it should be possible to realize different arrangements of the single-burners.

In the following sections, the concept of the modular combustor used for the investigations presented in this work is explained in detail. First, the design of the nozzle and the single burner will be discussed. Additionally, the way the single-burners are assembled together into the multiple-burner setup is described. The last part of this chapter focuses on the diagnostic techniques which were applied to investigate combustion instabilities in the combustor.

#### 4.1.1 Design of the Burner Nozzle

The nozzle is a double-concentric swirl nozzle with two swirlers and was used for studies in several subprojects of the Collaborative Research Centre 606. The inner, primary swirler has 8 swirl ducts with a rectangular flow cross-section of 5.2 mm x 6.7 mm that lead into a first conical and then circular duct with a diameter of 15 mm. The outer, secondary swirler contains 12 rectangular swirl ducts of 4 mm x 5.6 mm which lead to a partly conical duct with an outlet diameter of 25 mm. The fuel flows from the fuel supply pipe through two small chambers, which are connected by six ducts of 4 mm. The fuel exits the second chamber through 60 circumferentially distributed holes with a diameter of 0.5 mm and mixes with the air flow of the primary swirler (Figure 4.1).

The theoretical swirl number of each swirler calculated according to Equation (2.71) constitutes  $S_{th,IS} = 0.46$  for the inner swirler and  $S_{th,OTS} = 1.02$  for the outer swirler. Since the swirlers do not feature the same individual theoretical swirl number, the swirl number of resulting swirl flow depends on the ratio of the swirler mass flows (see equation (2.72)).

#### 4.1.2 Design of the Single-Burner

In order to be able to independently control the mass flow through each swirler, the air inlets for both swirlers are separated (Figure 4.2). The cross-section of the outer pipe is of quadratic shape (outside dimensions 100 mm x 100 mm) with a wall thickness of 5 mm, whereas the first inner pipe is circular, with an outside diameter of 80 mm and a wall thickness of 2 mm. Inside the inner pipe, a second circular pipe of 50 mm in outside diameter and a wall

## 4.1 Design Concept of the Modular Combustor

thickness of 2 mm is placed, whose outer wall serves as the inner boundary for the air flow inside the plenum. The pipe for the fuel supply of the nozzle is situated inside this third pipe.

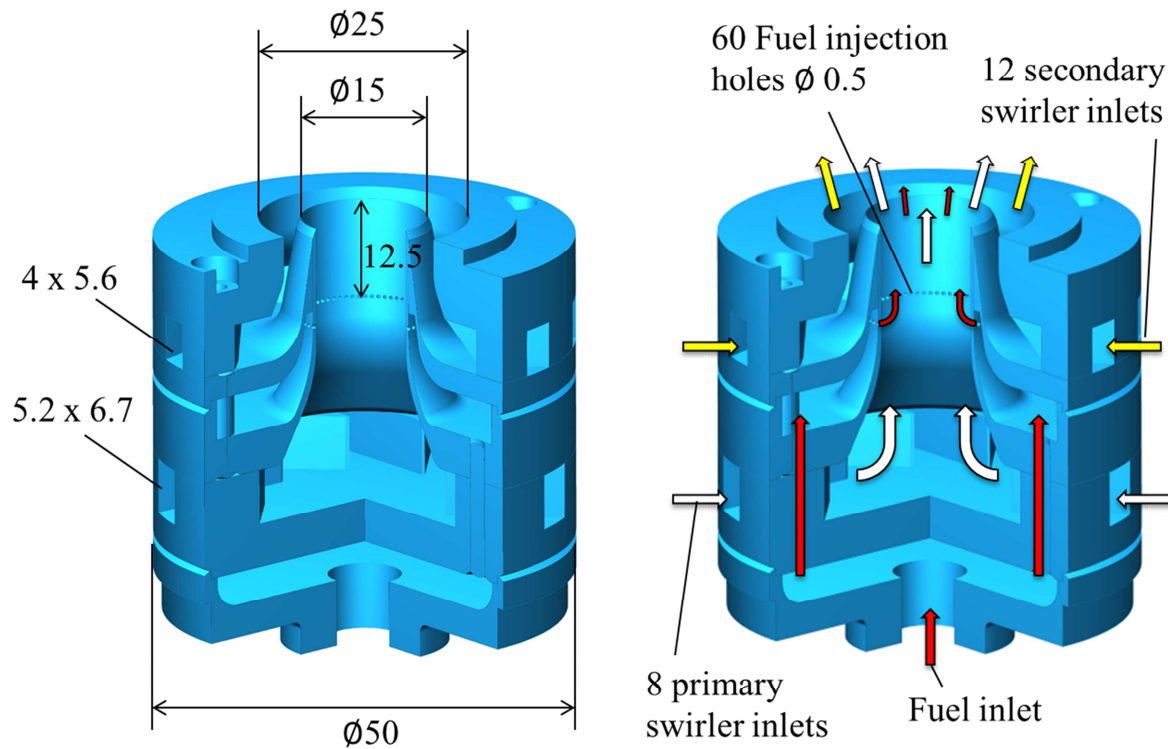


**Figure 4.1. Double-concentric swirl nozzle with two swirlers. The yellow arrows indicate the secondary air flow, the white arrows the primary air flow and the red arrows the fuel flow.**

The air for the secondary swirler is introduced through the upper inlet port and flows between the outer pipe and the first inner pipe. The flow is homogenised by a perforated plate with a free area of 10 % before it enters the inlets of the swirler. The air flow for the primary swirler enters the burner plenum through the lower inlet port. At first it flows through the outer quadratic pipe and is then also homogenised by a perforated plate with 10 % free area. It then flows between the first and the second inner pipe to the inlets of the swirler.

The nozzle is centred inside the top of the plenum. It is pressed inside the centring using a screw nut at the bottom in order to avoid bypass flow into the combustion chamber. The combustion chamber is equipped with four quartz glass windows, which are held by steel frames and form a quadratic flow cross section of 89 mm x 89 mm. The outlet is divided into a conical part, where the inner diameter decreases from 75 to 50 mm and a circular part with a constant inner diameter of 50 mm. The combustion chamber is centred on the top of the plenum and two pins of 2 mm in diameter circumvent a possible rotational movement due to vibrations.

In order to combine the single-burners into multiple-burner configurations, the outer pipe has seven additional openings, which are covered by caps in single-burner mode. This allows for combining the plenums of the single-burners while keeping the air inlets for the inner and outer swirlers connected. Adapters are placed inside the openings, which simplify the alignment of the burners. In addition, two glass windows are removed and adapters are inserted into the slots of the glass windows, in order to combine the combustion chambers of the single-burners into a unified combustion chamber with multiple flames.

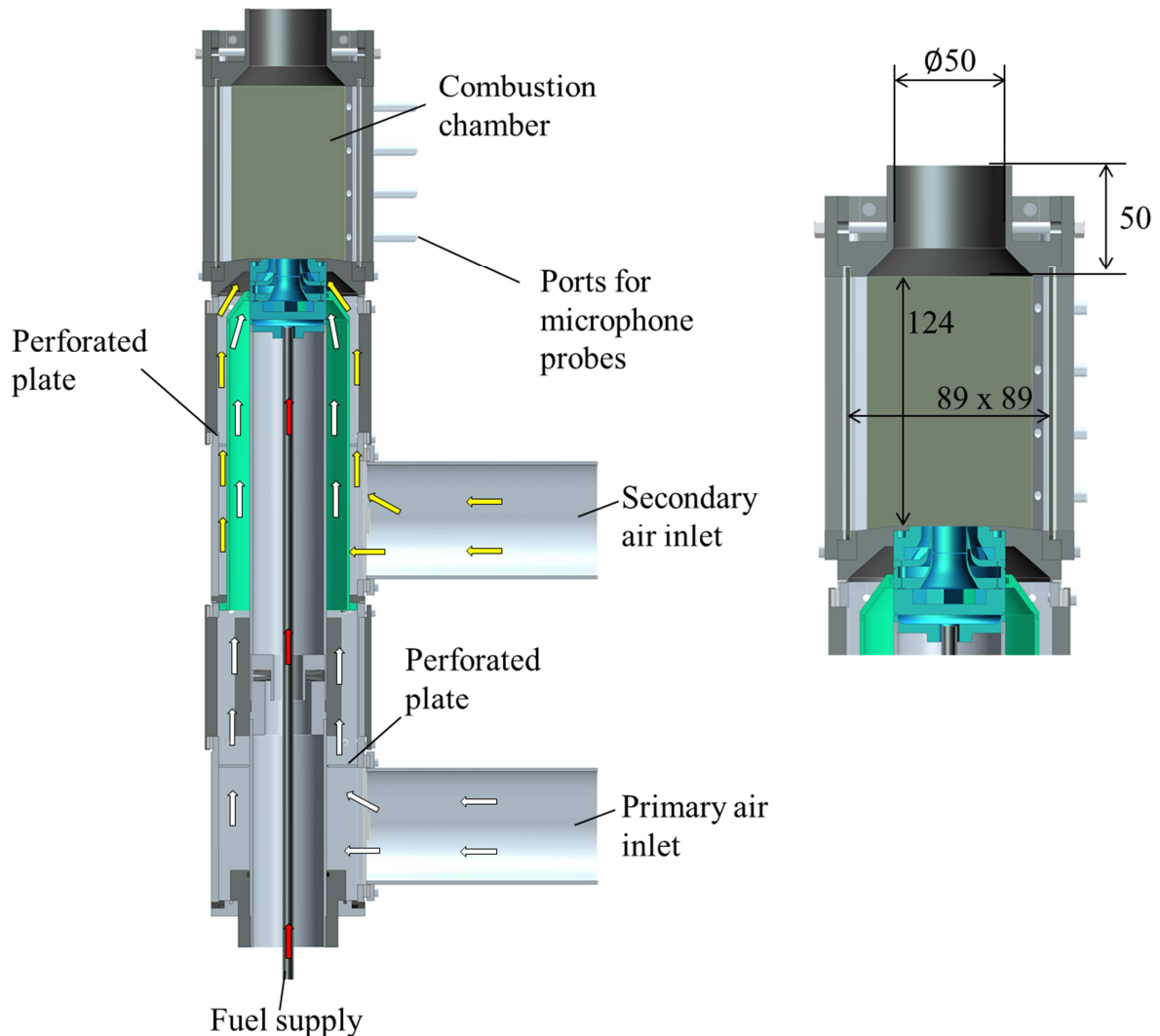


**Figure 4.2. Single-burner with two separated air inlets**

#### 4.1.3 Multiple-Burner Setups

As shown in Figure 4.3, in the first multiple-burner setup (MBS1) four single burners are linearly aligned (multiple-burner setup 1, MBS1). In this setup, the outer flames are bounded by three combustion chamber walls and have one neighbouring flame. The inner flames are bounded by two side walls and have two neighbouring flames

In the second multiple-burner setup (multiple-burner setup 2, MBS2) four burners are arranged in an “annular” arrangement (Figure 4.3). However, the inner and the outer

4.1 Design Concept of the Modular Combustor

boundary of the combined combustion chamber are of quadratic shape. Each flame is bounded by two side walls and two flames. The ratio of the distance between the burner centerlines  $s_{bc}$  and the diameter of the nozzle exit  $d_{nz}$  ( $= 25 \text{ mm}$ ) constitutes in both MBSs  $s_{bc}/d_{nz} = 4.1$ .

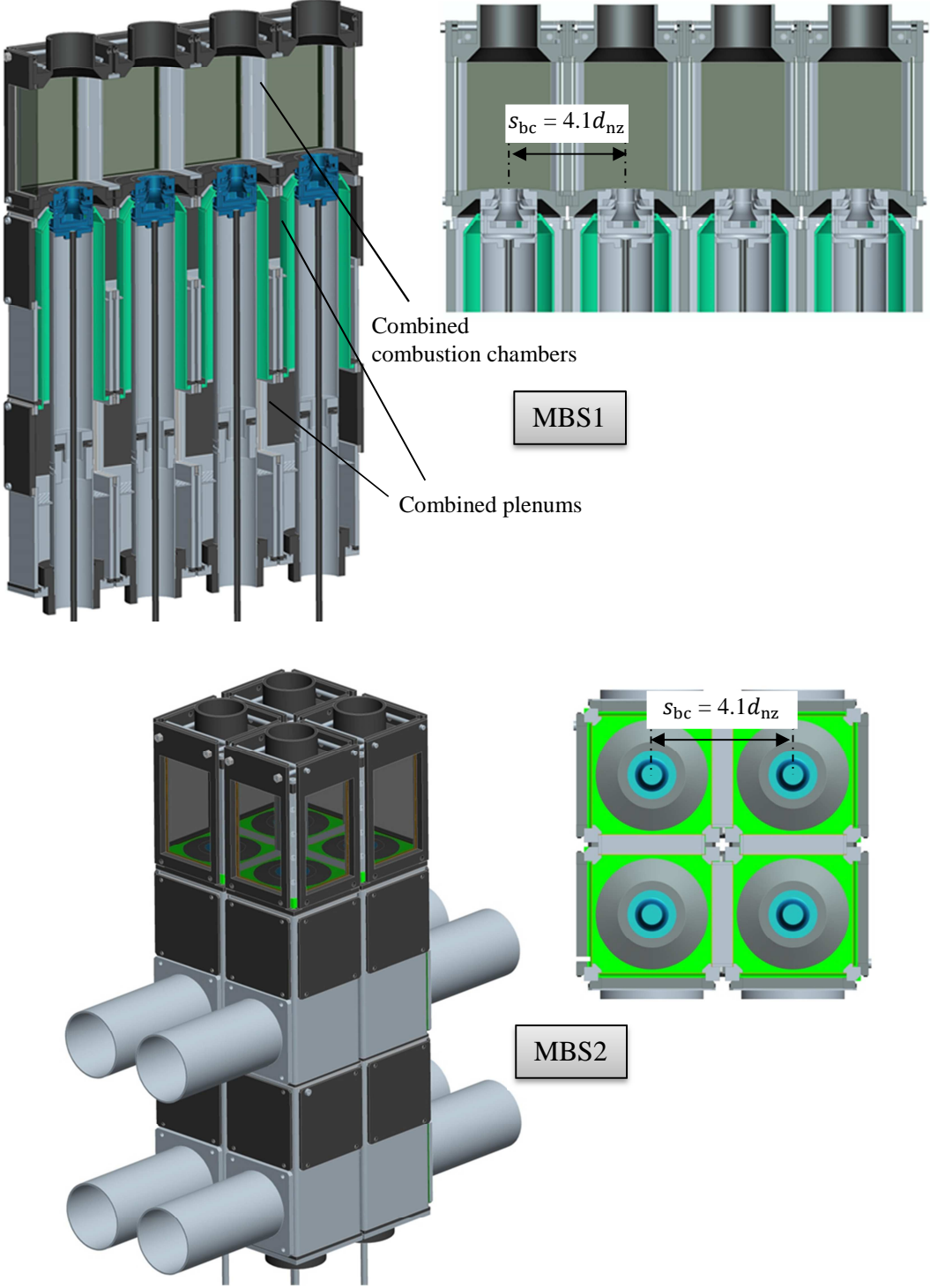


Figure 4.3. Modular combustor in MBS1 and MBS2

## 4.2 Test Rig and Diagnostic Methods

The combustor is mounted onto a sliding carriage which is mounted onto a frame construction. The combustor can be moved horizontally with electric motors and manually by a thread which is turned by using a hand wheel. The air is supplied by a compressor and flows through an air duct to the test rig, where it is split into two air flows. Each flow is controlled independently with a hand valve. The mass streams of air are measured upstream by two thermal Bronkhorst mass flow meters, with a deviation of 1 % for the upper value of the measurement range 0-80 m<sup>3</sup>/h (STP,  $T = 273$  K,  $p = 1013$  mbar). The air flows then enter the air distributors, which are needed to enable the air supply of all single burners in multiple-burner configuration. Flexible tubes connect the inlet ports of the combustor with the air distributors.

The flow of natural gas is controlled independently with M+W mass flow controllers for every burner. The measurement accuracy of the mass flow controllers constitutes 3 % for the upper value of the measurement range 0-100 l/min (STP).

### 4.2.1 Setup for the Measurement of Pressure Oscillations

Pressure oscillations in the combustion chamber and the plenum are measured by using three microphone probes with Bruel & Kjaer pressure field microphones. The probe, which is connected to the combustion chamber, is a coiled tube with a straight length of 4 m. This protects the microphone from the high temperatures in the combustion chamber. Additionally, a very small nitrogen flow is introduced into the microphone probe, which prevents exhaust gases from entering the probe. The microphones are connected to Bruel & Kjaer conditioning amplifiers. The output signal of the amplifiers is transformed with Fast Fourier Transformation (FFT) by an Agilent 35670a signal analyser.

Since the probes can alter the pressure signal and damp or amplify certain frequencies, it is necessary to measure the frequency response of the microphone probes. This is done with a small branch pipe tee which serves as calibration chamber. Two microphones are connected to the opposite openings, whereas one microphone is connected via the microphone probe. A small loudspeaker is connected to the third opening and sends a periodic computer generated chirp in the range of 20 to 1600 Hz into the branch pipe tee. The signal analyser puts the two microphone signals in reference and calculates the frequency response of the microphone probe.

### 4.2.2 High-Speed Measurements of OH\*-Chemiluminescence

The OH\*-chemiluminescence can be used as a local indicator for the heat release in laminar flames [133]. In the case of perfectly premixed turbulent flames, it can be used to monitor the integral heat release and for quantitative analysis of the heat release [134, 135]. In diffusion flames and partially-premixed or “technically premixed” flames, it has to be considered that

the OH\*-chemiluminescence also reacts to equivalence ratio fluctuations. Schuermans et al. derived in [134] the following relations for the OH\*-intensity fluctuations  $I'$  and heat release fluctuations  $Q'$  for low Mach number flows:

$$\frac{Q'}{\bar{Q}} = \frac{\dot{m}'}{\bar{\dot{m}}} + \frac{Y'_{\text{Fuel}}}{\bar{Y}_{\text{Fuel}}}, \quad (4.1)$$

$$\frac{I'}{\bar{I}} = \frac{\dot{m}'}{\bar{\dot{m}}} + \alpha \frac{Y'_{\text{Fuel}}}{\bar{Y}_{\text{Fuel}}}. \quad (4.2)$$

$\bar{Q}$ ,  $\bar{I}$ ,  $\bar{\dot{m}}$  and  $\bar{Y}_{\text{Fuel}}$  denote the mean values of heat release, OH\*-intensity, mass flow into the combustion chamber and fuel mass fraction. The factor  $\alpha$  describes the dependency of the OH\*-intensity on fluctuations of the fuel mass fraction  $Y'_{\text{Fuel}}$ . For perfectly premixed flames, the fluctuations of the fuel mass fraction vanish ( $Y'_{\text{Fuel}} = 0$ ). In this case, OH\*-intensity fluctuations can be used as a measure for heat release fluctuations.

In flames where equivalence ratio fluctuations are present ( $Y'_{\text{Fuel}} \neq 0$ ), it depends on the value of  $\alpha$  as to how far OH\*-intensity fluctuations represent heat release fluctuations. According to [134], typical values of  $\alpha$  in technical combustion chambers are in the range of 5-10. Therefore great care has to be taken in interpreting the results of OH\*-chemiluminescence imaging in case of non-perfectly premixed flames. Examples where OH\*-chemiluminescence imaging was used to monitor heat release oscillations in non-perfectly premixed flames are found in [98, 136, 137].

### 4.2.3 Recording and Analysis of the OH\*-Intensity Signal

The OH\*-chemiluminescence was recorded with a LaVision High-Speed-Star CMOS camera which is equipped with a signal intensifier. The chemiluminescence signal of the flame is filtered with a band-pass filter (308 nm) to filter the OH\*-chemiluminescence. In the MBS1 the OH\*-chemiluminescence of one of the inner flames was recorded. It was chosen to record the flame of the particular single-burner which was used in the SBS, to ensure a consistent comparison between the SBS and the MBS1. In the MBS2, the camera was put at an angle of about 40° to the combustion chamber walls in order to monitor two flames simultaneously and to avoid areas where the summed OH\*-intensity of both flames is recorded by the camera. However, as the flames are oscillating, a variable region of summed intensity persists.

Series of high-speed images also provide the possibility of a frequency-locked post-processing, in order to visualize certain modes in the flame oscillations. With consideration for the restrictions mentioned in 4.2.2, an analysis of the modes of the integral OH\*-intensity by Fast Fourier Transformation (FFT) can provide information if pressure and heat release oscillate at the same frequency.

### 4.3 Investigated Operating Points

The combustor employs separate air inlets for the swirlers and provides a high flexibility regarding its setup. As a consequence, a high flexibility concerning possible operating conditions for the combustor is also given. Therefore choices had to be made regarding the OPs to be investigated. The following section gives a summary of the operating conditions chosen for the microphone measurements.

Pressure oscillations were measured in all combustor setups without additional preheating of the combustion air for different thermal powers and equivalence ratios. In the SBS, the thermal power was varied from  $P_{th} = 15\text{-}30$  kW and in the MBSs from 60-120 kW (or 15-30 kW/burner). The range of the equivalence ratio stretches from  $\phi = 0.85$  down to a value of  $\phi = 0.55$ , depending on the lean stability limit. The combustor design also allows the operation of the combustor with different swirler mass flow ratios, since the mass flow through each swirler is controlled independently. The swirler mass flow ratio  $L$  is defined as the ratio of the air mass flow through the outer swirler to the air mass flow through the inner swirler:

$$L = \frac{\dot{m}_{OTS}}{\dot{m}_{IS}}. \quad (4.3)$$

At a value of  $L = 1.6$  both swirlers generate approximately the same pressure drop. Measurements were performed for all combustor setups for  $L = 1.2, 1.6$  and  $2.0$ . As discussed in 4.1.1, this leads to different theoretical swirl numbers for the swirl flow. The resulting values for  $S_{th}$  are shown in Table 4.1. Thus, the value of the swirler mass flow ratio  $L$  leads to changes in the flow field in the combustion chamber and influences the swirl-induced recirculation zone, which in turn leads to different flame shapes and flame characteristics.

$L$	1.2	1.6	2.0
$S_{th}$	0.7	0.78	0.82

**Table 4.1. Theoretical swirl number  $S_{th}$  at  $L = 1.2, 1.6, 2.0$**

Figure 4.4 shows the averaged OH\*-intensity for  $L = 1.2, 1.6, 2.0$  in the MBS1 at  $P_{th} = 25$  kW/burner,  $\phi = 0.7$ . It clearly illustrates that the value of  $L$  affects the flame shape. The most significant difference is that the flame becomes much shorter with increasing  $L$ . The augmented swirl intensity results in higher integral conversion rates, possibly caused by increased recirculation rates of burnt gases.

However, in technical combustors, the swirlers of double-concentric swirl nozzles normally employ combined swirler inlets and thus are operated with the same pressure drop. Hence, the

### 4.3 Investigated Operating Points

swirler mass flow ratio  $L = 1.6$  was used as the default setting and most of the investigations were carried out with this value. Table 4.2 gives an overview of the investigated OPs.

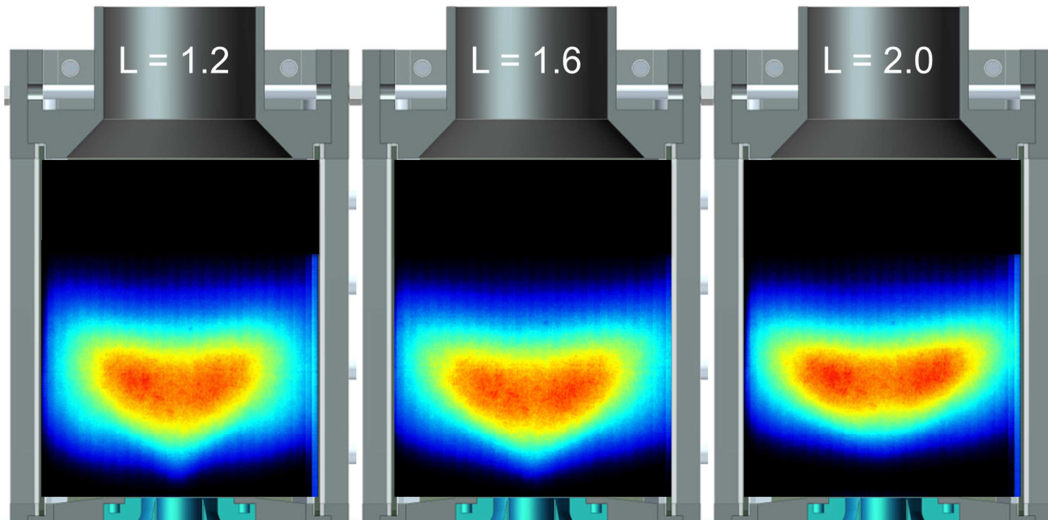


Figure 4.4. Average  $\text{OH}^*$ -intensity at  $L = 1.2, 1.6, 2.0$  in the MBS1 at  $P_{\text{th}} = 25 \text{ kW/burner}$ ,  $\phi = 0.7$

Combustor setup	$P_{\text{th}}$	$\Delta P_{\text{th}}$	$\phi$	$\Delta \phi$	$L$
SBS	15 – 30 kW	2.5 kW	0.85 – 0.6	0.05	1.6
MBS1 (4 burners)	60 – 120 kW	10 kW	0.85 – 0.6	0.05	1.6
MBS2 (4 burners)	60 – 120 kW	10 kW	0.85 – 0.6	0.05	1.6
SBS	15 – 30 kW	5 kW	0.85 – 0.6	0.05	1.2
MBS1 (4 burners)	60 – 120 kW	10 kW	0.85 – 0.6	0.05	1.2
MBS2 (4 burners)	60 – 120 kW	10 kW	0.85 – 0.6	0.05	1.2
SBS	15 – 30 kW	5 kW	0.85 – 0.55	0.05	2.0
MBS1 (4 burners)	60 – 120 kW	10 kW	0.85 – 0.6	0.05	2.0
MBS2 (4 burners)	60 – 120 kW	10 kW	0.85 – 0.6	0.05	2.0

Table 4.2. List of the OPs investigated in the SBS, MBS1 and MBS2.  $\Delta P_{\text{th}}$  and  $\Delta \phi$  denote the step size for the variations of thermal power and equivalence ratio.

## 4.4 Experimental Results

This section begins with the discussion of the overall sound pressure levels (OASPLs) measured in the different combustor setups. Subsequently, the typical combustor modes are presented followed up by their detailed analysis.

### 4.4.1 Overall Sound Pressure Levels and Lean Stability Limit

To give an impression as to how the combustion dynamics in the combustor are affected by different operating conditions, the overall sound pressure levels (OASPL) measured in the combustion chamber are plotted against the thermal power and the equivalence ratio in Figure 4.5. The white triangles mark the OPs with existing measurement data. The data in between is derived by data triangulation.

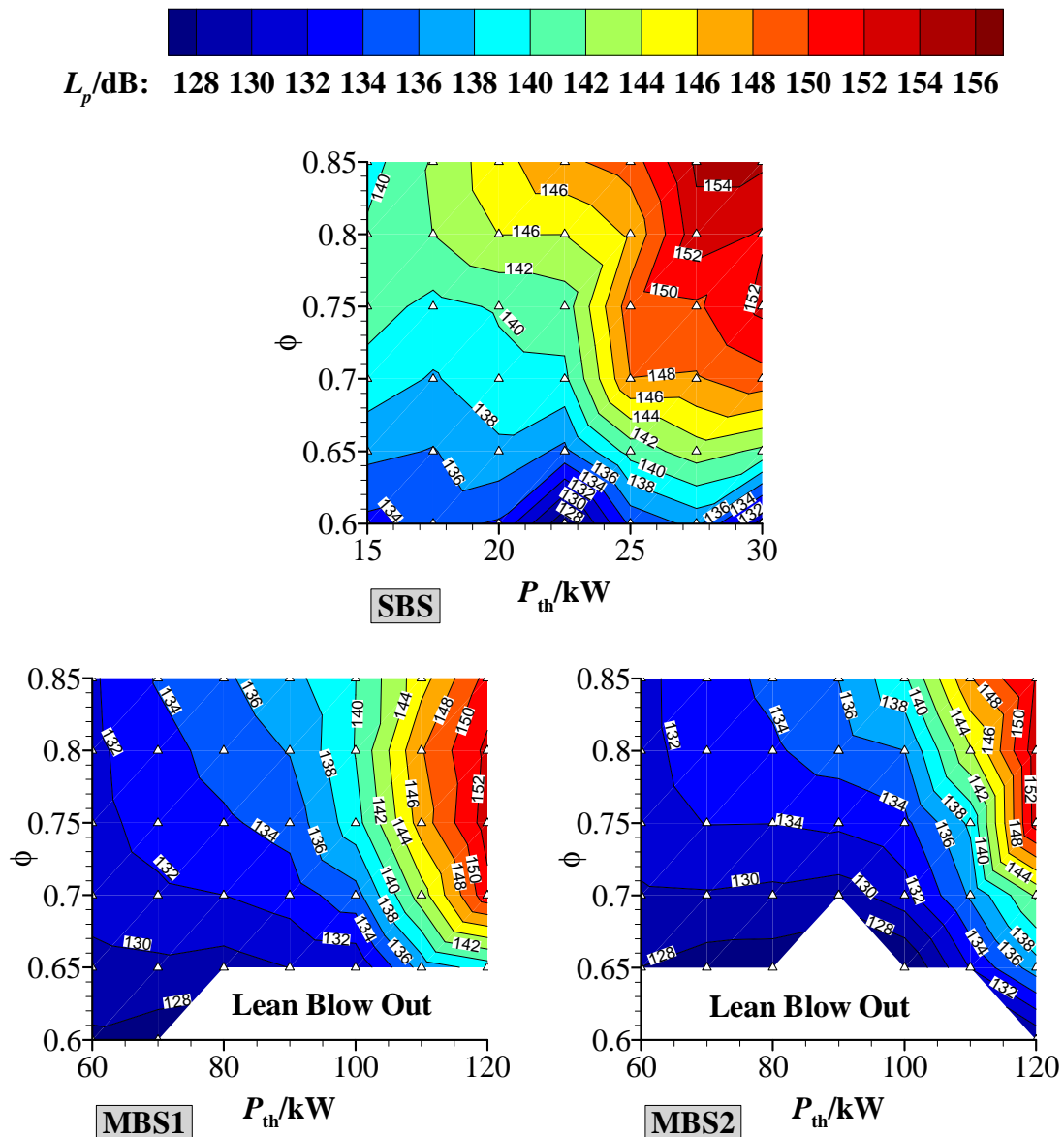


Figure 4.5. OASPL for all combustor setups in the combustion chamber at  $L = 1.6$

In all combustor setups the OASPL increases with increased thermal power. In the SBS, the OASPL augments continuously with the equivalence ratio up to the maximum of 156 dB at  $\phi = 0.85$ . In the MBSs, the peak values of the OASPL are slightly smaller with a value of 154 dB in both MBSs. In contrast to the SBS, the OASPLs in the MBSs do not increase continuously with the equivalence ratio and the maximums are observed at  $\phi = 0.75$  (MBS1) and  $\phi = 0.8$  (MBS2).

In the MBSs, the values of the OASPL are considerably lower than in the SBS in the range of  $P_{th} < 30$  kW/burner, but can exceed the OASPL in the SBS at  $P_{th} = 30$  kW/burner. This is illustrated in Figure 4.6 for  $\phi = 0.8$ . Depending on the operating conditions, more acoustic energy is dissipated in the MBSs and the multiple-flames setup damps the amplitudes of the pressure oscillations in the range of  $P_{th} < 30$  kW/burner.

The lean stability limit of the flame is also affected by the burner configuration. For the SBS, stable flames can be observed for all plotted OPs, whereas in the MBS1, the lean stability limit is exceeded in the range of  $P_{th} = 20$ -30 kW/burner and  $\phi = 0.65, 0.6$ . In the MBS2, it is only possible for  $P_{th} = 30$  kW/burner to operate the combustor at  $\phi = 0.6$ .

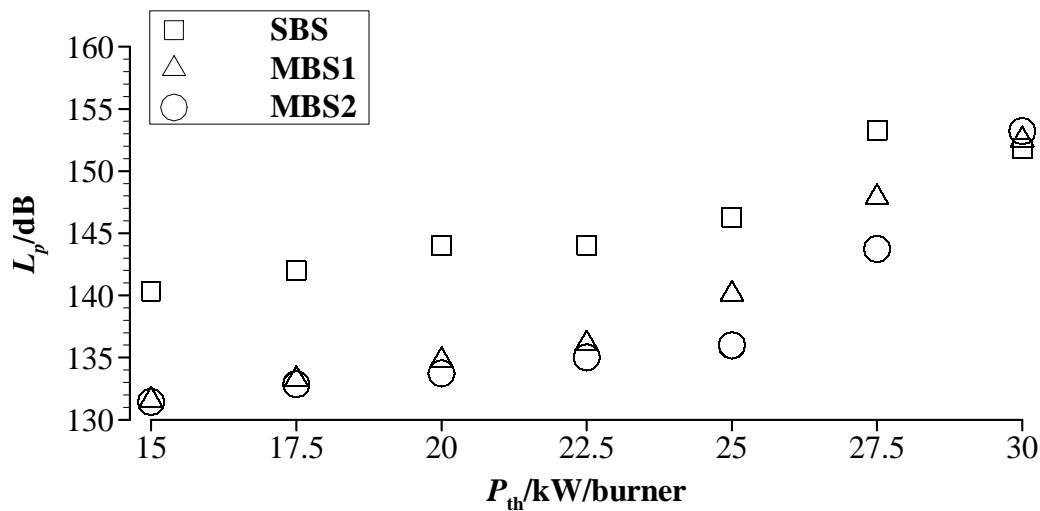


Figure 4.6. OASPL  $L_p$ /dB in all combustor setups with increasing  $P_{th}$ /burner at  $\phi = 0.8$

#### 4.4.2 Typical Combustor Modes in the Different Combustor Setups

In each combustor setup numerous dominant modes are found. In general, their amplitudes and in some cases their frequencies are dependent on the operating conditions. Some of the modes are observed in all combustor setups, in some cases at different operating conditions, whereas others are only observed in the SBS or the MBSs. In this section, an overview is given for the typical unstable modes observed in the investigated combustor setups. These modes are discussed in more detail in the subsequent sections.

#### 4.4.2.1 Low-Frequency Modes in the Frequency Range of 100-300 Hz

In the low-frequency range for  $P_{th} < 30$  kW, the pressure spectra in the combustion chamber of the SBS show a dominant frequency at around 140 Hz, as depicted in Figure 4.7 for  $P_{th} = 20$  kW/burner,  $\phi = 0.85, 0.7$  at  $L = 1.6$ . The frequency of the mode at  $\sim 140$  Hz is not affected by the equivalence ratio, and therefore is not influenced by the flow rate. However, its amplitude is significantly augmented at lower equivalence ratios. The first harmonic oscillation also seems to be excited at 280 Hz. The spectra of the MBSs both show dominant modes at 120-130 Hz. Unlike the mode at 140 Hz in the SBS, their frequencies increase with increasing flow rate.

At  $P_{th} = 30$  kW/burner,  $L = 1.6$ , the spectra of the SBS also show the mode with the flow rate-dependent frequency at  $\sim 160$  Hz for  $\phi = 0.85$  and 180 Hz for  $\phi = 0.75$  (Figure 4.8). At  $\phi = 0.75$ , an additional dominant frequency is observed at  $\sim 240$  Hz. At  $\phi = 0.85$ , the spectra of the MBSs show the mode with the flow rate-dependent frequency (similar to the SBS) at  $\sim 160$  Hz. In the MBS2, additional dominant modes are observed at  $\sim 180$  Hz and  $\sim 210$  Hz. The spectrum of the MBS1 is quite similar to the one of the SBS at  $\phi = 0.75$ , but the spectrum of the MBS2 differs significantly from the spectra of the other combustor setups, as only one peak at 200 Hz is observed. It is assumed that this dominant frequency is a similar oscillation to the one at 180 Hz at  $\phi = 0.85$ . A similar oscillation can also be found in the SBS and the MBS1 at different operating conditions, which is discussed in 4.5.1.4.

At  $\phi = 0.65$ , in the SBS-spectrum the mode with the flow rate-dependent frequency is still observed at a frequency of approximately 210 Hz. Both MBSs show a dominant pressure oscillation at  $\sim 225$  Hz with relatively high amplitudes of about 135 dB which is not observed in the SBS at  $L = 1.6$ . However, as indicated by the dashed line (Figure 4.8), it is possible to generate a similar oscillation in the SBS by decreasing the swirler mass flow ratio to  $L = 1.2$ .

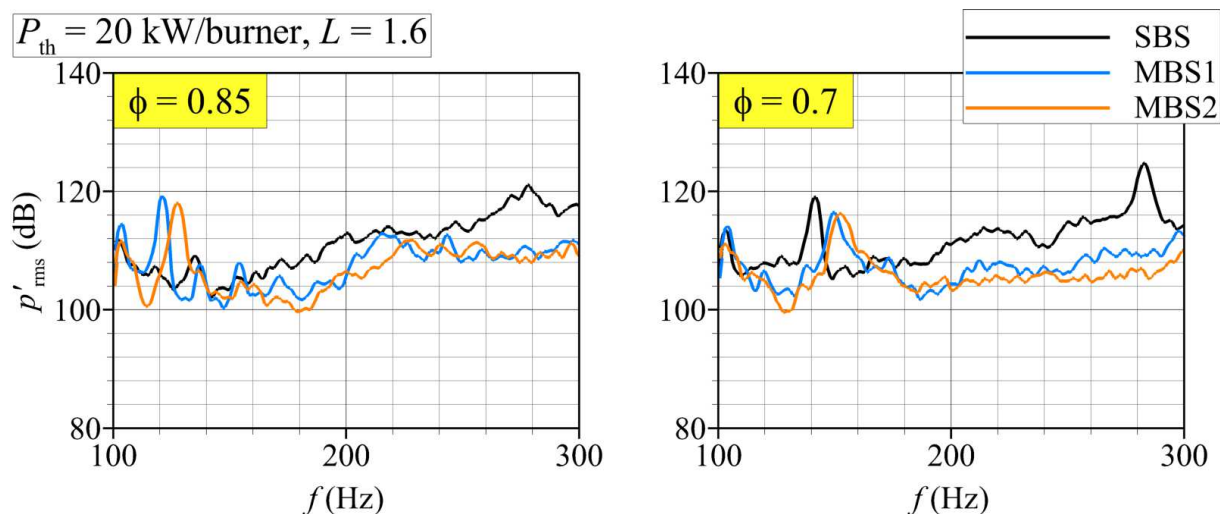


**Figure 4.7. Low-frequency modes in the combustion chamber in the SBS, MBS1 and MBS2 at  $P_{th} = 20$  kW/burner,  $\phi = 0.85, 0.7$ ,  $L = 1.6$**

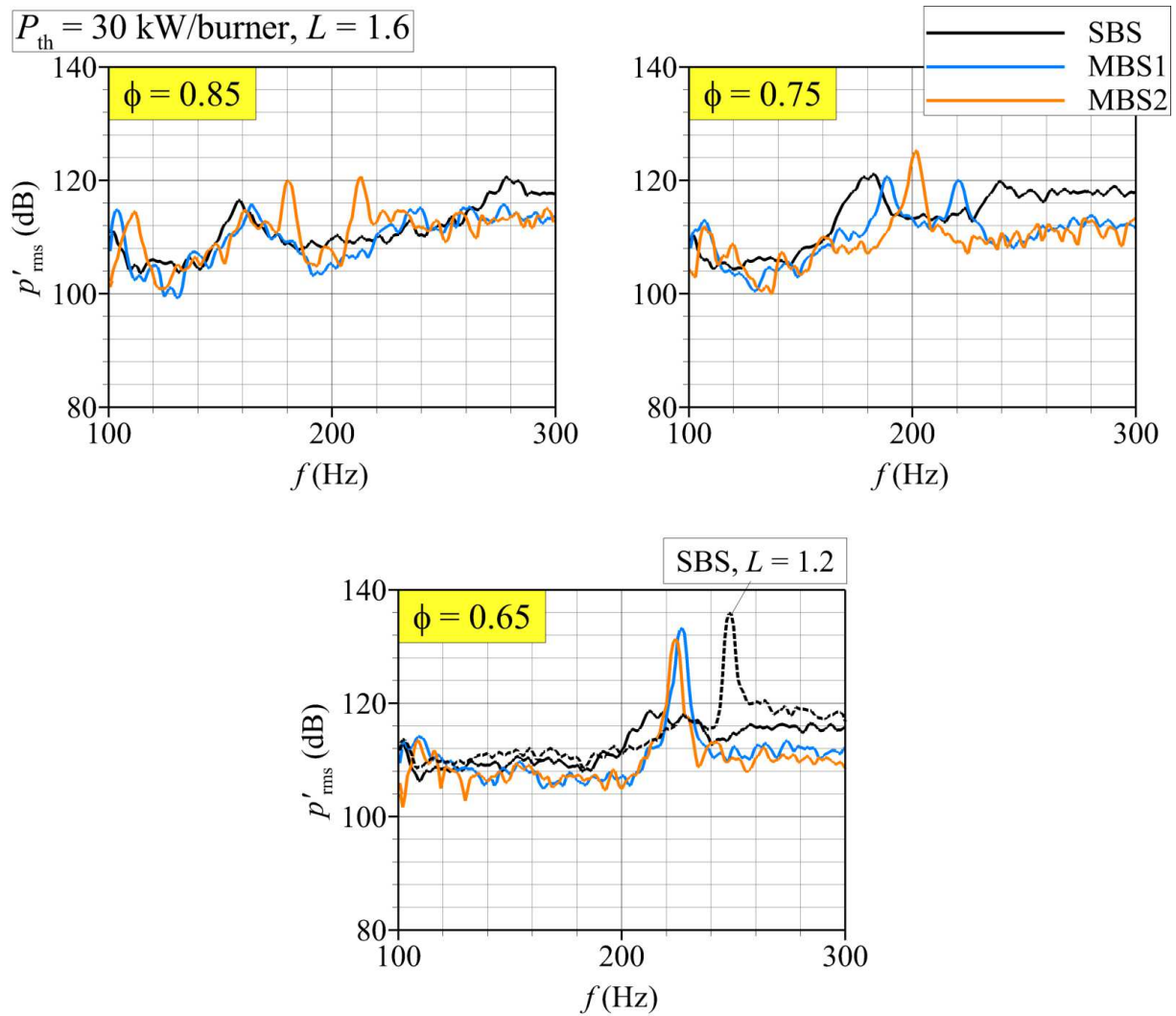


**Figure 4.8. Low-Frequency modes in the combustion chamber for the SBS, MBS1 and MBS2 at  $P_{th} = 30$  kW/burner,  $\phi = 0.85, 0.75, 0.65$ ,  $L = 1.6$**

#### 4.4.2.2 Unstable Mode in the Frequency Range of 400 Hz

In all combustor setups an unstable mode with very high amplitudes (values  $> 150$  dB) can be observed (see Figure 4.9). In the SBS, this mode can already be observed at  $P_{th} = 25$  kW/burner, whereas in the MBSs thermal power  $> 27.5$  kW/burner is necessary in order to generate the instability. The amplitude of the mode strongly decays in leaner flames which is visible in the spectrum for  $P_{th} = 30$  kW,  $\phi = 0.65$ . No influence of the flow rate on the frequency of the mode can be observed. Slight differences in frequency between the different OPs may be triggered by temperature effects.

#### 4.4.2.3 Unstable Mode in the SBS in the Frequency Range of 750 Hz

In the frequency range of around 750 Hz an unstable mode can be observed in the SBS (Figure 4.9). It is excited at around  $P_{th} = 30$  kW/burner in combination with an equivalence ratio of  $\phi = 0.85$ . Unlike the mode around 400 Hz, it is not observed in the MBSs, which is illustrated in Figure 4.10. In leaner flames, its amplitude decreases significantly. The frequency of the mode shows no dependency on the flow rate.

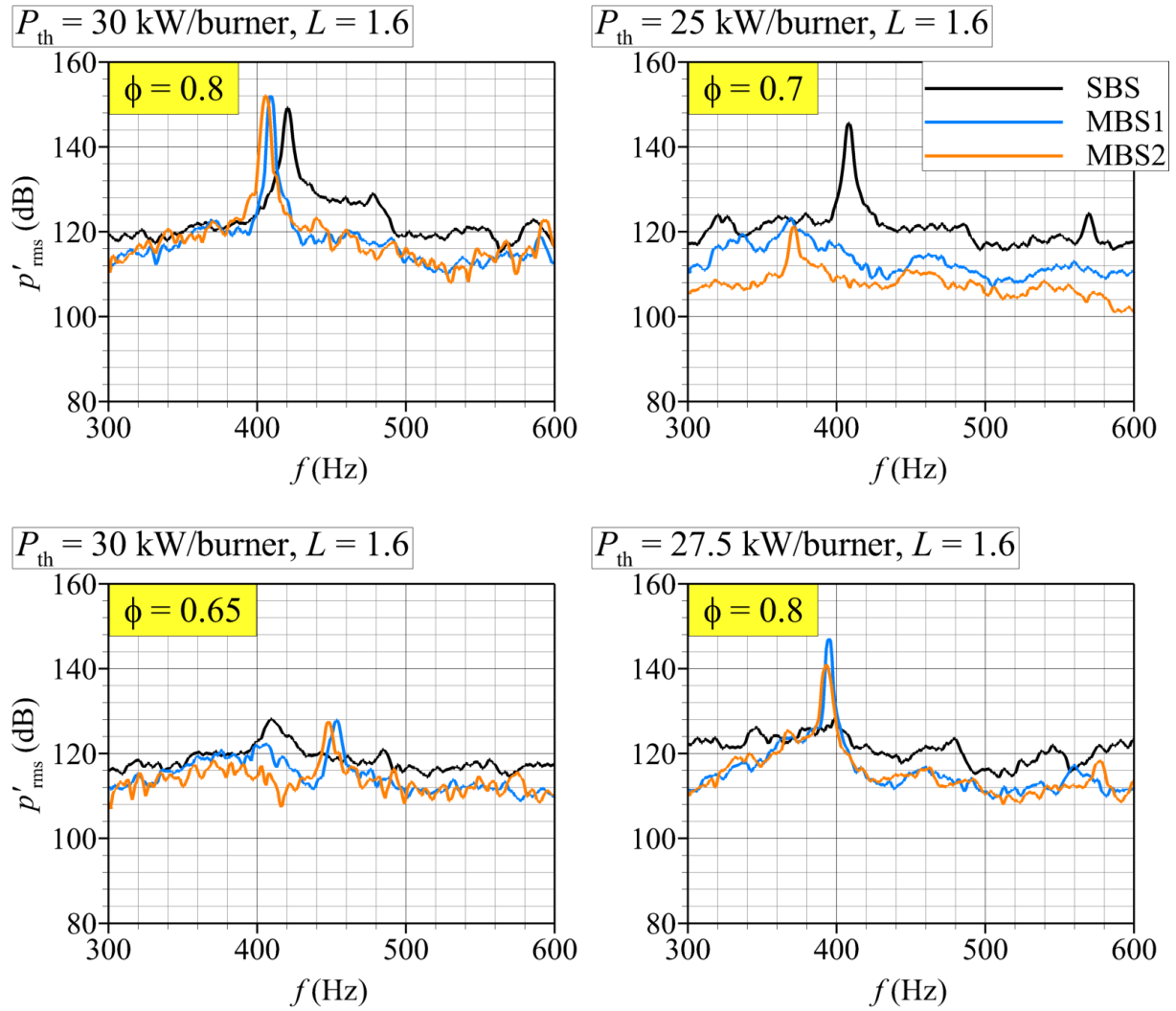


**Figure 4.9.** Unstable mode at  $\sim 400$  Hz in the combustion chamber in the SBS, MBS1 and MBS2 at different OPs,  $L = 1.6$

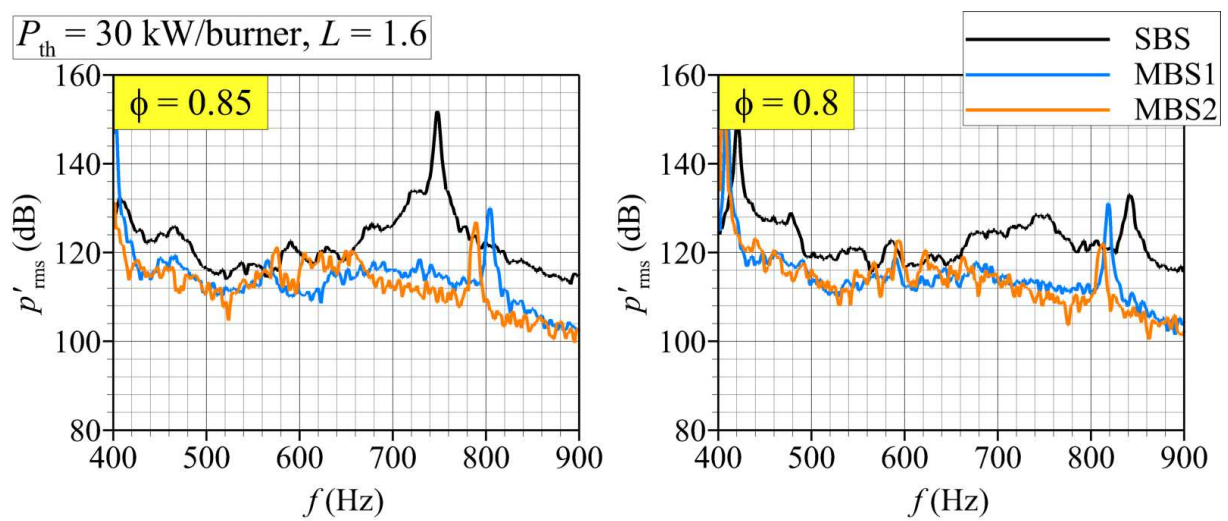


**Figure 4.10.** Unstable mode at  $\sim 750$  Hz in the SBS at  $P_{th} = 30$  kW/burner,  $\phi = 0.85, 0.8$ ,  $L = 1.6$

### 4.4.3 Summary of the Combustor Modes

As discussed in the previous section, similarities as well as differences are observed regarding the OASPLs and the frequencies and amplitudes of the dominant pressure modes in the different combustor setups.

The unstable modes with the highest amplitudes in the SBS are found around 400 Hz and 750 Hz. The amplitudes of these modes strongly depend on the thermal power and the equivalence ratio. The frequencies of these modes remain relatively constant with varying operating conditions. An overall increase in the amplitude is observed in richer flames. This is also reflected in the distribution of the OASPL. In addition, several modes are observed in the low frequency range of 140-210 Hz and around 240 Hz, which exhibit high amplitudes in the range of  $\phi = 0.65-0.75$ . At certain OPs, a low-frequency mode is observed, whose frequency increases with decreasing equivalence ratio, which indicates a dependency of its frequency on the overall flow rate.

In the MBSs, the major combustor modes are located at frequencies around 400 Hz and in the low frequency range. The mode at  $\sim 400$  Hz is only observed for high thermal power and equivalence ratios and can oscillate at very high amplitudes of 155 dB. In the low frequency range, the pressure spectra normally show dominant modes around 120-225 Hz. It is observed that the frequency of one of the low-frequency modes changes to higher values at lower equivalence ratios, i.e. with increasing flow rate of combustion air.

### 4.4.4 Definition of the Designations for the Different Combustor Modes

In order to simplify the understanding of the interpretations and the discussions of the results in the following sections and chapters, designations for the major combustor modes are defined. These are listed in Table 4.3.

Frequency range	Designation of the mode
140-160 Hz	“Low-Frequency-Mode1” (LF-Mode1)
190 Hz	190-Hz mode
160-210 Hz (SBS) 120-230 Hz (MBS1 and MBS2)	“Low-Frequency-Mode2” (LF-Mode2)
$\sim 240$ Hz (SBS) $\sim 220$ Hz (MBS1 and MBS2)	“Low-Frequency-Mode3” (LF-Mode3)
$\sim 400$ Hz	400-Hz mode
$\sim 750$ Hz (only SBS)	750-Hz mode

**Table 4.3. Designations of the typical combustor modes**

In the low-frequency range, three major modes are observed in addition to the 190-Hz mode. They are referred to by the designations “Low-Frequency-Mode1”, “Low-Frequency-Mode2”, “Low-Frequency-Mode3”. Low-Frequency-Mode2 refers to the mode with the flow rate-dependent frequency. The mode in the range of 140-160 Hz is called Low-Frequency-Mode1. The mode which exhibits frequencies of ~240 Hz in the SBS and ~220 Hz in the MBSs is called Low-Frequency-Mode3.

## 4.5 Detailed Analysis of the Combustor Modes

In the previous sections, an overview was given for the typical modes in the different combustor setups and how they are affected by thermal power, equivalence ratio, and swirler air mass flow ratio.

In this section, the major combustor modes listed in Table 4.3 are further analysed and discussed in order to identify their characteristics and excitation mechanisms. In addition, the aim is to investigate possible causes for the observed differences between the different combustor setups regarding the frequencies and amplitudes of the combustor modes. For this purpose, the pressure oscillations measured in the combustion chamber are investigated in reference to the pressure oscillations in the combustor plenums and the analysis of the recorded OH\*-chemiluminescence images.

### 4.5.1 Low-Frequency Modes

In this section, the low-frequency modes are studied in detail in order to investigate potential excitation mechanisms of the modes. Possible interactions between the modes are discussed.

#### 4.5.1.1 Low-Frequency Mode1 and the 190-Hz Mode at $L = 1.6$

As discussed in 4.4.2.1, high amplitudes of LF-Mode1 in the SBS are observed for  $L = 1.6$  at  $P_{th} = 20$  kW and  $P_{th} = 25$  kW, which is illustrated in Figure 4.11. The plot also shows the acoustic response in the inner plenum to the pressure oscillations in the combustion chamber. The augmented acoustic response in the frequency range of ~140 Hz indicates the presence of an eigenmode in the inner plenum.

At  $P_{th} = 20$  kW, decreasing the equivalence ratio results in a higher acoustic response in the inner plenum. This is not observed at  $P_{th} = 25$  kW, where the acoustic response remains relatively constant with changing equivalence ratio. This indicates that the air flow rate affects the acoustic response of the inner plenum, possibly by influencing the impedance of the perforated plate installed inside the inner plenum. Also the specific acoustic impedance of the flow inside the inner swirler is influenced by the air and fuel flow rates, which may lead to changes in the characteristics of the acoustic response of the inner plenum. In the spectrum of  $P_{th} = 25$  kW,  $\phi = 0.7$  an increase in the frequency of LF-Mode1 from ~140 Hz to ~160 Hz is observed. This may be caused by interference of LF-Mode1 with LF-Mode2. This is discussed further in 4.5.1.3.

In contrast to the SBS, the pressure spectra in the combustion chamber of the MBS1 in the low-frequency range are mostly dominated by LF-Mode2, whose frequency increases with the flow rate (Figure 4.12). This is also the case for the MBS2.

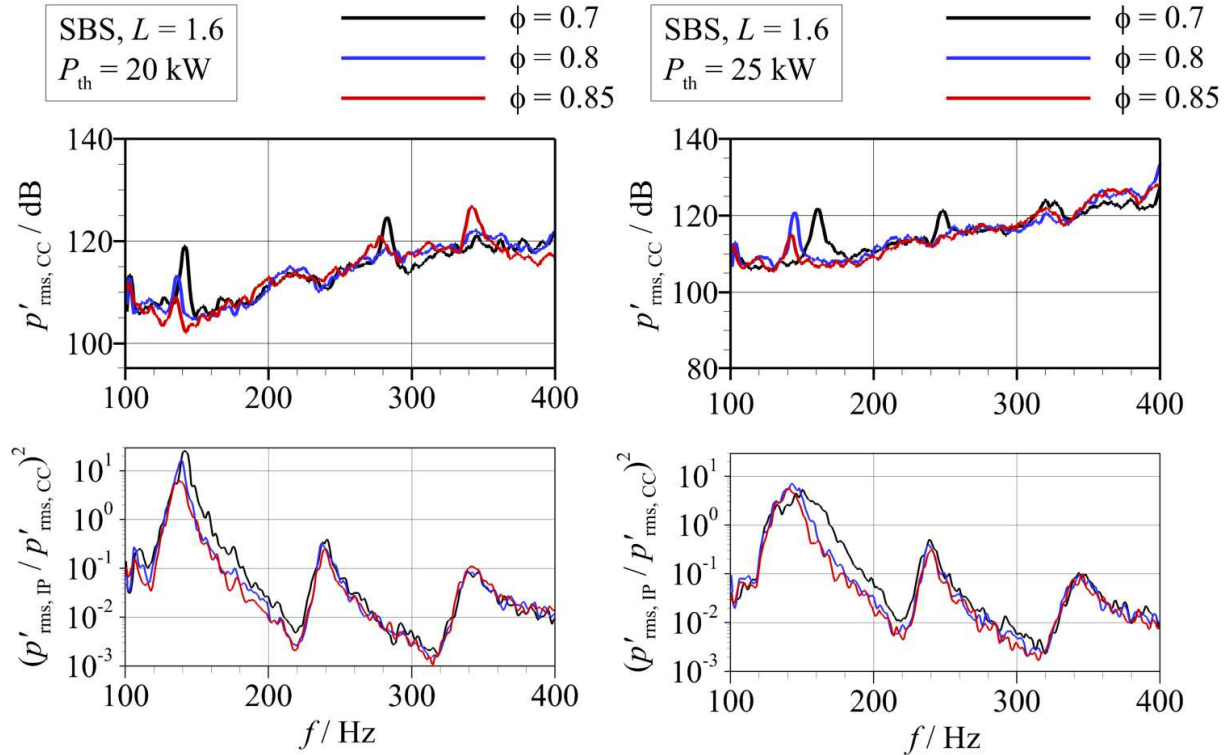


**Figure 4.11. SBS,  $L = 1.6$ : Pressure oscillations in the combustion chamber (CC) and acoustic responses in the inner plenum (IP) at different equivalence ratios at  $P_{th} = 20$  kW and  $P_{th} = 25$  kW**

However, it is observed at  $P_{th} = 20$  kW/burner,  $\phi = 0.85$  and  $P_{th} = 25$  kW/burner,  $\phi = 0.7$  that LF-Mode2 is amplified when its frequency approaches values of 120-140 Hz and around 190 Hz. The increased acoustic responses in the inner plenums of the MBS1 and the MBS2 indicate that natural frequencies of the inner plenums are present in these frequency ranges. The inner plenum works as a resonator and amplifies the oscillation of LF-Mode2. The frequency range of 120-140 Hz is approximately equal to the frequency range of LF-Mode1 observed in the SBS ( $\sim 140$  Hz) at the same thermal power per burner. The geometry of the inner plenum of a single-burner in the MBSs is equal to the inner plenum of the SBS, except for the missing walls where the single-burners are connected. Therefore it is expected that a similar eigenmode is found in the inner plenums of the MBSs. However, these geometric differences seem to result in significantly lower acoustic responses in the MBSs at  $P_{th} = 20$  kW/burner and  $P_{th} = 25$  kW/burner. The different geometries of the inner plenums of the SBS and the MBS2 may also be the reason that the high acoustic responses in the inner plenums of the MBSs at  $\sim 190$  Hz are not found in the SBS (Figure 4.12).

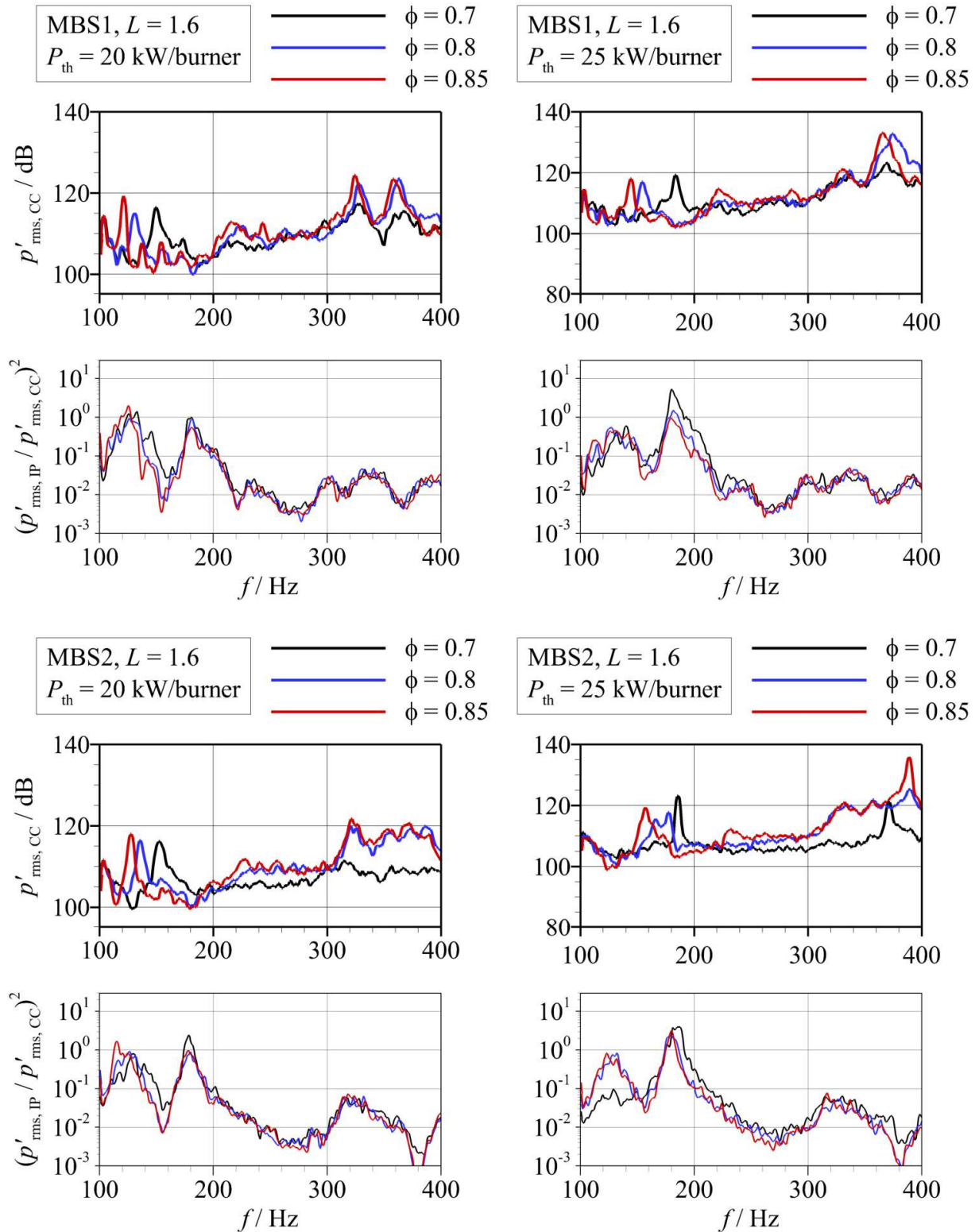


**Figure 4.12. MBS1, MBS2,  $L = 1.6$ : Pressure oscillations in the combustion chamber (CC) and acoustic responses in the inner plenum (IP) at  $P_{th} = 20$  kW/burner and  $P_{th} = 25$  kW/burner,  $\phi = 0.7, 0.8, 0.85$**

It is observed that changing the thermal power and the equivalence ratio also leads to changes in the acoustic responses of the inner plenums in the MBSs. With increasing thermal power and equivalence ratio, the acoustic response in the frequency range of LF-Mode1 decreases,

whereas an augmentation of the acoustic response in the frequency range of the 190-Hz mode is observed.

#### 4.5.1.2 Influence of the Swirler Mass Flow Ratio on LF-Mode1 and the 190-Hz Mode

Figure 4.13 shows the spectra of the pressure oscillations and the acoustic responses in the inner plenum in the low-frequency range for the SBS at  $P_{th} = 25$  kW,  $L = 1.2, 1.6$  and  $2.0$  for different equivalence ratios. At  $L = 1.2$ , the inner plenum features significantly lower acoustic responses in the frequency range of LF-Mode1 than at  $L = 1.6$  and shows increased acoustic responses in the frequency range of the 190-Hz mode. The amplitude of LF-Mode1 in the combustion chamber at this OP is also reduced, which expresses the importance of the acoustic response of the inner plenum for the excitement of LF-Mode1.

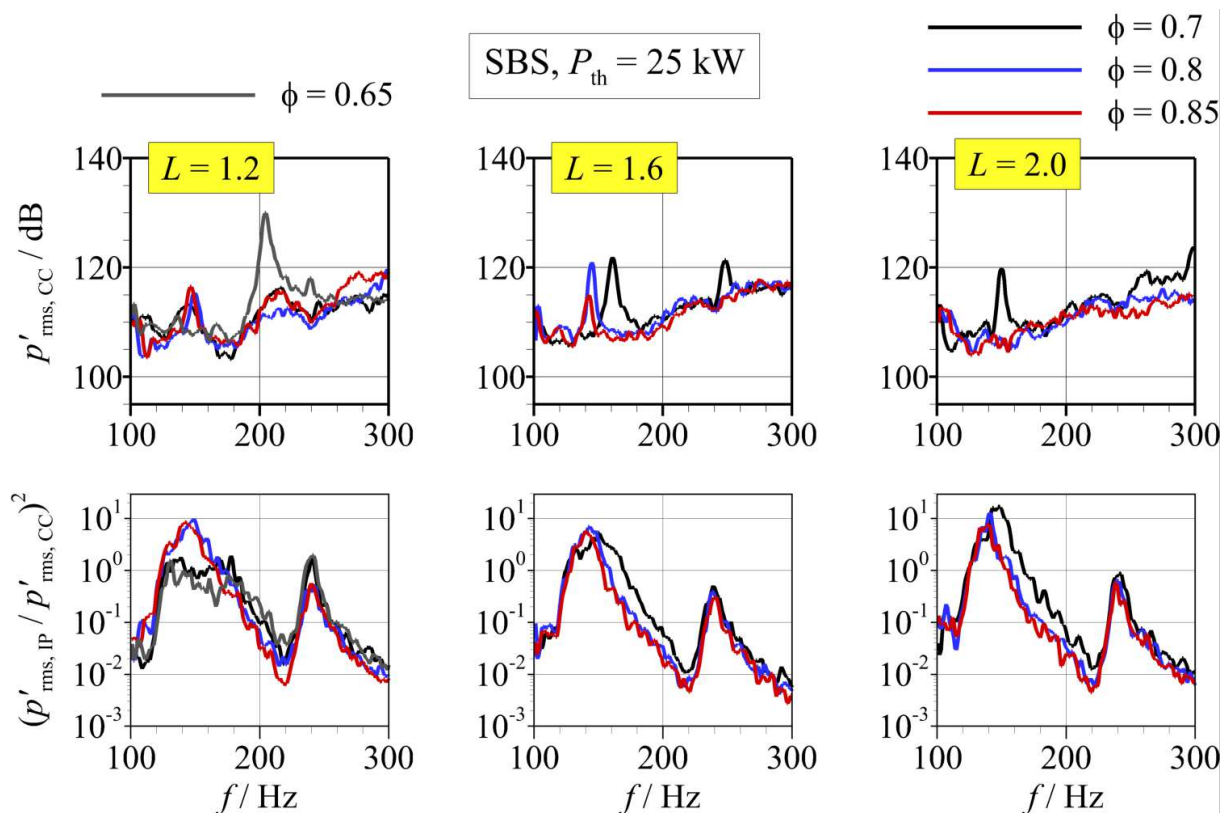


**Figure 4.13. SBS,  $L = 1.2, 1.6, 2.0$ : Pressure oscillations in the combustion chamber (CC) and acoustic responses in the inner plenum (IP) at different equivalence ratios and swirler mass flow ratios at  $P_{th} = 25$  kW,  $\phi = 0.65$  ( $L = 1.2$ ),  $0.7, 0.8, 0.85$**

This corroborates the assumption that LF-Mode1 is associated with a natural frequency of the inner plenum. Decreasing the equivalence ratio at  $L = 1.2$  from  $\phi = 0.7$  to a value of  $\phi = 0.65$  eventually results in the excitation of the 190-Hz mode in the SBS. The excitation of the 190-Hz mode is only observed at this specific OP. Since the acoustic response is comparable to  $\phi = 0.7$ , this is most likely the result of an increased thermoacoustic flame response.

At  $L = 2.0$ , a peak in the frequency range of LF-Mode1 is only visible in the combustion chamber spectrum at  $\phi = 0.7$ , although the acoustic response in the inner plenum does not show significant change. Thus, the lower amplitudes of LF-Mode1 at  $\phi = 0.85$  and  $\phi = 0.8$  at  $L = 2.0$  are most likely caused by reduced flame responses.

Figure 4.14 shows the influence of the swirler mass flow ratio on the low-frequency modes for the MBSs at  $P_{\text{th}} = 25$  kW/burner. Changing the swirler mass flow ratio to  $L = 1.2$  or  $L = 2.0$  strongly influences the pressure oscillations in the low-frequency range in the MBSs. In the spectra for  $L = 1.2$ , an obviously visible frequency scaling of the dominant modes with the flow rate is not observed, which complicates assigning the peaks to the corresponding modes. However, the spectra of the acoustic response in the inner plenum indicate that decreasing  $L$  to  $L = 1.2$  leads to a damping of LF-Mode1 in the inner plenum at  $\phi = 0.7$  in both MBSs, which is also observed in the SBS.

A reduction of the swirler mass flow ratio from  $L = 1.2$  to  $L = 1.6$  leads to an amplification of the 190-Hz mode in the combustion chamber in the MBSs. Since the acoustic responses in the inner plenums remain nearly constant, this is most likely caused by stronger flame responses. At  $L = 2.0$ , similar to  $L = 1.6$ , the dominant frequency in the MBS1 in the low-frequency range increases with the air flow rate and thus most likely corresponds to LF-Mode2. In the MBS2, the peaks in the low-frequency range are also almost certainly associated to LF-Mode2, as indicated by the increased frequency of the corresponding peak at lower equivalence ratios. However, at  $\phi = 0.7$ , the pressure spectrum in the combustion chamber also shows a high amplitude of the 190-Hz mode as well as an increased acoustic response of the inner plenum.

The results for  $L = 1.2$  and  $L = 2.0$  support the assumption that LF-Mode1 and the 190-Hz mode are associated with eigenmodes of the inner plenums. The acoustic response in the inner plenum in the frequency range of LF-Mode1 is significantly affected by the flow rate and the swirler mass flow ratio. Increasing the flow rate in the inner plenums tends to damp the acoustic response in the frequency range of LF-Mode1 in all combustor setups. This may be caused by an enhanced damping of the mode in the inner plenums or the inner swirlers, which is due to increased viscous effects that remove energy from the acoustic oscillation. The pressure amplitudes of both modes in the combustion chamber seem to be strongly dependent on the flame response.

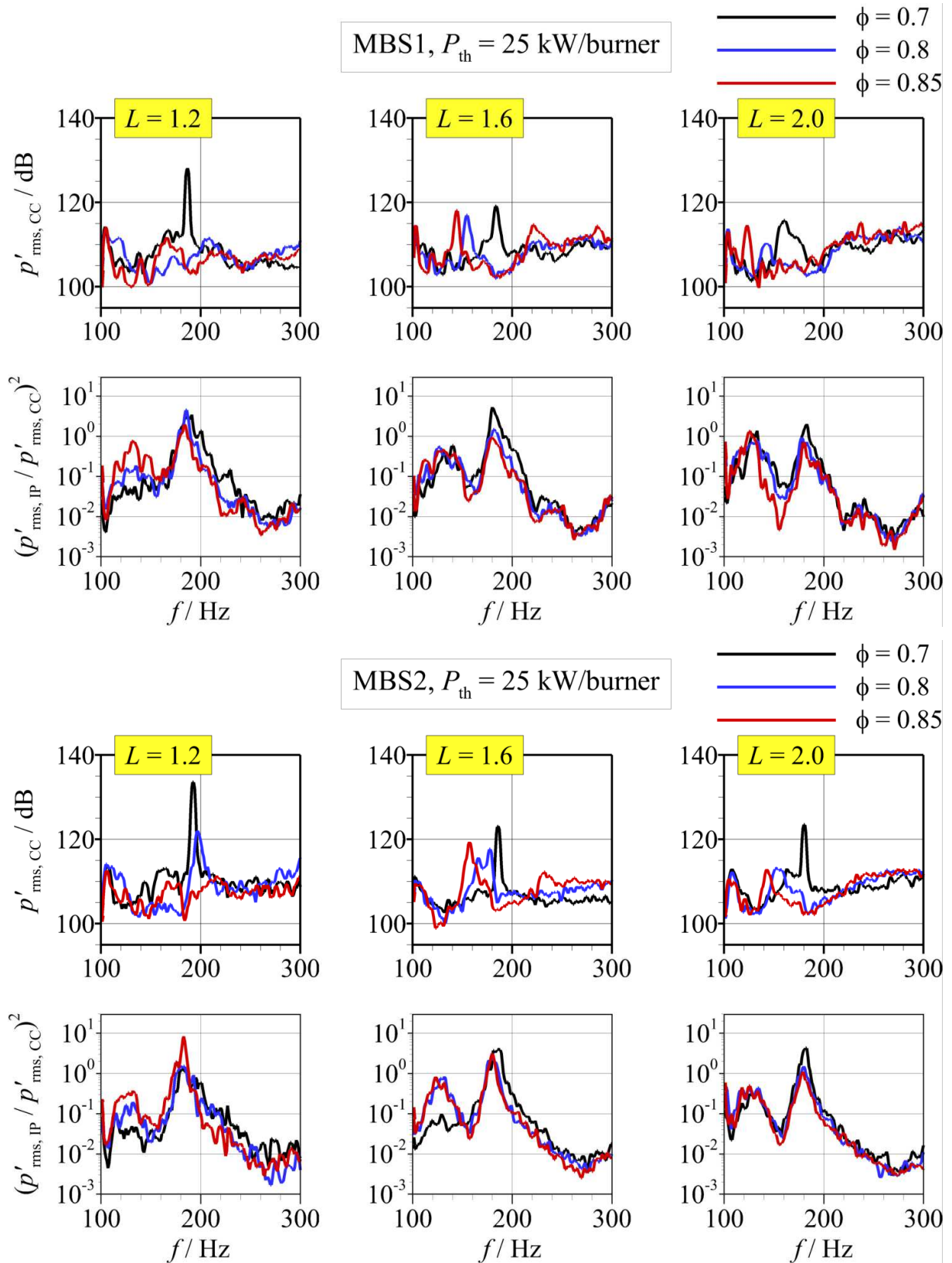


**Figure 4.14. MBS1, MBS2,  $L = 1.2, 1.6, 2.0$ : Pressure oscillations in the combustion chamber (CC) and acoustic responses of the inner plenum (IP) at different equivalence ratios and swirler mass flow ratios at  $P_{th} = 25 \text{ kW/burner}$ ,  $\phi = 0.7, 0.8, 0.85$**

#### 4.5.1.3 Low-Frequency Mode2 and Low-Frequency Mode3 at $L = 1.6$

In order to characterize LF-Mode2, first it is investigated whether or not the frequency of LF-Mode2 indeed shows a linear scaling with the bulk velocity. In addition, the acoustic responses in the plenums are analysed in order to gather more information about LF-Mode3 and the interactions of LF-Mode2 with LF-Mode1 and 190-Hz mode.

The pressure oscillations in the combustion chamber and the amplitude response of both plenums in the SBS are plotted in Figure 4.15 for  $P_{th} = 25$  kW and  $P_{th} = 30$  kW. Additionally, the graphs with the pressure spectra in the combustion chamber also show the curves of the Strouhal-Number. The Strouhal-Number  $St$  is calculated by

$$St = \frac{f \cdot d_{nz}}{\dot{V}_{n,nz}/A_{nz}}, \quad (4.4)$$

where  $\dot{V}_{n,nz}$  stands for the volumetric flow rate through the nozzle at STP.  $A_{nz}$  denotes the cross-sectional area of the nozzle outlet and  $d_{nz}$  is the outer diameter of the nozzle outlet.

As shown in the previous section, at  $\phi = 0.85$  and  $\phi = 0.8$ , the frequency of the dominant low-frequency mode is nearly identical ( $\sim 140$  Hz), since those oscillations represent oscillations of LF-Mode1. From  $\phi = 0.8$  down to  $\phi = 0.65$ , a scaling of the frequency with increasing bulk velocity is observed, which indicates that the peaks correspond to LF-Mode2. The peaks exhibit similar Strouhal-Numbers, which means that the frequency of LF-Mode2 grows almost linearly with the bulk velocity. When the value of the frequency of LF-Mode2 approaches that of LF-Mode1, the amplitude of the respective peak increases ( $\phi = 0.8, 0.75, 0.7$ ). This may be the result of a constructive interference of the two modes which leads to an amplification of LF-Mode2 due to high acoustic responses in the inner plenum. The inner plenum also shows a relatively strong acoustic response in the frequency range of LF-Mode3 at  $\sim 250$  Hz, which indicates the presence of a natural frequency of the inner plenum in this frequency range. At  $\phi = 0.65$ , the spectrum of the acoustic response of the inner plenum differs from the other equivalence ratios, since the highest responses are observed in the frequency range around 170 Hz. Despite the higher acoustic response in the corresponding frequency range, LF-Mode2 exhibits significantly lower amplitudes.

At  $P_{th} = 30$  kW, slightly lower Strouhal-Numbers ( $\sim 3\%$ ) are observed between  $\phi = 0.85-0.7$ , which may be caused by measurement uncertainties or different flow conditions in the combustion chamber due to the increased thermal power. The Strouhal-Numbers of the dominant peaks are in the range of 0.176-0.179, except for  $\phi = 0.65$ , where a slightly higher value is observed. Therefore the peaks most certainly represent oscillations of LF-Mode2. The spectra of the acoustic response of the inner plenum follows the tendency observed at  $P_{th} = 25$  kW, since the acoustic response diminishes in the frequency range of  $\sim 140$  Hz and increases in the frequency range of 180-200 Hz with increasing mass flow. The acoustic

## 4.5 Detailed Analysis of the Combustor Modes

response spectra in the inner plenum also show relatively high values in the frequency range of LF-Mode3 ( $\sim 240$  Hz). However, a significant peak in the frequency range of LF-Mode3 is only visible at  $\phi = 0.85$ . The amplitude of LF-Mode3 in the combustion chamber seems to be strongly influenced by the flame response.

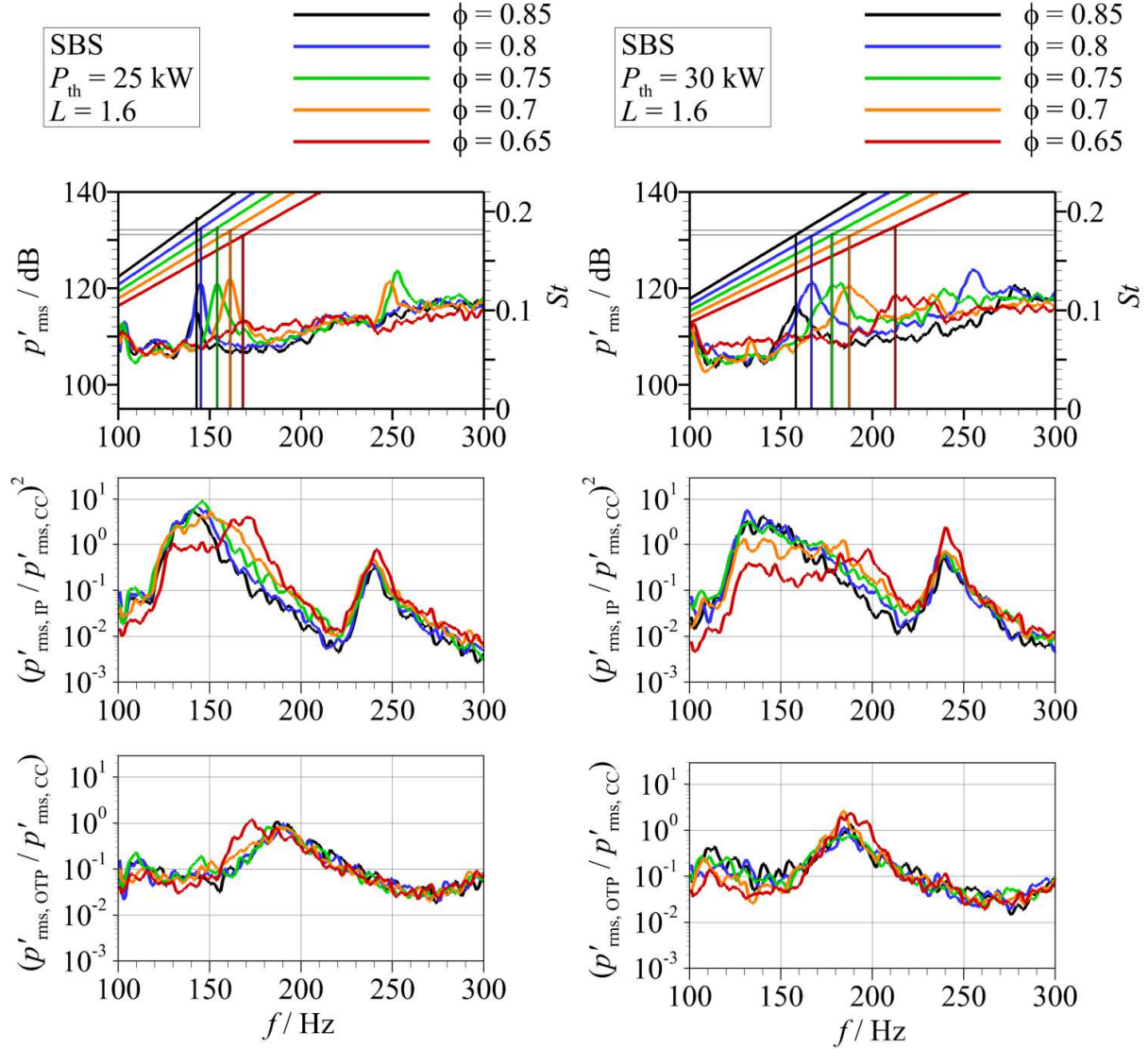


**Figure 4.15. SBS,  $L = 1.6$ : Pressure oscillations in the combustion chamber (CC) and acoustic responses in the inner plenum (IP) and the outer plenum (OTP) at  $P_{th} = 25$  kW and  $P_{th} = 30$  kW,  $\phi = 0.65-0.85$**

An analysis of the frequency scaling of LF-Mode2 in the MBSs at  $L = 1.6$  shows a nearly linear increase of LF-Mode2-frequency with the bulk velocity for most OPs (Figure 4.16, Figure 4.17). However, the spectra also indicate interferences between the low-frequency modes. For example, at  $P_{th} = 25$  kW/burner it is impossible to distinguish between LF-Mode2 and the 190-Hz mode at  $\phi = 0.7, 0.65$ . In the corresponding frequency range, only one peak with an augmented amplitude is observed. This may be the result of a constructive interference of LF-Mode2 in the combustion chamber and the 190-Hz mode in the inner plenum.

In the spectra of the pressure oscillations at  $\phi = 0.65$  in the MBS1 and at  $\phi = 0.65, 0.7$  in the MBS2 only one significant peak is observed at  $\sim 230$  Hz. The spectra indicate that this oscillation is associated with a constructive interference of LF-Mode2 with LF-Mode3. The spectra of the acoustic response do not indicate natural frequencies as the source of excitement for LF-Mode3. However, the value of the acoustic response is comparably high in both plenums, which may contribute to the sustainment of the pressure oscillation.

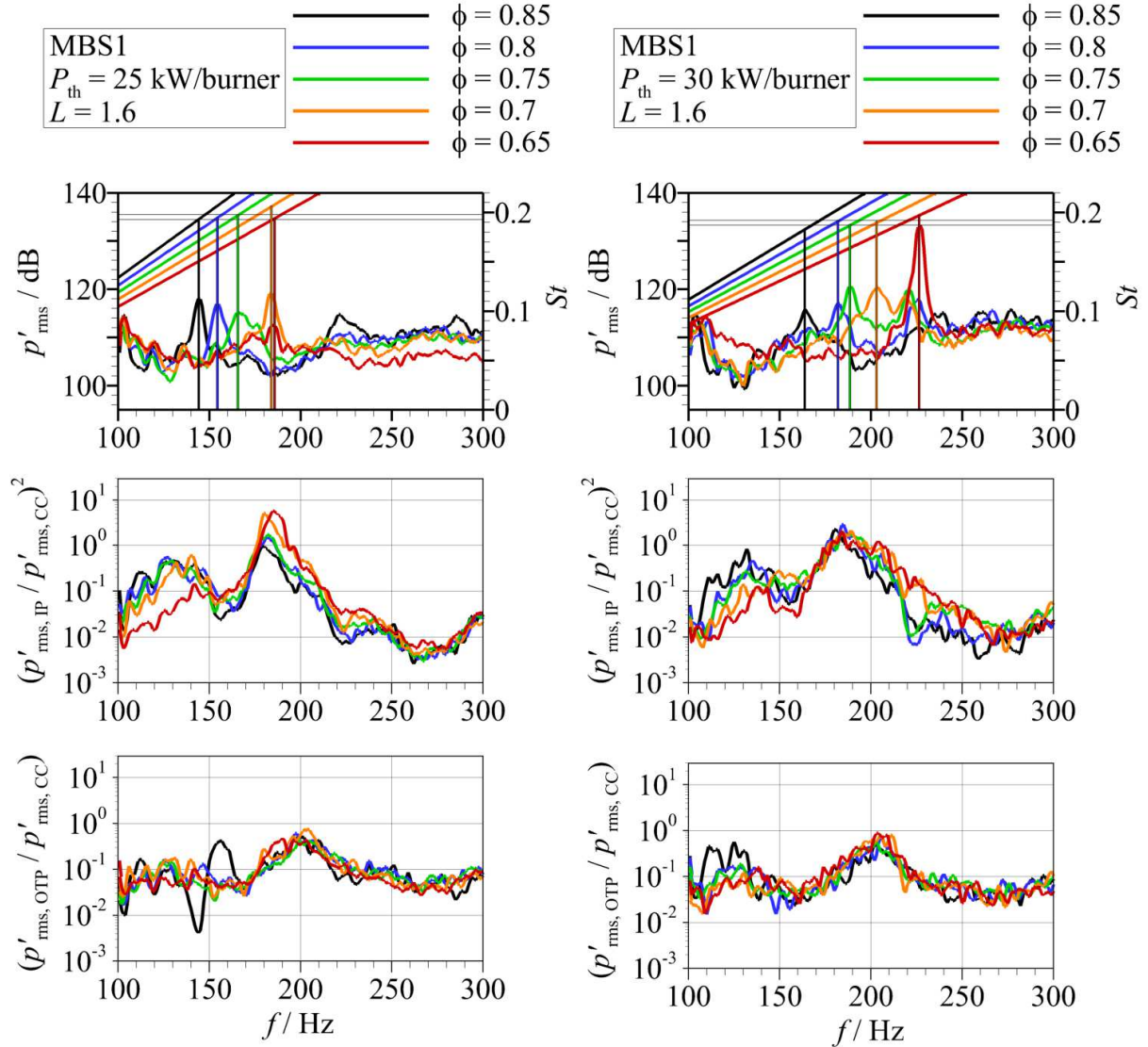


**Figure 4.16. MBS1,  $L = 1.6$ : Pressure oscillations in the combustion chamber (CC) and acoustic responses in the inner plenum (IP) and the outer plenum (OTP) at  $P_{th} = 25$  kW/burner and  $P_{th} = 30$  kW/burner,  $\phi = 0.65-0.85$**

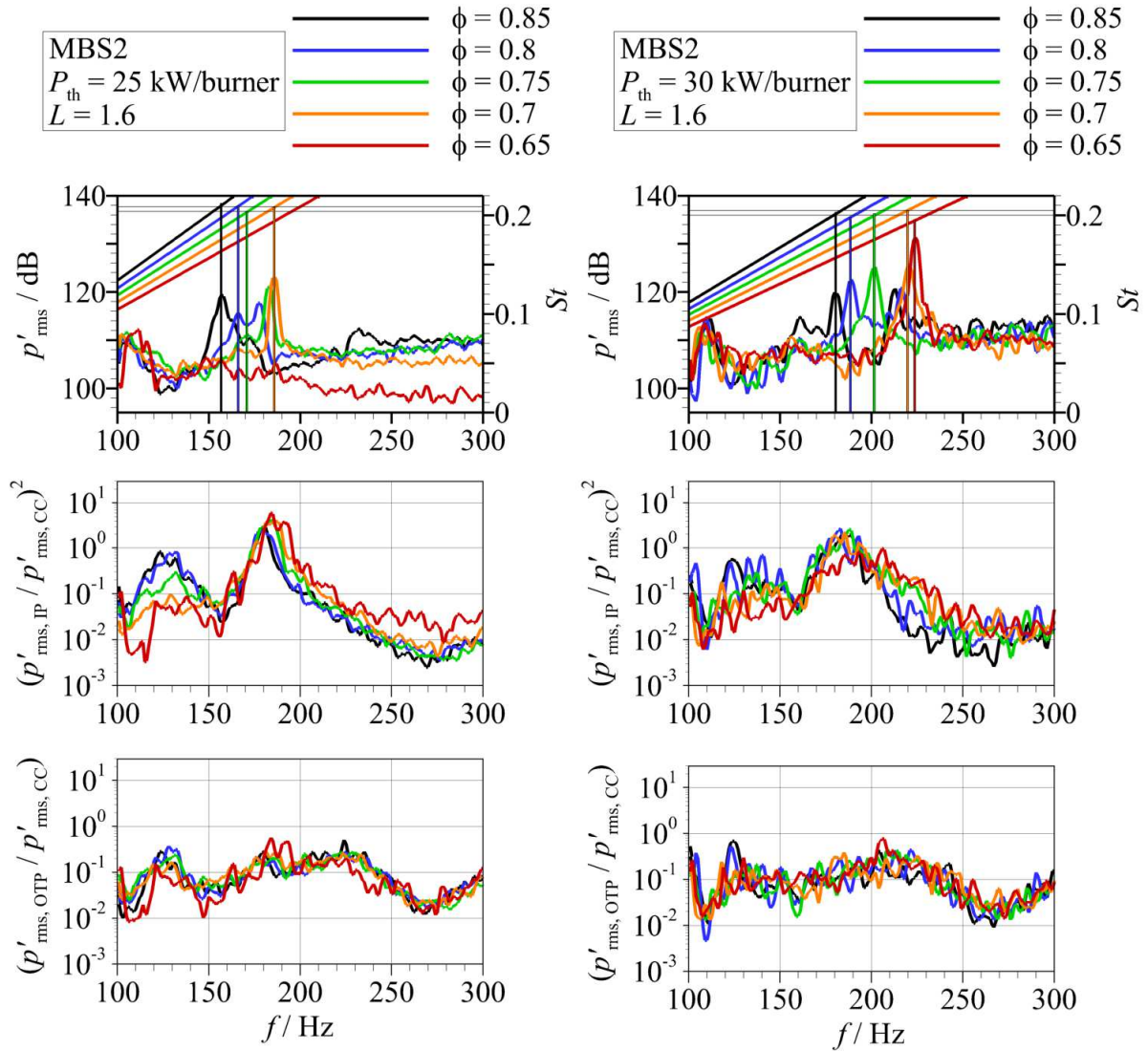


**Figure 4.17. MBS2,  $L = 1.6$ : Pressure oscillations in the combustion chamber (CC) and acoustic responses in the inner plenum (IP) and the outer plenum (OTP) at  $P_{th} = 25$  kW/burner and  $P_{th} = 30$  kW/burner,  $\phi = 0.65-0.85$**

#### 4.5.1.4 Influence of the Swirler Mass Flow Ratio on LF-Mode2 and LF-Mode3

Figure 4.18 shows the pressure spectra in the combustion chamber at  $P_{th} = 25$  kW/burner and  $P_{th} = 30$  kW/burner at  $L = 1.2$  and  $2.0$ . At  $L = 1.2$ , LF-Mode2 is only observed in the pressure spectrum of the SBS at  $P_{th} = 30$  kW,  $\phi = 0.85, 0.8$  and  $0.75$  at relatively low amplitudes. This indicates that LF-Mode2 is strongly damped compared to  $L = 1.6$  in all combustor setups.

In the SBS, LF-Mode3 shows a very high amplitude of  $\sim 135$  dB at  $P_{th} = 30$  kW,  $\phi = 0.65$ , which significantly exceeds the maximum amplitudes of LF-Mode3 at  $L = 1.6$  ( $\sim 123$  dB). In the MBSs the amplitudes of LF-Mode3 at  $P_{th} = 30$  kW/burner are strongly augmented in comparison to  $L = 1.6$ . The high pressure amplitudes suggest strong thermoacoustic feedback of the flame. The main difference observed for the SBS and the MBSs for the pressure oscillations in the low-frequency range at  $L = 1.6$  is that the maximum amplitudes of the unstable modes are significantly increased.

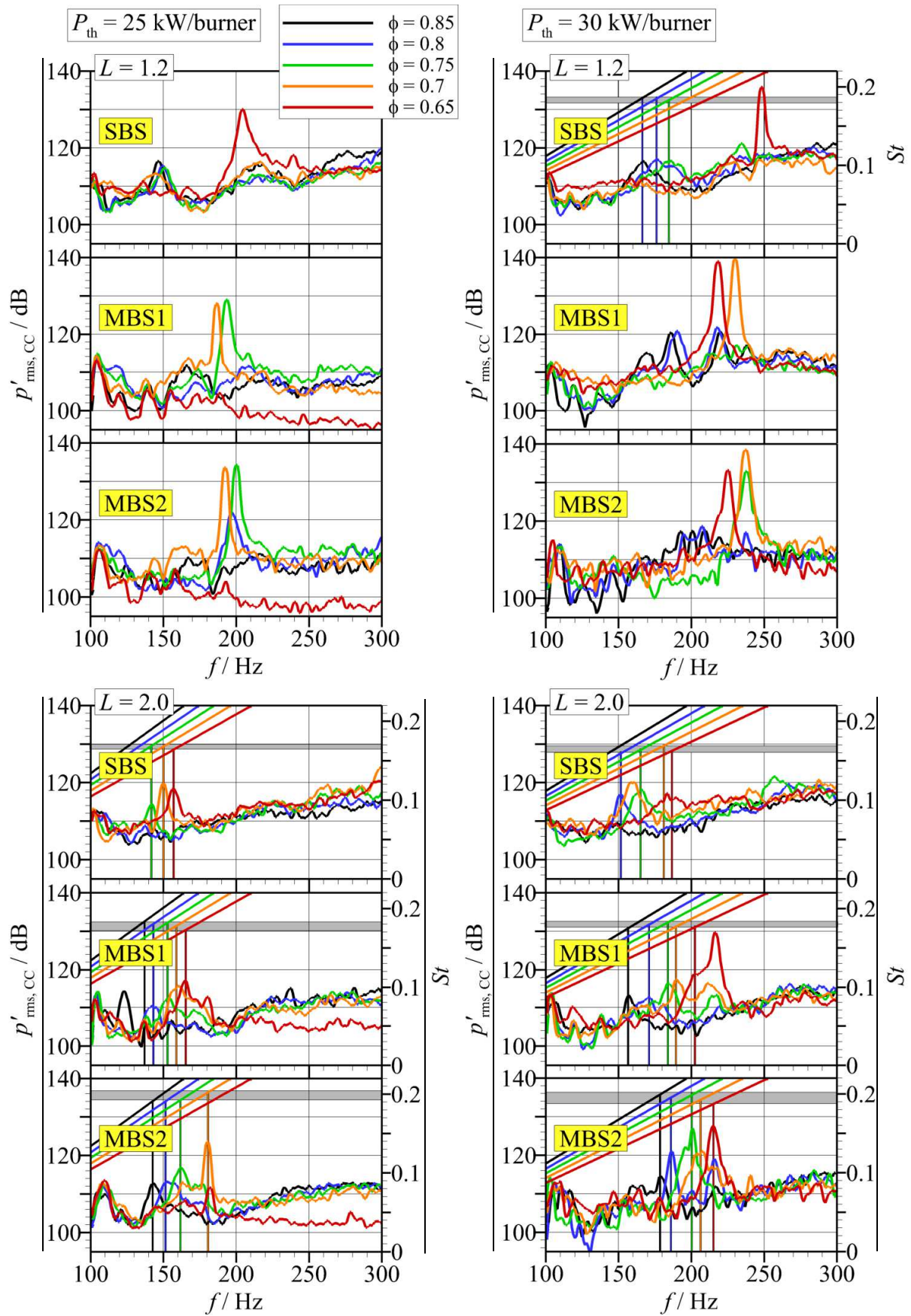


**Figure 4.18. SBS, MBS1, MBS2,  $L = 1.2, 2.0$ : Pressure oscillations in the combustion chamber (CC) at  $P_{th} = 25$  kW/burner and  $P_{th} = 30$  kW/burner,  $\phi = 0.65-0.85$**

#### 4.5 Detailed Analysis of the Combustor Modes

The spectra at  $L = 2.0$  show a clear scaling of the frequencies of the dominant low-frequency modes for most OPs. Therefore they most likely represent oscillations of LF-Mode2. However, nonlinearities of the frequency scaling are observed. These are most significant in the MBS2, indicated by the wider range of Strouhal-Numbers of the dominant modes. The range of the Strouhal-Numbers is indicated by the grey colour in the diagrams. In contrast to the OPs at  $L = 1.2$ , the maximum amplitudes of the unstable modes are lower than those at  $L = 1.6$  in all combustor setups.

Figure 4.19 shows the spectra of the acoustic responses in the plenums at  $L = 1.2, 1.6, 2.0$  for  $P_{th} = 30$  kW/burner and the equivalence ratios  $\phi = 0.65$  (SBS) and  $\phi = 0.7$  (MBS1, MBS2). The spectra of all combustor setups comply with the assumption that the higher pulsation levels of the pressure in the combustion chamber at  $L = 1.2$  are mainly caused by an increased thermoacoustic feedback of the flame, since no significantly higher acoustic responses in the plenums are observed. The spectra of the SBS show increased acoustic responses in the inner plenum at  $L = 1.2$  in the relevant frequency range of 240-250 Hz at  $P_{th} = 30$  kW,  $\phi = 0.65$ . However, the differences to the acoustic responses at  $L = 1.6$  are not very significant and therefore most likely not sufficient enough to generate the increased pulsation levels.

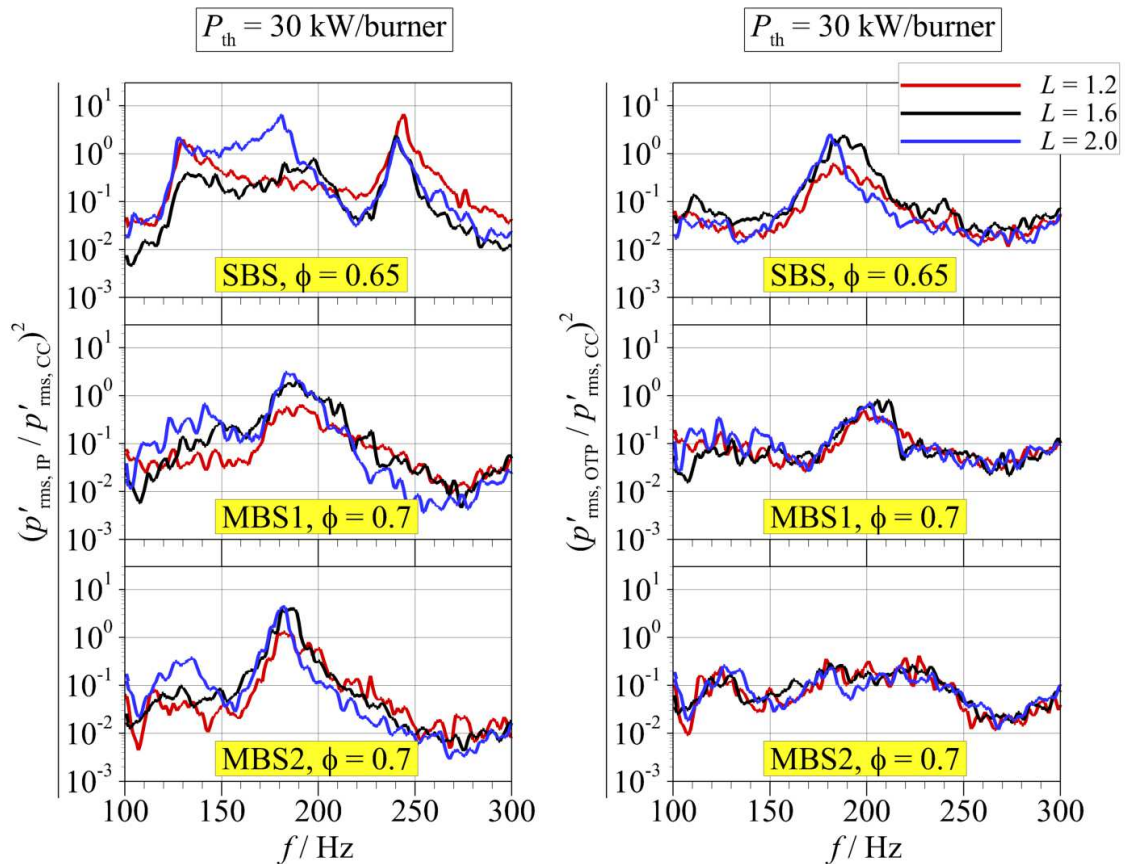
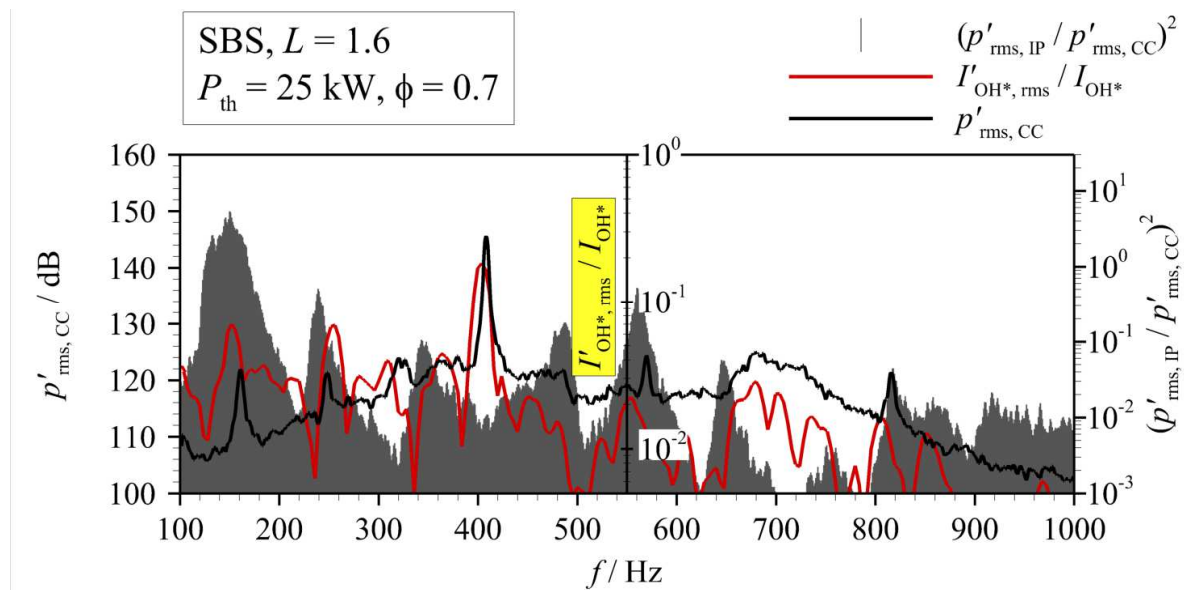


**Figure 4.19. SBS, MBS1, MBS2,  $L = 1.2, 1.6, 2.0$ : Acoustic responses in the inner plenum (IP) and the outer plenum (OTP) at different OPs**

#### 4.5.1.5 OH\*-Intensity Responses to the Low-Frequency Pressure Oscillations

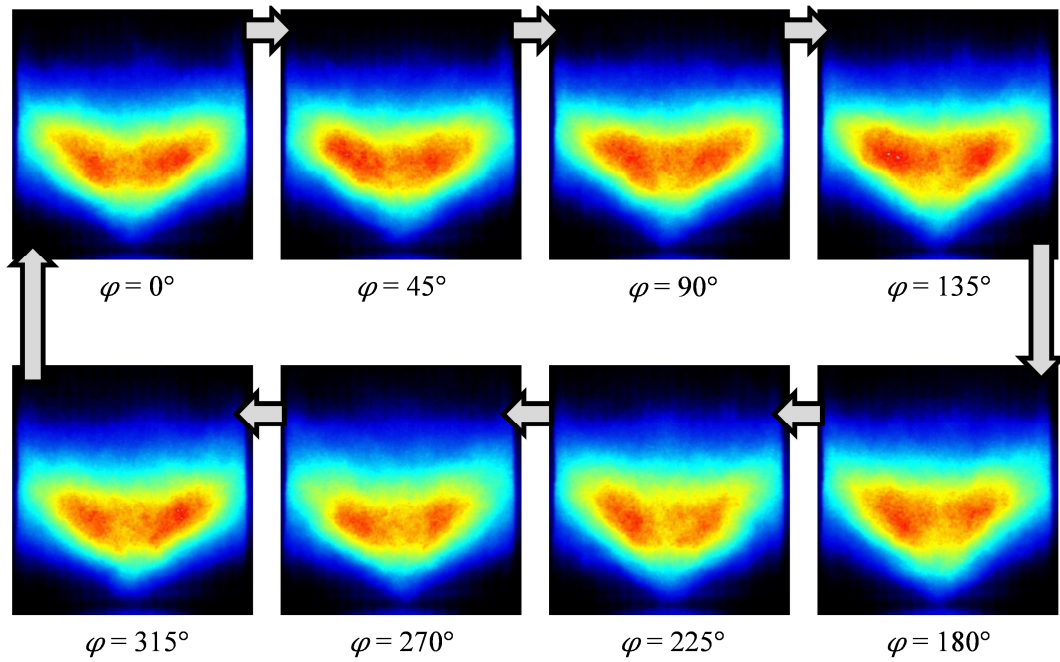
In this section the images of the high-speed OH\*-chemiluminescence recordings are analysed, in order to characterize the flame responses to the low-frequency pressure oscillations. Spectra of the OH\*-intensity oscillations are compared to spectra of pressure oscillations in the combustion chamber and acoustic responses in the plenum for certain OPs. The amplitudes of the OH\*-intensity  $I'_{OH^*,rms}$  oscillations are normalized with the mean OH\*-intensity  $I_{OH^*}$ .

Figure 4.20 shows the spectrum of the OH\*-intensity oscillations in the SBS at  $P_{th} = 25$  kW,  $\phi = 0.7$ ,  $L = 1.6$ , along with the spectra of the pressure oscillations in the combustion chamber and the acoustic response in the inner plenum. In section 4.5.1.3, it was noted that the low-frequency pressure oscillation at 160 Hz at this OP represents a combined pressure mode of LF-Mode1 and LF-Mode2. The spectrum of the OH\*-intensity shows a high amplitude in the corresponding frequency range. The strong acoustic responses in the inner plenum contribute substantially to the low-frequency OH\*-intensity oscillations. Since the flames are not perfectly premixed, it is possible that the OH\*-intensity not only represents oscillations of the flame's heat release, but also oscillations of the equivalence ratio.



**Figure 4.20. SBS,  $P_{th} = 25$  kW,  $\phi = 0.7$ ,  $L = 1.6$ : Pressure and OH\*-intensity oscillations in the combustion chamber (CC) and acoustic response in the inner plenum (IP)**

Figure 4.21 illustrates the oscillation cycle of the OH\*-intensity at 160 Hz. The images are derived from frequency-locked averaging of the high-speed images. The flame periodically propagates upstream towards the exit of the inner swirler. However, the flame oscillation is not very intense. The smallest distance between the position of the flame root and the nozzle is visible at  $\varphi = 180^\circ$ . The periodic propagation of the flame towards the nozzle exit indicates the presence of an instability of the IRZ, which is discussed in the following paragraph in reference to the results obtained for the MBS1 at equivalent operating conditions.



**Figure 4.21. SBS,  $P_{th} = 25$  kW,  $\phi = 0.7$ ,  $L = 1.6$ : Oscillation cycle of OH\*-intensity at 160 Hz; the images show a weak flame oscillation near the nozzle exit.**

In the MBS1, the dominant frequencies the OH\*-signal mostly coincide with the dominant frequencies of the pressure oscillations (Figure 4.22). However, this is not the case for the corresponding peak of LF-Mode1 at  $\sim 140$  Hz and the peak at  $\sim 190$  Hz. Although the amplitude of the pressure oscillation at 190 Hz is significantly higher, the peak of the OH\*-intensity oscillation at the frequency of LF-Mode1 exceeds the amplitude of the peak at 190 Hz. In 4.5.1.3 it was suggested that the pressure oscillation at 190 Hz represents an oscillation of LF-Mode2, amplified by a constructive interference with the 190-Hz mode in the inner plenum. A visualization of the oscillations at 140 Hz by frequency-locked averaging of the high-speed OH\*-images only gives inconclusive results, which is most likely due to the interference of several dominant frequencies in a narrow frequency range.

Similar to the SBS, a periodic propagation of the flame towards the nozzle exit is observed in the high-speed images. The snapshots shown in Figure 4.23 indicate that this oscillation is much more intense in the SBS, since the region of increased OH\*-intensity is significantly wider in the SBS near the nozzle exit. The spectra of the average OH\*-intensity oscillations in the yellow rectangles show that the OH\*-oscillation in the frequency range of LF-Mode1 is much more dominant near the nozzle exit in both combustor setups. The pressure oscillation of LF-Mode1 in the inner plenum possibly induces changes in the structure and width of the IRZ, as it modulates the velocity at the outlet of the inner swirler.

Since the theoretical swirl number of the inner swirler is considerably lower than the one of the outer swirler, an increase in the outlet velocity of the inner swirler results in a decrease in the overall swirl number near the nozzle exit and leads to a contraction of the IRZ. Swirl number oscillations in a swirl burner were also reported in [109].

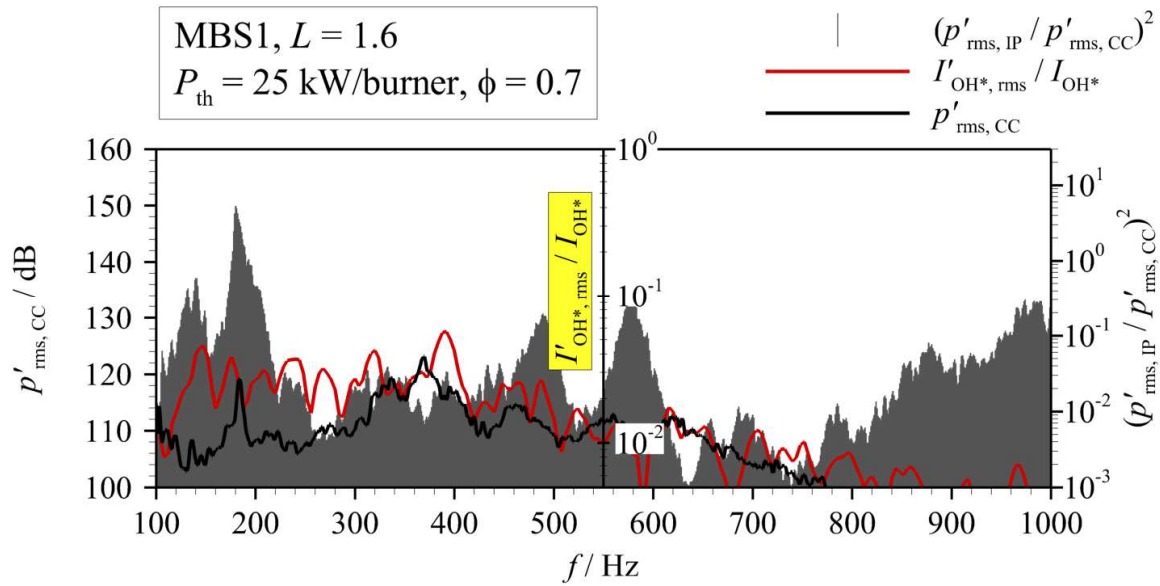


**Figure 4.22. MBS1,  $P_{th} = 25$  kW/burner,  $\phi = 0.7$ ,  $L = 1.6$ : Pressure and OH\*-intensity oscillations in the combustion chamber (CC) and acoustic response in the inner plenum (IP)**

With decreasing outlet velocity of the inner swirler, the IRZ re-expands and is possibly penetrated by the main fuel flow, which leads to an increased transport of fuel into the IRZ. As the IRZ is quite narrow near the nozzle exit, the local reaction may take place at comparably fuel rich conditions. This would explain the relatively high response of the OH\*-intensity to the pressure oscillation of LF-Mode1, since, as discussed in 4.2.2, the OH\*-intensity shows a significant reaction to equivalence ratio oscillations. In the SBS, the oscillation is likely more intense because LF-Mode1 in the inner plenum and LF-Mode2 oscillate at similar frequencies. This may generate a closed feedback loop where the inner plenum serves as a resonator for the pressure oscillation of LF-Mode2 in the combustion chamber. In the MBS1, the frequency of LF-Mode2 is about 50 Hz higher than that of LF-Mode1, which hinders the generation of a similar feedback loop. The pressure oscillation of LF-Mode2 in the MBS1 seems to be amplified by the strong acoustic response in the frequency range around 190 Hz in the inner plenum. However, as discussed in the previous paragraph, the OH\*-intensity oscillation has a stronger response to the pressure oscillation of LF-Mode1. A possible explanation for this is that the inner plenum also acts as a resonator for the pressure oscillation at 180 Hz of LF-Mode2 in the combustion chamber, but does not affect the structure of the IRZ or the mixing process near the nozzle exit.

Based on these observations, it is concluded that LF-Mode2 is most likely caused by vortex shedding in the shear layer of the swirl flow, since the high-speed images in Figure 4.23 indicate the presence of such vortices in the swirl flow. A similar oscillation with a Strouhal-Number of  $St = 0.25$  was found in the shear layer of a swirl flow by Schildmacher et al. [138]. The Strouhal-Number of LF-Mode2 has comparable values of around 0.18. The frequency of vortex shedding typically increases with the flow velocity. It also strongly

#### 4.5 Detailed Analysis of the Combustor Modes

influences the mixing process of fuel and air in the combustion chamber. In the SBS, LF-Mode1 and LF-Mode2 oscillate at similar frequencies. The interaction of the modes at the discussed OP possibly intensifies the OH\*-intensity oscillations, as LF-Mode2 may contribute to the discussed mixing of fuel into the IRZ near the nozzle exit. In the MBS1, LF-Mode2 and LF-Mode1 oscillate at different frequencies; no interaction between the modes takes place. This results in two characteristic OH\*-intensity oscillations at 140 Hz and 180 Hz. The fact that LF-Mode2 features different frequencies in the SBS and the MBS1 indicates differences in the flow fields of the SBS and the MBS1.

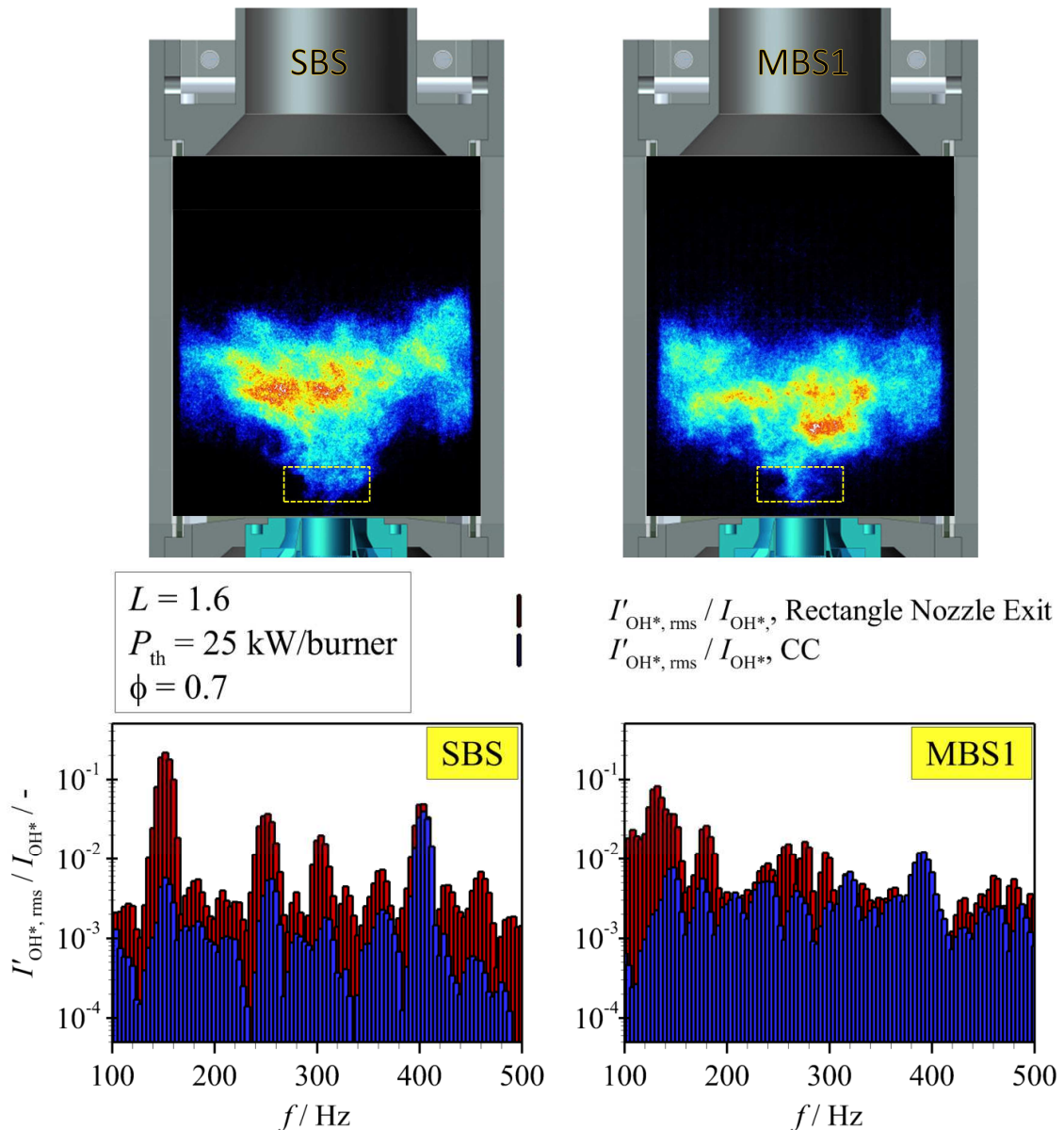


**Figure 4.23. SBS, MBS1,  $P_{th} = 25 \text{ kW/burner}$ ,  $\phi = 0.7$ ,  $L = 1.6$ : High speed snapshots of the OH\*-chemiluminescence and comparison of the overall OH\*-intensity spectra in the combustion chamber (CC) and OH\*-intensity near the nozzle outlet**

The spectrum of the OH\*-intensity oscillation in the MBS2 at  $P_{th} = 25$  kW/burner,  $\phi = 0.7$ ,  $L = 1.6$  (Figure 4.24) is different from the SBS and the MBS1. In the SBS and the MBS1, several dominant frequencies are found in the OH\*-intensity spectrum, whereas the spectrum of the MBS2 shows only one dominant frequency in the range  $\sim 190$  Hz and its harmonic mode at  $\sim 380$  Hz. The maximum amplitude exceeds the maximum amplitudes in the low-frequency range in the SBS and MBS1. The OH\*-intensity oscillations match with the dominant frequencies visible in the pressure spectrum and the acoustic response of the inner plenum.

Since the OH\*-intensity mainly oscillates in a very narrow frequency range, it is possible to visualize the oscillation cycle via frequency-locked averaging at 190 Hz. The resulting images show a periodic increase of the width and length of the flame (Figure 4.25). The spectra in Figure 4.26 illustrates that decreasing  $L$  to  $L = 1.2$  at the same thermal power and equivalence ratio leads to an increase in the amplitude of the pressure oscillation and the OH\*-intensity oscillation at 190 Hz. Figure 4.27 shows the corresponding oscillations of the recorded flames in the MBS2. The flame oscillation is similar to the one observed at  $L = 1.6$ , but the intensity of the oscillation is augmented. The flames periodically contract and stretch towards the exits of the nozzle and the combustion chamber, accompanied by a significant increase of the OH\*-intensity in the stretched state.

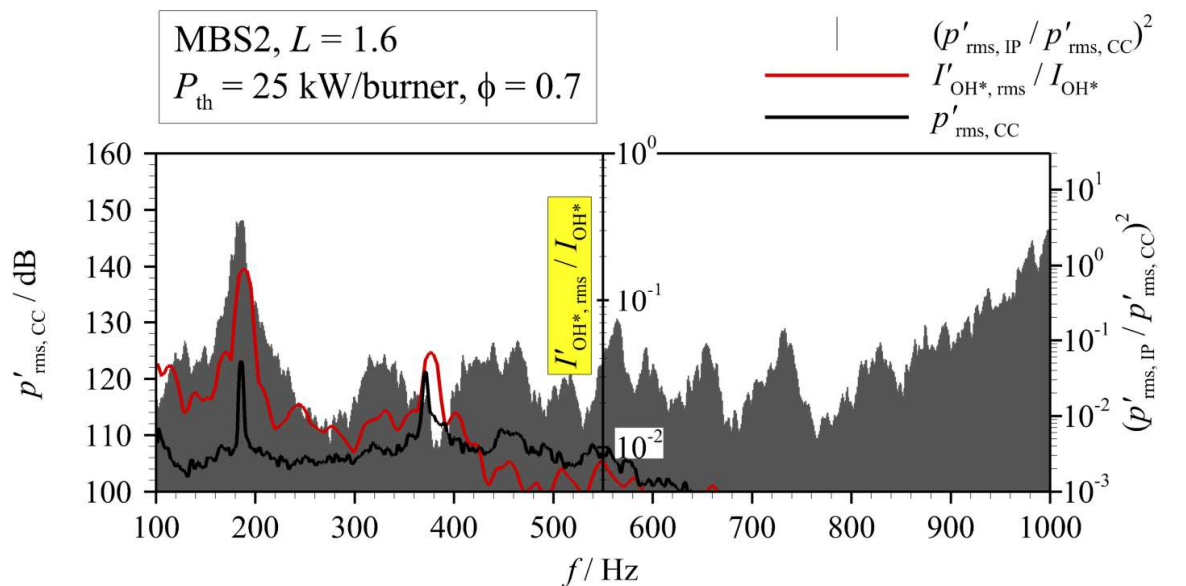


**Figure 4.24. MBS2,  $P_{th} = 25$  kW/burner,  $\phi = 0.7$ ,  $L = 1.6$ : Pressure and OH\*-intensity oscillations in the combustion chamber (CC) and acoustic response in the inner plenum (IP)**

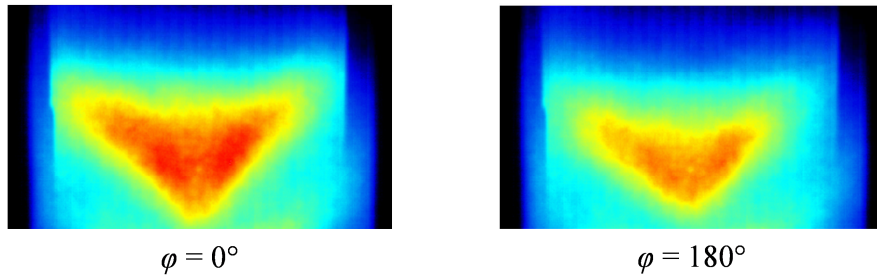


**Figure 4.25.** MBS2,  $P_{th} = 25$  kW/burner,  $\phi = 0.7$ ,  $L = 1.6$ : Oscillation cycle of the OH\*-intensity at 190 Hz

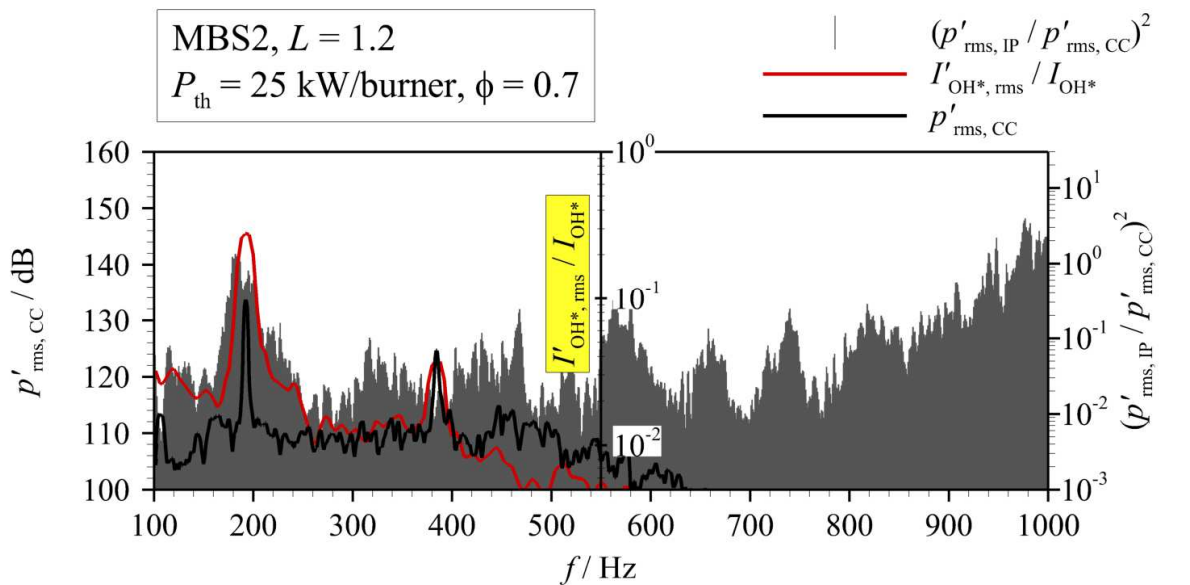


**Figure 4.26** MBS2,  $P_{th} = 25$  kW/burner,  $\phi = 0.7$ ,  $L = 1.2$ : Pressure and OH\*-intensity oscillations in the combustion chamber (CC) and acoustic response in the inner plenum (IP)

In the MBS1, the flame oscillation also switches to a similar pulsating flame oscillation (Figure 4.28) when the value of  $L$  decreases from  $L = 1.6$  to  $1.2$ . The frequency of the oscillation constitutes  $\sim 190$  Hz, which is visible in the OH\*-intensity spectrum in Figure 4.29. Compared to  $L = 1.6$ , the flame shows a stronger thermoacoustic response, which explains the augmented pressure amplitude. In the SBS, the 190-Hz mode is also observed in the pressure and OH\*-intensity spectrums when the swirler mass flow ratio is decreased to  $L = 1.2$  and the equivalence ratio is lowered to  $\phi = 0.65$  (Figure 4.30). This also leads to a significant increase in the maximum amplitude of the OH\*-intensity oscillations. The frequency-locked averaged images in Figure 4.31 show that the flame oscillation associated with the 190-Hz mode in the SBS is equivalent to the pulsating flame mode observed in the MBSs.

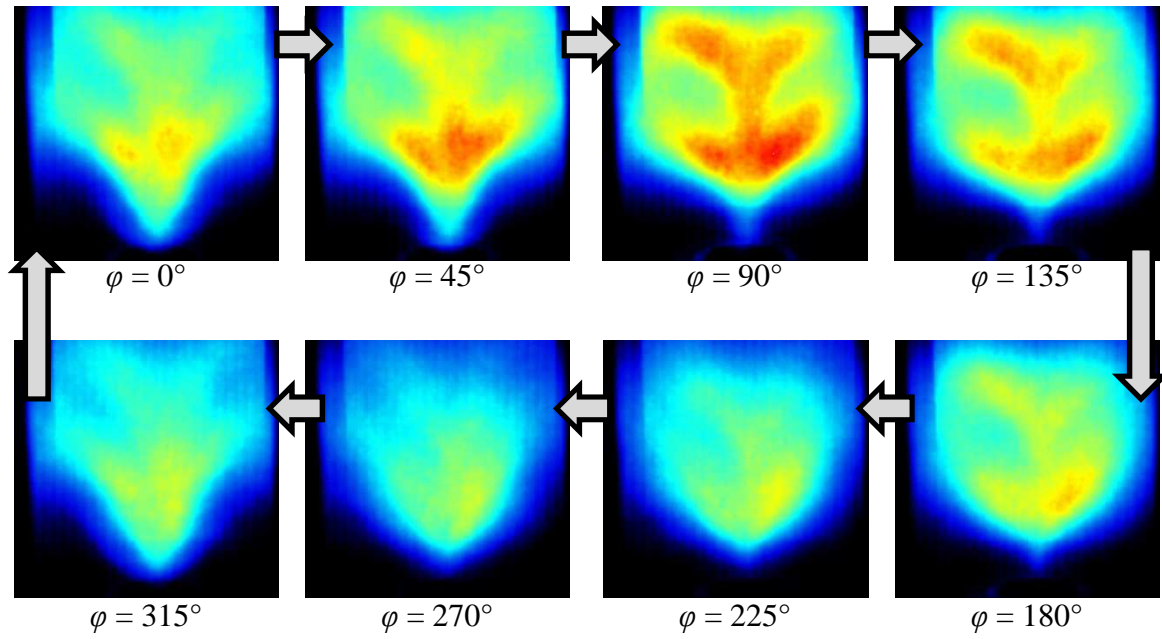


Figure 4.27. MBS2,  $P_{th} = 25$  kW/burner,  $\phi = 0.7$ ,  $L = 1.2$ : Oscillation cycle of the OH\* intensity at 190 Hz

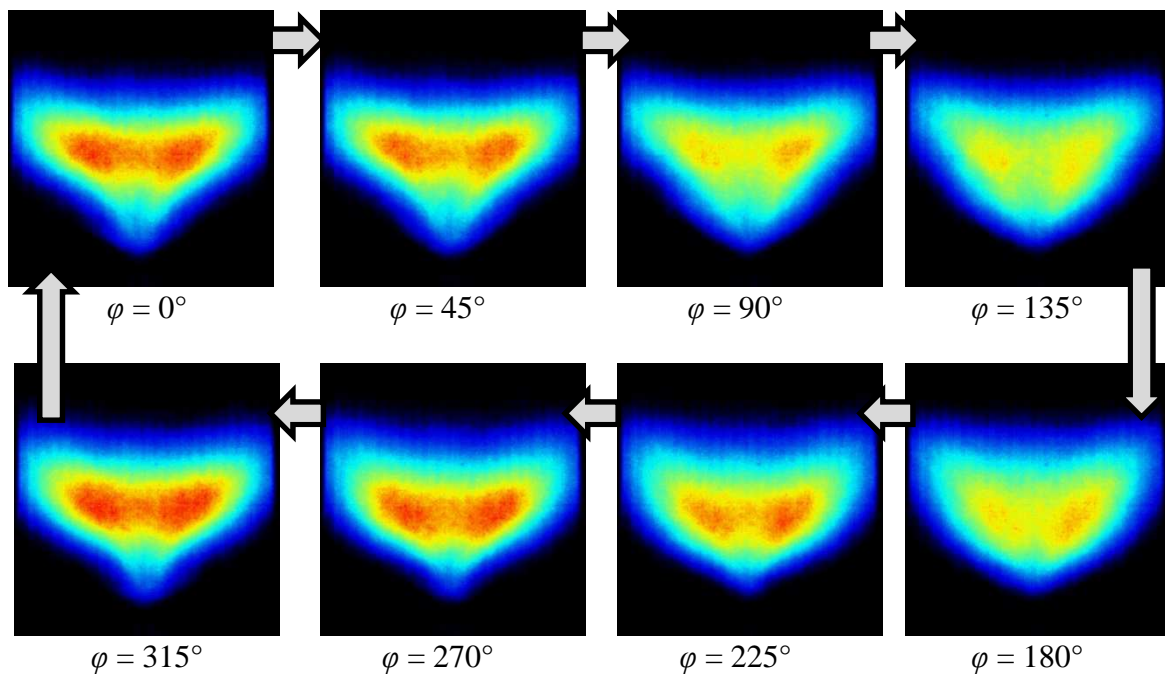
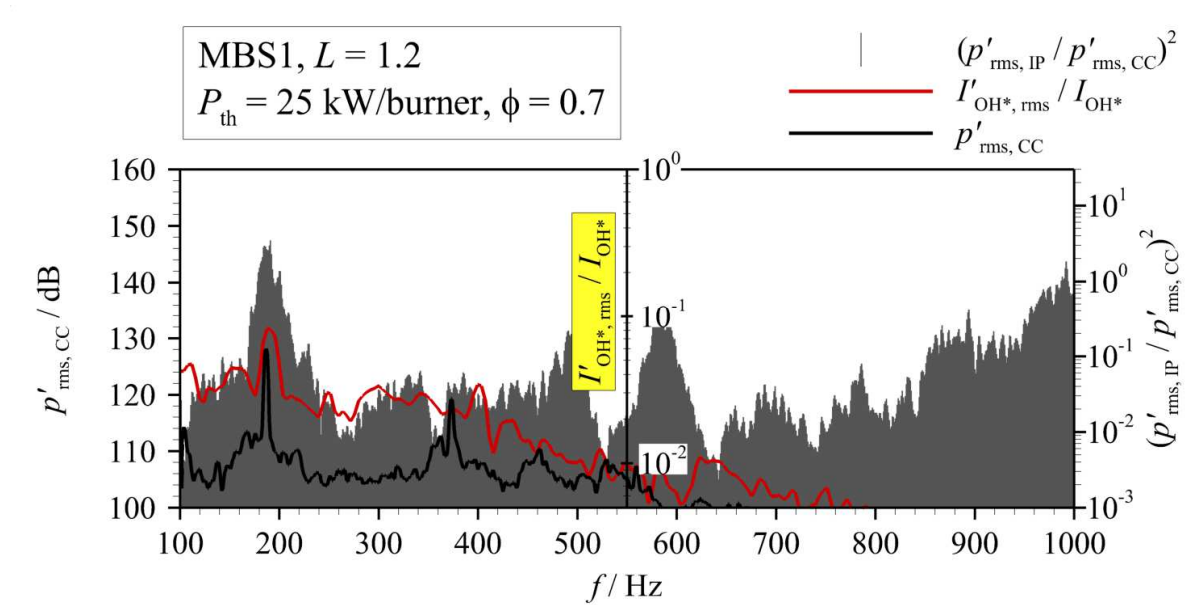
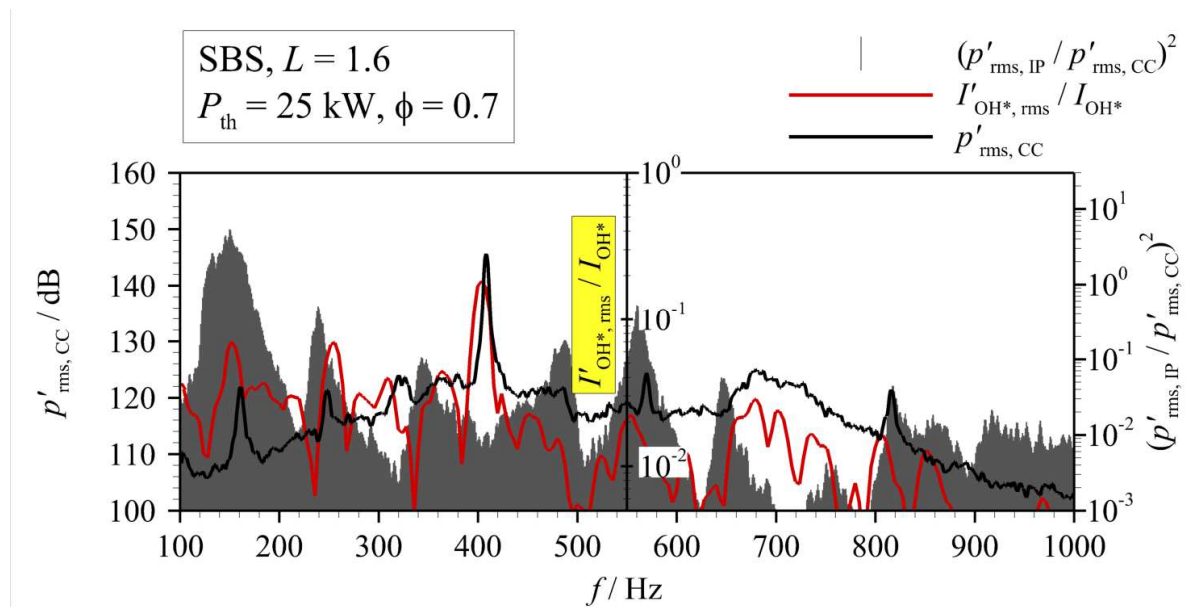


Figure 4.28. MBS1,  $P_{th} = 25$  kW/burner,  $\phi = 0.7$ ,  $L = 1.2$ : Oscillation cycle of the OH\* intensity at 190 Hz



**Figure 4.29. MBS2,  $P_{th} = 25$  kW/burner,  $\phi = 0.7$ ,  $L = 1.2$ : Pressure and OH\*-intensity oscillations in the combustion chamber (CC) and acoustic response in the inner plenum (IP)**



**Figure 4.30. SBS,  $P_{th} = 25$  kW,  $\phi = 0.7$ ,  $L = 1.6$ : Pressure and OH\*-intensity oscillations in the combustion chamber (CC) and acoustic response in the inner plenum (IP)**

High pressure and OH\*-intensity amplitudes in the frequency range of LF-Mode3 (~240 Hz) are found in the SBS at  $P_{th} = 30$  kW,  $\phi = 0.65$  at  $L = 1.2$  (Figure 4.32). The spectrum of the acoustic response of the inner plenum indicates that it serves as a resonator for the pressure oscillation in the combustion chamber. The oscillation cycle of the flame is shown in Figure 4.33.

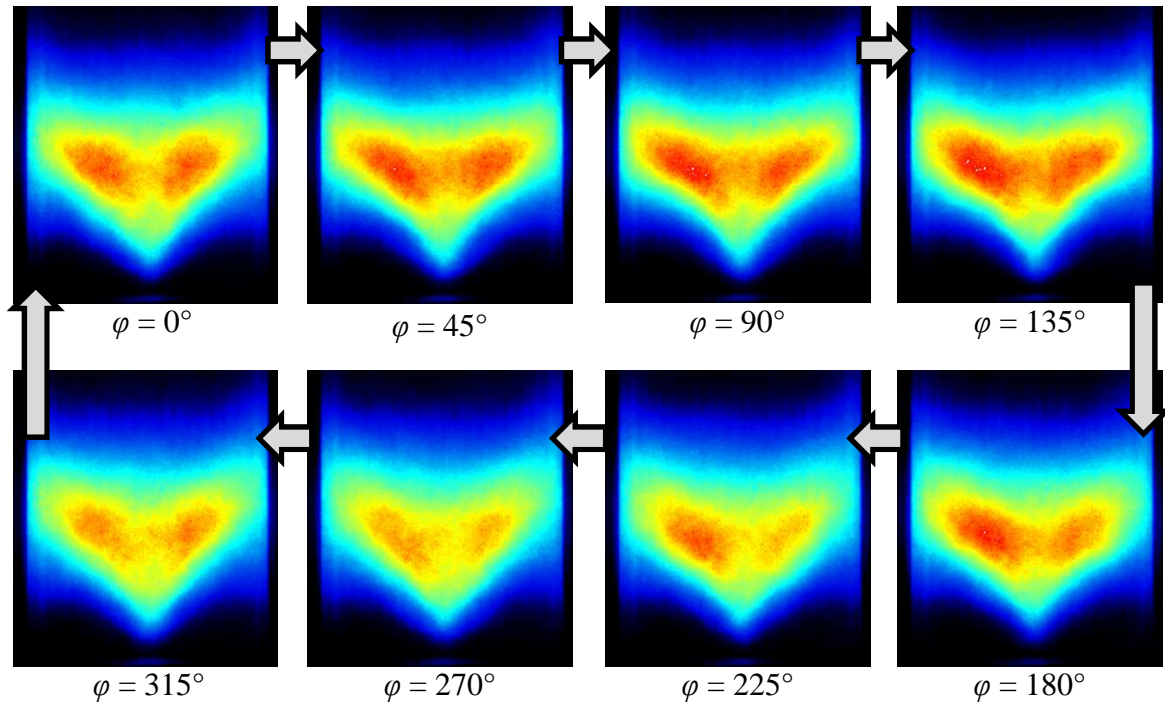


Figure 4.31. SBS,  $P_{th} = 25$  kW,  $\phi = 0.65$ ,  $L = 1.2$ : Oscillation cycle of the OH\*-intensity at 190 Hz

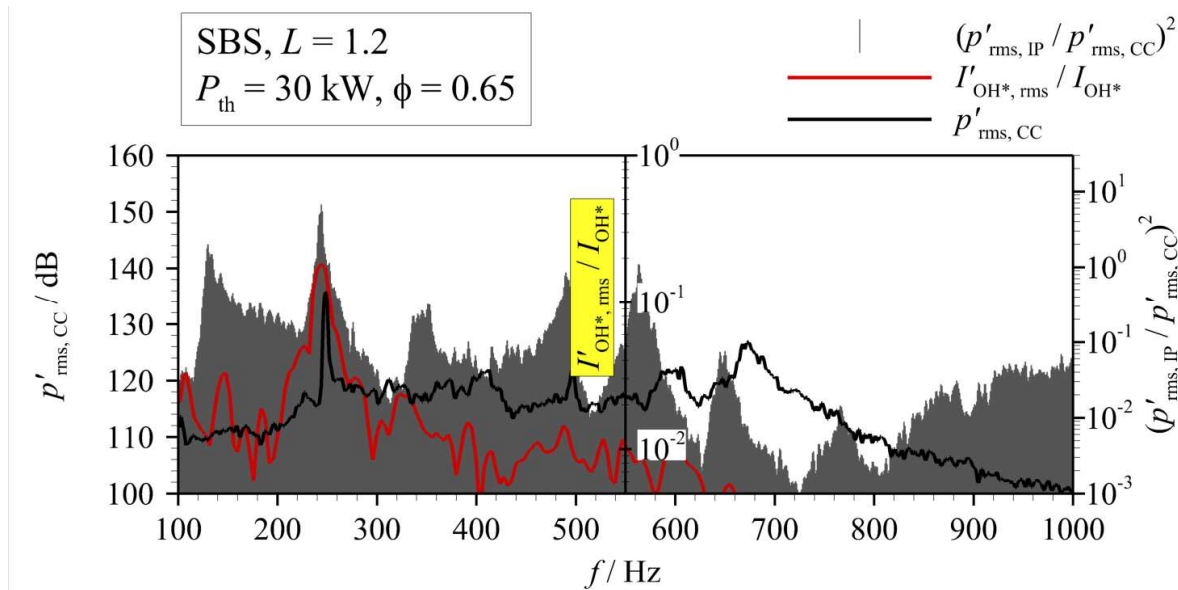
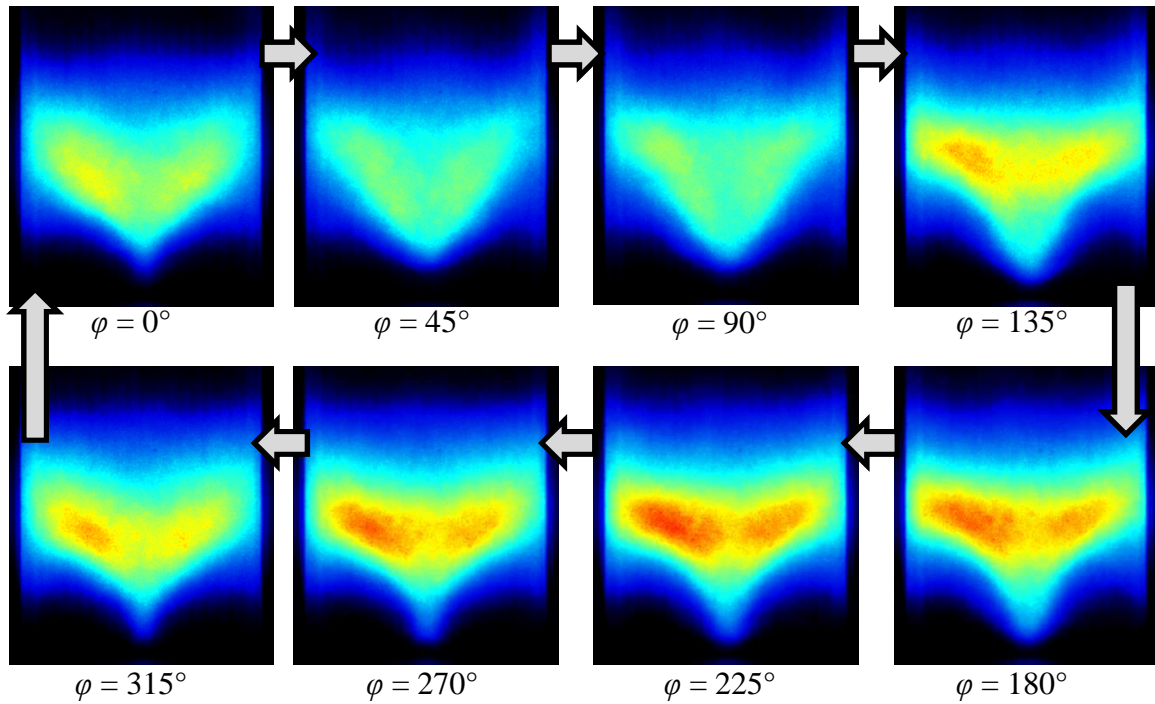
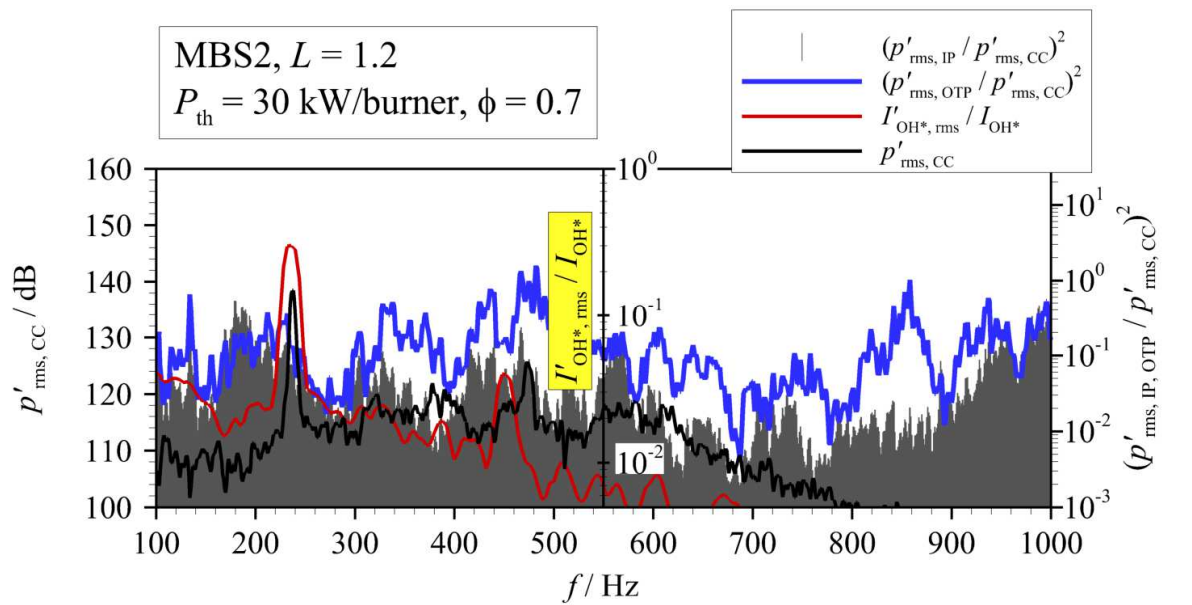


Figure 4.32. SBS,  $P_{th} = 30$  kW,  $\phi = 0.7$ ,  $L = 1.2$ : Pressure and OH\*-intensity oscillations in the combustion chamber (CC) and acoustic response in the inner plenum (IP)

A periodic pulsation of the flame is visible, which seems to be similar to the previously illustrated flame oscillations corresponding to the 190-Hz mode. High amplitudes of the pressure and OH\*-intensity oscillations in the frequency range of LF-Mode3 are also found in the MBS2 at  $P_{th} = 30$  kW/burner,  $\phi = 0.7$  at  $L = 1.2$ . The spectra of the acoustic responses in the inner plenum and the outer plenum show local maxima in the nearby frequency range (Figure 4.34). The frequency-locked averaged images also show the pulsating flame mode, as depicted in Figure 4.35.



**Figure 4.33.** SBS,  $P_{th} = 30$  kW,  $\phi = 0.65$ ,  $L = 1.2$ : Oscillation cycle of the OH\*-intensity at 240 Hz



**Figure 4.34.** MBS2,  $P_{th} = 30$  kW/burner,  $\phi = 0.7$ ,  $L = 1.2$ : Pressure and OH\*-intensity oscillations in the combustion chamber (CC) and acoustic response in the inner plenum (IP) and the outer plenum (OTP)

Figure 4.36 shows high-speed snapshots taken at the OPs which display the pulsating flame. The images illustrate the periodic formation of ring vortices. According to [103], these ring vortex structures are caused by pulsating inflow into the combustion chamber. The ring vortices initially consist of fresh gases and are characterized by rapid and intense mixing with burnt gases. As a result, the enclosed fresh gases impulsively react, which leads to a

significant augmentation of the heat release. The results indicate that the ring vortex formation is associated with the potential acoustic eigenmodes in the plenums. According to [139], the product of the amplitude and the Strouhal-Number of a mass flow perturbation has to reach a certain value in order to induce the formation of ring vortices. This may explain why the frequencies of the pulsating flame oscillations match or are found close to frequencies where high acoustic responses in one of the plenums or both plenums are observed. At those frequencies it is more likely that high pressure amplitudes are generated in the plenums which in turn induce the necessary amplitude of the mass flow oscillation. In order to amplify the oscillation, the flame response has to reach a sufficient phase angle, which is influenced by the characteristic time delay of the flame. In general, the phase angle of the flame response increases with the frequency of the mass flow oscillation. The fact that differences between the combustor setups are observed regarding the frequencies of the pulsating flame oscillations and the operating conditions under which they occur indicates that the combustor setups affects the characteristic time delay of the flame.

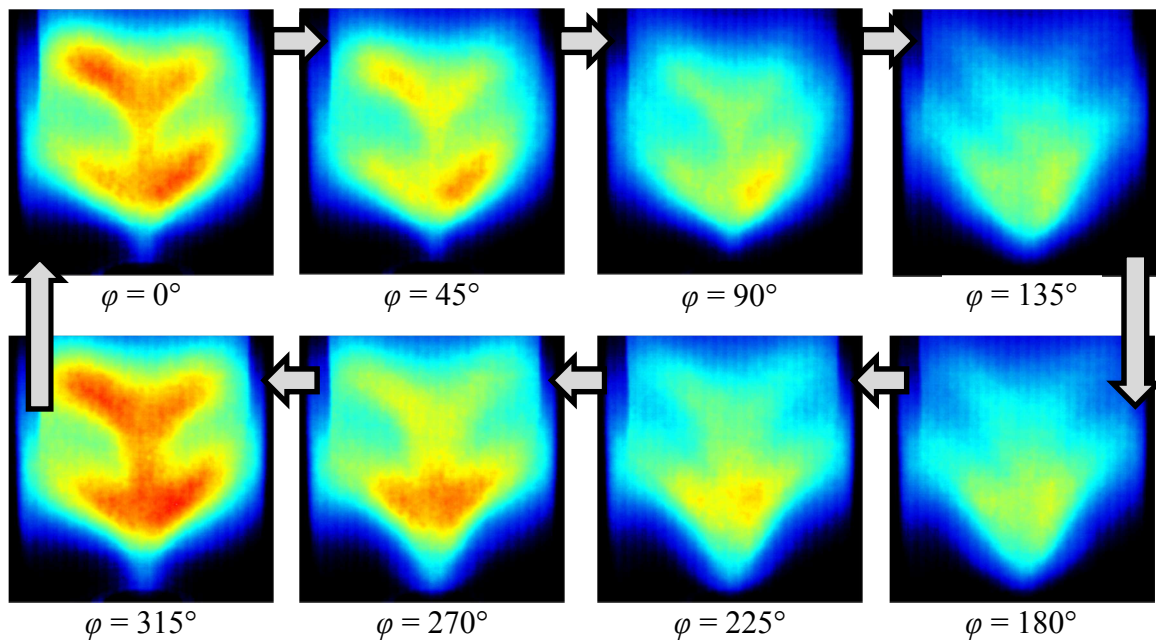
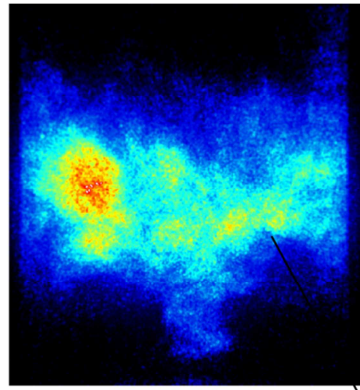


**Figure 4.35.** MBS2,  $P_{th} = 30$  kW/burner,  $\phi = 0.7$ ,  $L = 1.2$ : Oscillation cycle of the OH\*-intensity at 230 Hz

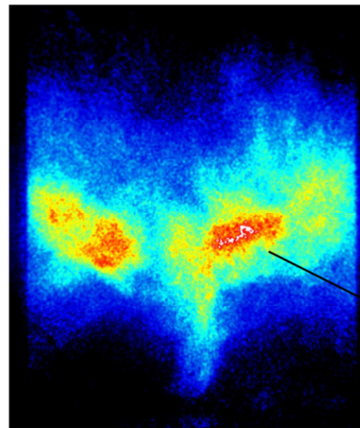
#### 4.5.1.6 Summary and Discussion of the Results for the LF-Modes

The characteristics of the low-frequency combustor modes were analysed in this section. The results indicate that the acoustic response characteristics of the plenums significantly affect the pressure oscillations in the combustion chamber. LF-Mode1 seems to be mainly the result of the excitation of a natural frequency of the inner plenum by the flame. The pressure oscillation of LF-Mode1 in the inner plenum modulates the flow rate at the outlet of the inner swirler and causes periodic changes of the swirl number. This leads to periodic mixing of fuel into the IRZ near the nozzle exit, which causes oscillations of the OH\*-intensity in this region, due to equivalence ratio and heat release oscillations.

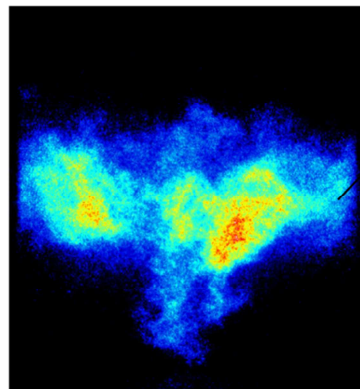
SBS,  $L = 1.2$   
 $P_{th} = 25 \text{ kW}$ ,  $\phi = 0.65$



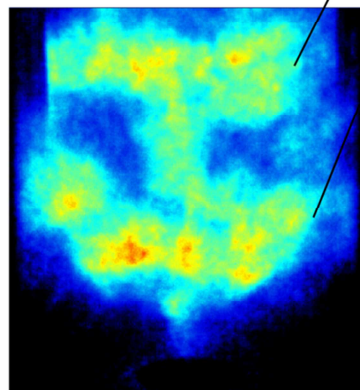
SBS,  $L = 1.2$   
 $P_{th} = 30 \text{ kW}$ ,  $\phi = 0.65$



MBS1,  $L = 1.2$   
 $P_{th} = 25 \text{ kW}$ ,  $\phi = 0.7$



MBS2,  $L = 1.2$   
 $P_{th} = 30 \text{ kW}$ ,  $\phi = 0.7$



Formation of  
ring vortex structures

**Figure 4.36. High-speed snapshots of the OH\*-chemiluminescence taken at the OPs where intense flame pulsation are observed**

The analysis of the pressure spectra and the OH\*-intensity recordings indicates that the main source of excitement for LF-Mode2 is a periodic flow instability, since the frequency of LF-Mode2 shows a nearly linear scaling with the bulk velocity. It was concluded that LF-Mode2 is excited by vortex-shedding at the outer or inner shear layer of the swirl flow. This assumption may also explain why the amplitude of LF-Mode2 is strongly influenced by the swirler mass flow ratio, since changes of the swirler mass flow ratio strongly affect the flow conditions in the shear layers of the swirl flow. Different frequencies were found for LF-Mode2 in the SBS and the MBSs, which indicates differences in the flow fields in the combustion chamber.

Regarding LF-Mode3, the results indicate that similar to LF-Mode1, the pressure oscillations of LF-Mode3 are mainly caused by the excitation of natural frequencies in the plenum by the flame. In the SBS, the spectra of the acoustic responses in the plenums show an increased response of the inner plenum in the corresponding frequency range. In the MBSs, the acoustic response in the frequency range of LF-Mode3 is significantly smaller. This is possibly caused by the different geometries of the inner plenums in the SBS and the MBSs.

The results indicate that the 190-Hz mode in the MBSs also represents an eigenmode of the inner plenum, since the spectra of all discussed OPs show increased acoustic responses in the frequency range around 190 Hz. However, in the SBS increased acoustic response in the frequency range around 190 Hz is only observed for certain operating conditions. This also may be explained by different acoustic impedances of the inner plenums of the SBS and the MBSs.

At certain OPs, augmented pressure amplitudes of the 190-Hz mode and LF-Mode3 are observed in the combustion chamber. It was concluded that this is caused by two mechanisms. The first mechanism represents a constructive interference of the 190-Hz mode or LF-Mode3 with LF-Mode2. For example, this is observed in the MBS1 at  $P_{th} = 25$  kW/burner,  $\phi = 0.7$ ,  $L = 1.6$ , where the inner plenums acts as a resonator for the pressure oscillation at ~190 Hz of LF-Mode2 in the combustion chamber. The second mechanism leads to significantly higher amplitudes and is characterized by a very intense flame oscillations. The high-speed images show the periodic formation of ring vortices, which lead to intense heat release oscillations. The coupling between the pressure and heat releases oscillations in the combustion chamber induces high pressure amplitudes in the combustion chamber, which in turn modulate the flow of the fuel-air mixture into the combustion chamber. It was observed that the flame pulsation frequencies match with or are close to frequencies where the plenums show high acoustic responses. The assumption was made that the low damping rates in the plenums at these frequencies increase the probability for the necessary mass flow oscillation amplitude, which is crucial for the formation of ring vortex structures.

### 4.5.2 400-Hz Mode

The 400-Hz mode represents a major combustor mode in all combustor setups. In the MBSs, it even is the mode that has the highest amplitudes. It is observed for high thermal power ( $P_{th} > 25$  kW/burner).

Figure 4.37-Figure 4.39 show the pressure oscillations in the combustion chamber and the plenums and the acoustic responses of the plenums in the frequency range 300-500 Hz in all combustor setups at  $L = 1.6$ . The high pulsation levels of the 400-Hz mode which result in amplitudes of up to 154 dB clearly indicate the presence of combustion instabilities and strong thermoacoustic flame responses.

In the SBS, high amplitudes ( $> 145$  dB) of the 400-Hz mode are already observed at  $P_{th} = 25$  kW. It is clearly visible that the highest amplitudes are reached at  $\phi = 0.8, 0.75, 0.7$ . Relatively high pressure amplitudes are also measured in the plenums, although the acoustic responses in the frequency range around 400 Hz are significantly lower than those observed in the frequency ranges of the low-frequency modes, especially in the inner plenum. On the other hand, the values of the acoustic responses still significantly exceed the absolute minimum values. Hence, the acoustic response characteristics of the plenums may contribute to the oscillation of the 400-Hz mode, but the results and the very high amplitudes clearly indicate that the main source of excitement is a strong thermoacoustic feedback of the flame.

In contrast to the SBS, amplitudes of  $> 145$  dB of the 400-Hz mode are not observed in the MBSs at  $P_{th} = 25$  kW/burner. On the other hand, the maximum amplitudes in the MBSs at  $P_{th} = 30$  kW/burner exceed those observed in the SBS. Similar to the SBS, the 400-Hz mode shows augmented amplitudes in the MBSs at  $\phi = 0.8, 0.75, 0.7$ . However, in contrast to the SBS, in the MBSs high pressure amplitudes are also visible at  $\phi = 0.85$ . The acoustic responses of the plenums in the MBSs around 400 Hz are similar to those in the SBS, except for the outer plenum in the MBS1, which shows considerably higher responses than the other setups. The observed distortions of the acoustic response curves in the MBS2 may be caused by vibrations of the combustor housing which are excited by the high pressure amplitudes in the combustor. Due to the fixed mounting of the microphones to the combustor housing, the vibrations are also transferred to the microphones and possibly distort the measured pressure signal. The reason why this is especially noticeable in the MBS2 may be due to the arrangement of the single-burners in the MBS2. It is possible that the more compact combustor structure is more sensitive to the excitement by pressure oscillations.

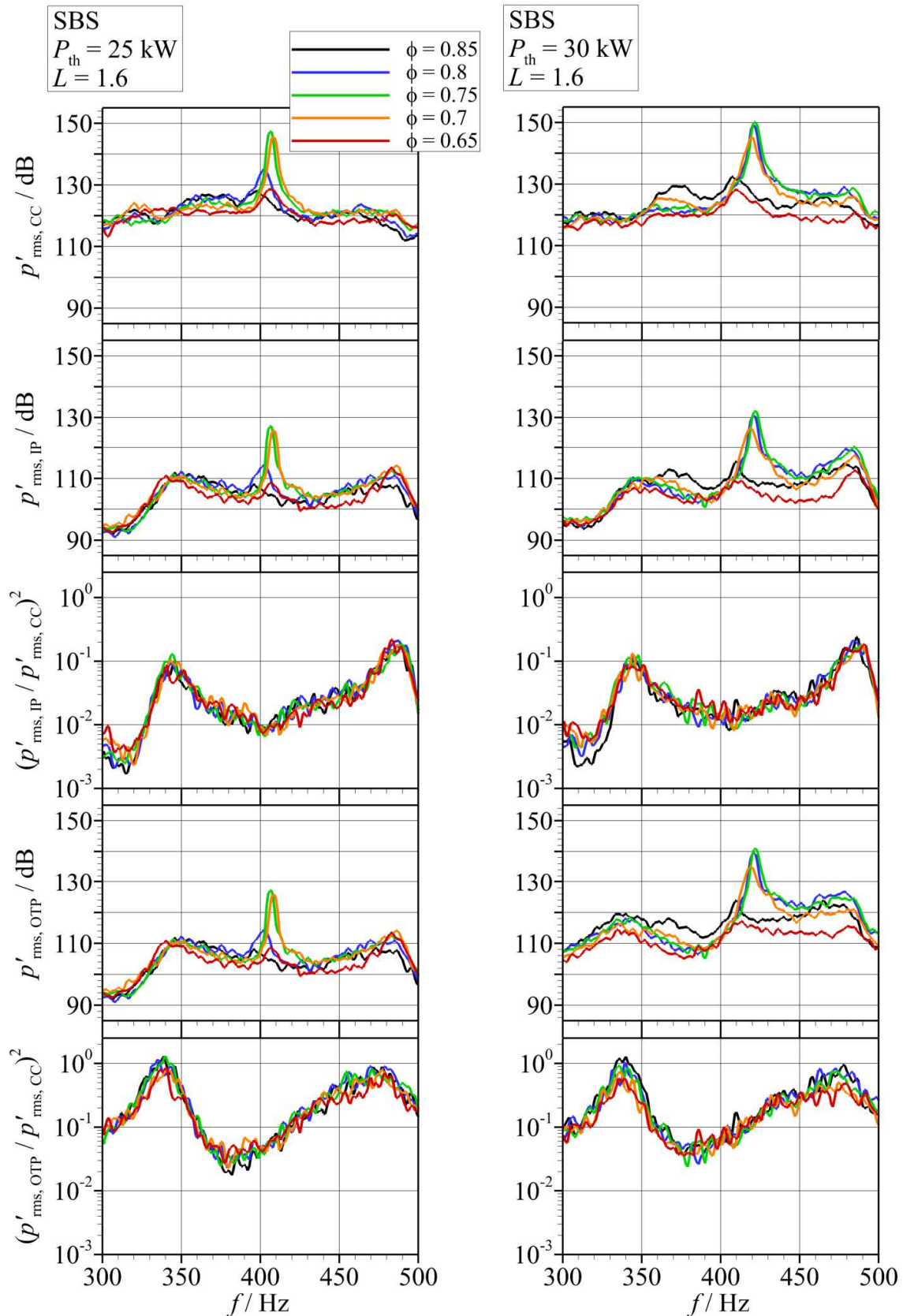


**Figure 4.37. SBS,  $L = 1.6$ : Pressure oscillations in the combustion chamber (CC) and the plenums and acoustic responses in the plenums at  $P_{th} = 25 \text{ kW}$  and  $P_{th} = 30 \text{ kW}$  at  $\phi = 0.65-0.85$**

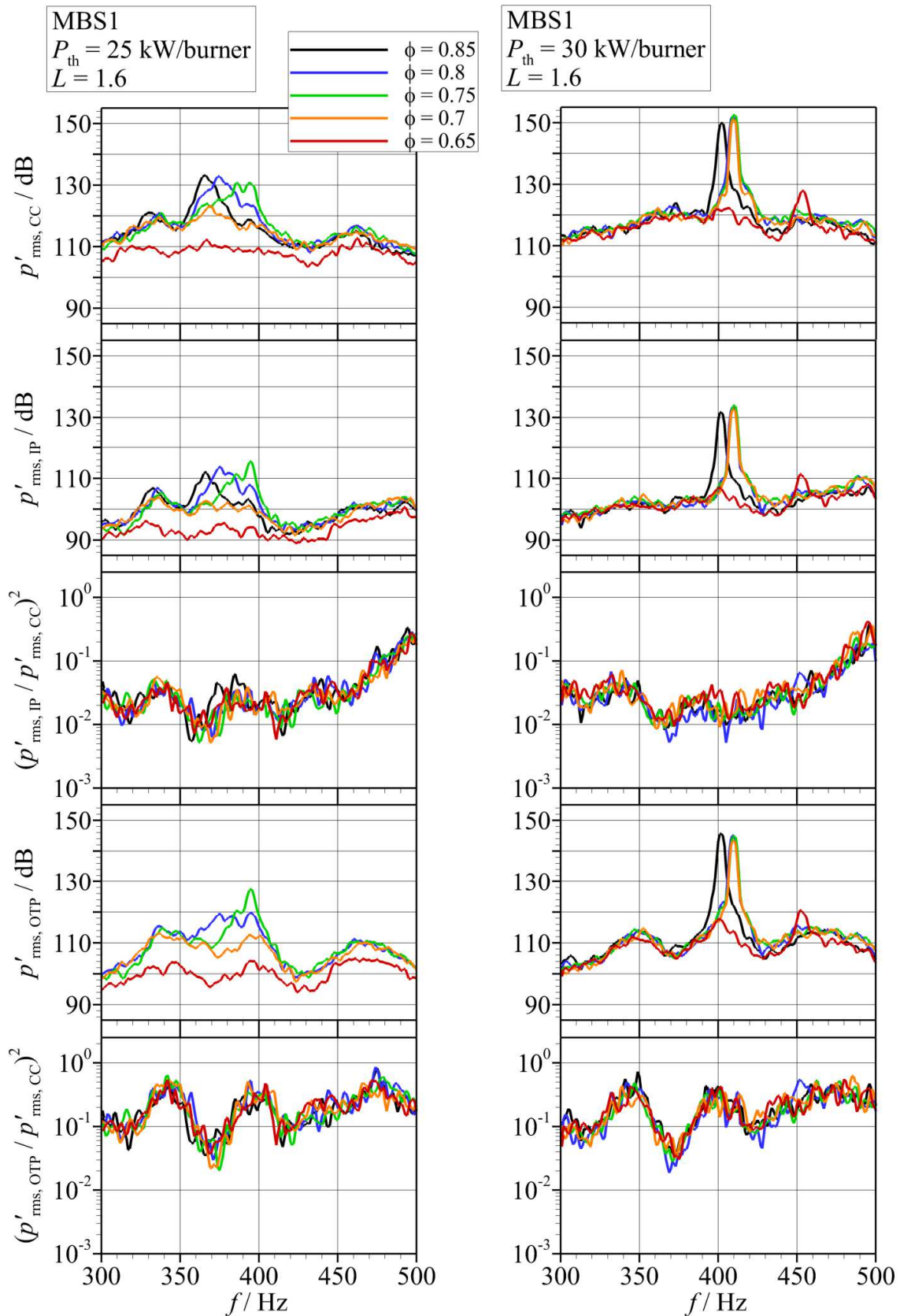


**Figure 4.38. MBS1,  $L = 1.6$ : Pressure oscillations in the combustion chamber (CC) and the plenums and acoustic responses in the plenums at  $P_{th} = 25$  kW/burner and  $P_{th} = 30$  kW/burner at  $\phi = 0.65-0.85$**

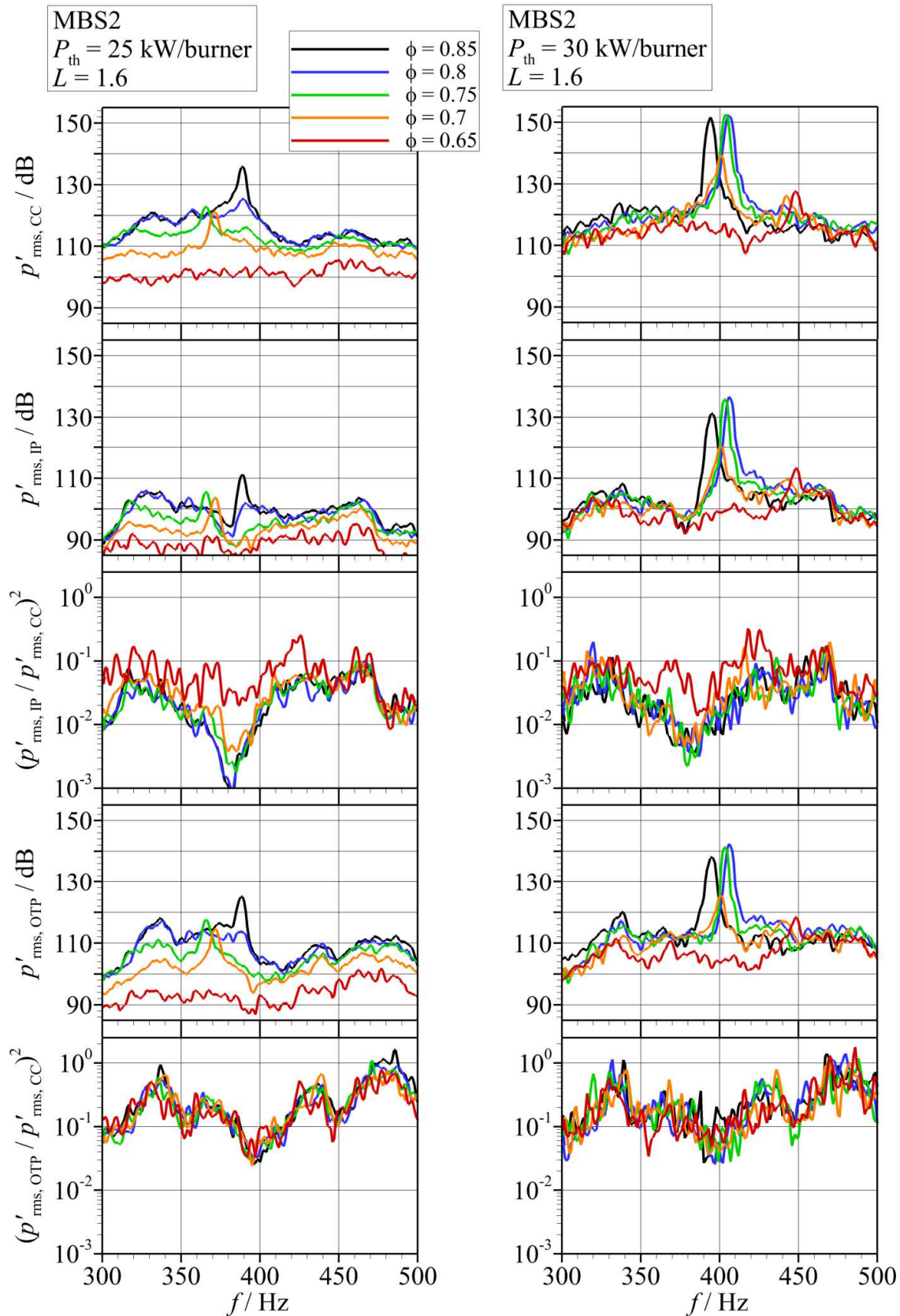


**Figure 4.39. MBS2,  $L = 1.6$ : Pressure oscillations in the combustion chamber (CC) and the plenums and acoustic responses in the plenums at  $P_{th} = 25$  kW/burner and  $P_{th} = 30$  kW/burner at  $\phi = 0.65-0.85$**

### 4.5.2.1 Influence of the Swirler Mass Flow Ratio on 400-Hz Mode

The spectra of the pressure oscillations in the combustion chamber at  $L = 1.2, 1.6, 2.0$  for  $P_{th} = 25$  kW/burner and  $P_{th} = 30$  kW/burner at  $\phi = 0.85, 0.8, 0.7$  are illustrated in Figure 4.40 for all combustor setups.

The influence of the swirler mass flow ratio on the 400-Hz mode is much more significant in the SBS than in the MBSs. In the SBS at  $P_{th} = 25$  kW, switching from  $L = 1.6$  to  $L = 1.2$  or  $L = 2.0$  results in a reduced oscillation of 400 Hz-Mode. The damping is more substantial at  $\phi = 0.7$ , where a decrease in the amplitude from  $\sim 145$  dB at  $L = 1.6$  to  $\sim 135$  dB at  $L = 2.0$  is observed. At  $L = 1.2$  an even stronger reduction to 122 dB is observed.

In the MBS1 at  $P_{th} = 25$  kW/burner, the 400-Hz mode is also damped at  $L = 1.2$  and  $L = 2.0$  and shows the lowest amplitudes at  $L = 1.2$  for all equivalence ratios. In contrast to that, the influence of the swirler mass flow ratio on the amplitude the 400-Hz mode in the MBS2 is strongly dependent on the equivalence ratio. At  $\phi = 0.85$  and  $0.8$ , the 400-Hz mode is strongly damped at  $L = 1.2$  compared to  $L = 1.6$ , whereas at  $L = 2.0$ , the amplitude of the 400-Hz mode increases at  $\phi = 0.8$ . At  $\phi = 0.7$ , a contradictive behaviour in comparison to  $\phi = 0.8$  is observed, since the amplitude augments with decreasing swirler mass flow ratio.

At  $P_{th} = 30$  kW/burner, the combustor dynamics are also strongly affected by the value of  $L$ . In the SBS, the maximum amplitudes of the 400-Hz mode are now found in the spectra at  $L = 1.2$  for  $\phi = 0.85, 0.8$ . At  $\phi = 0.7$ , a reduction in the amplitude of around 5 dB is observed when  $L$  is decreased from 1.6 to 1.2. At  $L = 2.0$ , the mode is damped at  $\phi = 0.8, 0.7$ , whereas for  $\phi = 0.85$  the amplitude increases slightly.

Decreasing  $L$  from 1.6 to 1.2 results in an amplitude increase of the 400-Hz mode at  $\phi = 0.85, 0.8$  and a strong damping of the 400-Hz mode at  $\phi = 0.7$  in both MBSs. At  $L = 2.0$ , the 400-Hz mode is damped for all equivalence ratios in the MBS1, whereas in the MBS2 its amplitude decreases slightly at  $\phi = 0.85, 0.8$  and is slightly increased at  $\phi = 0.7$ .

Since thermal power, equivalence ratio and swirler mass flow ratio significantly influence the amplitude of the 400-Hz mode, it can be stated that the excitation and the amplitude of the 400-Hz mode are mainly determined by the flame characteristics. This is also corroborated by spectra of the acoustic responses in Figure 4.41, since the value of  $L$  only slightly affects the response characteristics in the relevant frequency range. Thus, the observed differences in amplitude are most likely not caused by altered response characteristics of the plenums.

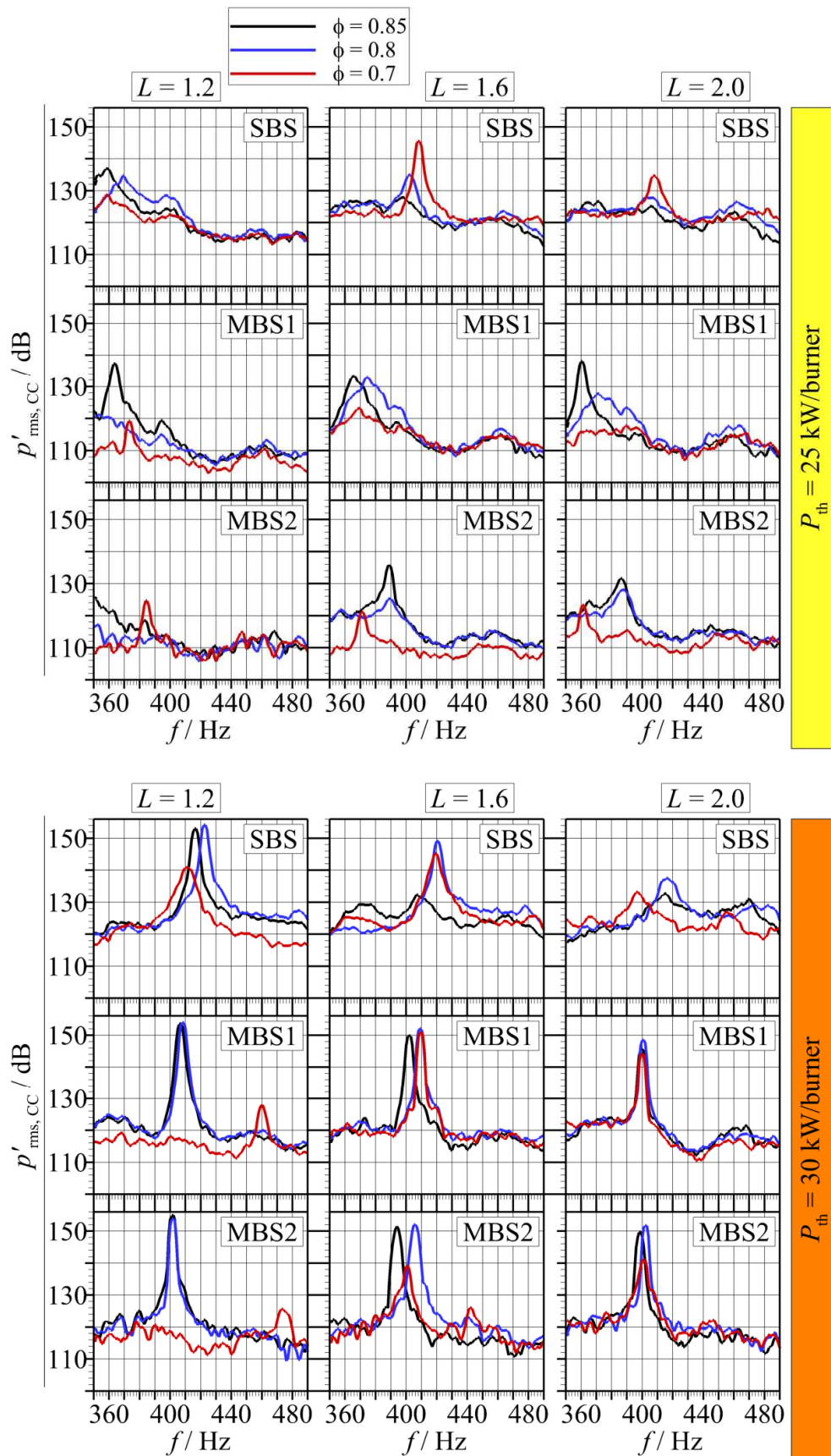


**Figure 4.40. SBS, MBS1, MBS2,  $L = 1.2, 2.0$ : Pressure oscillations in the combustion chamber (CC) at  $P_{th} = 25$  kW/burner and  $P_{th} = 30$  kW/burner,  $\phi = 0.7, 0.8, 0.85$**

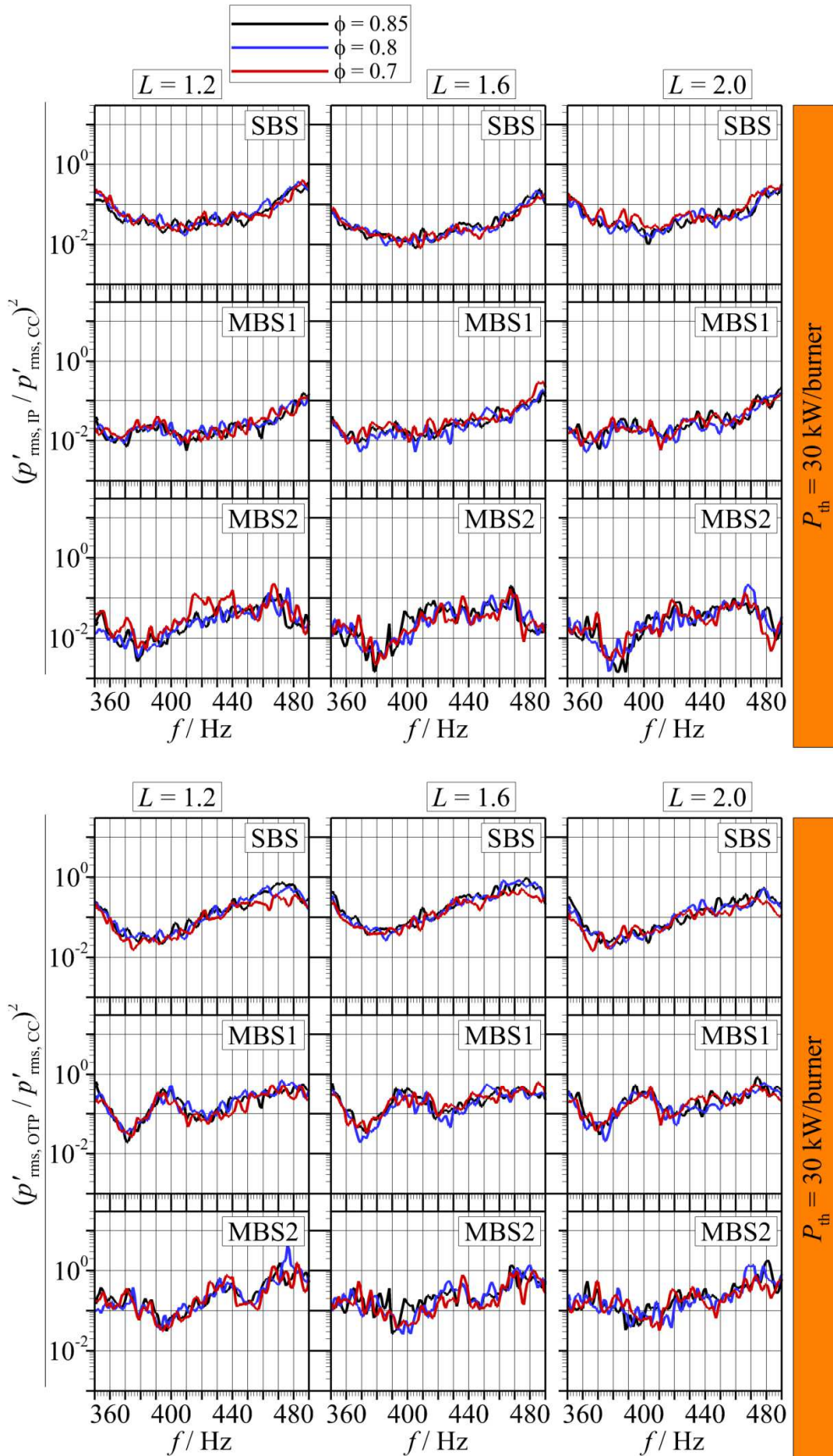


**Figure 4.41. SBS, MBS1, MBS2,  $L = 1.2, 1.6, 2.0$ : Acoustic responses in the inner plenum and the outer plenum at  $P_{th} = 30$  kW/burner,  $\phi = 0.7, 0.8, 0.85$**

#### 4.5.2.2 OH\*-Intensity Responses to the 400-Hz Mode

The spectra of the pressure oscillations in the combustion chamber and the corresponding OH\*-intensity oscillations in the SBS and the MBSs for  $P_{th} = 30$  kW/burner,  $\phi = 0.85$  at  $L = 1.2, 1.6, 2.0$  are shown in Figure 4.42, Figure 4.43 and Figure 4.44. The spectra of the OH\*-intensity illustrate the strong correlation between the pressure amplitude of the 400-Hz mode and the flame response.

In the SBS, the maximum pressure amplitude of the 400-Hz mode as well as the highest OH\*-intensity amplitude are observed at  $L = 1.2$ . At  $L = 1.6$  and  $L = 2.0$ , the OH\*-intensity oscillations of the 400-Hz mode are drastically reduced compared to  $L = 1.2$ . The MBSs show basically the same tendency, but the decrease of the OH\*-intensity amplitude compared to  $L = 1.2$  is much smaller. The smallest differences between the peak amplitude of the OH\*-intensity oscillation of the 400-Hz mode is observed in the MBS2, which corresponds with the pressure amplitudes.

In the SBS, the decrease of the OH\*-intensity oscillation at 400 Hz is accompanied by an increase of the OH\*-intensity oscillation of the 750-Hz mode, which is expected regarding the increased pressure amplitude of the 750-Hz mode. This is discussed in more detail in 4.4.2.3.

Due to the high oscillation levels of the OH-intensity, it is possible to visualize the corresponding flame oscillation of the 400-Hz mode via frequency-locked averaging. Figure 4.45 illustrates the oscillation cycle in the SBS. Figure 4.46 and Figure 4.47 show the oscillation cycles in the MBS1 and the MBS2, respectively. The character of the flame oscillation of 400-Hz mode is very similar in all combustor setups. The flames periodically propagate further downstream towards the combustion chamber outlet and simultaneously expand in the radial direction. In the expanded state, a significantly increased OH\*-intensity is observed.

Selected snapshots of the high-speed recording for all discussed OPs show the presence of ring vortex structures in all combustor setups (Figure 4.48). Therefore the feedback loop driving the combustion instability is similar to the one observed for the 190-Hz mode and LF-Mode3 discussed in 4.5.1.5.

The most significant difference regarding the 400-Hz mode in the SBS and the MBSs is characterized by the fact that in the SBS high pressure amplitudes  $> 145$  dB are already observed at  $P_{th} = 25$  kW, as discussed in 4.5.2. Figure 4.49 shows the OH\*-intensity spectrum at  $P_{th} = 25$  kW,  $\phi = 0.7$  for  $L = 1.6$ . The pulsation is less intense compared to the OPs that were already discussed in this section, and several modes in the low-frequency range are visible in the spectrum. However, the dominant OH\*-intensity oscillation is located at 400 Hz and the high-speed images also show the formation of ring vortices (Figure 4.50). This clearly indicates that the observed flame oscillation is similar to the oscillations of the 400-Hz mode observed in flames at the discussed OPs at  $P_{th} = 30$  kW/burner.

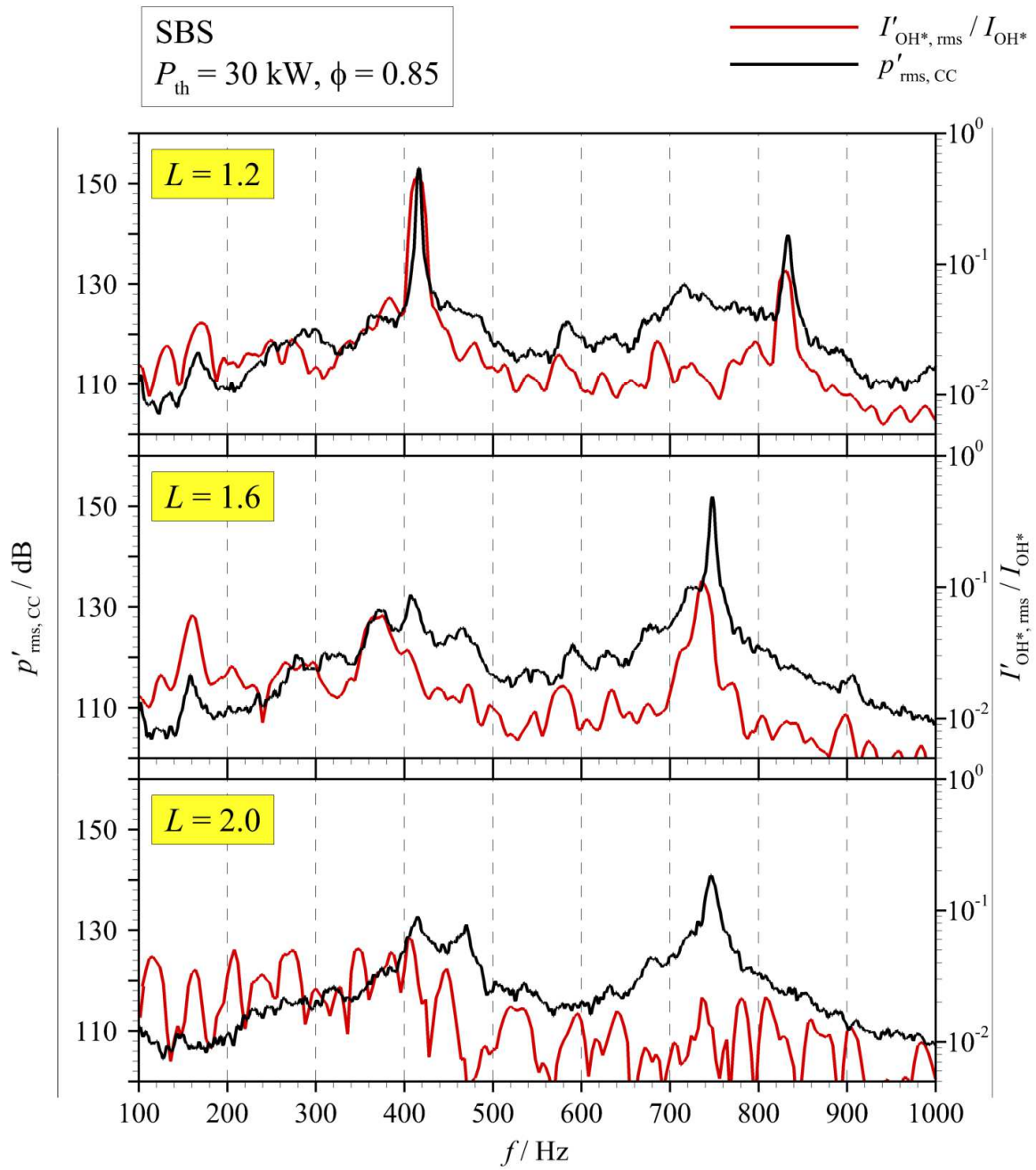


Figure 4.42. SBS,  $L = 1.2, 1.6, 2.0$ : Pressure and OH\*-intensity oscillations in the combustion chamber (CC) at  $P_{th} = 30 \text{ kW}, \phi = 0.85$

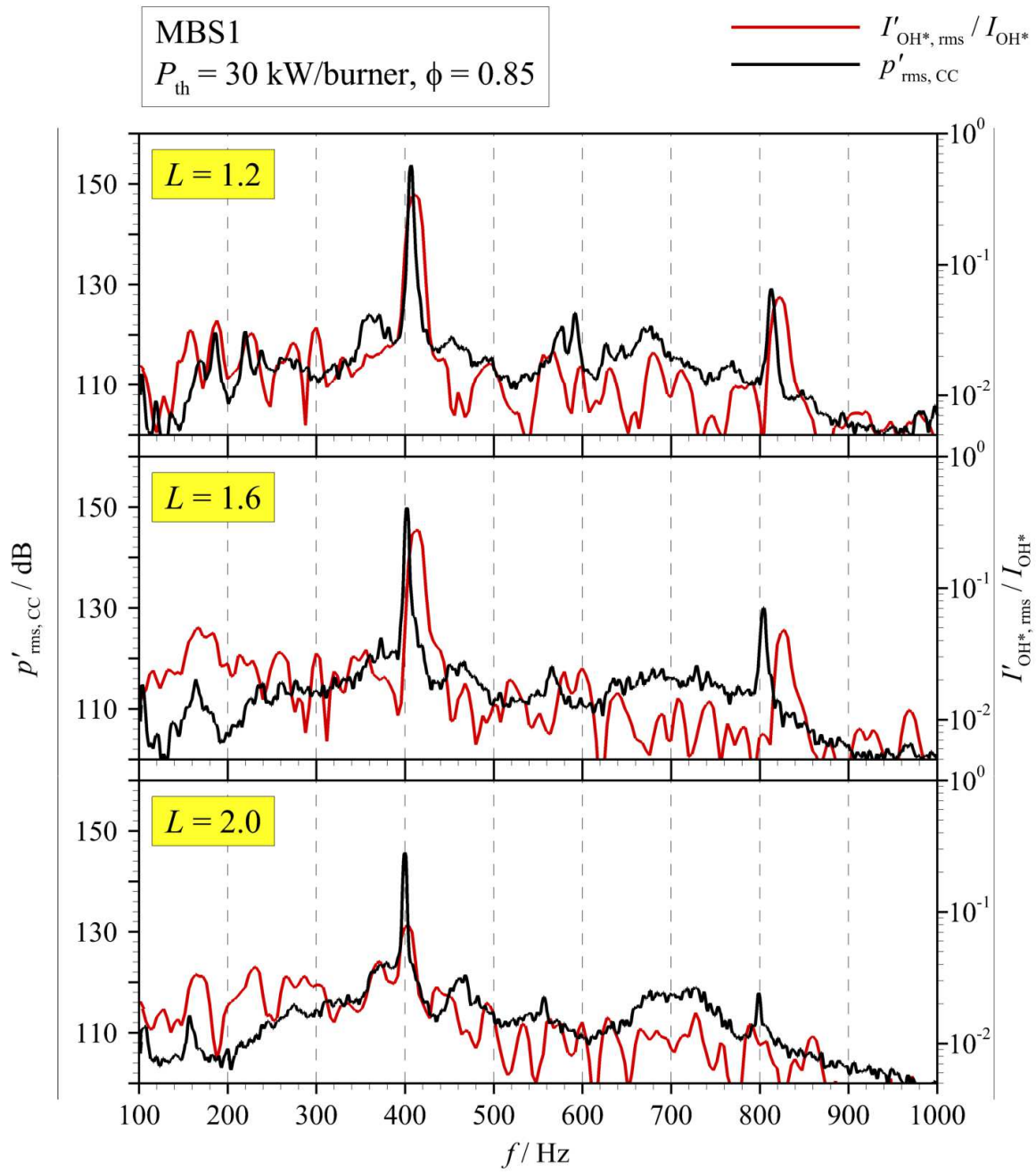


Figure 4.43. MBS1,  $L = 1.2, 1.6, 2.0$ : Pressure and OH\*-intensity oscillations in the combustion chamber (CC) at  $P_{th} = 30 \text{ kW/burner}, \phi = 0.85$

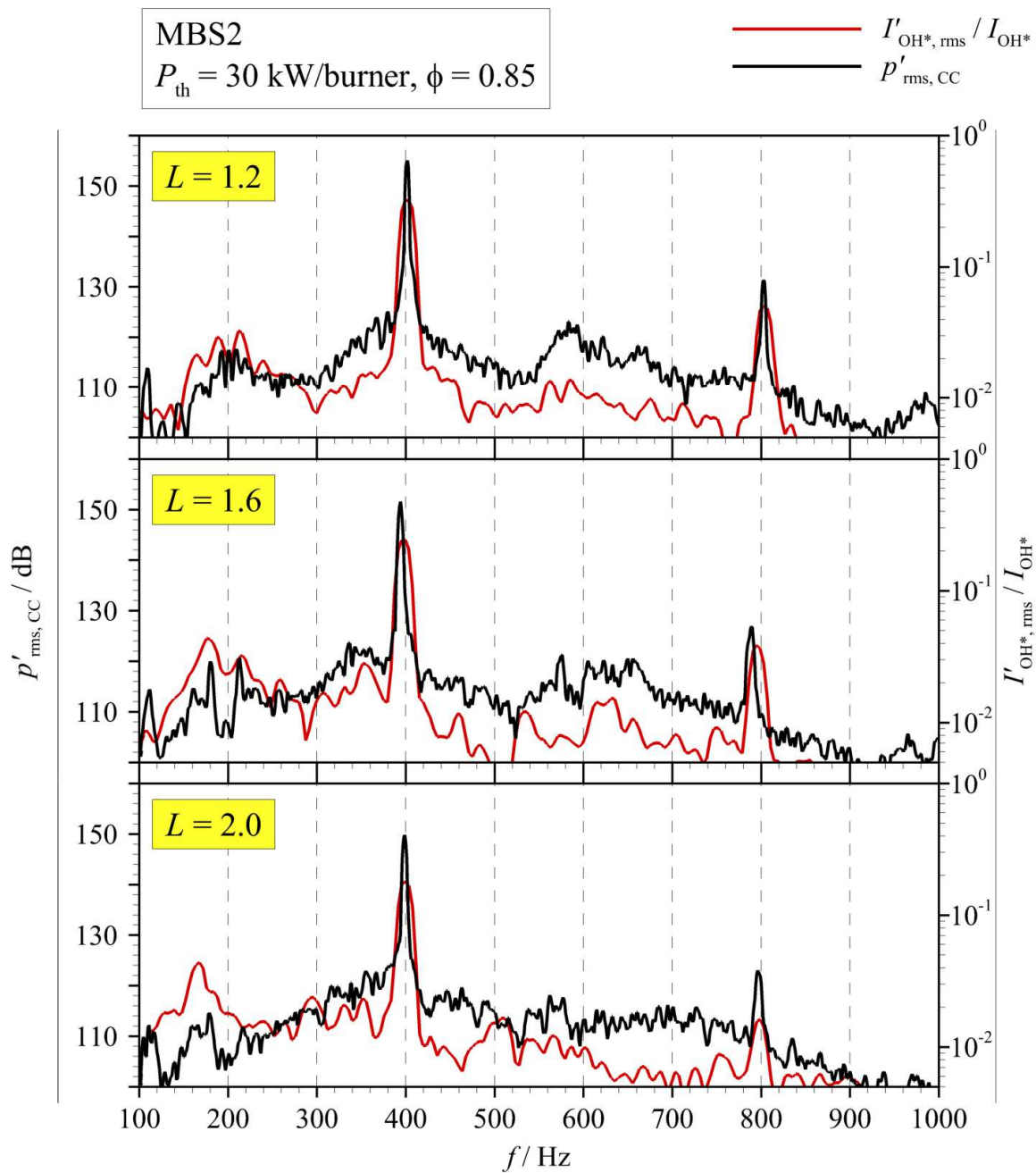


Figure 4.44. MBS2,  $L = 1.2, 1.6, 2.0$ : Pressure and OH\*-intensity oscillations in the combustion chamber (CC) at  $P_{th} = 30 \text{ kW/burner}, \phi = 0.85$

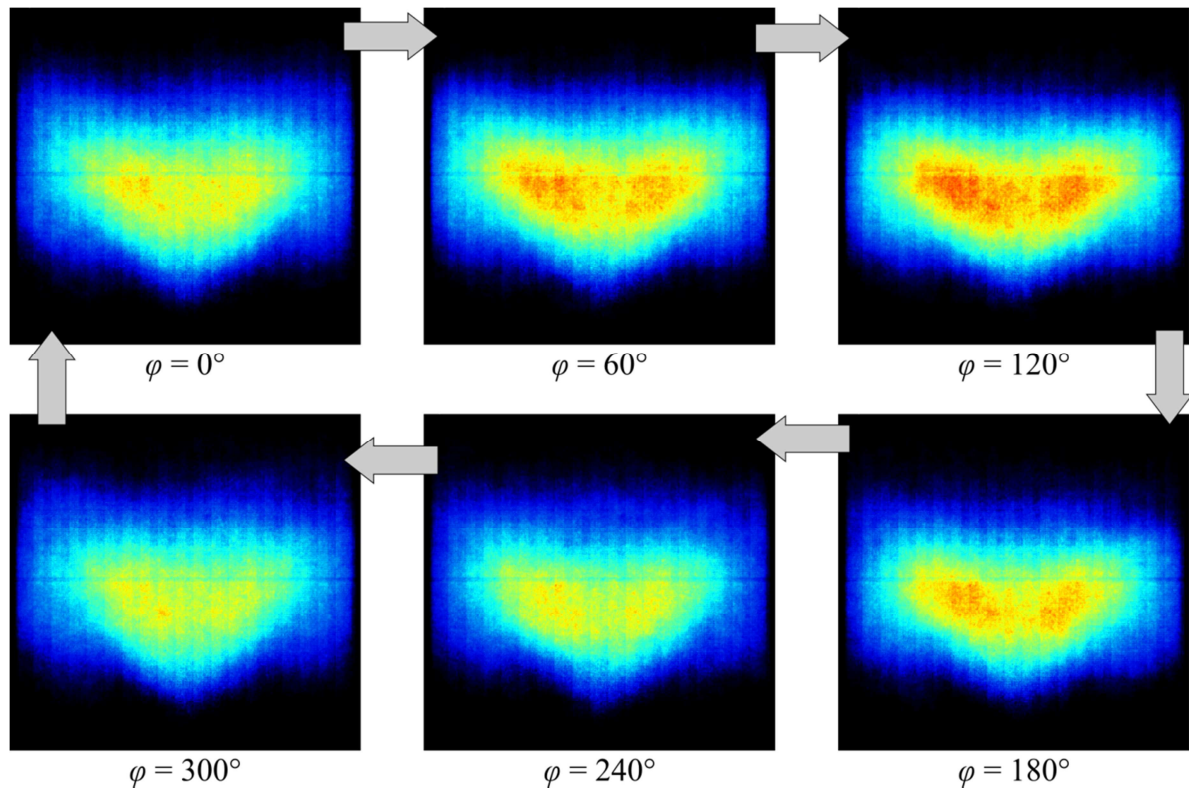


Figure 4.45. SBS,  $P_{th} = 30$  kW,  $\phi = 0.85$ ,  $L = 1.2$ : Oscillation cycle of the OH\*-intensity at 400 Hz

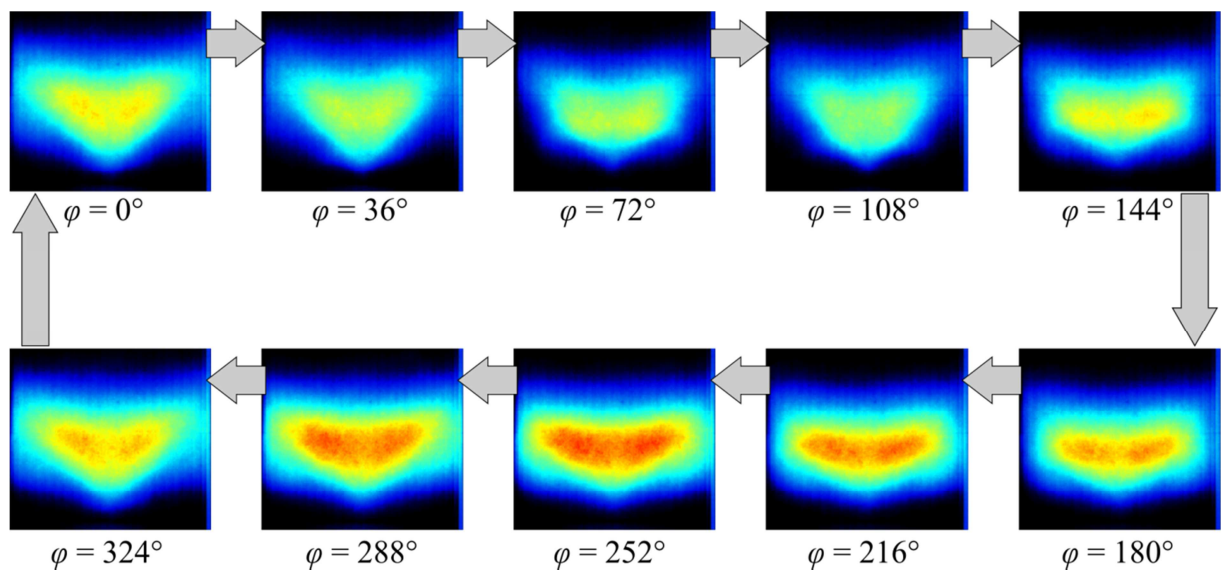
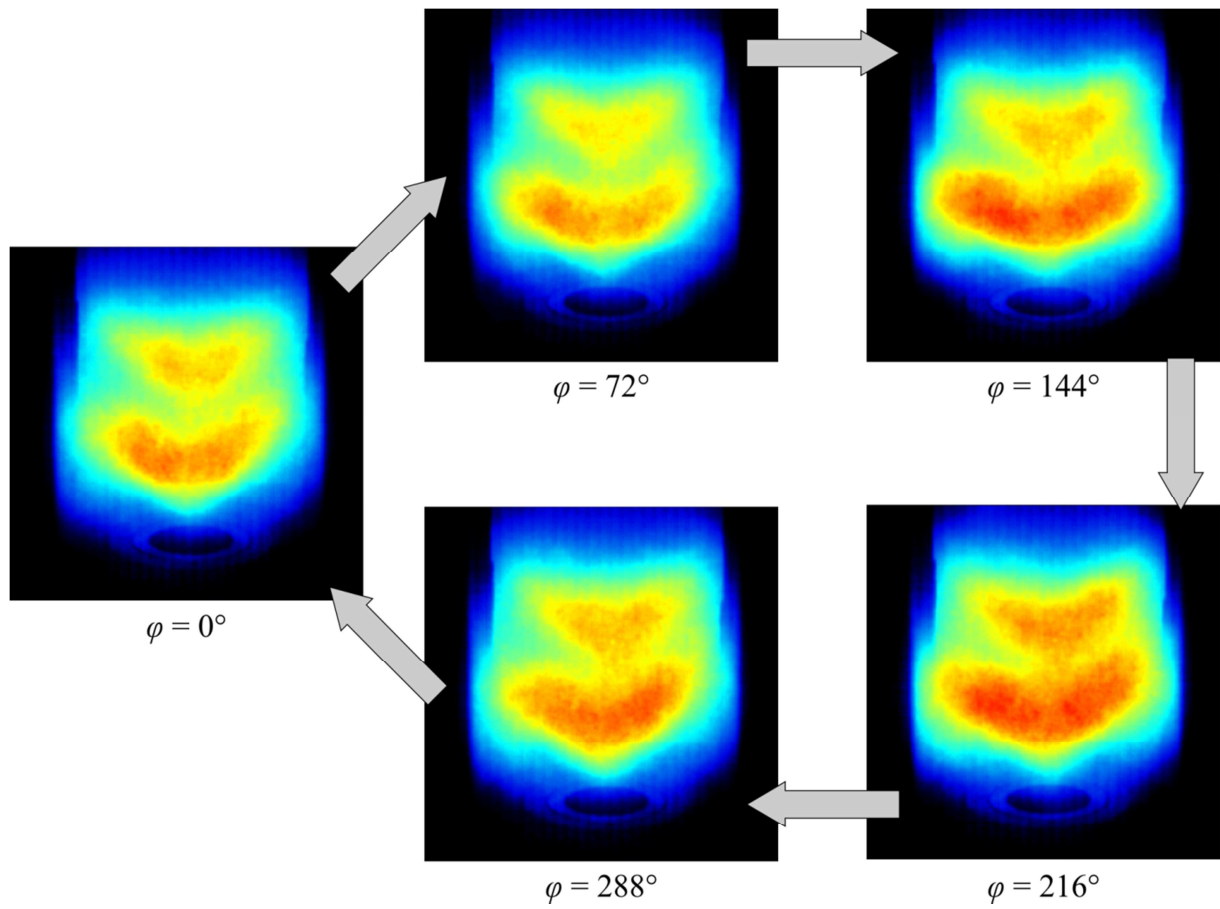
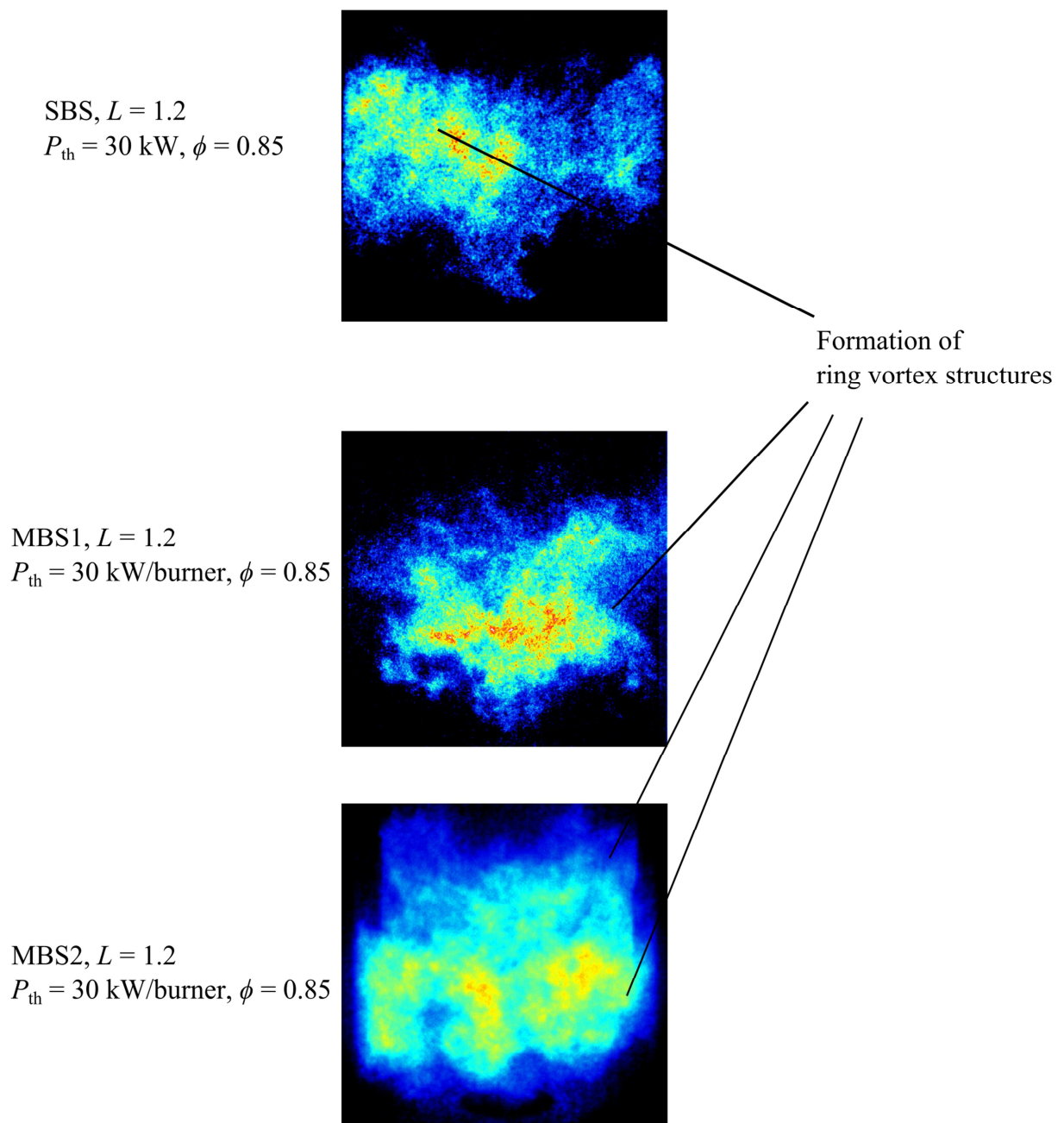


Figure 4.46. MBS1,  $P_{th} = 30$  kW/burner,  $\phi = 0.85$ ,  $L = 1.2$ : Oscillation cycle of the OH\*-intensity at 400 Hz



**Figure 4.47.** MBS2,  $P_{th} = 30$  kW/burner,  $\phi = 0.85$ ,  $L = 1.2$ : Oscillation cycle of the OH\*-intensity at 400 Hz



**Figure 4.48. SBS, MBS1, MBS2: High-speed snapshots of the OH\*-chemiluminescence at OPs with high pulsation levels of the 400-Hz mode**

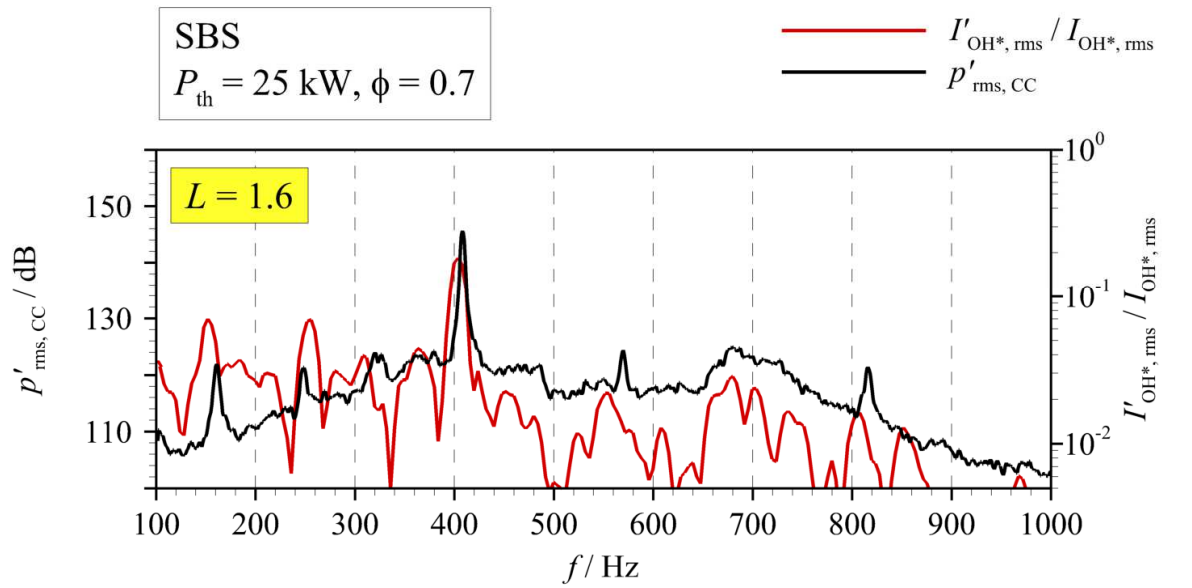


**Figure 4.49. SBS,  $L = 1.6$ : Pressure and OH\*-intensity oscillations in the combustion chamber (CC) at  $P_{th} = 25$  kW,  $\phi = 0.7$**

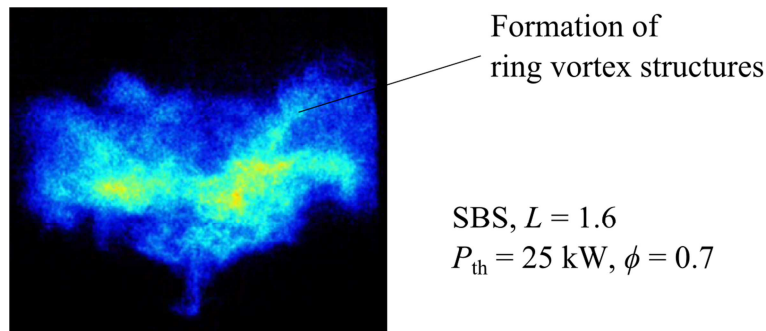


**Figure 4.50. SBS,  $L = 1.6$ : High-speed snapshot of the OH\*-chemiluminescence which shows the periodic formation of ring vortex structures corresponding to the 400-Hz mode**

#### 4.5.2.3 Summary and Discussion of the Results for the 400-Hz Mode

The formation of ring vortex structures was identified as the main driving mechanism of the 400-Hz mode. The analysis of the acoustic responses of the plenums does not indicate the presence of natural frequencies in the frequency range of 400 Hz. Therefore the pulsation may be driven mostly by the flame itself. This may explain why 400 Hz-Mode is only observed at high thermal powers. The amount of energy transferred to the pressure oscillation must be high enough to overcome the damping effects in the plenums at 400 Hz.

As discussed in 4.5.1.5, the characteristic time delay of the flame plays an important role in the process of generating ring vortices. Lohrmann showed in [139] that higher swirl numbers reduce the frequency-dependent phase angle of the flame response to mass flow perturbations. A similar observation was reported in [140]. This explains the strong influence of the swirler mass flow ratio on the 400-Hz mode, since it changes the swirl number and therefore affects the characteristic time delay of the flame.

### 4.5.3 750-Hz Mode

The 750-Hz mode is the second major combustor mode of the SBS, after the 400-Hz mode, since it also reaches pressure amplitudes  $> 150$  dB. At a swirler mass flow ratio of  $L = 1.6$ , these high pressure amplitudes are observed at  $P_{th} = 30$  kW,  $\phi = 0.85$  (Figure 4.51). At  $P_{th} = 25$  kW, the pressure spectra in the SBS show a dominant peak at around 680 Hz. Considering the similar frequency range of this mode and the fact that it also reaches its maximum amplitudes at high equivalence ratios, this peak may represent an equivalent oscillation to the 750-Hz mode at  $P_{th} = 30$  kW.

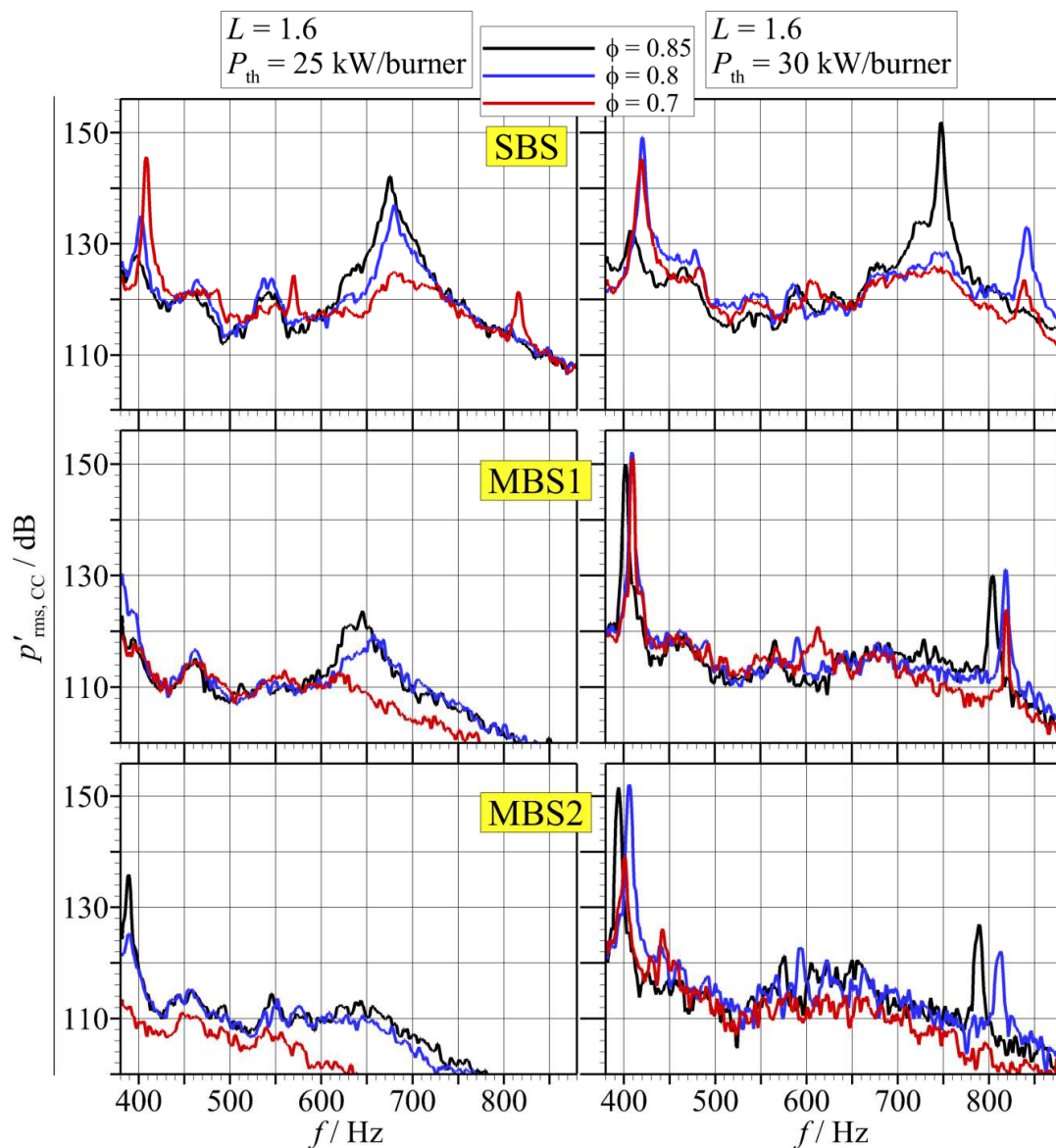


**Figure 4.51. SBS, MBS1, MBS2,  $L = 1.6$ : Pressure and OH\*-intensity oscillations in the combustion chamber (CC) at  $P_{th} = 25$  kW/burner and 30 kW/burner,  $\phi = 0.85, 0.8, 0.7$**

Unlike the 400-Hz mode, the 750-Hz mode is not excited in the MBSs. The peaks at  $\sim 800$  Hz represent a harmonic oscillation to the 400-Hz mode. In the MBS1 at  $P_{th} = 25$  kW/burner, a dominant mode is observed at 660 Hz, which demonstrates a similar behaviour to the mode at 680 Hz in the SBS, since its amplitude increases with  $\phi$ . The maximum amplitudes have values around 122 dB, which is considerably smaller than the maximum amplitudes in the SBS.

Figure 4.52 shows the pressure spectra in the frequency range of the 750-Hz mode for all combustor setups at  $P_{th} = 30$  kW/burner,  $\phi = 0.7, 0.8, 0.85$  for  $L = 1.2, 1.6, 2.0$ . In the SBS at  $L = 1.2$ , the oscillation of the 750-Hz mode is strongly attenuated. This is also the case at  $L = 2.0$ , except for  $\phi = 0.85$ , where the 750-Hz mode features an amplitude of around 140 dB. In the MBSs, a dominant peak in the frequency range of the 750-Hz mode is not observed at  $L = 1.2, 2.0$ .

The spectra of the acoustic responses in the plenums do not show strong responses in the corresponding frequency range (Figure 4.53). This indicates that the 750-Hz mode is mainly driven by an increased thermoacoustic flame response.

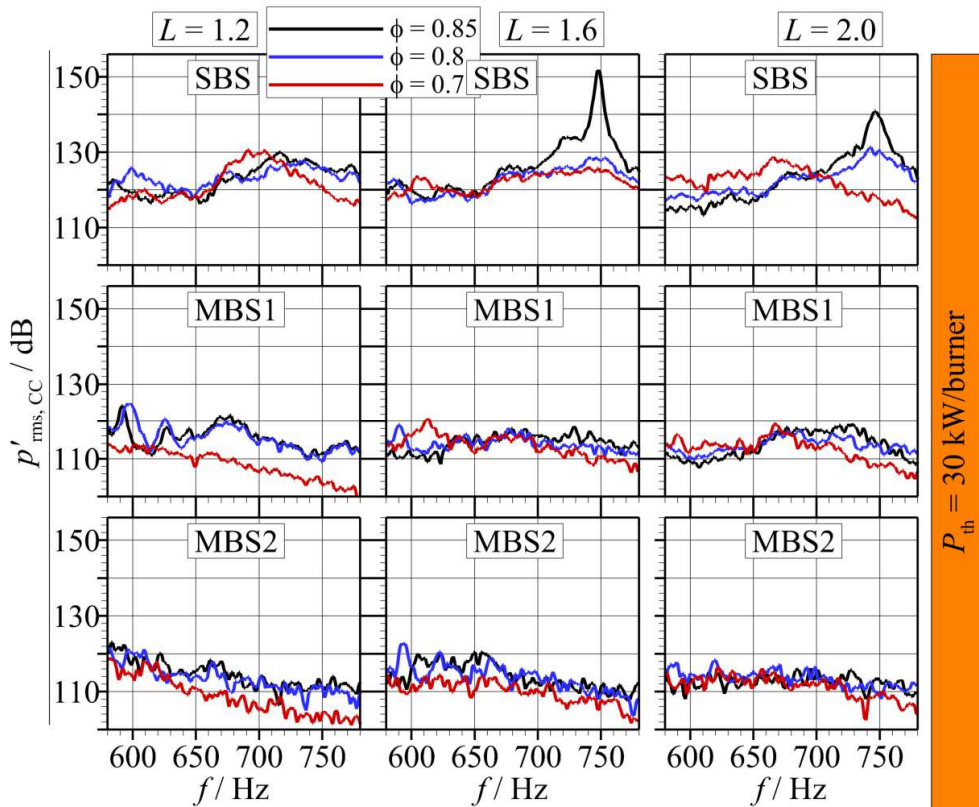


**Figure 4.52. SBS, MBS1, MBS2,  $L = 1.2, 1.6, 2.0$ : Pressure oscillations in the combustion chamber (CC) at  $P_{th} = 30$  kW/burner,  $\phi = 0.85, 0.8, 0.7$**

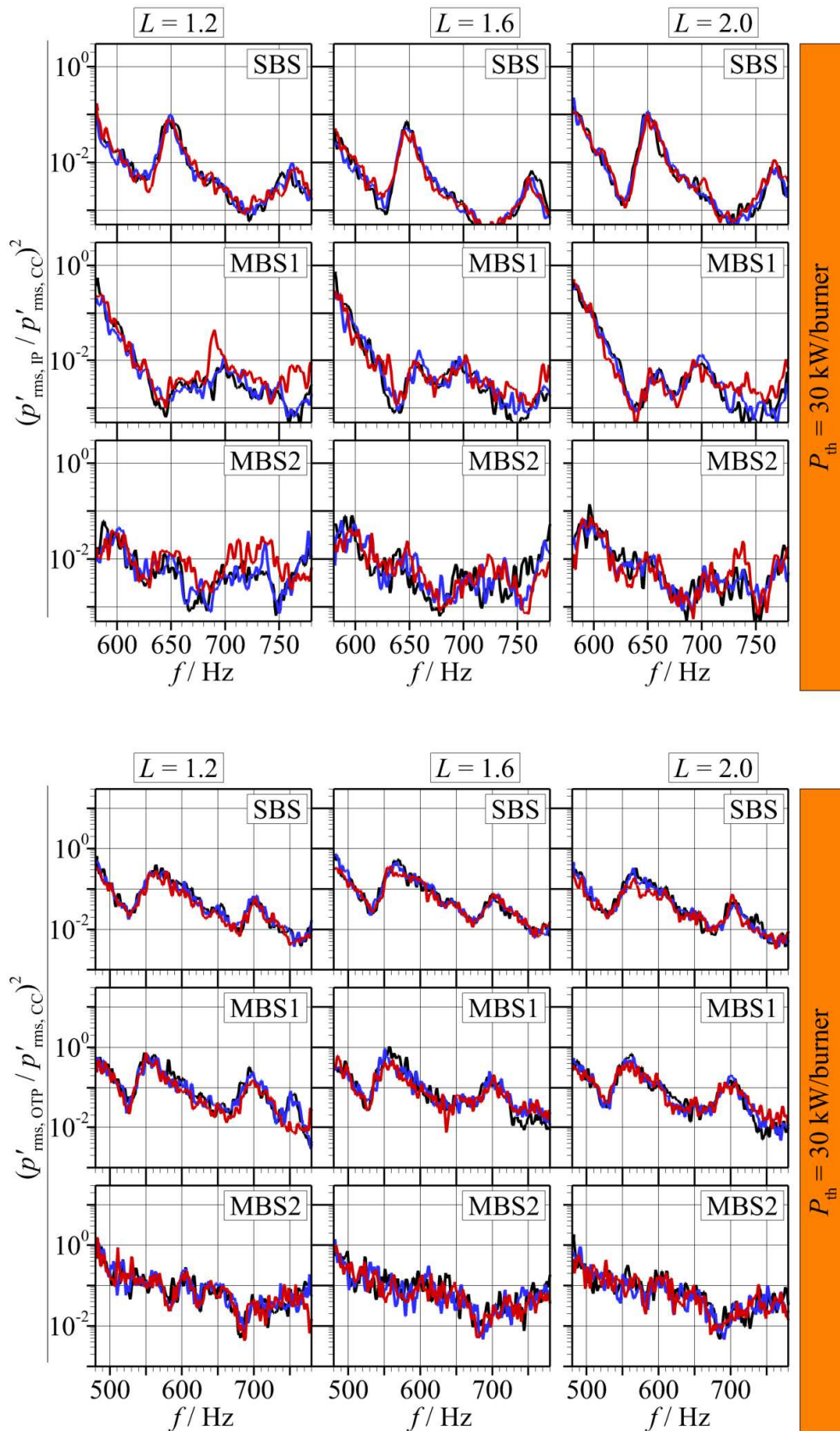
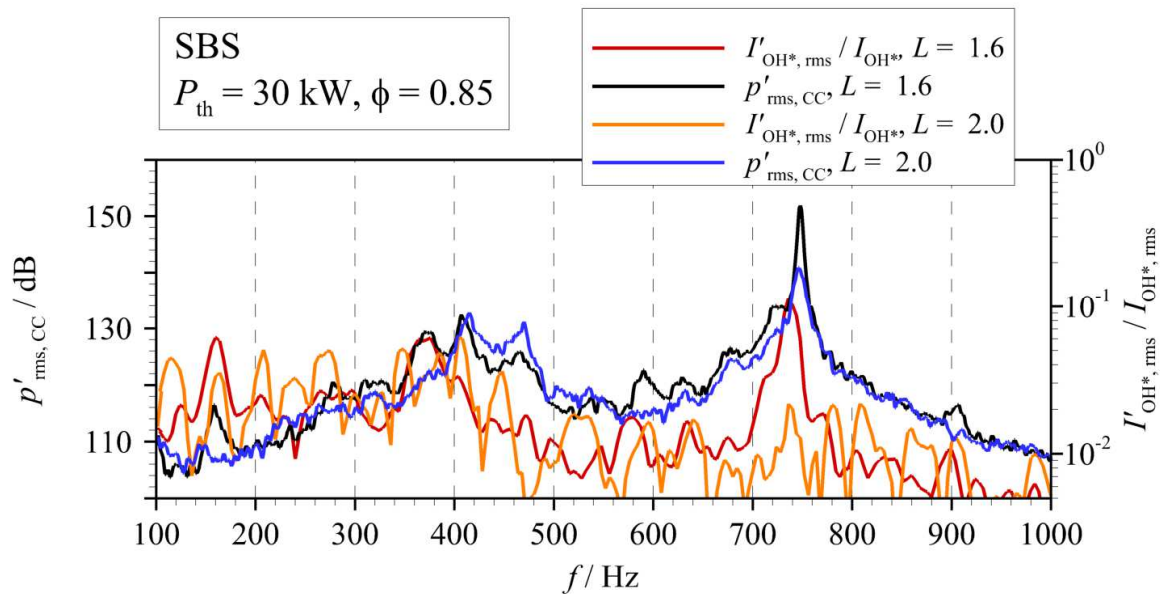


Figure 4.53. SBS, MBS1, MBS2,  $L = 1.2, 1.6, 2.0$ : Acoustic responses in the inner plenum (IP) and the outer plenum (OP) at  $P_{\text{th}} = 30 \text{ kW/burner}$ ,  $\phi = 0.85, 0.8, 0.7$

#### 4.5.3.1 OH\*-Intensity Responses to the 750-Hz Mode and Estimation of the Helmholtz-Resonator Frequency of the Combustion Chamber

The spectra of the OH\*-intensity oscillations for the OP  $P_{th} = 30$  kW,  $\phi = 0.85$ ,  $L = 1.6$ , illustrate that the 750-Hz mode represents the dominant mode in the pressure and the OH\*-intensity spectrum. In Figure 4.54, they are shown together with the spectra at  $L = 2.0$ . Although the pressure amplitude of the 750-Hz mode is still relatively high with a value of  $\sim 140$  dB at  $L = 2.0$ , a significant decrease in the OH\*-intensity amplitude is observed. This indicates that comparably small heat release oscillations can be sufficient in order to generate high pressure amplitudes of the 750-Hz mode.



**Figure 4.54. SBS,  $L = 1.6, 2.0$ : Pressure and OH\*-intensity oscillations in the combustion chamber (CC) at  $P_{th} = 30$  kW/burner,  $\phi = 0.85$**

The high-speed OH\*-images also show the formation of ring vortices in the combustion chamber. However, in comparison to the ring-vortex formation observed for the 400-Hz mode, the flame remains much more compact and the ring-vortices start to form near the bottom wall of the combustion chamber (Figure 4.55). The flame only slightly oscillates in the axial direction. The frequency-locked averaged images for the 750-Hz mode shown in Figure 4.56 corroborate the observations made for the high-speed images, as only a slight stretching of the flame towards the combustion chamber exit is visible. The biggest difference between the images represents the level of OH\*-intensity, which reaches its maximum at  $\phi = 0^\circ$ , where the flame shows the maximum expansion.

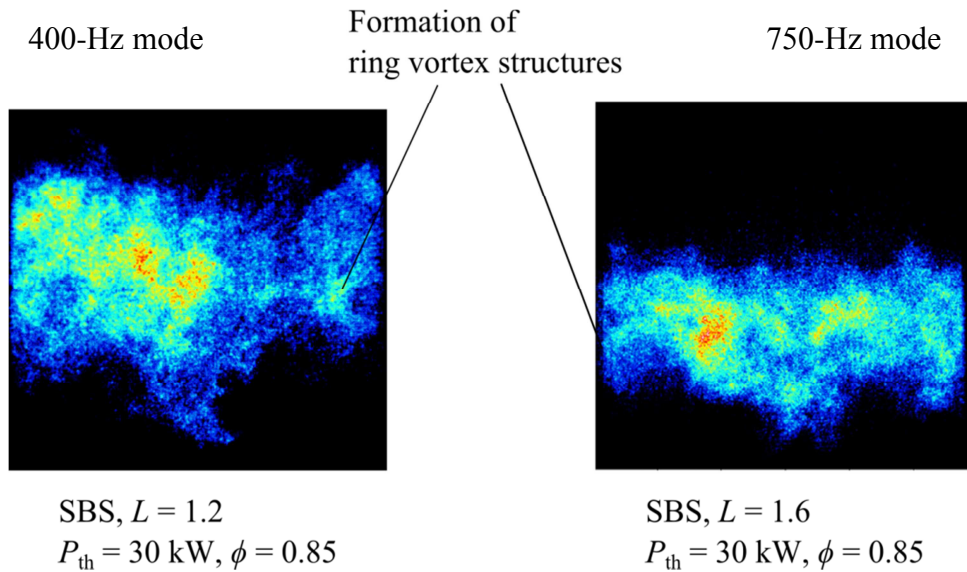


**Figure 4.55. SBS,  $L = 1.2/1.6$ : Comparison of the ring-vortex formation in the SBS associated with the 400-Hz mode and the 750-Hz mode at  $P_{th} = 30$  kW,  $\phi = 0.85$**

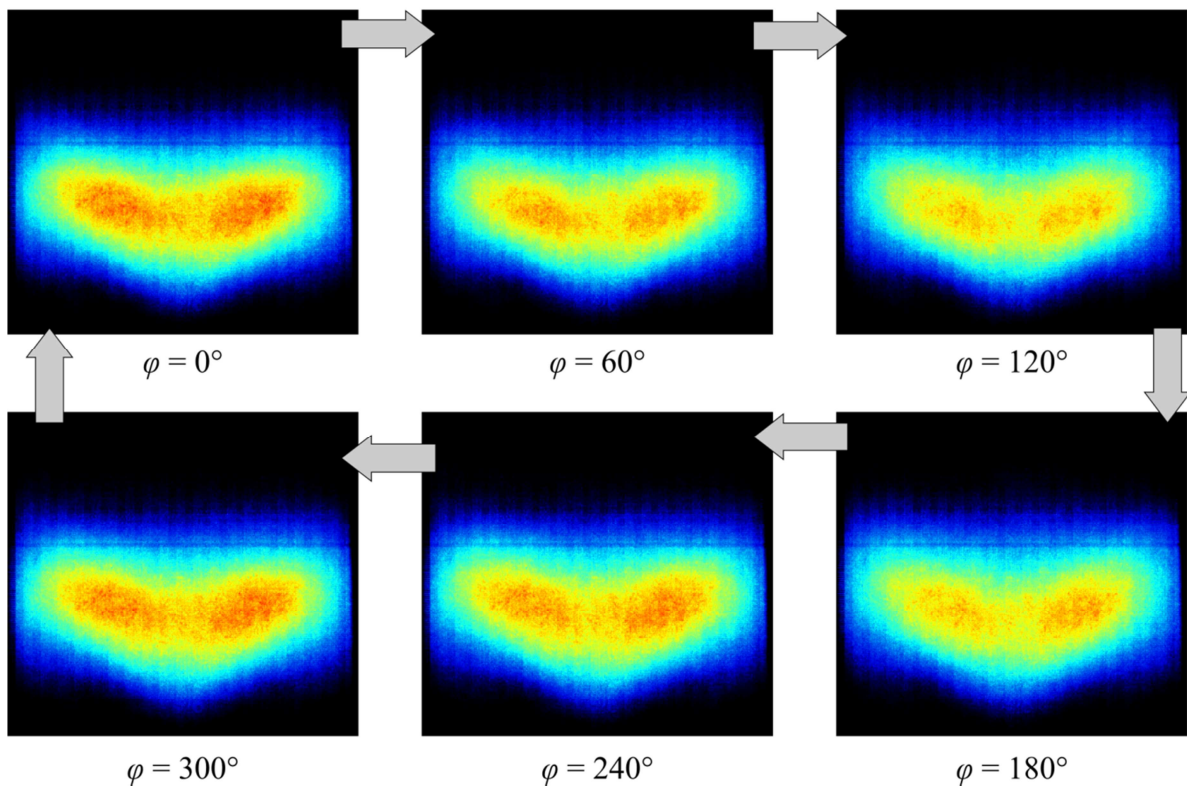


**Figure 4.56. SBS,  $L = 1.6$ : Oscillation cycle of the OH\*-intensity at 750 Hz at  $P_{th} = 30$  kW,  $\phi = 0.85$**

Although the high-speed recording images also show the formation of ring-vortex structures during the oscillation of the 750-Hz mode, the excitement mechanism of 750-Hz mode seems to differ from that of 400 Hz mode. High pressure amplitudes of the 400-Hz mode are usually accompanied by very intense OH\*-intensity oscillations. As discussed in the beginning of this section, this is not always the case for the 750-Hz mode. A reason why a comparably small heat release oscillation can sustain a combustion instability with a very high pressure

amplitude may be an increased acoustic response of the combustion chamber due to a natural frequency. A standing quarter-wave in the axial direction of the combustion chamber would have a frequency of approximately 1200 Hz at typical conditions ( $c_0 = 850$  m/s), which is not in the range of the frequency of the 750-Hz mode. Eigenmodes of cavities which feature lower frequencies than quarter-wave eigenmodes are usually Helmholtz-Resonator modes. Figure 4.57 shows the Helmholtz-Resonator frequency of the combustion chamber depending on temperature. A constant, homogenous temperature field in the combustion chamber is assumed and the Helmholtz-Resonator frequency is calculated using Equations (3.3) and (3.4). A calculation of the equilibrium temperature with CHEMKIN under atmospheric conditions ( $p_0 = 1$  bar,  $T_0 = 293$  K) gives a value for the equilibrium temperature of approximately  $T_{eq} = 2080$  K (including the products of dissociation reactions  $H_2$ , CO) for a mixture of  $CH_4$  and air with an equivalence ratio of  $\phi = 0.85$ .

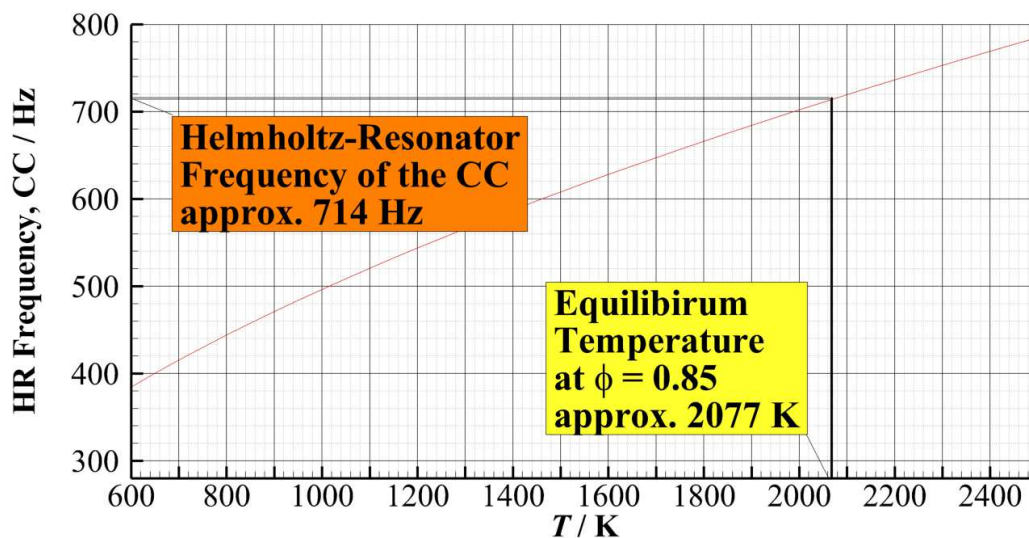


**Figure 4.57. Helmholtz-Resonator frequency of the combustion chamber (CC) in the SBS dependent on the mean temperature**

The resulting value of  $\sim 714$  Hz for the Helmholtz-Resonator frequency is in the range of the typical frequencies of the 750-Hz mode. The effects of the nozzle outlet are neglected in this calculation, as well as the non-stationary, and most likely not homogeneous temperature field inside the combustion chamber.

The coupling of the flame oscillation with the Helmholtz resonance in the combustion chamber in the range of  $\sim 714$  Hz would explain why the relatively small heat release oscillations in the frequency range of 750-Hz mode are sufficient to sustain the pressure oscillation observed at  $P_{th} = 30$  kW,  $\phi = 0.85$ ,  $L = 2.0$ . Note that calculating the Helmholtz-Resonator frequencies of the combustion chambers of the MBSs according to Equations (3.3) and (3.4) leads to values similar to the SBS ( $\sim 700$  Hz). The 750-Hz mode is possibly damped in the MBSs due to different characteristics of the thermoacoustic flame response in the MBSs.

In [141] two possible feedback mechanisms between the Helmholtz-Resonator pressure oscillation and the flame's heat release are discussed by Thring which may sustain a combustion instability induced by a Helmholtz-Resonator oscillation. In the first feedback loop described by Thring, the overall pressure increase in the combustion chamber brings the flame front closer towards the nozzle exit and increases the percentage of the combustion chamber volume which is occupied by hot reaction products. As a result, the temperature in the combustion chamber increases and the additional expansion of the hot gases causes the pressure to rise even more. In the second mechanism, the combustion-induced expansion of the gases in the combustion chamber overcompensates for the reduced flow rate of unburned fuel-air-mixture and sustains the pressure oscillation.

Both mechanisms can lead to an increase in the overall heat release, since the reaction rate increases with rising temperature inside the combustion chamber and the decreased flow velocities may lead to an increase in the flow region where the flame is able to stabilize, which in turn results in an increase in the flame surface area. When the pressure in the combustion chamber decreases again, it causes the reverse effects. The flow rate into the combustion chamber increases and an augmented amount of the fuel-air-mixture enters the combustion chamber and starts to react after a characteristic time delay. The rising pressure in the combustion chamber increases the combustion intensity and the next oscillation cycle starts. Therefore the oscillating pressure causes an oscillating heat release, which further intensifies the pulsation and excites an intense combustion instability, when the phase angle between pressure and heat release oscillation does not exceed  $90^\circ$  (Rayleigh's Criterion). Since the combustion chamber pressure directly affects the heat release rate, it is most likely that for a Helmholtz-Resonator oscillation of the combustion chamber the Rayleigh-Criterion is fulfilled [103].

#### **4.5.4 Pressure Oscillations in the Non-Reactive Flow**

Measurements of pressure oscillations in the non-reactive flow were also conducted for the SBS and the MBS2. The corresponding results are discussed in this section.

The analysis of the different combustor modes in the previous chapters indicated that some of the combustor modes are mainly excited due to the presence of natural frequencies in the plenums. Natural frequencies of the different combustor components should also be observed in the spectra of the pressure oscillations of the cold flow. Only the air flows were sent through the combustor while conducting these experiments.

##### **4.5.4.1 Pressure Oscillations in the Non-Reactive Flow in the SBS**

The spectra of the pressure oscillations in the combustion chamber in the non-reactive flow show dominant frequencies in the range of 800-1000 Hz (Figure 4.58). The results indicate that the observed peaks correspond to the same oscillation, whose frequency scales with the flow rate. The peaks associated with the oscillations feature a similar Strouhal-Number in the

range of  $St = 1.11$ - $1.15$ . The tone generated by this oscillation is also very audible. A possible explanation is that the tone is associated with a PVC, which is often found in the swirl flows, or a radial-axial vortex shedding at the nozzle exit, which is typically induced by the PVC. The characteristics of PVCs in the swirl flows are extensively discussed in literature. Some key references are given by [104, 106, 107].

The broadband character of the pressure oscillations in the low-frequency spectrum and the presence of several dominant frequencies in the non-reactive flow in the SBS complicate the characterization of the peaks. In Figure 4.59, the spectra are plotted against the combustor flow rate and the pressure amplitude in the combustion chamber represents the contour variable. The spectra show a pressure oscillation with a Strouhal-Number of about  $St \approx 0.172$ , which is slightly smaller than the Strouhal-Number of LF-Mode2 observed in the reactive flow. Therefore, this mode most likely represents the pressure oscillation of LF-Mode2 in the non-reactive flow. A higher Strouhal-Number for LF-Mode2 in the reactive flow is expected due to the increased temperatures and the augmented velocities induced by the addition of the fuel flow. The spectrum of the pressure oscillations in the inner plenum shows dominant peaks in the frequency range of LF-Mode1 and LF-Mode3. Several additional peaks are observed, which mainly match with the previously discussed acoustic response spectra of the inner plenum, which is also the case for the acoustic response spectra of the outer plenum (Figure 4.60). The spectrum of the outer plenum shows an increased amplitude of the PVC-oscillation because the microphone in the outer plenum is located much closer to the nozzle exit than the one in the inner plenum. In both plenums, the amplitudes of the dominant modes are only slightly affected by the flow rate.

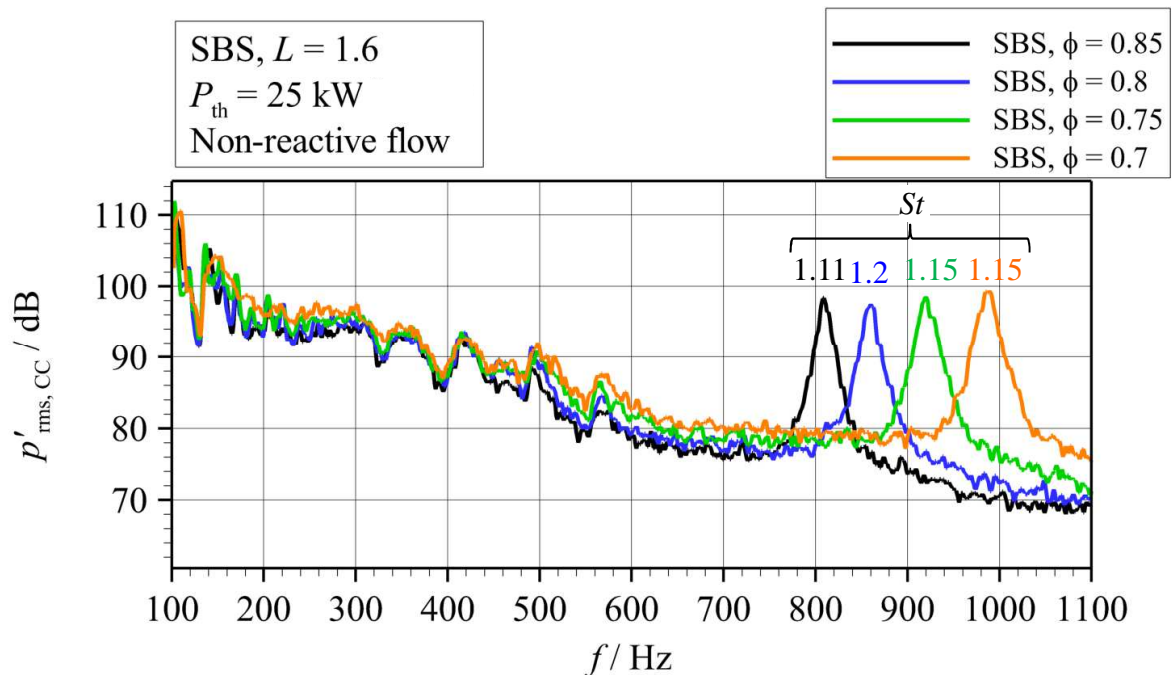


**Figure 4.58. SBS,  $L = 1.6$ : Pressure oscillations in the combustion chamber (CC) in the non-reactive flow at  $P_{th} = 25 \text{ kW}$ ,  $\phi = 0.7, 0.75, 0.8, 0.85$**

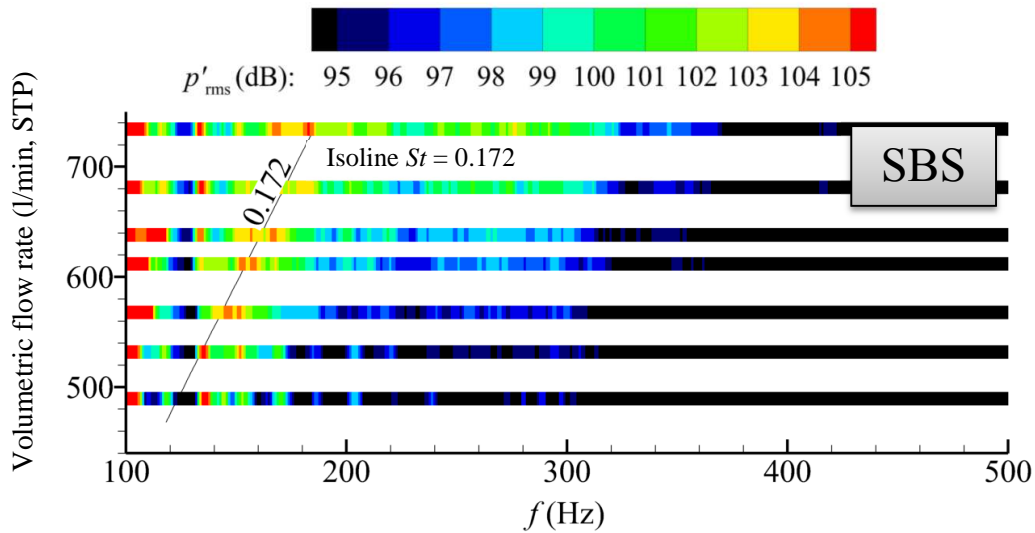


Figure 4.59. SBS,  $L = 1.6$ : Pressure oscillations in the combustion chamber at different volumetric flow rates

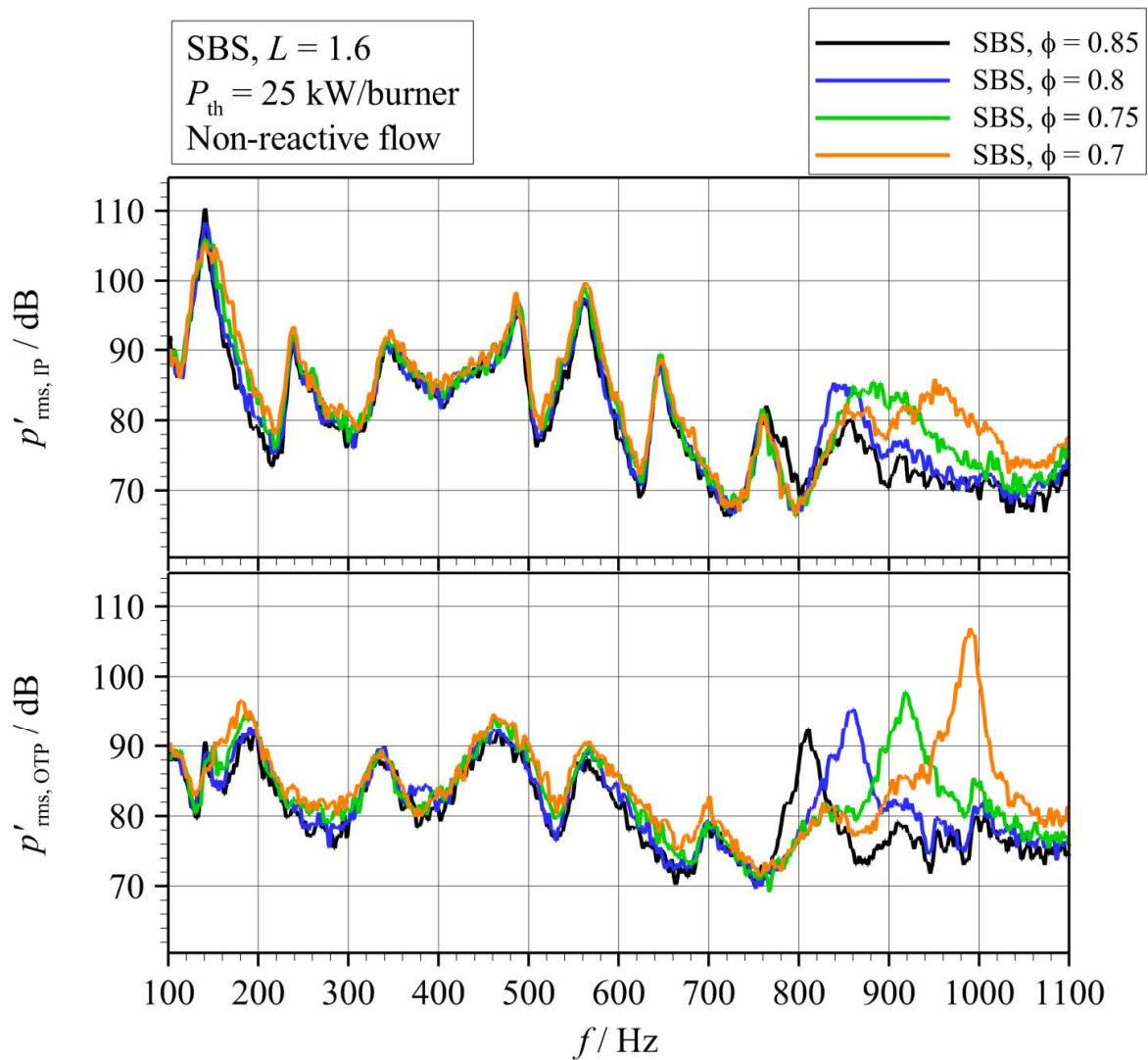


Figure 4.60. Pressure oscillations in the inner plenum (IP) and the outer plenum (OTP) in the non-reactive flow at  $P_{th} = 25$  kW,  $\phi = 0.7, 0.75, 0.8, 0.85$

## 4.5.4.2 Pressure Oscillations in the Non-Reactive Flow in the MBS2

Figure 4.61 illustrates that the mode with the flow rate-dependent frequency observed in the SBS in the frequency range between 800 Hz and 1000 Hz is also present in the combustion chamber of the MBS2. The fact that two peaks with slightly different frequencies are observed may be the result of slight differences between the single swirl flows. These differences are possibly caused by small geometrical variances between the swirlers, since they were manufactured without CNC. The Strouhal-Numbers for the different OPs shown in Figure 4.61 represent the average of the Strouhal-Numbers of the respective peaks.

In Figure 4.62, the isoline  $St = 0.17$  marks the peaks that supposedly correspond to LF-Mode2. Similar to the spectra of the SBS, the presence of numerous peaks in the low-frequency range makes a clear identification of the observed peaks difficult. The Strouhal-Number of  $St \approx 0.17$  is similar to the one observed in the non-reactive flow in the SBS and also close to the Strouhal-Number  $St \approx 0.21$  of LF-Mode2 observed in the reactive flow.

The major difference from the SBS is seen in the 190-Hz mode, which is the dominant mode in the spectrum of the inner plenum (Figure 4.63). The high amplitude of the 190-Hz mode in the pressure spectra of the non-reactive flow corroborates the assumption that the mode represents a natural frequency of the inner plenum of the MBS2.

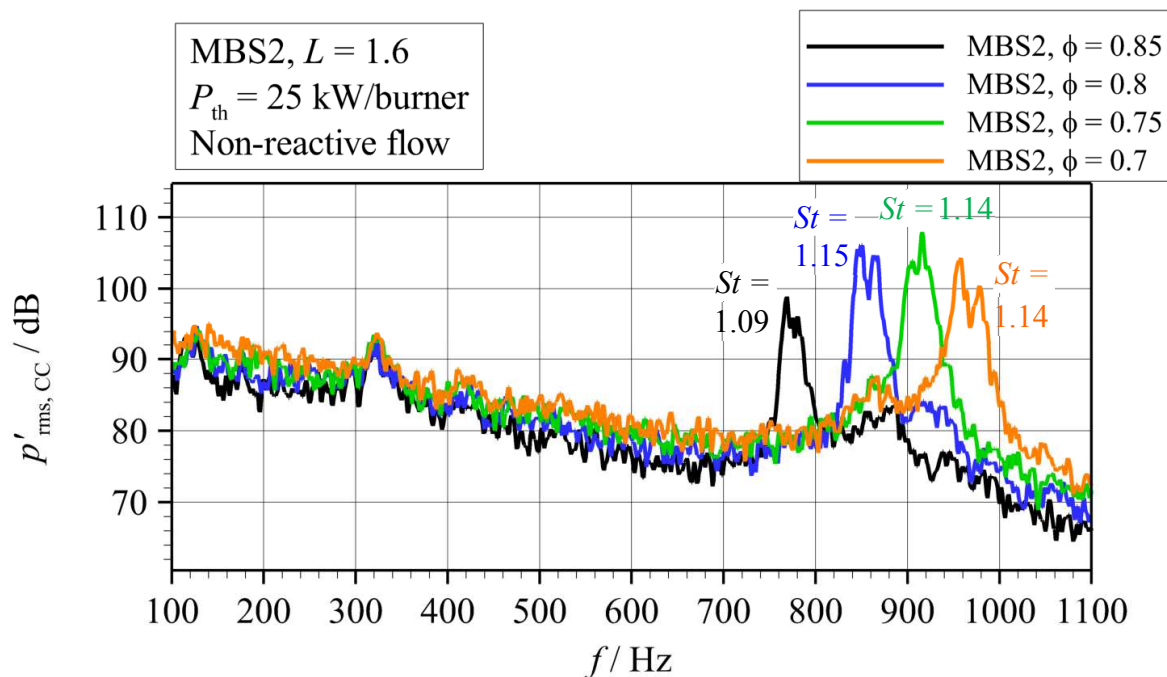


**Figure 4.61. MBS2,  $L = 1.6$ : Pressure oscillations in the combustion chamber (CC) in the non-reactive flow at  $P_{th} = 25$  kW/burner,  $\phi = 0.7, 0.75, 0.8, 0.85$**

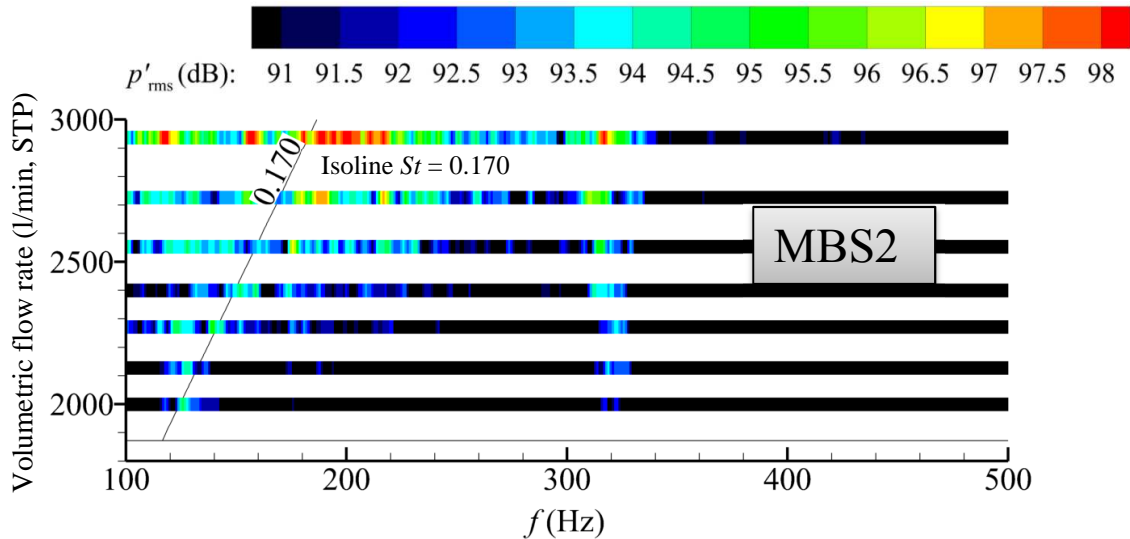


**Figure 4.62. MBS2,  $L = 1.6$ : Pressure oscillations in the combustion chamber (CC) at different volumetric flow rates**

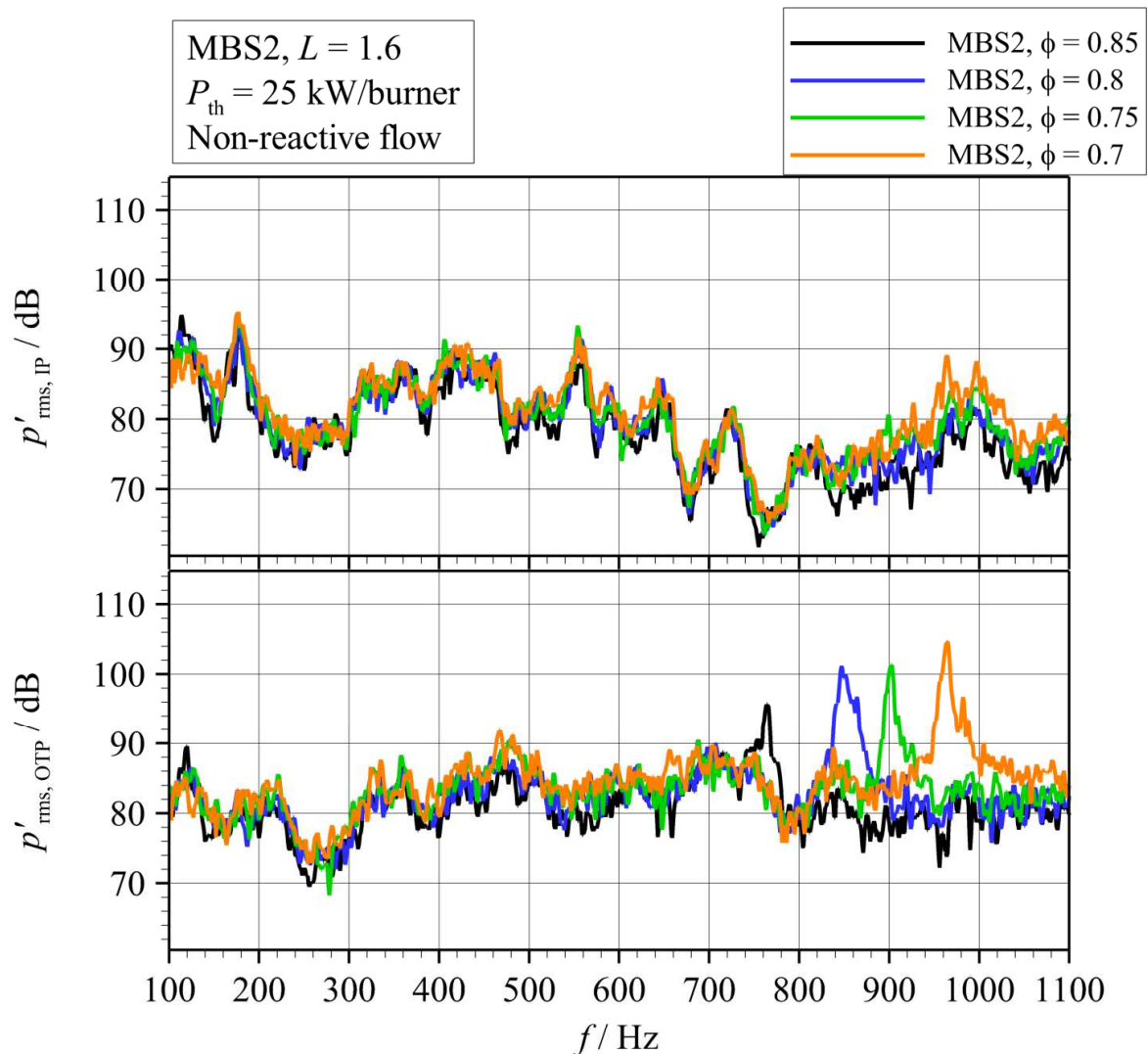


**Figure 4.63. MBS2,  $L = 1.6$ : Pressure oscillations in the inner plenum (IP) and the outer plenum (OTP) in the non-reactive flow at  $P_{th} = 25$  kW/burner,  $\phi = 0.7, 0.75, 0.8, 0.85$**

### 4.5.5 Discussion of the Stability Charts of the Combustor Setups

Figure 4.64 shows the stability charts of the combustor setups at different swirler mass flow ratios  $L$ . The symbols mark OPs, where unstable combustor modes with pressure amplitudes of  $p'_{\text{rms}} > 130$  dB are observed. The different colours and sizes of the symbols indicate the frequency range and the amplitude range of the observed modes.

In the SBS, it is clearly visible that with rising swirler mass flow ratio, unstable combustor modes tend to emerge at lower equivalence ratios and thermal power. The augmentation of the swirl number due to the increased swirler mass flow ratio apparently widens the thermoacoustic response spectrum of the flame. In addition, the higher swirl intensity seems to increase the probability that combustor modes with frequencies between  $f = 600\text{-}900$  Hz are excited in the SBS. These findings comply with observations discussed in [20], where the combustion dynamics of a variable swirl number system are investigated. The results presented in this work indicate that increasing the swirl intensity broadens the response spectrum of the flame and decreases the phase angle between mass flow oscillations at the nozzle outlet and the corresponding flame response. This can be explained by an augmented reaction density in flames with higher swirl intensity, which leads to a shorter flame length [15]. Therefore, increasing the swirl intensity augments the critical mass flow perturbation frequency which results in an unstable phase angle of the flame response.

At  $L = 1.2$  in the SBS, no combustor modes with amplitudes  $> 140$  dB are observed for the frequency range 600-900 Hz. On the other hand, low-frequency combustor modes with amplitudes  $> 130$  dB are generated, which is not the case at  $L = 1.6, 2.0$ . Similar to the influence of the swirl number on the phase angle of the flame response, lower swirl intensities increase the characteristic time delay of the flame. As a consequence, a phase angle of the flame response which is sufficient to generate unstable combustor modes is reached at lower frequencies. This may explain why intense low-frequency modes are only observed at  $L = 1.2$ .

When comparing the stability chart of the SBS and the MBSs at  $P_{\text{th}} = 30$  kW/burner, it is noteworthy that the combustor dynamics of the SBS at  $L = 1.2$  and the MBSs at  $L = 1.6$  show many similarities regarding frequency and intensity of the observed combustor modes. In all combustor setups, the 400-Hz mode features amplitudes of  $> 140$  dB at  $\phi = 0.85, 0.8, 0.75, 0.7$ , whereas at  $\phi = 0.65$ , a low-frequency mode is excited. The equivalent flame characteristics may be explained by the investigations made by Hirsch et al. in [27]. Based on the observations made in [142], Hirsch et al. argue that the observed differences in the flow field between the single-burner combustor and the annular combustor are caused by different flow regimes of the swirl jet. In the first regime, where the ratio of the combustion chamber area and the area of the nozzle exit  $A_{\text{CC}}/A_{\text{nz}}$  is sufficiently high, the flow field in the combustion chamber resembles that of a free swirl jet. When the ratio  $A_{\text{CC}}/A_{\text{nz}}$  is decreased to a critical value, the swirl jet angle increases significantly and attaches to the wall. The swirl

flow has switched from the “free jet” regime into the “wall jet” regime. The wall jet features a wider inner recirculation zone combined with smaller outer recirculation zones. The critical value of the ratio  $A_{CC}/A_{nz}$  that leads to the switch from the free jet regime to the wall jet regime depends on the effective swirl number of the swirl jet. In the annular combustion chamber the swirl intensity is reduced due to the momentum exchange between the adjacent swirl jets. These have opposite swirl directions with respect to the axis of the swirl jet considered, which reduces the angular momentum flux entrained in the ORZs. Thus, the swirl jets in the annular combustion chamber switch to the free jet regime for lower values of  $A_{CC}/A_{nz}$ .

Therefore the combustor dynamics of the SBS at  $L = 1.2$  are similar to those of the MBSs at  $L = 1.6$  because the corresponding swirl flows are possibly all in the free jet regime. In the MBSs, this is induced by the missing side walls and the momentum exchange between the adjacent swirl jets. In the SBS, the swirl flow is in the free jet regime as a result of the decreased swirl intensity due to the reduction of swirler mass flow ratio to  $L = 1.2$ .

However, the results for the MBSs at  $L = 1.2$  indicate that the differences in the thermoacoustic behaviour cannot only be caused by two different flow regimes, since the combustion dynamics in the MBSs are strongly affected by the swirler mass flow ratio, although the swirl jets may feature the characteristics of a free jet. It is clearly visible, that low-frequency combustor modes are much more frequently observed at  $L = 1.2$  than at  $L = 1.6$ . The decrease of the swirler mass flow ratio in combination with the multiple-burner arrangement possibly leads to a significant decrease in the swirl intensity in the combustion chamber flow. This results in an increased characteristic time delay of the flame, which in turn results in stronger responses of the flame to low-frequency mass flow oscillations.

It is concluded that the main reason for the observed differences in the combustor dynamics between the SBS and the MBSs is the momentum exchange between the adjacent swirl jets in the MBSs which results in a decrease in the swirl intensity. The lower swirl intensities lead to higher characteristic time delays of the flame in the MBSs and stronger flame responses to low-frequency perturbations. The effect that the multiple-burner arrangement reduces the swirl intensity in the combustion chamber flow may be even more significant in the MBS2, as all swirl jet have two adjacent swirl jets. As a result, low-frequency modes are observed even more frequently in the MBS2 than in the MBS1.

These findings may also explain why increasing the swirler mass flow ratio to  $L = 2.0$  seems to only slightly affect the combustion dynamics in the MBSs. The increase in swirl intensity induced by the increased mass flow through the outer swirler leads to a wider swirl jet angle near the nozzle exit and possibly increases the burner-to-burner flow interaction. However, this may result in a further decrease of the entrained angular momentum flux and may compensate for the effect on the increased swirl intensity at  $L = 2.0$ .

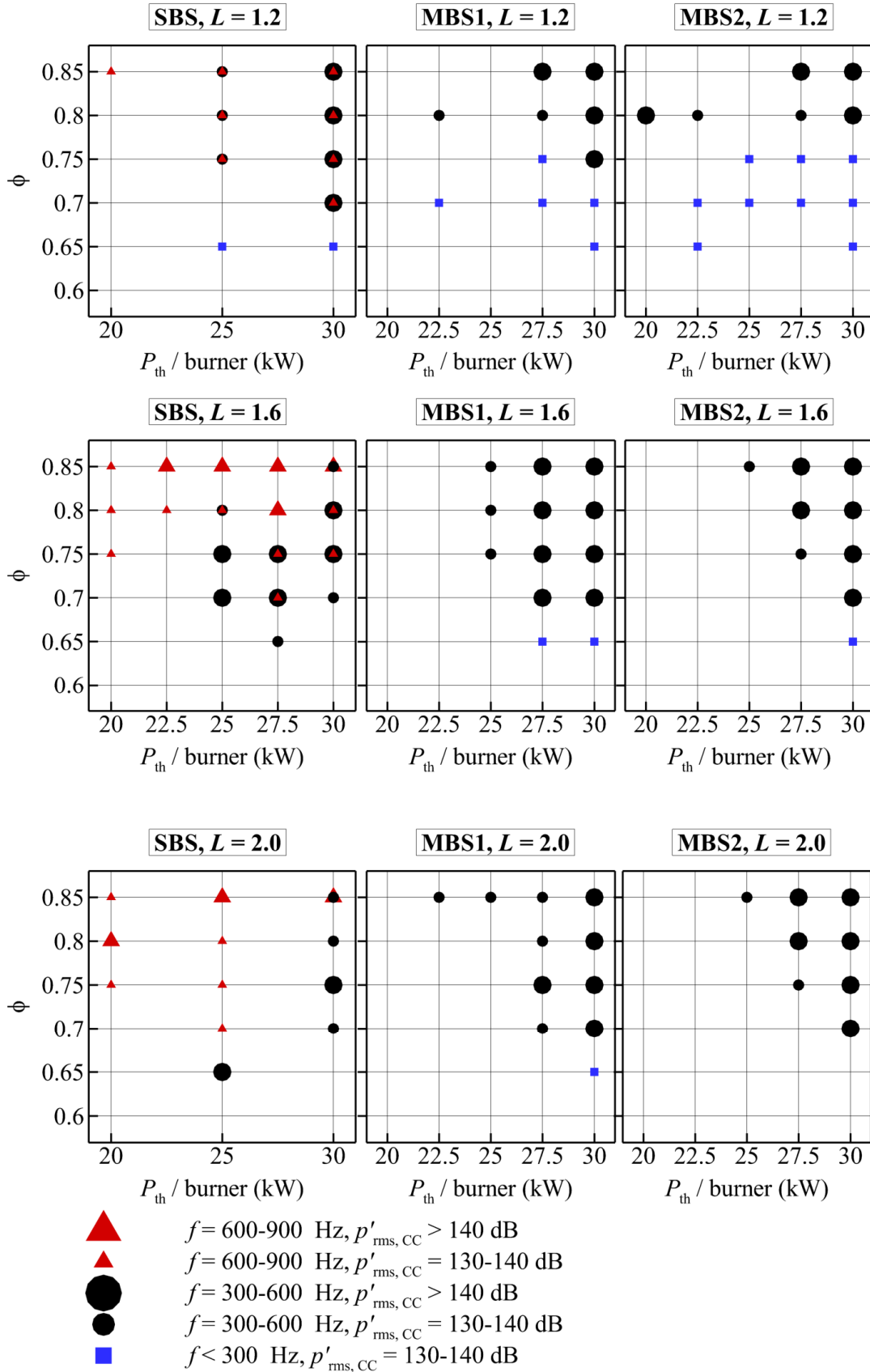


**Figure 4.64. Stability charts of the combustor setups for  $L = 1.2, 1.6, 2.0$ . The symbols mark OPs, where unstable combustor modes with pressure amplitudes of  $p'_{\text{rms,CC}} > 130 \text{ dB}$  are observed in the combustion chamber. The different colors and sizes of the symbols indicate the frequency range and amplitude range of the modes.**

## 5. Numerical Investigations

This chapter is devoted to the numerical investigations, which were performed for the SBS and the MBS2. After a brief description of the flow solver, the computational grids and the boundary conditions that were used are described. In the subsequent sections, the investigated OPs are introduced and the results of the simulations that were performed are described.

### 5.1 Numerical Setup

#### 5.1.1 Flow Solver

The simulations were performed with the open source software package OpenFOAM 2.1.1. It contains software libraries which allow for the development and implementation of numerical solvers for continuum mechanics problems. Numerous CFD-solvers for specific applications are already implemented which employ the finite-volume method with a cell-centred storage arrangement. The solver used in the LES-studies conducted in the scope of this work uses a fully implicit compressible formulation of the balance equations shown in 2.1 and the pressure-implicit split operator (PISO) technique for the pressure correction. The convective and diffusion fluxes were discretised using second order schemes based on central differencing. The Crank-Nicholson scheme was used for the discretization of time. To increase the stability of the computation, the Crank-Nicholson scheme was blended with the Euler scheme using a blending factor of 0.6, which still provides second-order accuracy. For detailed information about the applied numerical techniques, the reader is referred to literature [143, 144].

The Smagorinsky-Model was used to model the subgrid-scale turbulence, with a constant value for the Smagorinsky constant of  $C_s = 0.1$ . The turbulent Schmidt and Prandtl-Numbers were set to constant values of  $Sc_t = Pr_t = 0.7$ . The computational grid was used for the LES-filtering, where the filter width  $\Delta$  was calculated using the cubic root of the cell volume.

As discussed in 2.3.5, the UTF-C-Model was used to model the turbulent flame. Therefore, in addition to the balance equations of momentum, mass and enthalpy, balance equations are also solved for the mixture fraction, the mixture fraction variance and the reaction progress variable. The chemistry look-up table was built based on computations of a laminar 1D-premixed flame at atmospheric conditions ( $p = 1 \text{ bar}$ ,  $T = 293 \text{ K}$ ). In the simulations,  $\text{CH}_4$  was used instead of natural gas. The impact of the different fuels in the experiments and the LESs should be very small, due to the high percentage of methane ( $> 90 \%$ ) in the natural gas used in the experiment.

### 5.1.2 Geometric Model and Computational Grid

Most parts of the geometrical model for the SBS (Figure 5.1) were derived from the 3D-CAD model of the SBS. The computational grid for the simulation of the SBS shown in Figure 5.2 was constructed using the commercial software ANSYS IcemCFD and contains about 6.5 million nodes. The grid of the SBS was built as a block-structured grid and the domain contains about 6500 blocks. The Fluent V6 output interface of IcemCFD was used to output the grid as an unstructured grid. The “fluent3DMeshtoFoam” converter included in the OpenFOAM package was applied to convert the Fluent V6 mesh to the OpenFOAM mesh format. In order to avoid a boundary condition at the outlet of the combustion chamber, additional geometry was added to the CAD model. The inlets were set at the location where the perforated plates are located in the SBS. The boundary conditions are discussed in detail in the next section.

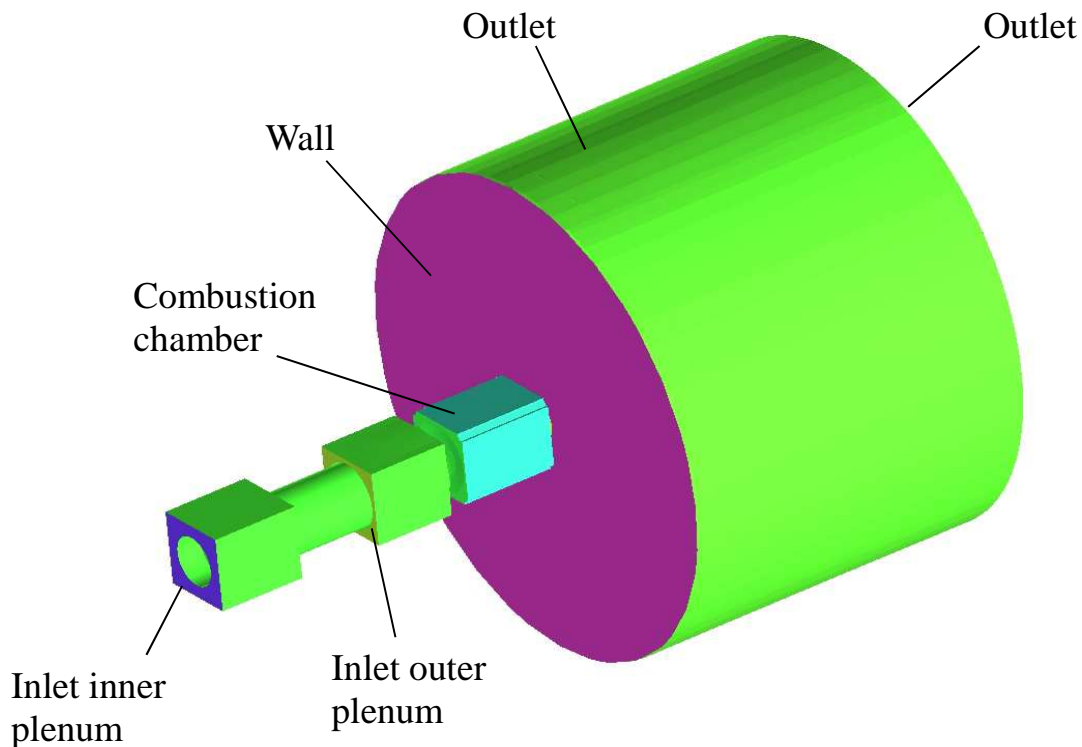


**Figure 5.1. Geometry of the SBS used for the LESs**

In the SBS the 60 fuel inlets are discretised with 16 cells and the grid is refined in the region where the fuel jets mix with the air flow. This was done to capture the main physics of the mixing process of fuel and air. The fuel enters the computational domain upstream of the fuel injection holes at the modelled section of the fuel manifold. The grid resolution is reduced in the combustor plenums in order to reduce the necessary computational resources.

Figure 5.3 shows the geometrical model for the MBS2. The volume of the mesh region between the outlet of the domain and the combustion chamber outlet is reduced and is of quadratic shape. This is a result of the construction process of the MBS2-grid. In order to

create the grid for the MBS2, the grid for the SBS was modified and rotated. In addition to the already mentioned removal of the mesh refinement, the volumes of the interface regions between the single-burners were added and the shape of the “atmosphere” mesh region was altered from the cylindrical shape to a rectangular shape. The latter modification simplifies the connection of the mesh regions between the combustion chamber outlets and the outlets of the computational domains.

A cut plane of the grid used for the MBS2 is shown in Figure 5.4. The grid for the MBS2 does not feature the refined mesh region. Since it contains about 21 million nodes, it was necessary to increase the possible time step, which still provides a stable running simulation, in order to realize the simulation in an acceptable period of time. Therefore, the grid for the MBS2 is about 30-50 % coarser in the mixing region and the fuel inlets are resolved with 8 cells. Like in the real MBS2, the combustion chambers and the plenums of the single-burners are connected.

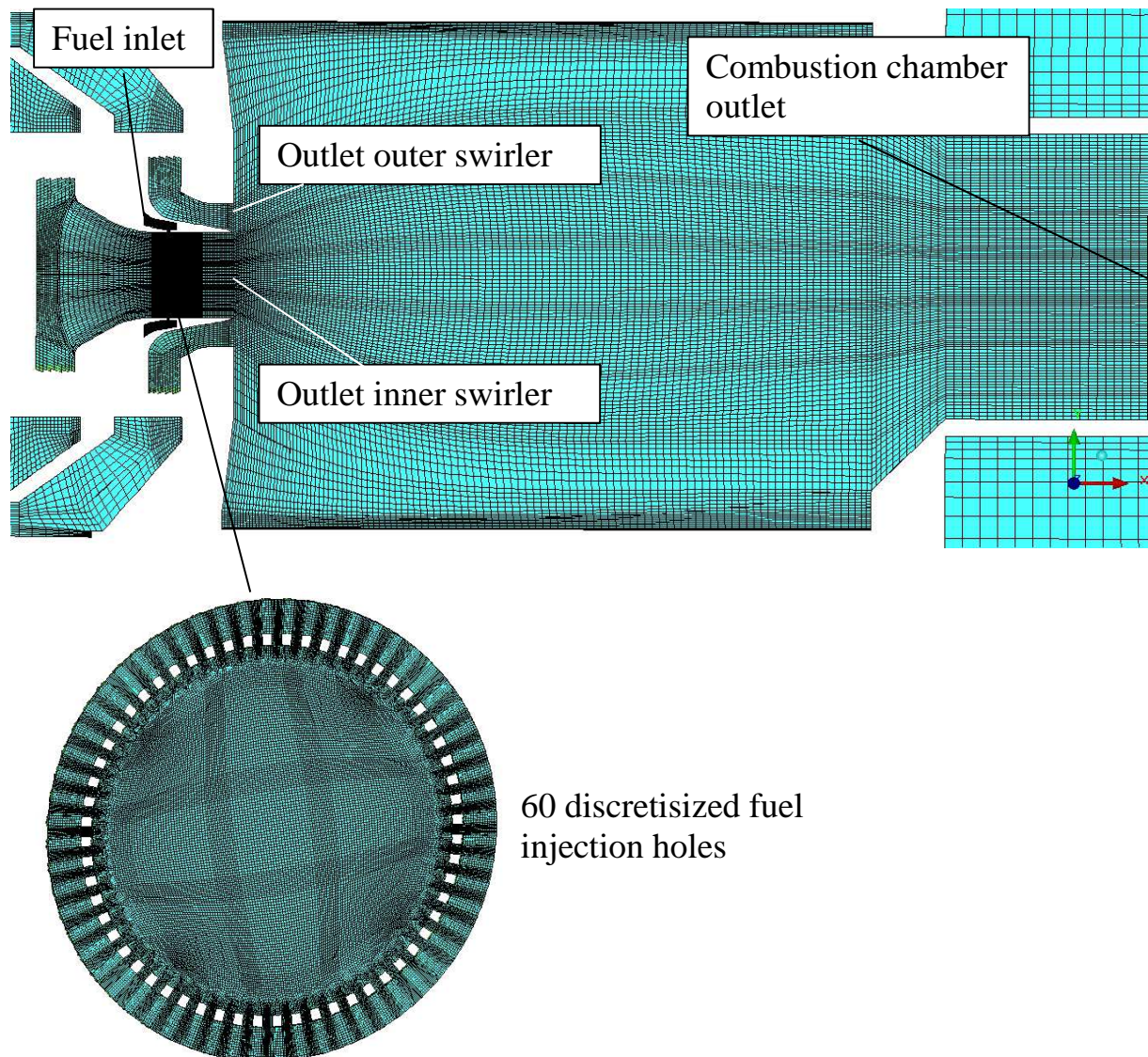


Figure 5.2. Cut plane through the computational grid used for the LESs of the SBS

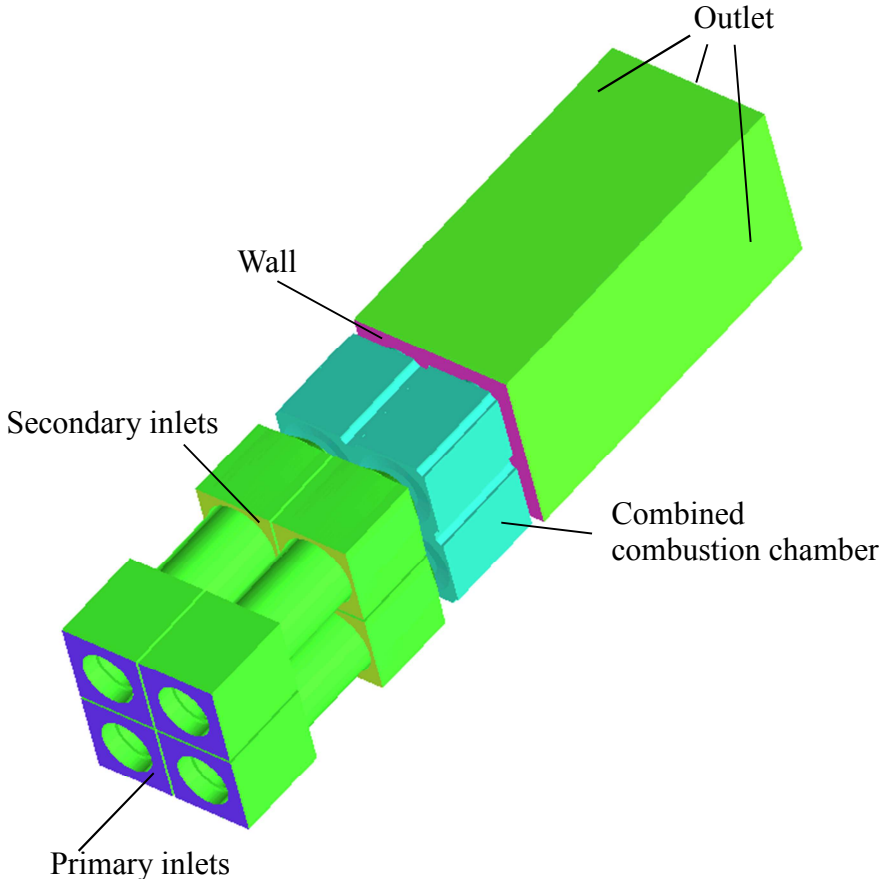


Figure 5.3. Geometry of the MBS2 used for the LESs

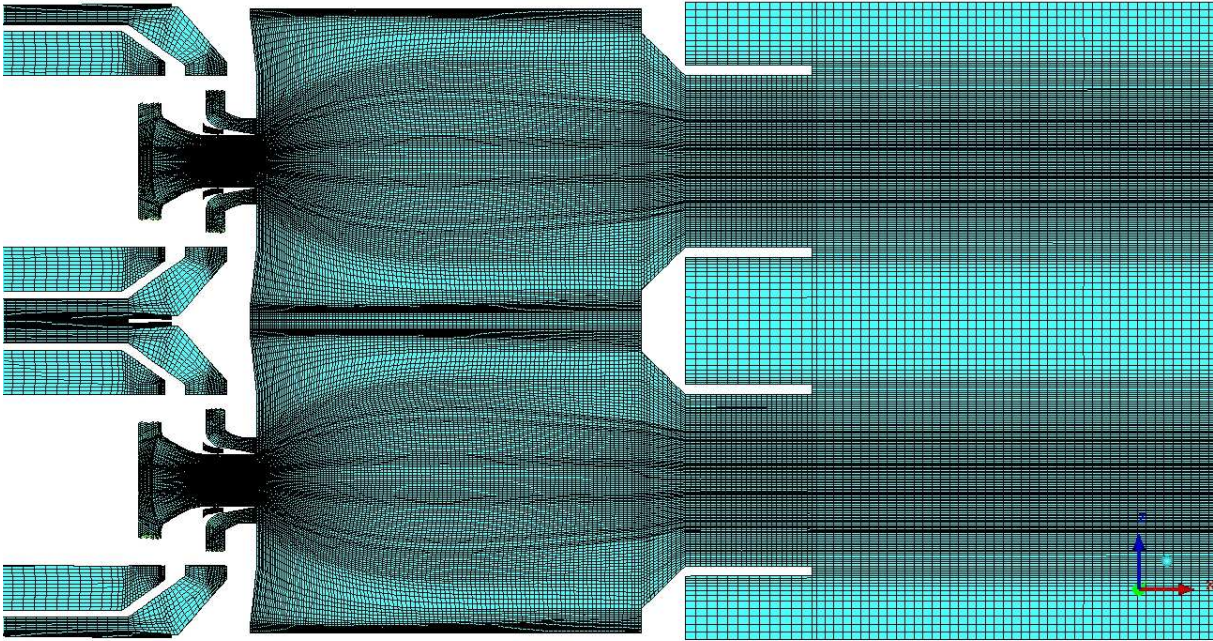


Figure 5.4. Cut plane through the computational grid used in the LESs for the MBS2

### 5.1.3 Boundary Conditions

Performing compressible Large-Eddy Simulation requires using adequate boundary conditions (BCs) for the pressure at the outlets and the inlets. Zero gradient boundary conditions reflect pressure waves, whereas physical outlets and inlets are normally non-reflective. Therefore the application of zero gradient BCs for pressure can lead to pressure oscillations in the computation that are not present in reality. In OpenFOAM, the “waveTransmissive” BC is available, which was used for modelling the outlets. The approach of the “waveTransmissive” BC implemented in OpenFOAM is a simplification of the approach presented in [145]. The calculation of the pressure at the outlet is described in the following [146].

First the velocity of the outgoing pressure wave  $\omega$  is calculated by

$$\omega = u_i \cdot \vec{n} + \sqrt{1/\psi}, \quad (5.1)$$

where  $\vec{n}$  corresponds to the normal vector at the outlet and  $\psi$  denotes the compressibility of the fluid. The velocity of the pressure wave is used to calculate the pressure wave coefficient  $\alpha$  and the relaxation coefficient  $b$ :

$$\alpha = \omega \frac{\Delta t}{\delta}, b = \omega \frac{\Delta t}{l_\infty}, \quad (5.2)$$

where  $\delta$  refers to the cell-face distance coefficient and  $\Delta t$  to the time step. The value of the outlet pressure is then calculated by using the following properties:

$$p_{\text{trans}} = \frac{p_0 + bp_\infty}{1 + b}, \Xi = \frac{1 + b}{1 + \alpha + b}, \quad (5.3)$$

where  $p_0$  is the pressure of the previous time-step and  $p_\infty$  the value of the far-field pressure. To calculate the outlet pressure  $p_{\text{outlet}}$ , the value of  $p_{\text{trans}}$  is relaxed using the relaxation factor  $\Xi$  with the pressure in the cell ( $p_{\text{cell}}$ ) closest to the outlet:

$$p_{\text{outlet}} = \Xi p_{\text{trans}} + (1 - \Xi). \quad (5.4)$$

The values of the pressure  $p_\infty$  and  $l_\infty$  are defined by the user. A higher value of  $l_\infty$  causes the BC to be less reflective. Unfortunately, when the value of  $l_\infty$  is set too high, the BC tends to drift from the value set for the far-field pressure. Thus, the value of  $l_\infty$  has to be adjusted for every specific problem. In the simulations discussed in this work, the value of  $l_\infty$  was set to

1 m, as it was observed that values in the range of the length of the computational domain usually provide good results.

A non-reflective BC for inlets is not implemented in OpenFOAM. A BC with a fixed total pressure is available, which includes the compressibility of the fluid in the calculation of the inlet pressure. However this allows little control over the actual mass flow rate, since no fixed mass flow rate can be set. The modelling of the inlets of the combustor investigated in the present work is even more delicate than the modelling of non-reflective inlets. Perforated plates, similar to the ones installed in the plenums, typically show complex acoustic impedances. This means that their reflection coefficient is frequency-dependent and specific frequencies are damped. In addition, their acoustic impedance is influenced by the mean flow and therefore depends on the operating conditions.

One possibility to deal with the acoustics of perforated plates in simulations is to apply adequate models [132], which are unfortunately not available in OpenFOAM. Another way to circumvent this problem is to resolve the openings of the perforated plates. However, this would significantly increase the demands on the computational grid, resulting in very long computation times. Moreover, this only transfers the problem from the modelling of the perforated plate to the modelling of non-reflective inlet, which, as mentioned above, is also not included in OpenFOAM. Consequently, it was decided to place the numerical inlets at the location of the perforated plates and to define a zero gradient BC for the pressure. Therefore the perforated plates are assumed to be fully reflective. This was considered to be the best compromise, since several models predict an increasing acoustic impedance of a perforated plate and therefore a more wall-like behaviour with increasing bulk flow [132]. This was also observed in the study discussed in [147].

The velocity in the vicinity of walls was modelled using the wall function provided by Spalding in [148], which is implemented in OpenFOAM. At the inlets, constant mass flows are defined for the velocity BCs in the LESs of the SBS. For the MBS2, the velocities were imposed at the inlets, superimposed by cell-limited random velocity fluctuations. This was done to provide some small additional initial perturbations, in order to shorten the time for the LES to develop potential unstable modes. At the outlets, a zero gradient BC was applied for the velocity in case of outgoing flow. For incoming flow, the velocity value was set to zero.

The temperature at the inlets was set to value of 293 K. The walls and the outlets were modelled as adiabatic. The heat loss at the combustion chamber walls in the real combustor was estimated to be small compared to the thermal power of the flame.

The mixture fraction constitutes unity at the fuel inlet and zero at the air inlets, since the flame is not premixed. For the mixture fraction variance and the progress variable zero gradient BC were defined at all boundaries.

## 5.2 Investigated Operating Points

LESs at two OPs were performed for the SBS:  $P_{\text{th}} = 25$  kW,  $\phi = 0.7$  and  $P_{\text{th}} = 30$  kW,  $\phi = 0.85$ , each for a swirler mass flow ratio of  $L = 1.6$ . For each OP, the non-reactive and the reactive flow were simulated. As explained in the discussion of the experimental results, the 400-Hz mode shows a high amplitude in the SBS at  $P_{\text{th}} = 25$  kW,  $\phi = 0.7$ , whereas at  $P_{\text{th}} = 30$  kW,  $\phi = 0.85$ , an oscillation of the unstable mode at the 750-Hz mode is observed in the experiment. In addition, Particle-Image-Velocimetry (PIV) measurements of the flow fields in the combustion chamber were provided by the DLR Stuttgart for these OPs, which allows a comparison of the LES results to experimentally obtained velocities.

In order to investigate the influence of the multiple-burner arrangement on the flow fields as well as the pressure and heat release oscillations, LESs of the non-reactive and the reactive flow in the MBS2 at  $P_{\text{th}} = 30$  kW/burner,  $\phi = 0.85$ ,  $L = 1.6$  were performed. An additional purpose of the LESs was to find possible excitation mechanisms of the 400-Hz mode in the MBS2, which shows very high amplitudes in the experiment at this OP.

The operating conditions and the corresponding mass flow rates are shown in Table 5.1. The simulations of the non-reactive and the reactive flows in the SBS were performed with a constant time step of  $\Delta t = 1e-07$  s, which resulted in a maximum Courant number of  $Co \approx 0.5$ . The simulation of the non-reactive flow in the MBS2 was run using a constant time step of  $\Delta t = 1e-06$  s, which resulted in a maximum Courant number of  $Co \approx 2.0$ . For a stable computation of the reactive flow in the MBS2, the maximum value of the Courant number needed to stay in the range of  $Co \approx 0.5$ , which lead to a constant time step of  $\Delta t = 2e-07$  s. The length of the computed period of time constitutes  $\sim 0.1$  s for all performed simulations.

	$P_{\text{th}}/\text{burner}$	$\phi$	$\dot{m}_{\text{OTS}}/\text{burner}$	$\dot{m}_{\text{IS}}/\text{burner}$	$\dot{m}_{\text{CH}_4}/\text{burner}$	$L$
<b>SBS</b>	25 kW	0.7	453.6 g/min	283.5 g/min	28.4 g/min	1.6
<b>SBS, MBS2</b>	30 kW	0.85	448.3 g/min	280 g/min	34.1 g/min	1.6

**Table 5.1. Operating conditions for the performed LESs in the SBS and the MBS2.**

## 5.3 Numerical Results

In this section, the results of the performed LESs are discussed, starting with the results of the simulations of the non-reactive flows. Subsequently the results of the simulations of the reactive flows are presented.

With the exception of the PIV measurements, the experimental results shown in this section correspond to the experiments discussed in Chapter 4.

The flow quantities in the discussion (such as velocity, pressure, temperature, etc.) represent the filtered quantities, which for convenience reasons are not marked with the corresponding favre-filtered superscript. Therefore any quantity  $g$  in this section corresponds to its resolved component ( $g \rightarrow \tilde{g}$ ). The time-averaged value of any resolved quantity is marked with an overbar ( $\bar{g}$ ).

### 5.3.1 Non-Reactive Flow

#### 5.3.1.1 LES Single-Burner Setup, $P_{th} = 25 \text{ kW}$ , $\phi = 0.7$ , $L = 1.6$

Figure 5.5 shows the results for the mean values of the axial velocity  $\bar{u}_{ax}$ , the radial velocity  $\bar{u}_r$  and the tangential velocity  $\bar{u}_t$  of the PIV measurements in comparison to the LESs at four different axial positions in the combustion chamber.

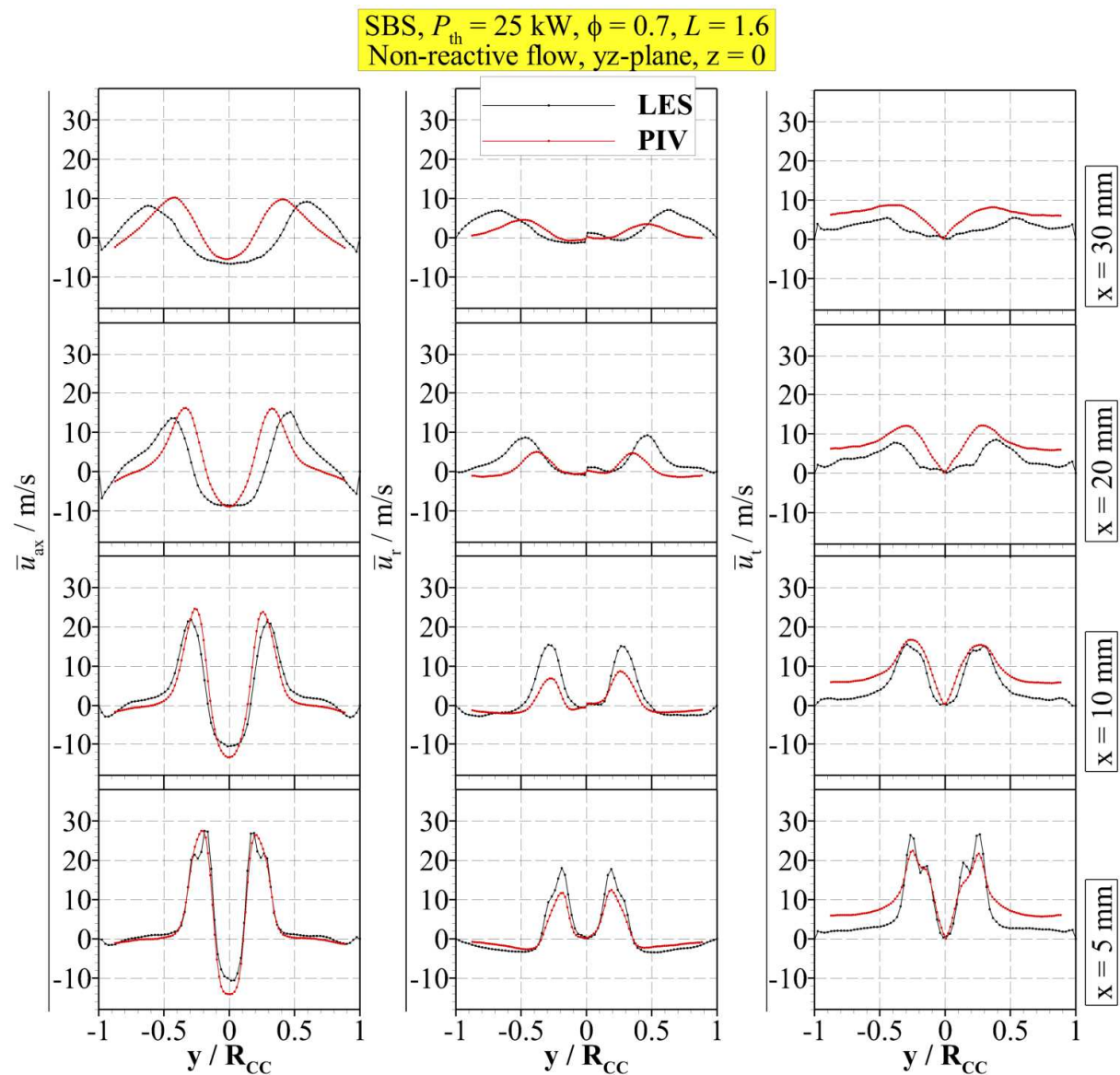


**Figure 5.5. SBS,  $P_{th} = 25 \text{ kW}$ ,  $\phi = 0.7$ ,  $L = 1.6$ : Profiles of the time-averaged velocity in the non-reactive flow at different axial distances to the nozzle in the LES and the experiment**

In general, a good agreement between the simulation and the experiments is visible. Especially near the nozzle exit the velocity profiles correspond very well.

The LES shows higher radial velocities, which results in flatter profiles of both the axial velocity and the tangential velocity, due to the increased radial transport. Therefore a wider angle of the swirl jet is observed in the contour plot shown in Figure 5.6. The inner vortex structure of the swirl flow reaches down to the bottom of the inner swirler. The LES shows higher tangential velocities than in the experiment near the nozzle exit, whereas further upstream the measured values for  $\bar{u}_t$  exceed the ones of the simulation.

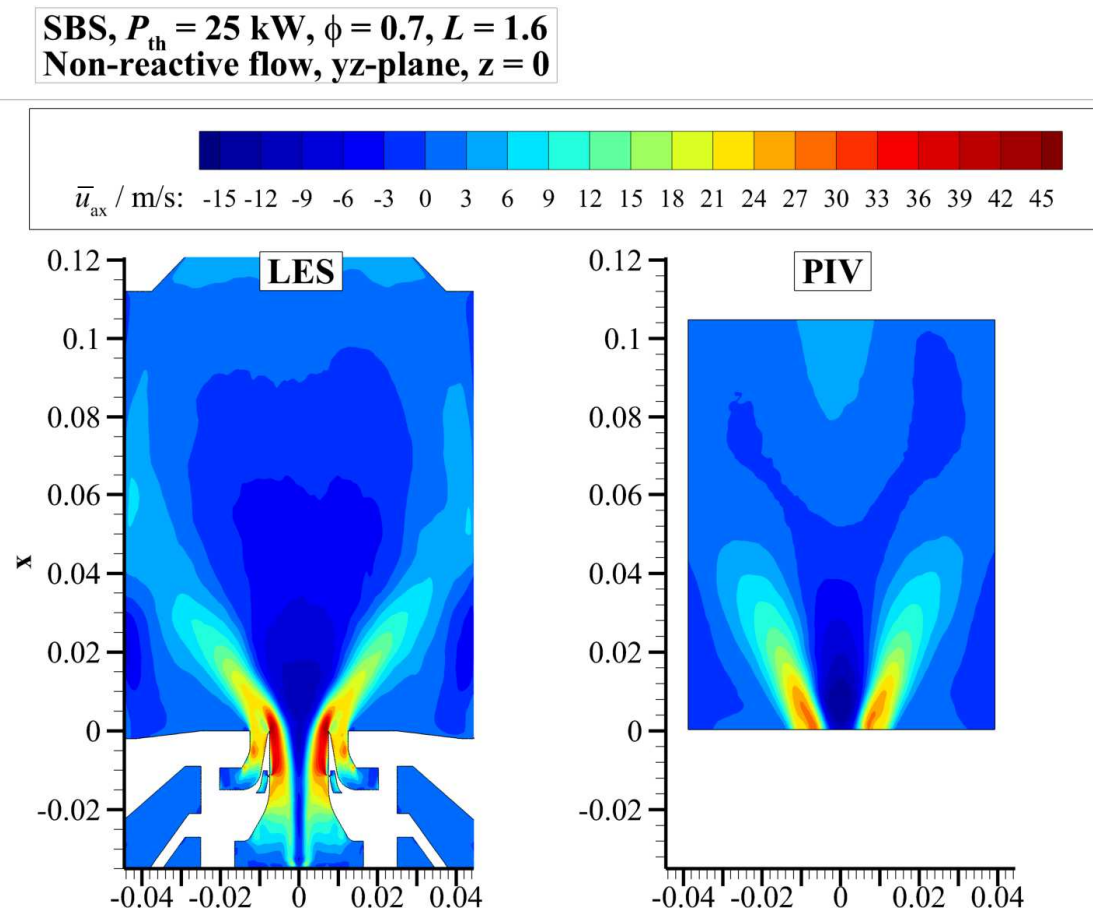


**Figure 5.6. SBS,  $P_{th} = 25$  kW,  $\phi = 0.7$ ,  $L = 1.6$ : Contour plots of the time-averaged axial velocity in the non-reactive flow in the LES and the experiment**

A possible explanation for the deviation between of the values of the LES and the experiment may be the increased velocity fluctuations in the LES (Figure 5.7). Up to a distance of  $x = 20$  mm the calculated axial, radial and tangential fluctuations mostly exceed the measured values. The augmented turbulence intensity leads to an increased angular momentum flux in the radial direction, which results in a wider inner recirculation zone.

A comparison of the pressure spectrum of the experiment and the LES shows that the LES is able to reproduce the main characteristics of the pressure oscillations in the combustion chamber. However, the dominant frequency at around 1000 Hz observed in the experiment

features significantly smaller amplitudes in the LES. As illustrated by the contour plot of the axial velocity and the spectrum of the axial velocity in the monitor point 1 (MP1) in Figure 5.8, this peak possibly represents an oscillation associated with the vortex shedding frequency at the outlet of the inner swirler. The deviation between the experiment and the LES may be caused by the missing fuel flow in the experiment. The fuel flow in the LES possibly increases the turbulence near the exit of the inner swirler which results in an increased dissipation of the shed vortices.

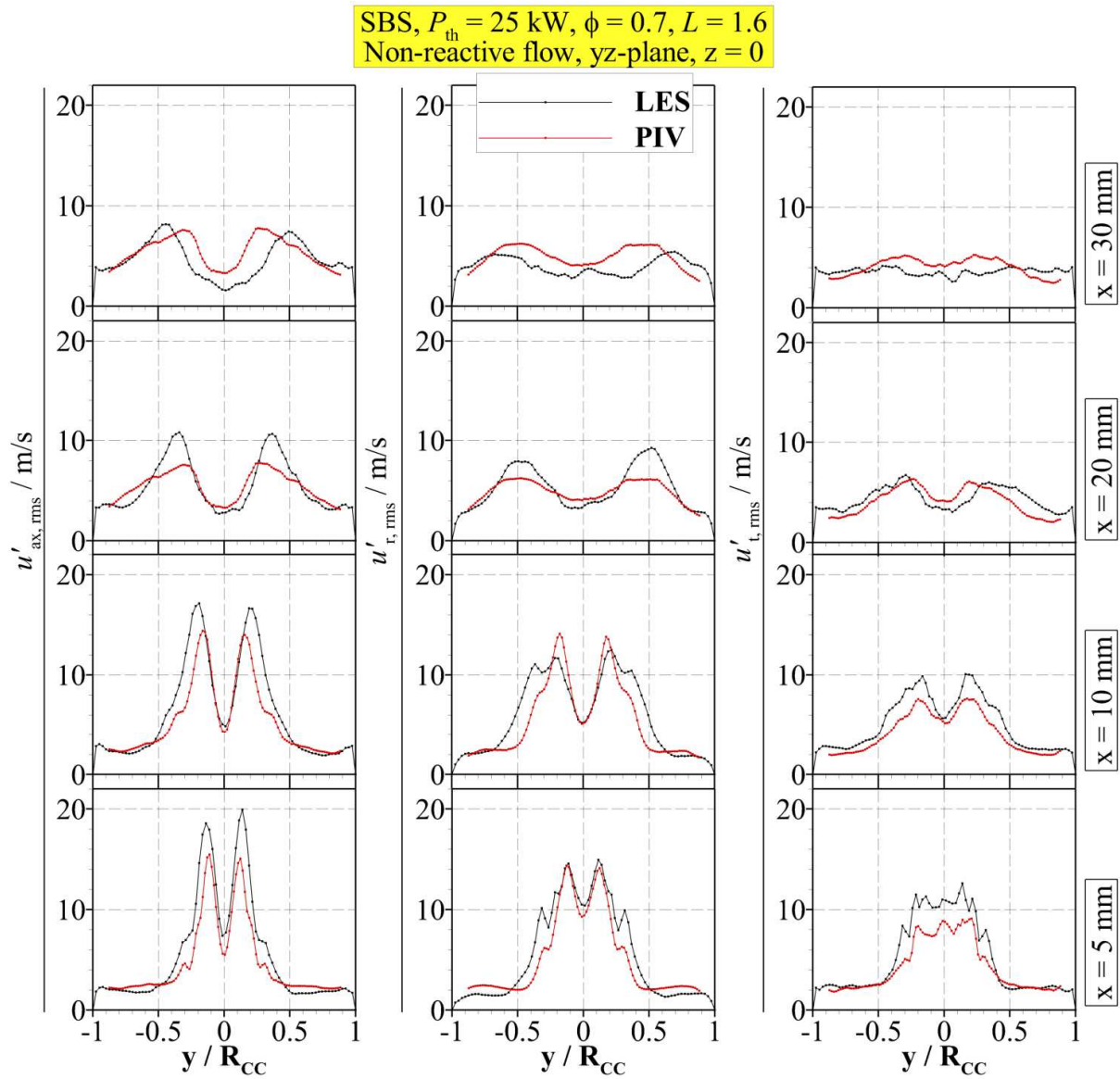


**Figure 5.7.** SBS,  $P_{th} = 25$  kW,  $\phi = 0.7$ ,  $L = 1.6$ : RMS velocity fluctuations in the non-reactive flow at different axial distances to the nozzle in the LES and the experiment

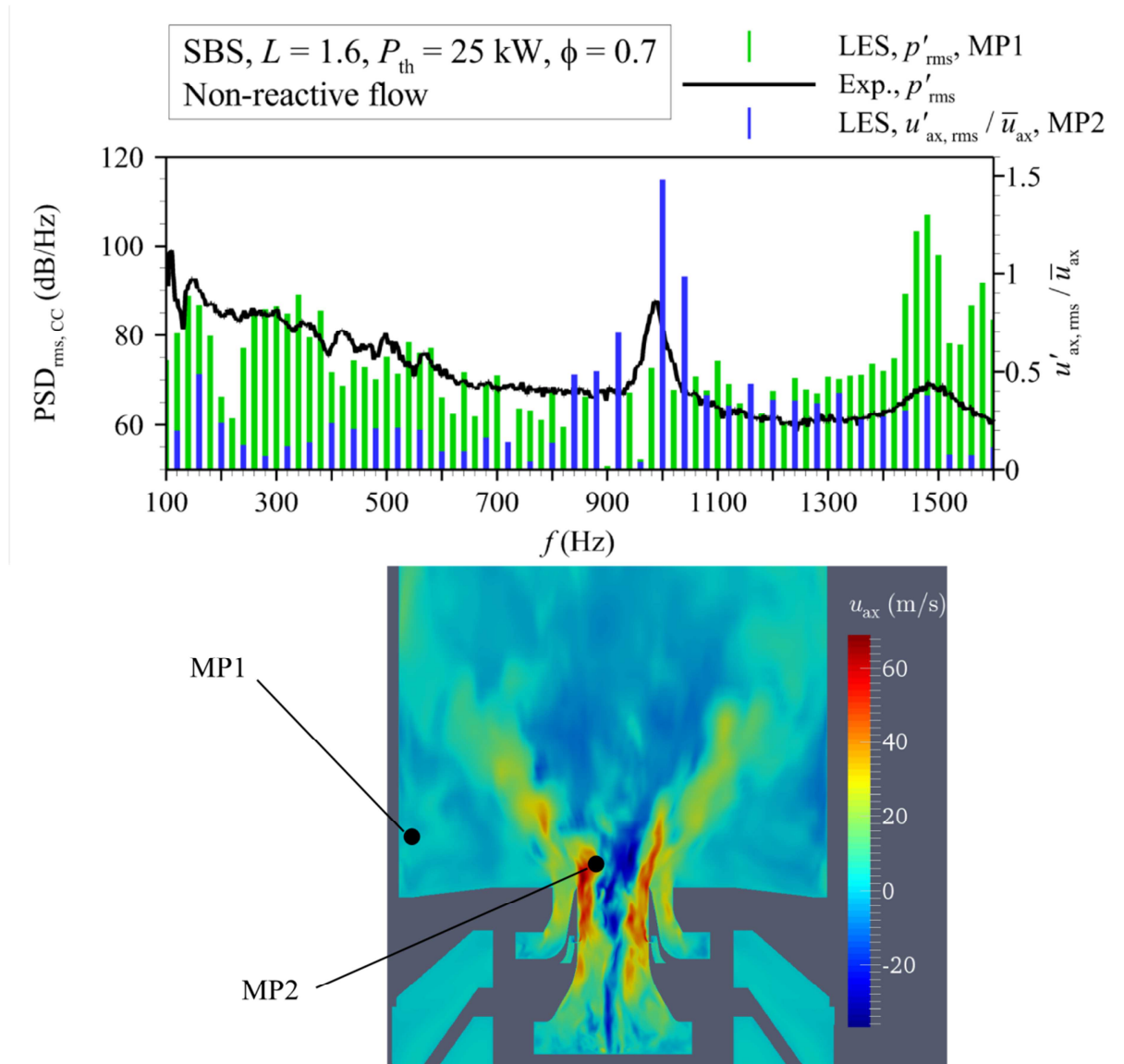


**Figure 5.8. SBS,  $P_{th} = 25$  kW,  $\phi = 0.7$ ,  $L = 1.6$ : Spectra of pressure oscillations in the combustion chamber in the experiment and at MP1 in the LES and velocity spectrum at MP2; contour plot of the instantaneous axial velocity**

The spectra of the pressure oscillations in the inner plenum at MP4 (Figure 5.9) indicate that the LES overestimates the pressure oscillations in the inner plenum. This may explain why the velocity fluctuations are increased in the LES, since the augmented pressure oscillations lead to increased flow rate oscillations. The two dominant modes in the measured pressure spectrum at  $\sim 140$  Hz and  $\sim 520$  Hz are also visible in the spectrum of the LES, but show much higher amplitudes, especially the oscillation at  $\sim 520$  Hz. As illustrated in the contour plot of the  $p'_{rms}$  -values in the inner plenum, the high amplitude of the  $\sim 520$ -Hz mode is due to the formation of a standing half-wave in the inner plenum. The formation of this standing wave is fostered by the zero gradient pressure BC, which has infinite impedance and is therefore perfectly reflective for any incoming pressure waves, whereas the perforated plate installed in the real combustor causes a frequency-dependent damping of the incoming pressure waves and may lead to attenuation of the modes (see 5.1.3). The lack of attenuation

compared to the experimental setup is most likely responsible for the overestimation of the pressure amplitudes in the inner plenum in the LES. In the spectrum of the MP3 in the inner swirler, the oscillation at  $\sim 140$  Hz features an even higher amplitude, whereas the oscillation at  $\sim 520$  Hz is slightly damped. Due to the matching frequencies, the oscillation at  $\sim 140$  Hz most likely represents the equivalent oscillation to LF-Mode1. The pressure spectrum of the LES in the inner plenum also shows increased amplitudes in the frequency range of LF-Mode3, which complies with the findings in the discussion of the experiments.

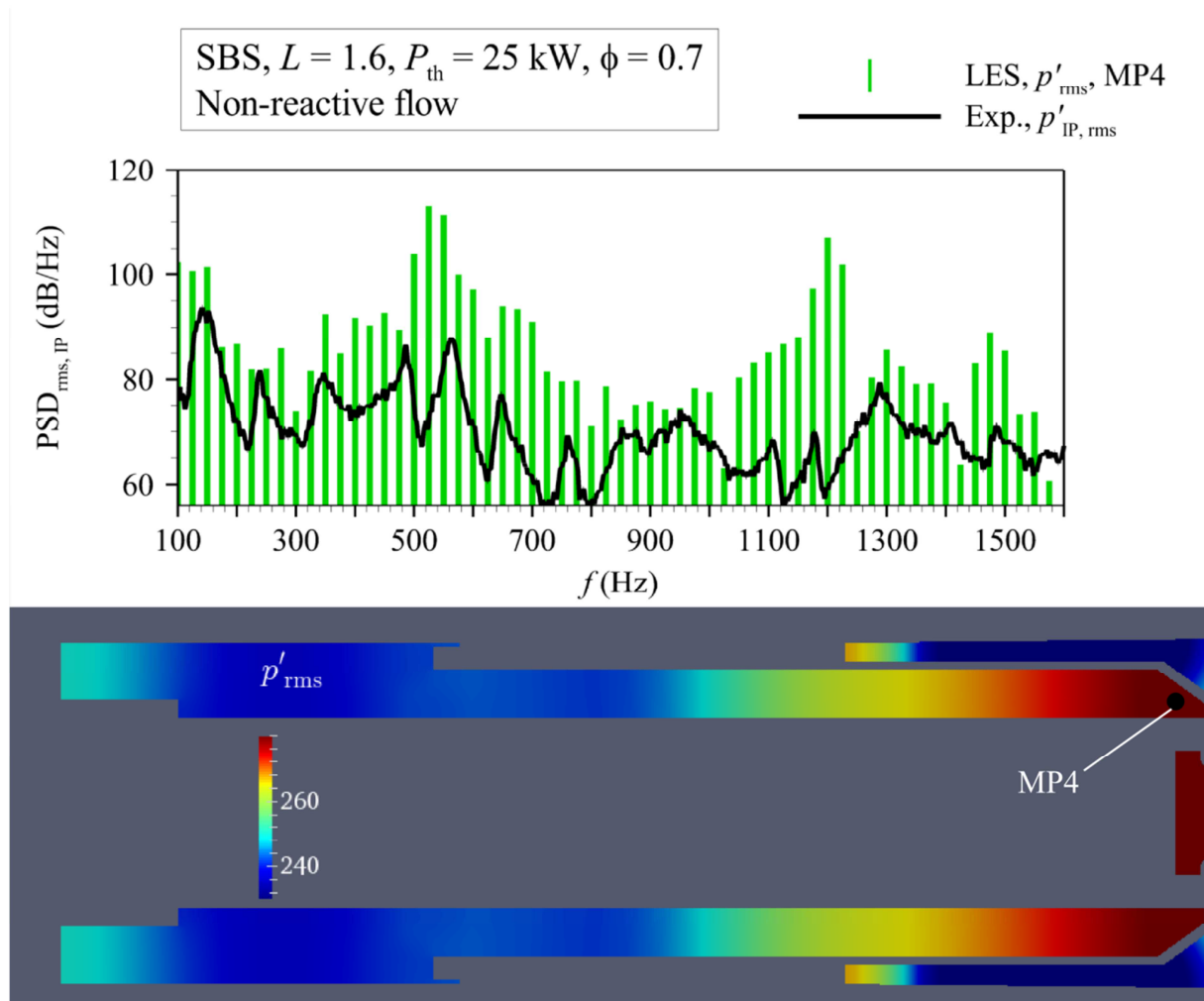


**Figure 5.9. SBS,  $P_{th} = 25$  kW,  $\phi = 0.7$ ,  $L = 1.6$ : Spectrum of the pressure oscillations in the inner plenum (IP) in the non-reactive flow in the LES and the experiment; contour plot of the standing half-wave in the inner plenum in the LES**

As indicated by the high  $p'_{rms}$  -values near the isoline  $\bar{u}_{ax} = 0$ , the pressure oscillations in the inner swirler also strongly affect the structure of the IRZ, since they directly influence the pressure gradient which enables the formation of the IRZ. LF-Mode1 is the dominant pressure mode in the inner swirler at MP3, as illustrated in Figure 5.10. The spectrum of the mixture fraction at MP3 (Figure 5.11) also shows a dominant frequency in the frequency range of LF-Mode1 (130-140 Hz).

These findings corroborate the assumption made in 4.5.1.5, where it is stated that the oscillation of LF-Model1 causes a periodic change in the width of the IRZ near the nozzle exit, which in turn evokes a periodically increased mixing of fuel into the IRZ. However, the maximum amplitudes in the spectrum of the mixture fraction oscillations are observed at 1100 Hz.

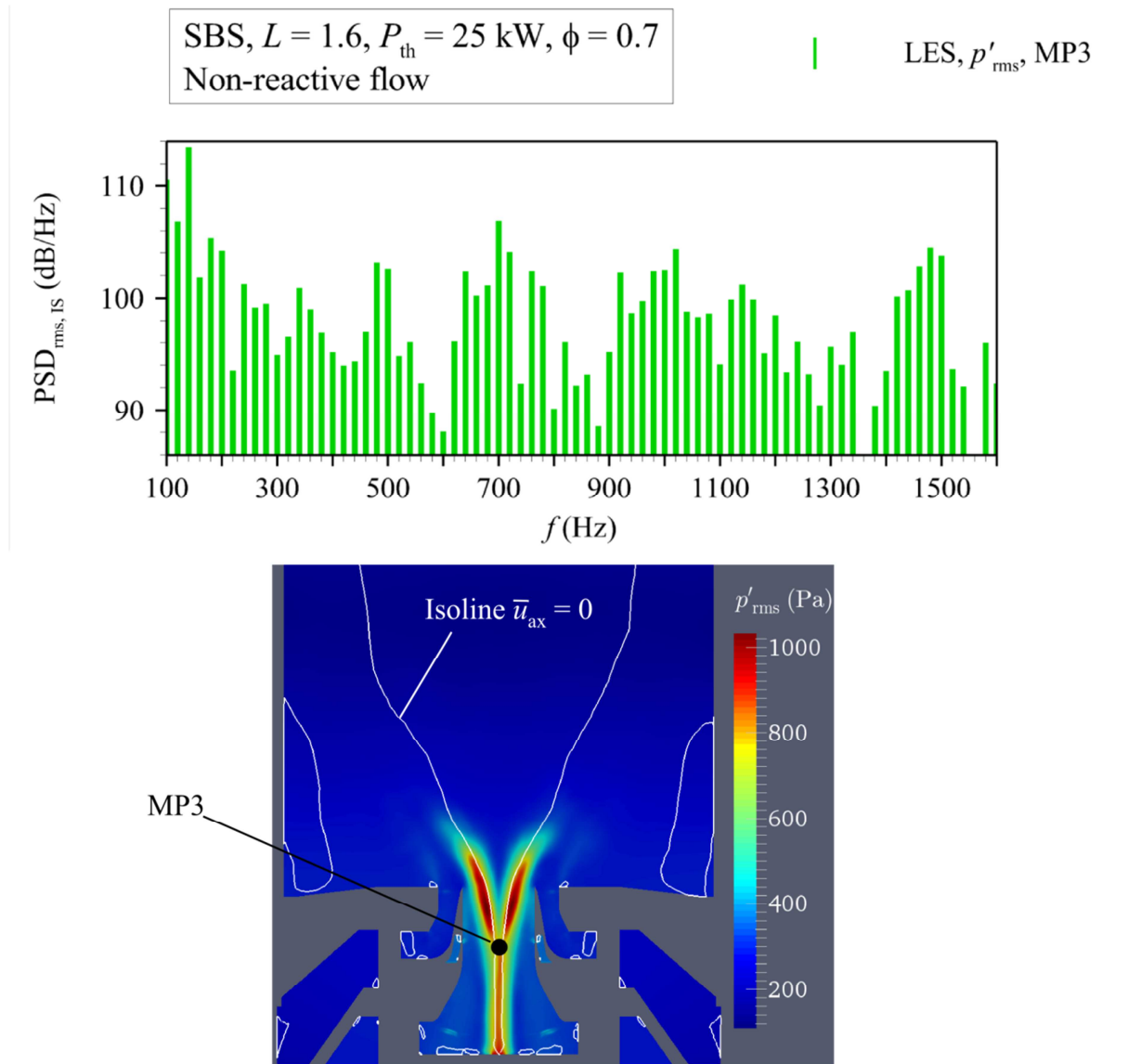


**Figure 5.10. SBS,  $P_{th} = 25$  kW,  $\phi = 0.7$ ,  $L = 1.6$ : Spectrum of the pressure oscillations in the inner swirler (IS) at MP3 in the non-reactive flow in the LES**

A possible explanation for this mixture fraction oscillation is the PVC, which strongly affects the mixing process of fuel and air flow, as illustrated in Figure 5.12. The PVC interacts with the fuel jets due to its tumbling movement and increases the mixture intensity, as indicated by the isoline of the stoichiometric mixture fraction. The presence of the PVC near the nozzle exit also indicates that the velocity fluctuations near the nozzle exit are not only associated with acoustic oscillations, but are also caused by hydrodynamic pressure oscillations induced by the PVC.

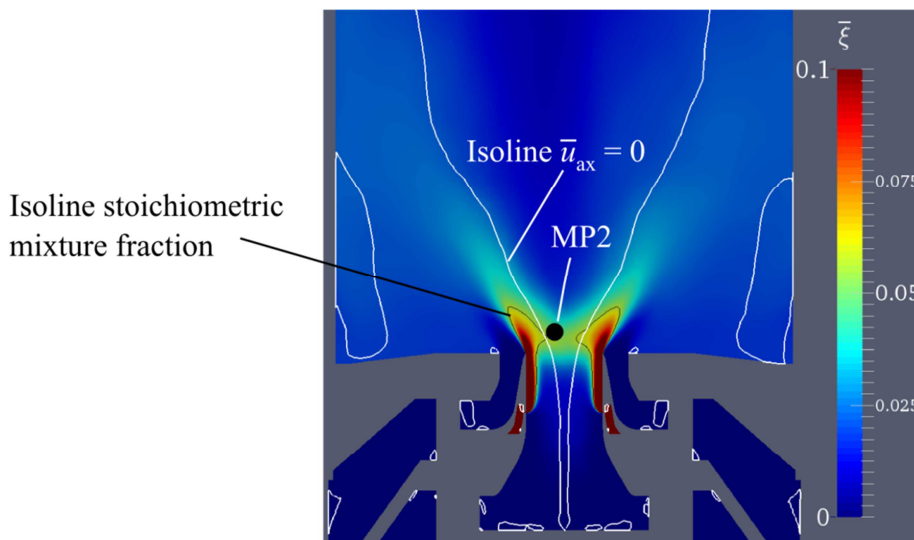
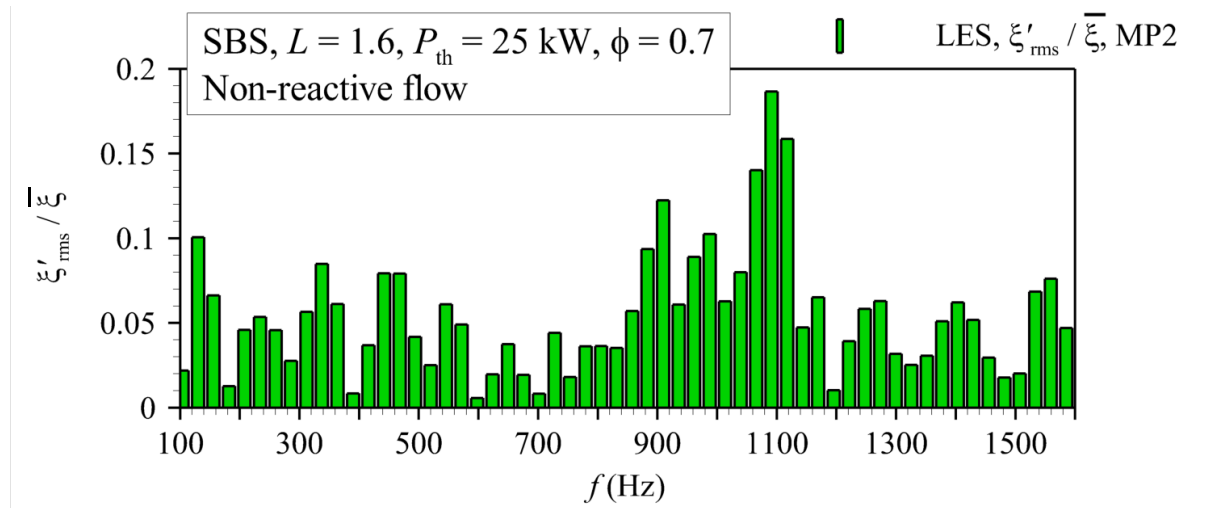


**Figure 5.11.** SBS,  $P_{th} = 25$  kW,  $\phi = 0.7$ ,  $L = 1.6$ : Spectrum of the mixture fraction oscillations at MP2 and isoline of the stoichiometric mixture fraction near the nozzle exit in the non-reactive flow in the LES

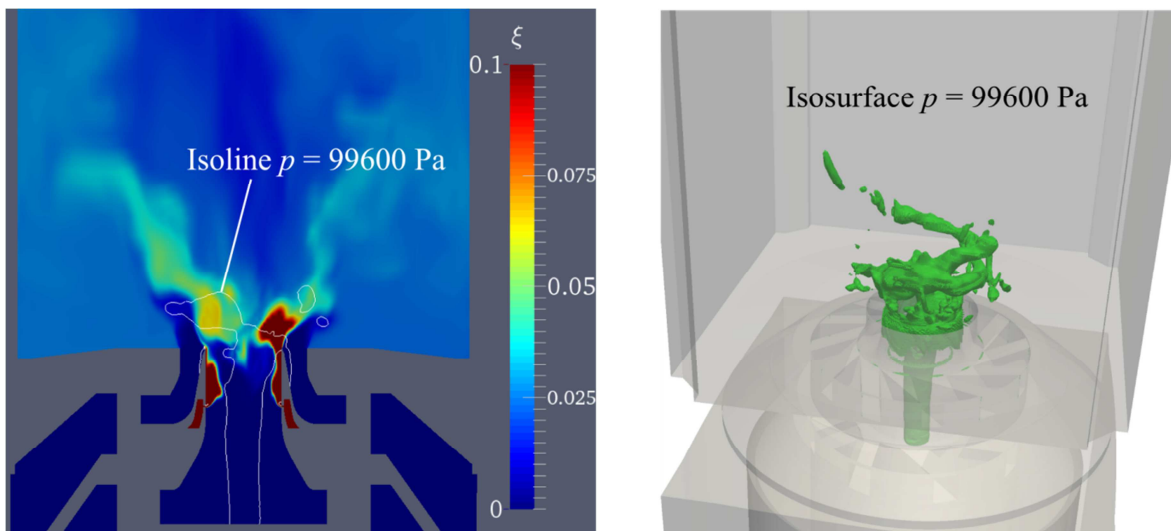


**Figure 5.12.** SBS,  $P_{th} = 25$  kW,  $\phi = 0.7$ ,  $L = 1.6$ : Visualization of the PVC with the isosurface at  $p = 99600$  Pa in the LES of the non-reactive flow

### 5.3.1.2 LES Single-Burner Setup, $P_{th} = 30 \text{ kW}$ , $\phi = 0.85$ , $L = 1.6$

#### Comparison of the calculated velocity fields with the PIV measurements

Figure 5.13 shows the velocity profiles of the PIV measurements and the LES in the non-reactive flow at different distances to the nozzle exit at the OP  $P_{th} = 30 \text{ kW}$ ,  $\phi = 0.85$  at  $L = 1.6$ . The air mass flow rates through the swirlers are only slightly decreased in comparison to the previously discussed OP and the fuel mass flow rate is decreased by 20 %. Since the fuel mass flow rate is still very small compared to the air mass flow, the flow fields in the combustion chamber at both OPs are expected to be very similar.

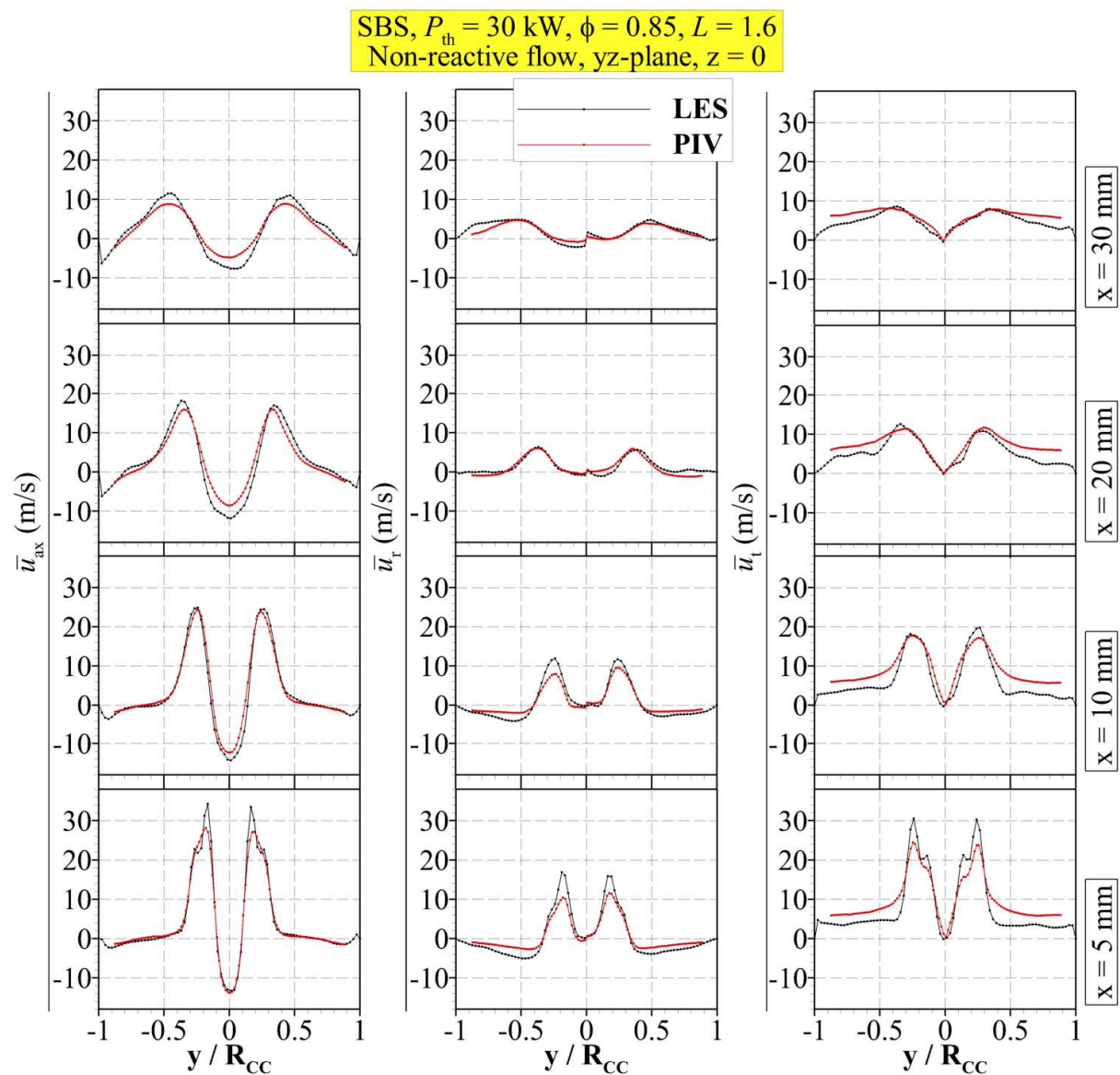
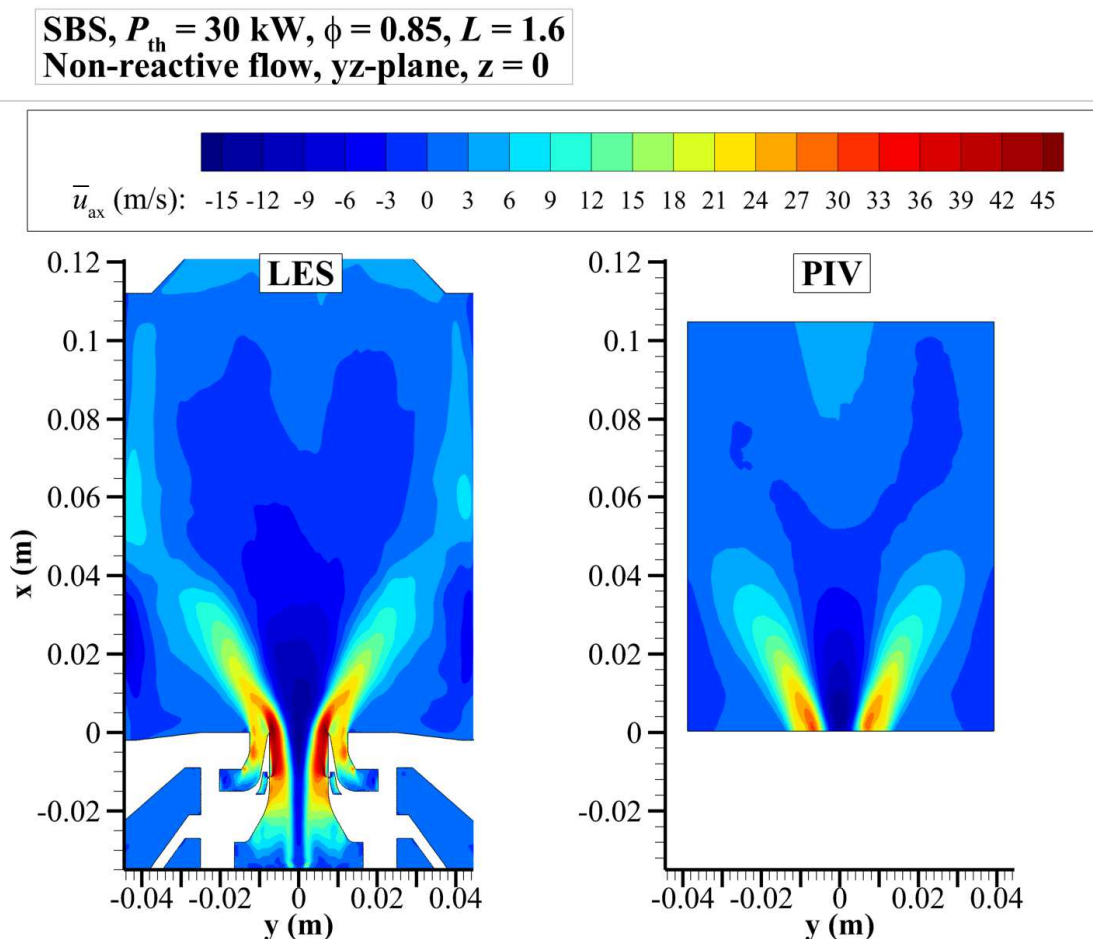


Figure 5.13. SBS,  $P_{th} = 30 \text{ kW}$ ,  $\phi = 0.85$ ,  $L = 1.6$ : Time-averaged velocity profiles in the non-reactive flow at different axial distance to the nozzle in the LES and the experiment

This is indeed the case for the results of the PIV measurements. The results of the LES also show similar results for the two OPs, but the differences between the mean velocity fields are greater than in the experiment. The LES for the OP  $P_{\text{th}} = 30 \text{ kW}$ ,  $\phi = 0.85$  shows a narrower jet angle of the swirl flow than at  $P_{\text{th}} = 25 \text{ kW}$ ,  $\phi = 0.7$ , as illustrated in the contour plot of the axial velocity in Figure 5.14. This results in a much better agreement between the results of the LES and the PIV measurements, which is also the case for the RMS-values of the velocity fluctuations (Figure 5.15). Especially at  $x = 20 \text{ mm}$  and  $x = 30 \text{ mm}$ , the deviations of the mean velocities between the experiment and the LES are significantly reduced. Regarding the velocity fluctuations, the PIV results and the LES both show increased values at  $P_{\text{th}} = 30 \text{ kW}$ ,  $\phi = 0.85$ , but the difference between the OPs is more significant for the PIV results. The reduction of the width of the IRZ observed in the LES with increasing fuel flow is something that can be expected, since the increased fuel mass flow rate augments the axial momentum flux of the flow in the inner swirler. This is illustrated by the increased maximum of the calculated mean axial velocity at  $P_{\text{th}} = 30 \text{ kW}$ ,  $\phi = 0.85$  at  $x = 5 \text{ mm}$ .



**Figure 5.14. SBS,  $P_{\text{th}} = 30 \text{ kW}$ ,  $\phi = 0.85$ ,  $L = 1.6$ : Contour plots of the time-averaged axial velocity in the non-reactive flow in the LES and the experiment**

The turbulent kinetic energy in the inner swirler at  $P_{th} = 30$  kW,  $\phi = 0.85$  is increased compared to  $P_{th} = 25$  kW,  $\phi = 0.7$  (Figure 5.16). This is most likely the result of the increased fuel flow rate. The increased turbulent kinetic energy leads to a more broadband distribution of the pressure oscillations in the combustion chamber at MP1 at  $P_{th} = 30$  kW,  $\phi = 0.85$  (Figure 5.17). The augmented turbulent intensity near the nozzle outlet also influences the mixture fraction oscillations.

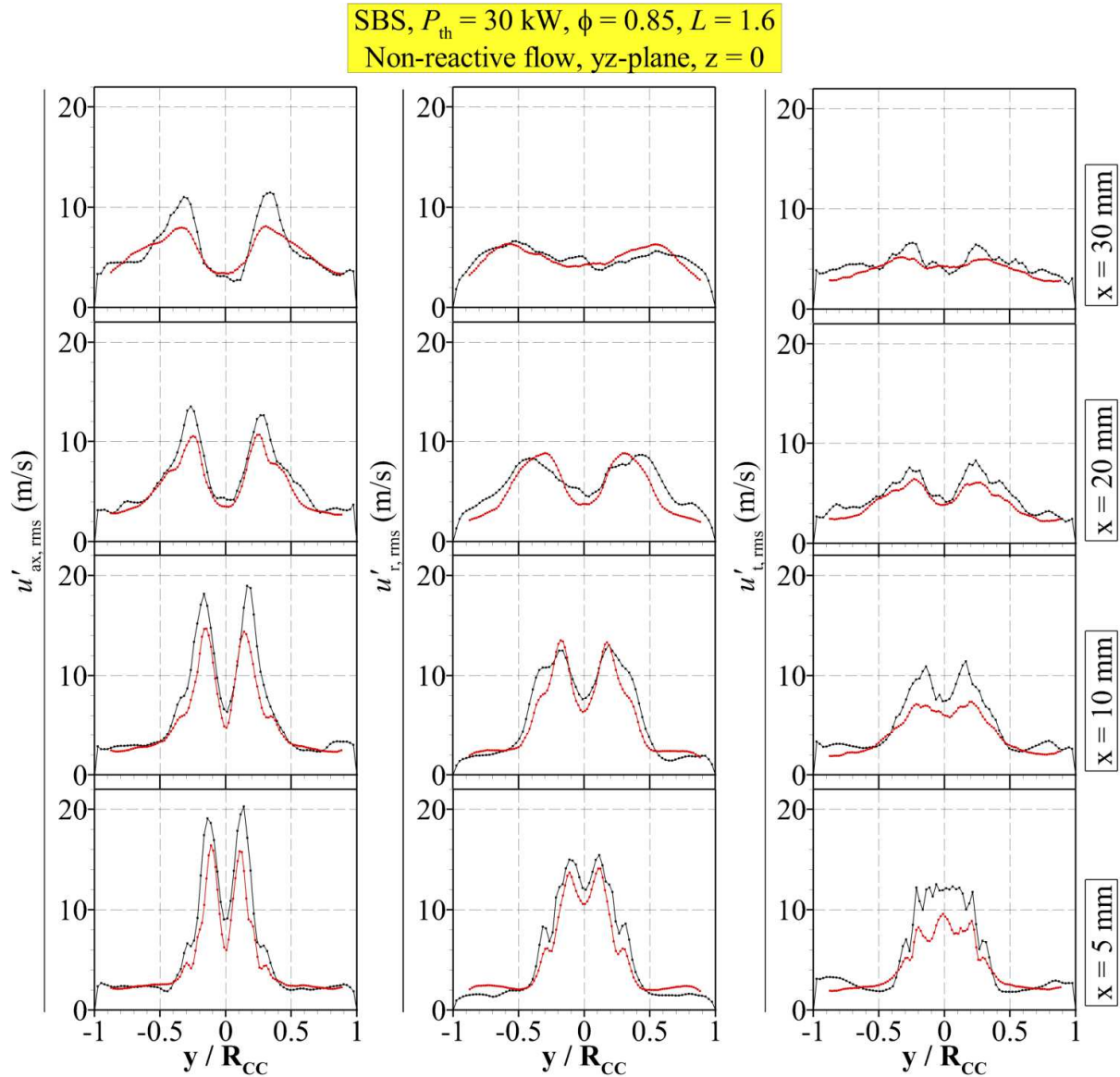


**Figure 5.15. SBS,  $P_{th} = 30$  kW,  $\phi = 0.85$ ,  $L = 1.6$ : RMS velocity fluctuations in the non-reactive flow at different axial distance to the nozzle in the LES and the experiment**

The spectra of the mixture fraction oscillations at MP3 indicates that the mixture fraction oscillation associated with LF-Mode1 is reduced at  $P_{th} = 30$  kW,  $\phi = 0.85$ , as illustrated in the spectrum in Figure 5.18. Also the modes around 350 Hz, 450 Hz and 900 Hz show reduced amplitudes. Therefore the flow characteristics near the nozzle outlet are very sensitive to changes of the fuel flow rate.

The PVC remains the main source of the mixture fraction oscillations at MP2. The isoline of the mean stoichiometric mixture fraction shows that stoichiometric mixtures are also found at the burner axis, which is most likely the result of the increased fuel flow rate. Figure 5.19 shows a visualization of the PVC with an isosurface/isoline at  $p = 99600$  Pa. The contour plot of the mixture fraction illustrates the strong influence of the PVC on the mixing process.

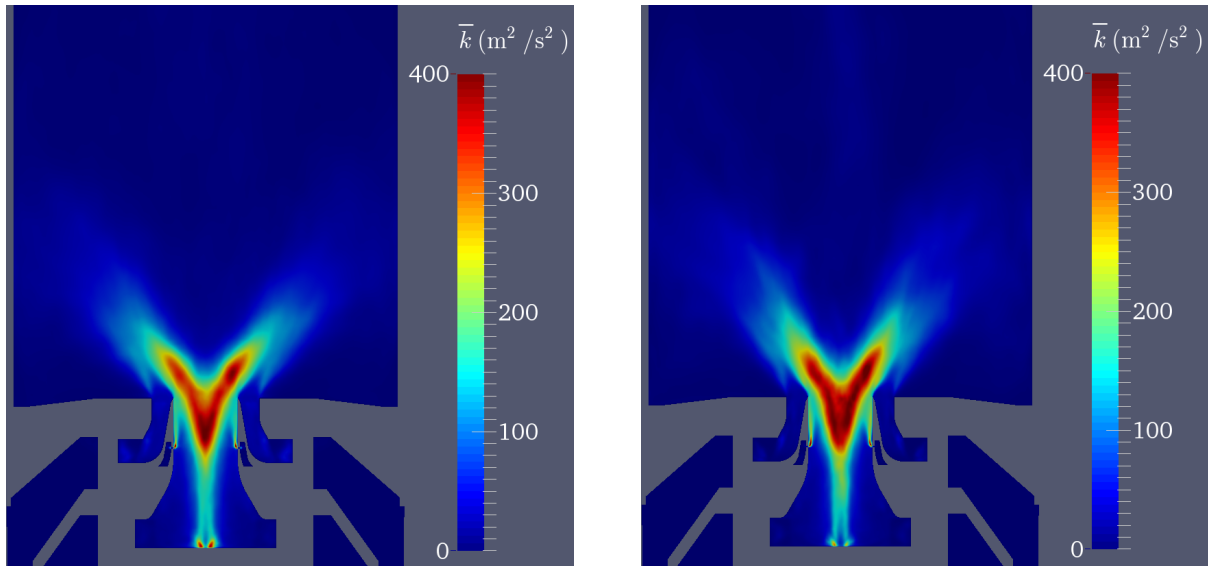


**Figure 5.16** SBS,  $L = 1.6$ : Contour plots of the time-averaged turbulent kinetic energy in the non-reactive flow in the LES at  $P_{th} = 25$  kW,  $\phi = 0.7$  (l.h.s.) and  $P_{th} = 30$  kW,  $\phi = 0.85$  (r.h.s.)

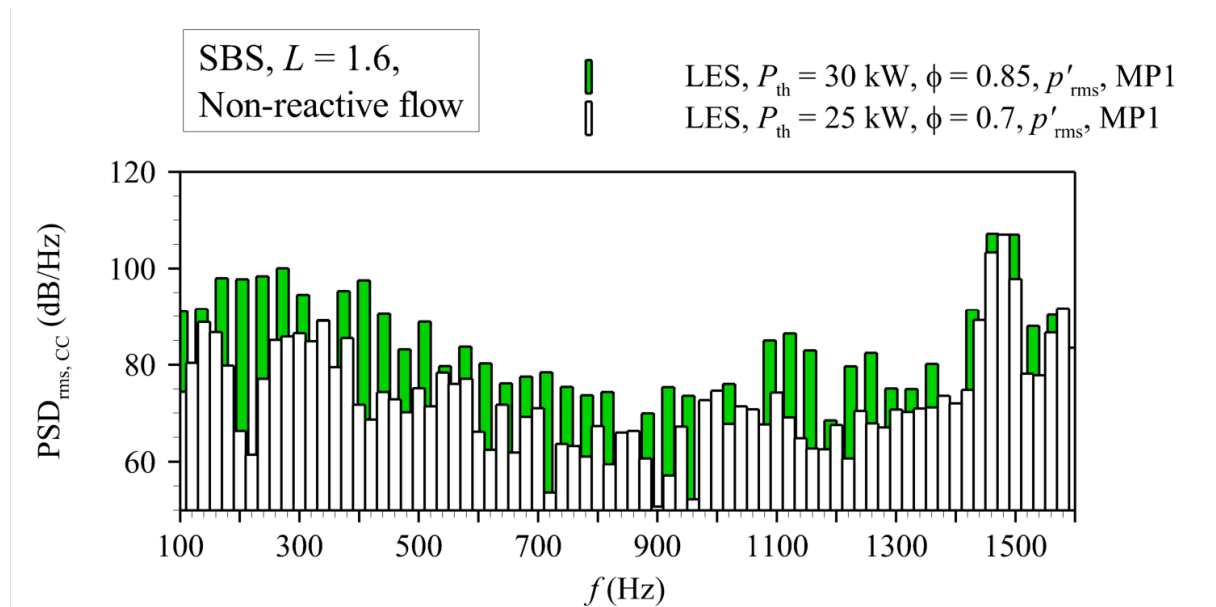


**Figure 5.17.** SBS,  $L = 1.6$ : Comparison of the spectra of the pressure oscillations in the combustion chamber (CC) at MP1 for  $P_{th} = 25$  kW,  $\phi = 0.7$  and  $P_{th} = 30$  kW,  $\phi = 0.85$  in the non-reactive flow in the LES

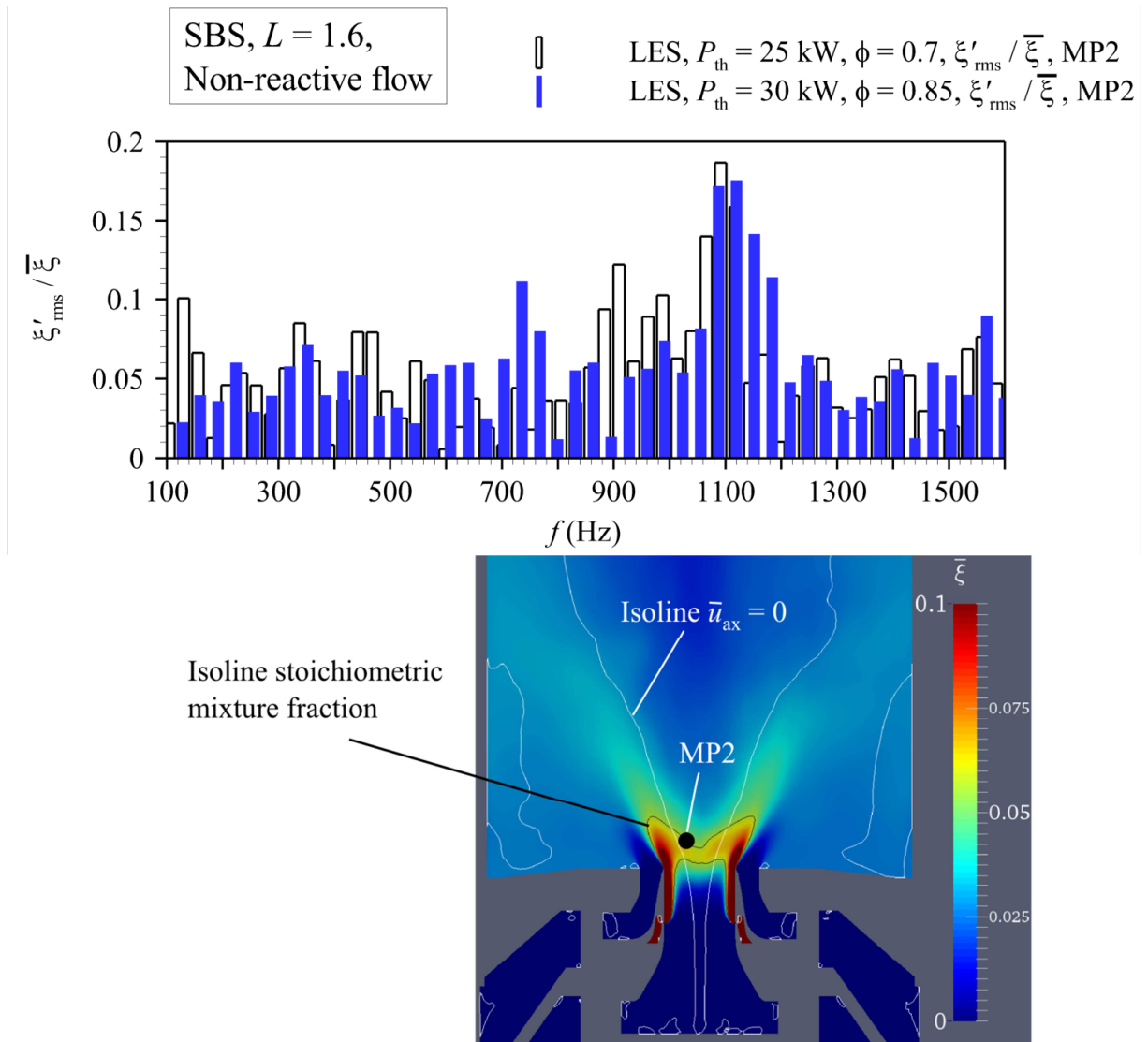


**Figure 5.18.** SBS,  $P_{th} = 30$  kW,  $\phi = 0.85$ ,  $L = 1.6$ : Spectrum of the mixture fraction oscillations at MP2; isoline of the stoichiometric mixture fraction in the LES in the non-reactive flow

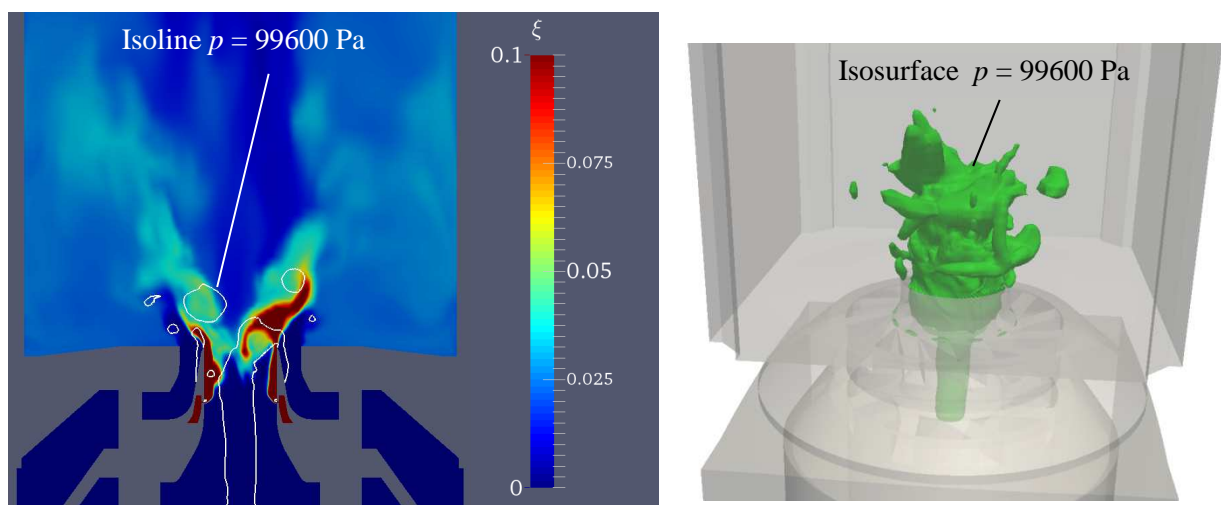


**Figure 5.19.** SBS,  $P_{th} = 30$  kW,  $\phi = 0.85$ ,  $L = 1.6$ : Visualization of the PVC with an isosurface at  $p = 99600$  Pa for the LES of the non-reactive flow

5.3.1.3 LES Multiple-Burner Setup 2,  $P_{th} = 30\text{kW}/\text{burner}$ ,  $\phi = 0.85$ ,  $L = 1.6$ *Comparison of the Mean Velocities in the SBS and the MBS2*

Figure 5.20 shows the computed velocity profiles at different axial positions in the SBS and the MBS2 at  $P_{th} = 30\text{ kW}/\text{burner}$ ,  $\phi = 0.85$  at  $L = 1.6$ . Values  $> 1$  of the normalized  $y$ -coordinate indicate the side of the adjacent burner in the MBS2. At  $x = 5\text{ mm}$ , the velocities in the SBS and the MBS2 are quite similar. The flow in the SBS features a higher absolute value of the maximum negative velocity in the IRZ at the burner axis. Also the maxima of the axial velocity in the positive  $x$ -direction and the tangential velocity are higher in the SBS. However, the radial velocities in the MBS2 exceed the ones in the SBS.

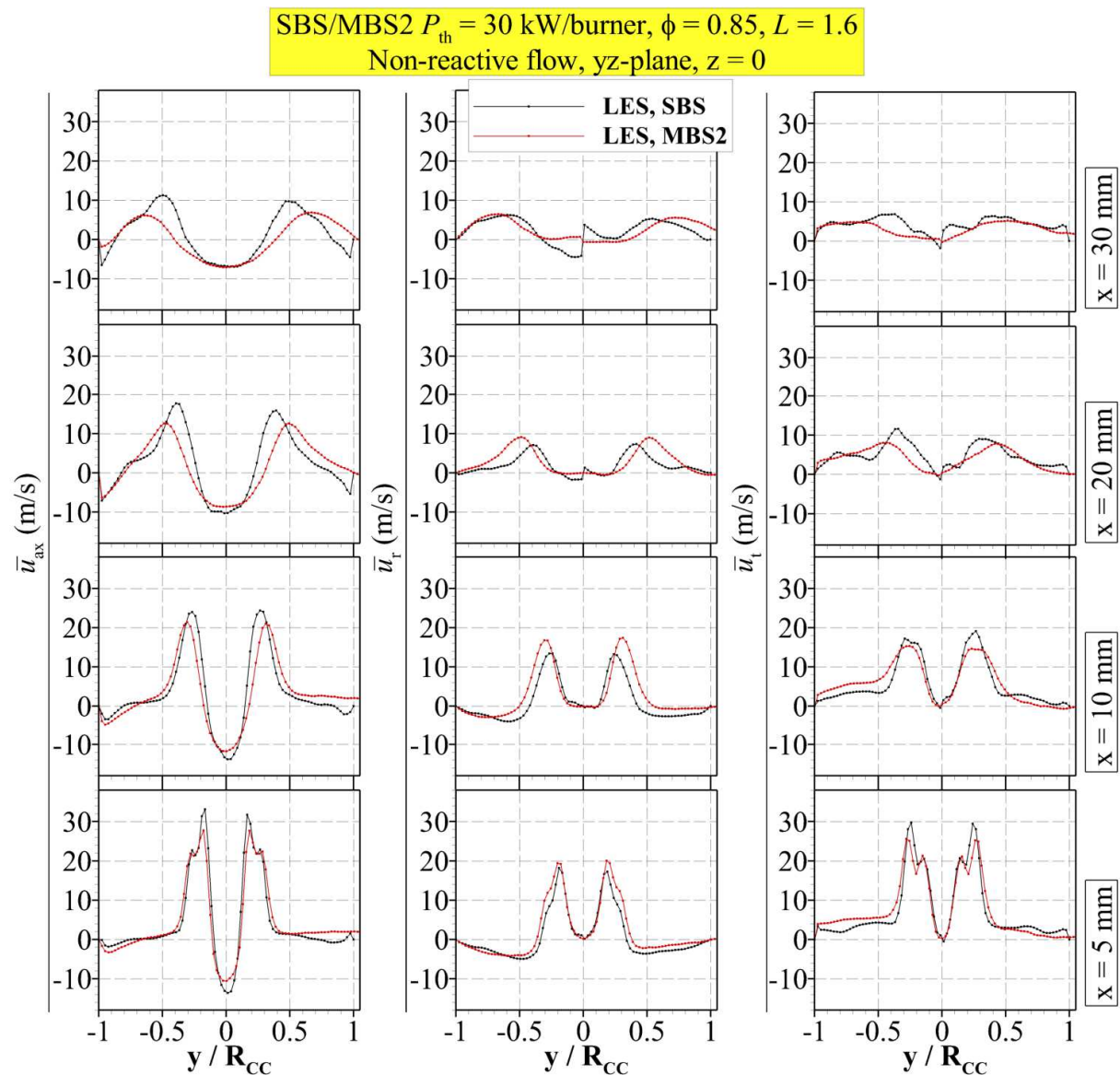


**Figure 5.20. SBS, MBS2,  $P_{th} = 30\text{ kW}/\text{burner}$ ,  $\phi = 0.85$ ,  $L = 1.6$ : Time-averaged velocity profiles in the non-reactive flow**

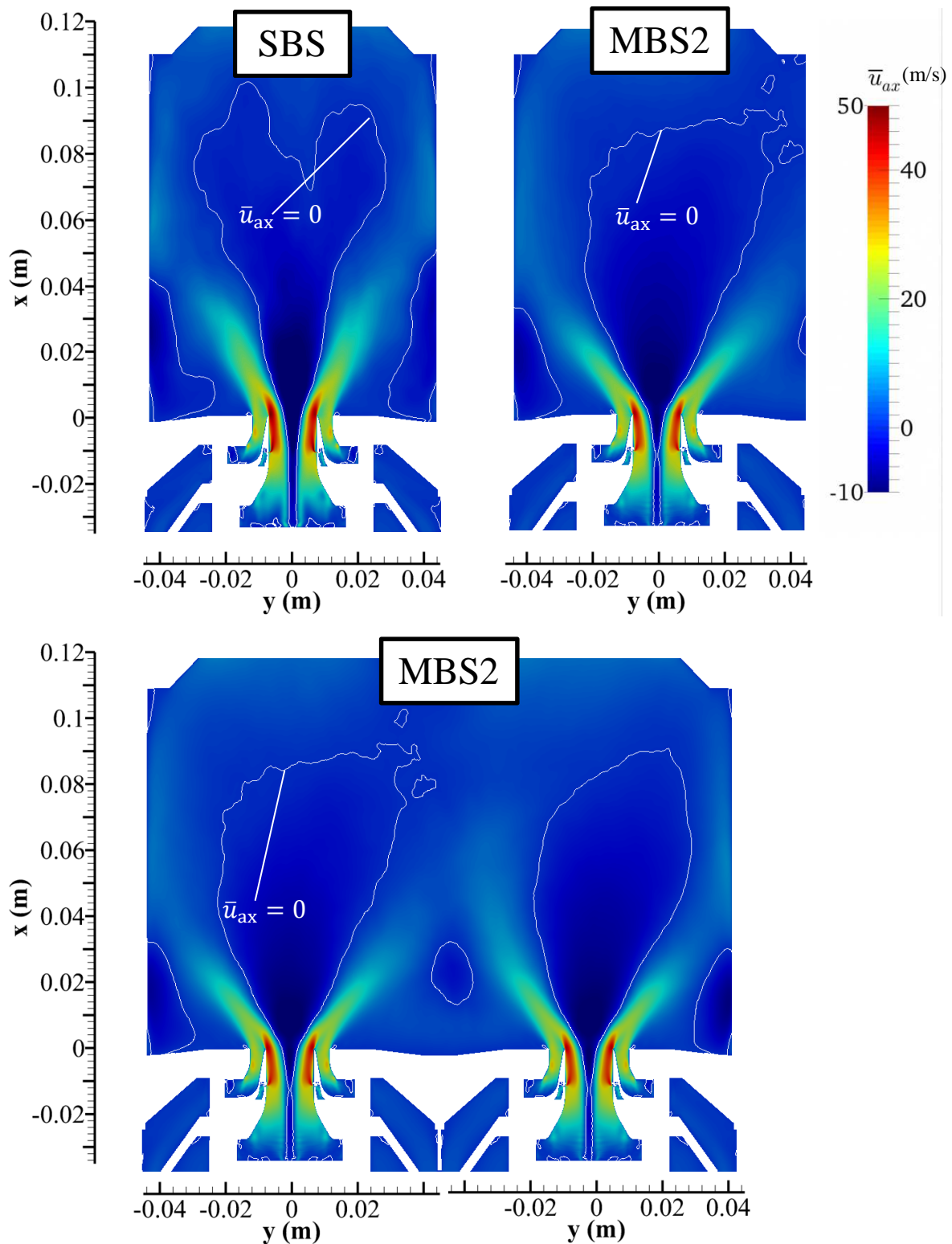


**Figure 5.21. SBS, MBS2,  $P_{th} = 30$  kW/burner,  $\phi = 0.85$ ,  $L = 1.6$ : Axial velocities and recirculation zones in the non-reactive flow**

At the axial positions farther downstream, it is noticeable that the maximum of the tangential velocity in the flow field of the MBS2 is located at higher radial distances than in the SBS. This is also the case for the radial velocities, which also attain higher maximum values in the

MBS2 than in the SBS. In the MBS2, the transport of angular momentum to greater radii seems to be more intense. As a consequence, the IRZ is wider in the MBS2 than the in the SBS, which is also illustrated by the contour plots of the axial velocities and the isoline at  $\bar{u}_{ax} = 0$  in Figure 5.21. The swirl flow in the MBS2 attaches to the wall at a smaller axial distance to the nozzle. In addition, it can be observed that the ORZs of the adjacent swirl jets combine to form a unified recirculation zone.

The profiles of the RMS velocity fluctuations are shown in Figure 5.22. The profiles comply with the observations made for the mean flow fields. The velocity fluctuations in the radial direction are significantly increased in the MBS2 compared to the SBS, especially in the direction of the adjacent burner. The augmented radial velocity fluctuations in the MBS2 possibly cause the increased transport of angular momentum in the radial direction.

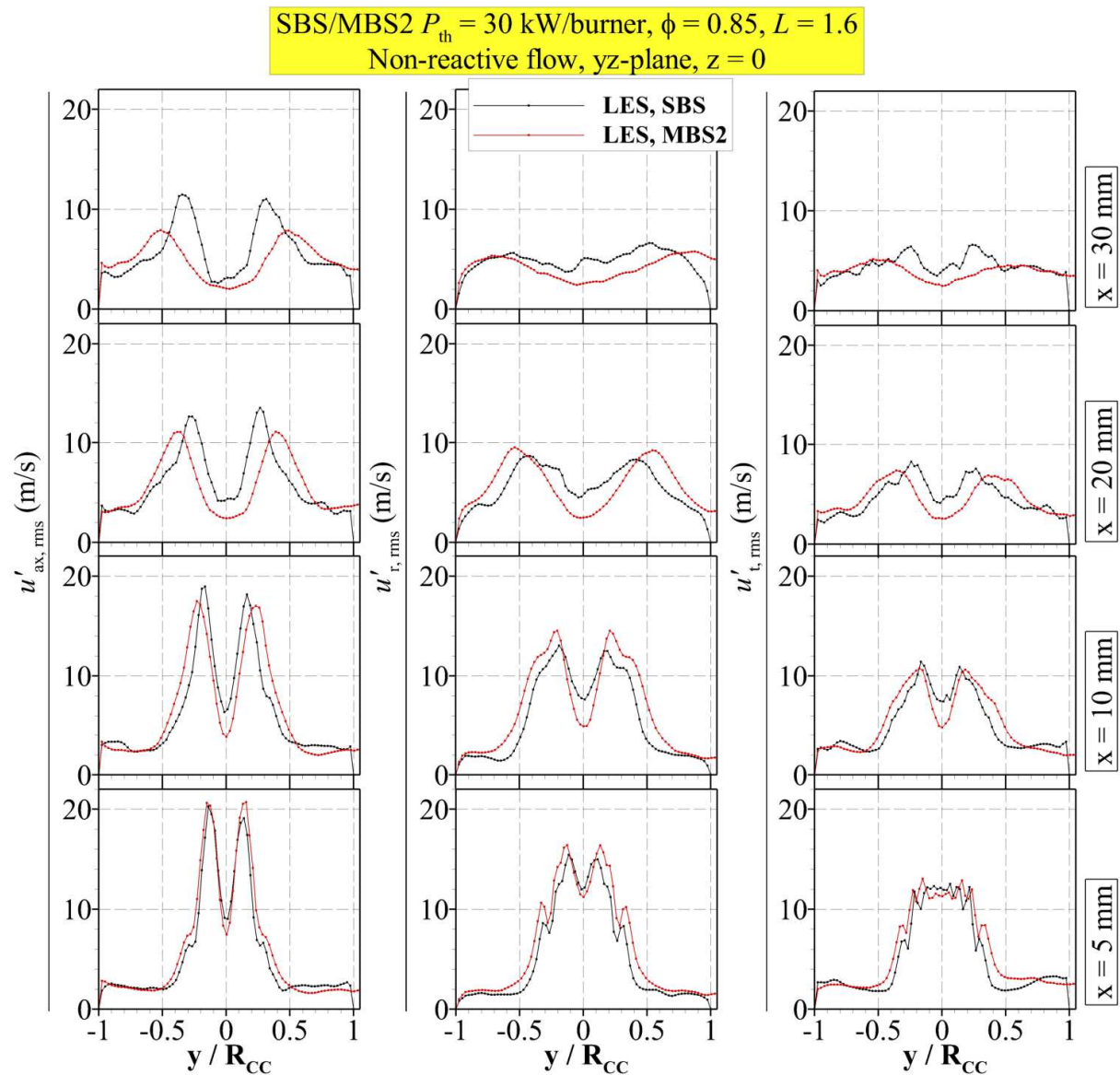


**Figure 5.22. SBS, MBS2,  $P_{th} = 30$  kW/burner,  $\phi = 0.85$ ,  $L = 1.6$ : RMS velocity fluctuations in the non-reactive flow**

Figure 5.23 shows the vectors of the velocity components in the  $yx$ -plane at  $x = 0.03$  m. The co-rotating swirl jets induce a secondary flow in the centre of the combustion chamber which rotates in the opposite direction of the swirl jets.

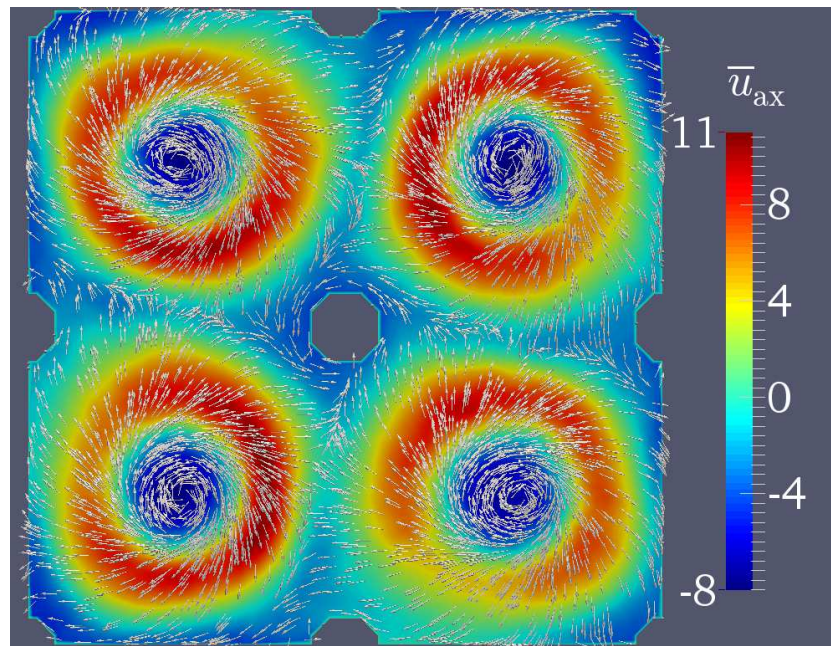


**Figure 5.23. MBS2,  $P_{th} = 30$  kW/burner,  $\phi = 0.85$ ,  $L = 1.6$ : Vectors of the velocity components in the  $yz$ -plane at  $x = 0.03$**

#### *Oscillations of Pressure, Velocity and Mixture Fraction*

Figure 5.24 compares the pressure oscillations in the combustion chamber computed by the LES with the measured pressure spectrum. A good agreement between the measured and the computed spectrum is observed.

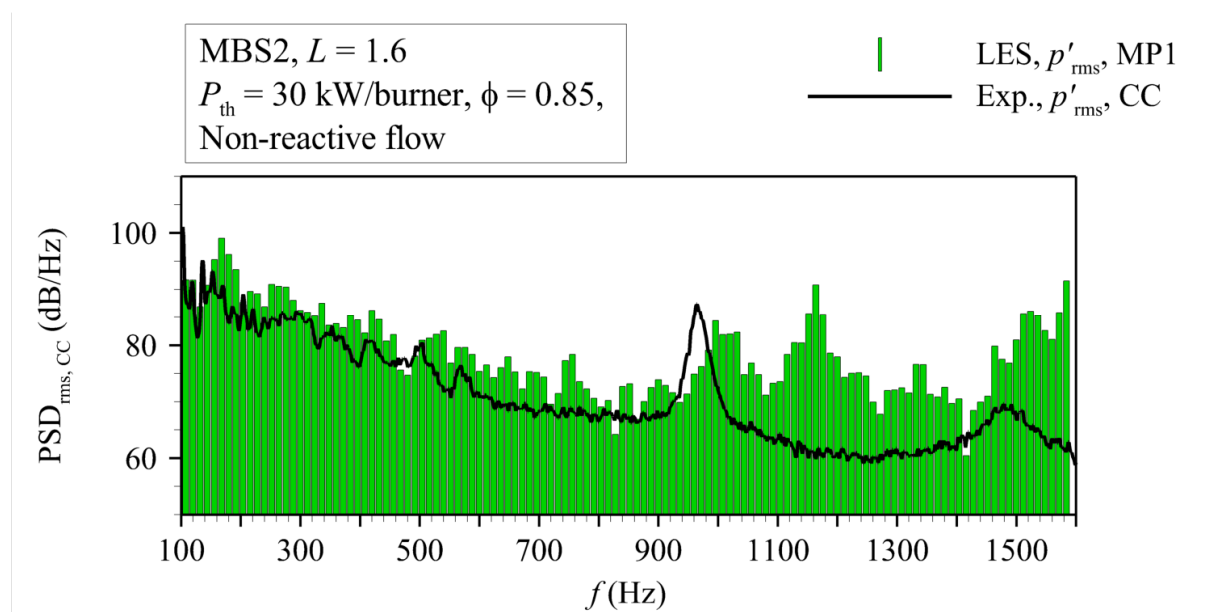


**Figure 5.24. MBS2,  $P_{th} = 30$  kW/burner,  $\phi = 0.85$ ,  $L = 1.6$ : Comparison of the measured and computed pressure oscillations in the combustion chamber**

The deviation of the peaks at around 1000 Hz in the LES may be caused by the missing fuel flow in the experiment which leads to a smaller frequency of the described vortex shedding at the nozzle outlet. The frequency at  $\sim 1150$  Hz in the LES-spectrum most likely belongs to the PVC and represents hydrodynamic pressure oscillations, which are not captured by the microphone in the experiment.

The spectrum of the mixture fraction oscillations at MP2 (Figure 5.25) comply with the assumption that the peak in the computed pressure spectrum corresponds to the PVC. Similar to the SBS, the dominant frequency is found around 1150 Hz. The amplitudes of the mixture fraction oscillations in the MBS2 are generally smaller than in the SBS. The most significant differences are the peaks in the spectrum of the SBS at 360 Hz and 750 Hz, which are not observed in the MBS2.

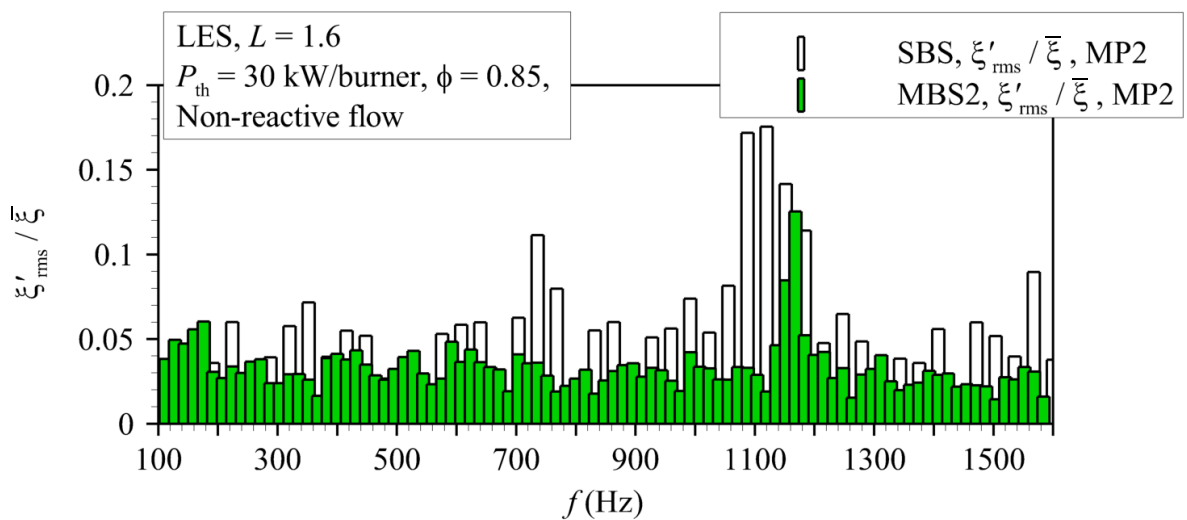


**Figure 5.25. SBS, MBS2,  $P_{th} = 30$  kW/burner,  $\phi = 0.85$ ,  $L = 1.6$ : Mixture fraction oscillations in the non-reactive flow at MP2**

The PVC can be visualized by an isosurface of the pressure at  $p = 99600$  Pa, as shown in Figure 5.26. It is clearly visible that the PVC strongly affects and intensifies the mixing process of air and fuel. The spectra of the axial velocity in the inner swirler at MP3 and the inner plenum at MP4 (Figure 5.27) illustrate that the multiple-burner arrangement has a destabilizing effect on the IRZ. The amplitudes of the axial velocity oscillations in the inner plenum are significantly smaller in the MBS2 and only one peak in the range of the 190-Hz mode is observed. However, the velocity perturbations in the region at the onset of the IRZ in the inner swirler exceed the ones in the SBS by an order of magnitude. The contour plots of the mixture fraction oscillations in Figure 5.28 also illustrate the higher mixing intensity in the MBS2 in the radial direction, whereas the SBS shows a higher mixing rate in the axial direction, which is indicated by the isoline of the stoichiometric mixture fraction.

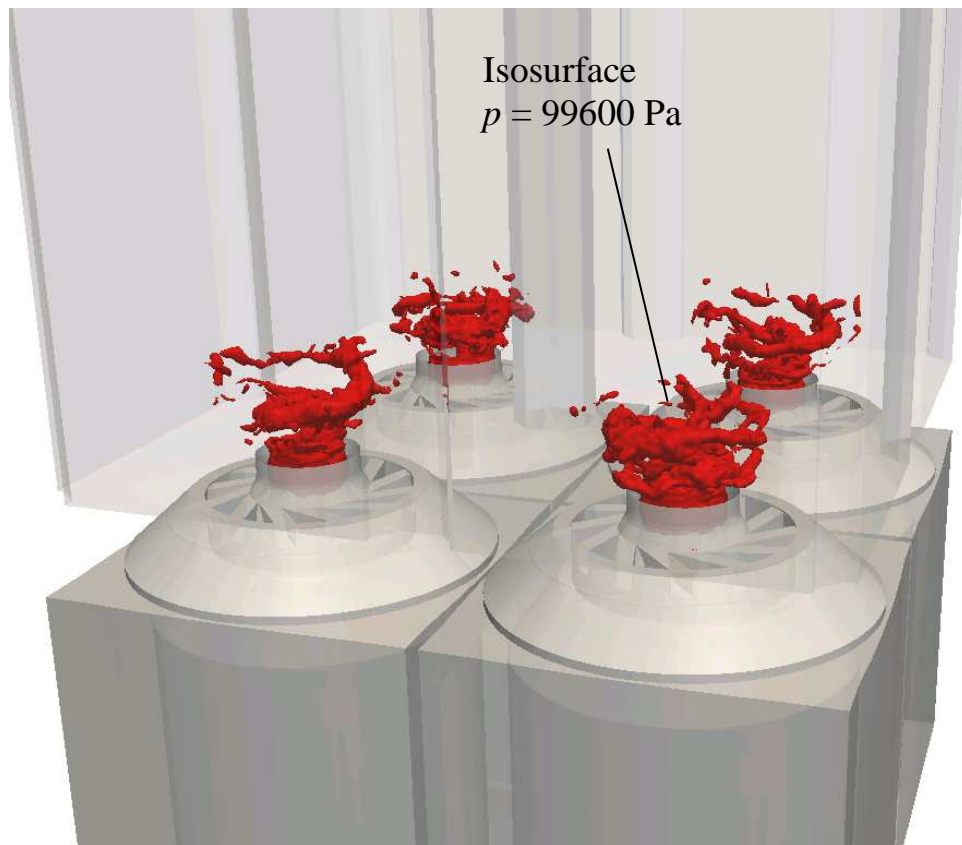
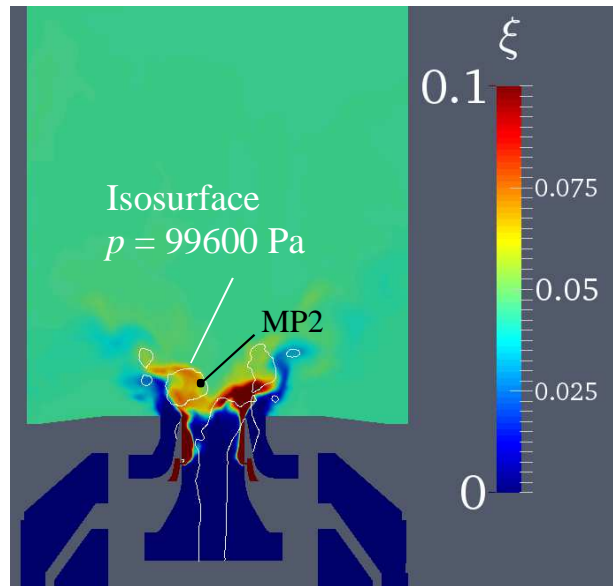


**Figure 5.26.** MBS2,  $P_{th} = 30$  kW/burner,  $\phi = 0.85$ ,  $L = 1.6$ : Visualization of the PVC with the isosurface at  $p = 99600$  Pa in the MBS2

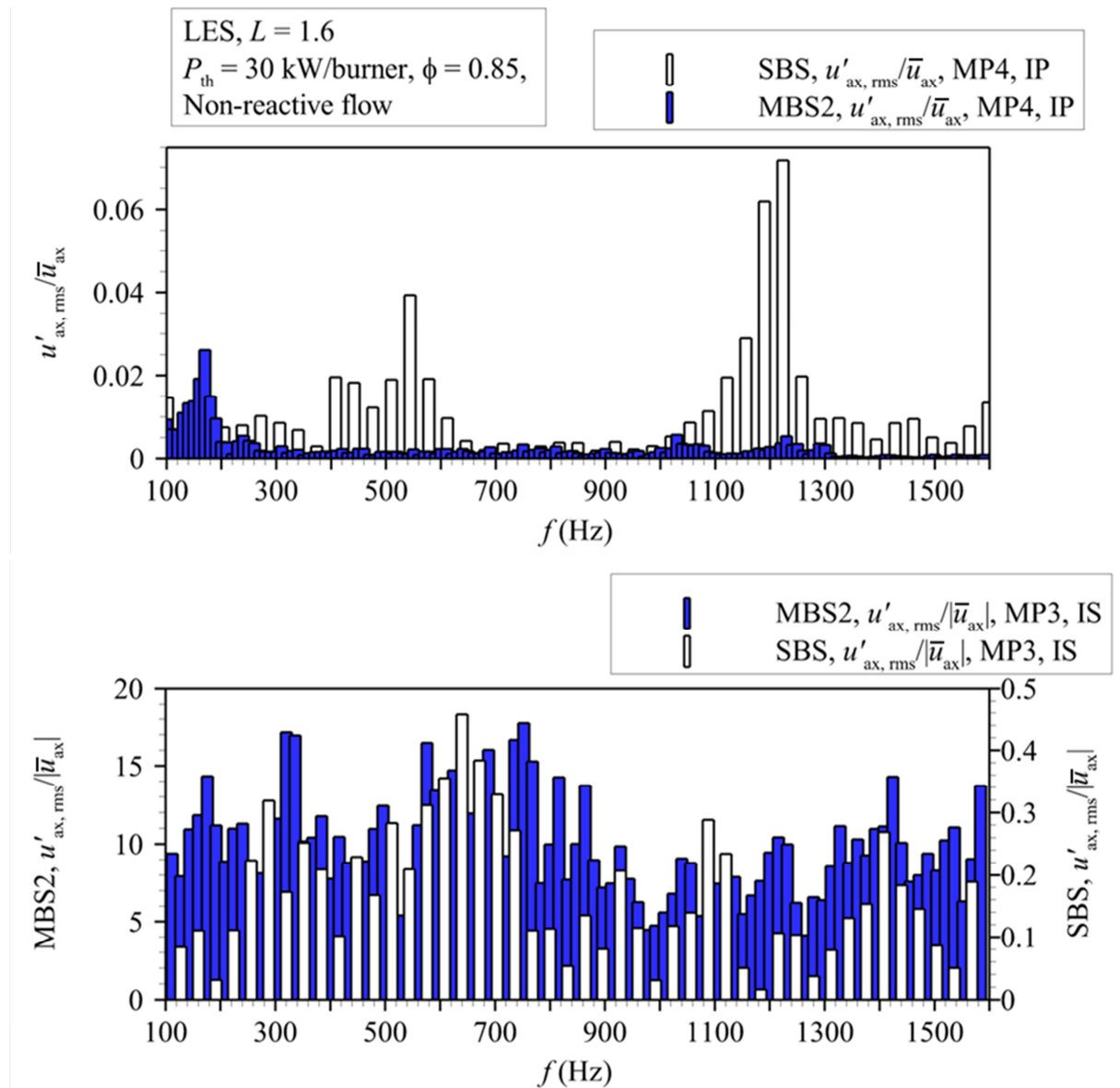


Figure 5.27. SBS, MBS2,  $P_{th} = 30$  kW/burner,  $\phi = 0.85$ ,  $L = 1.6$ : Axial velocity oscillations at MP3 in the inner swirler (IS) and at MP4 in the inner plenum (IP)

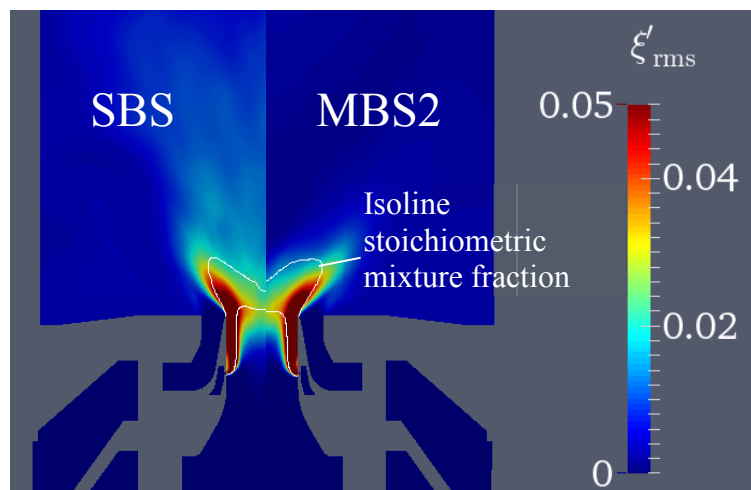
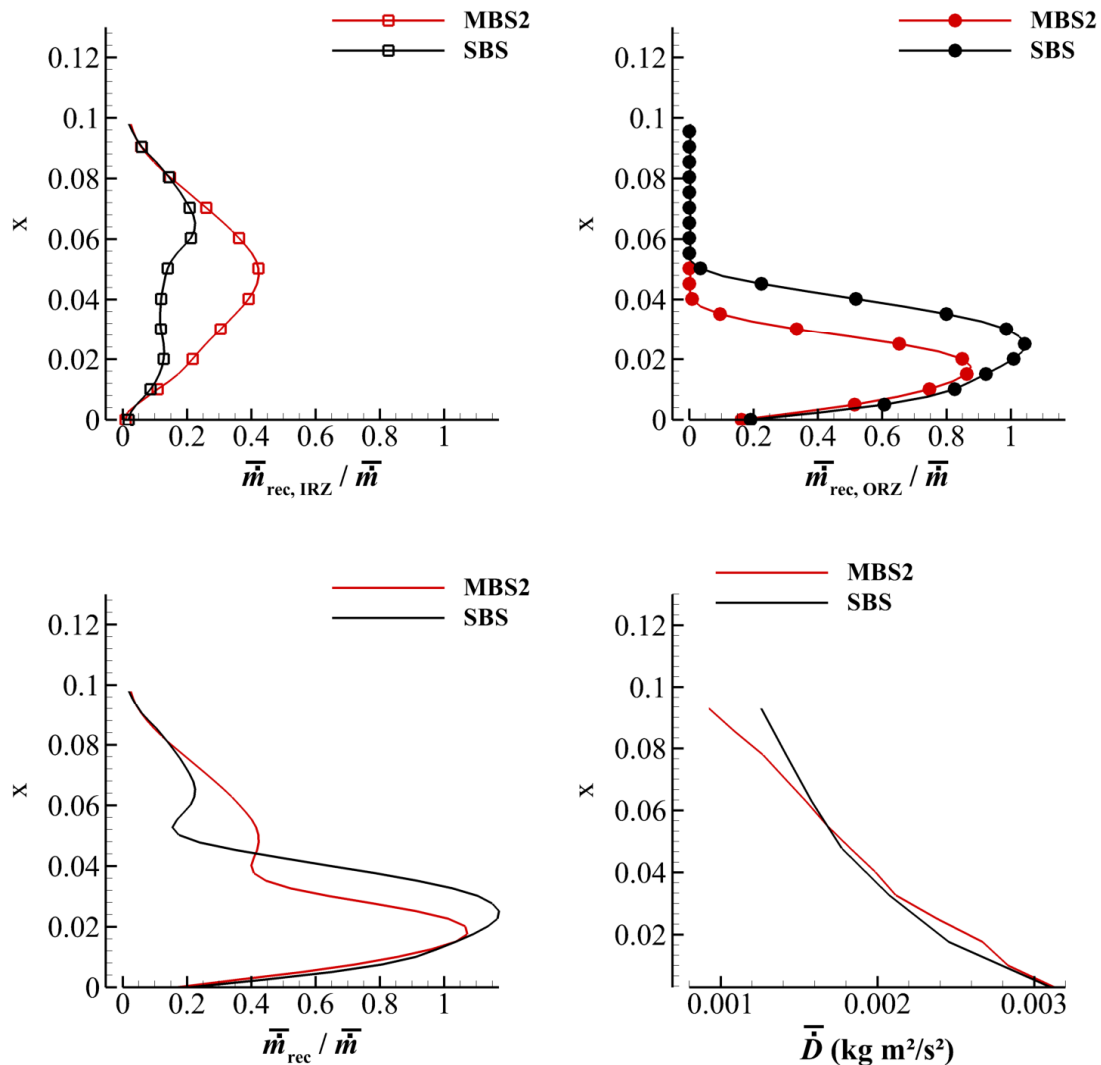


Figure 5.28. SBS, MBS2,  $P_{th} = 30$  kW/burner,  $\phi = 0.85$ ,  $L = 1.6$ : RMS mixture fraction oscillations and isoline of the stoichiometric mixture fraction in the non-reactive flow

### Mean Recirculation Rates in the SBS and the MBS2 in the Non-Reactive Flow

Figure 5.29 compares the mass flow recirculation rates in the IRZ and the ORZ, the global mass flow recirculation rate and the angular momentum flux. The terms of the turbulent fluctuations were neglected in the calculation of the angular momentum flux. In the MBS2, the mass recirculation rates and the angular momentum flux were calculated for one single-burner, which was extracted from the flow region.



**Figure 5.29.** SBS, MBS2 at  $P_{th} = 30$  kW/burner,  $\phi = 0.85$ ,  $L = 1.6$ : Mass flow recirculation rates and angular momentum flux

It is clearly visible that the MBS2 features a significantly higher inner recirculation rate, whereas a higher amount of mass is recirculated in the ORZs of the SBS. The characteristics of the swirl flow in the MBS2 are much more comparable to a swirl jet in wall jet regime, in spite of the missing side walls and the slightly reduced angular momentum flux around  $x = 0.08$ .

The swirl flow in the SBS features the characteristics of a free-jet, with high mass flow recirculation rates in the ORZs. The slight decrease of the angular momentum flux in the MBS2 with increasing axial distance to the nozzle may be caused by the reduction of the angular momentum due to the adjacent swirl jet described by Hirsch et al in [27], as already discussed in 4.5.5.

### 5.3.2 Reactive Flow

#### 5.3.2.1 LES Single-Burner Setup, $P_{th} = 25 \text{ kW}$ , $\phi = 0.7$ , $L = 1.6$

##### *Comparison of the calculated velocity fields with the PIV Measurements*

At  $P_{th} = 25 \text{ kW}$ ,  $\phi = 0.7$ , the mean velocity profiles of all velocity components derived from the LES agree quite well with measured values, which is visible in Figure 5.30.

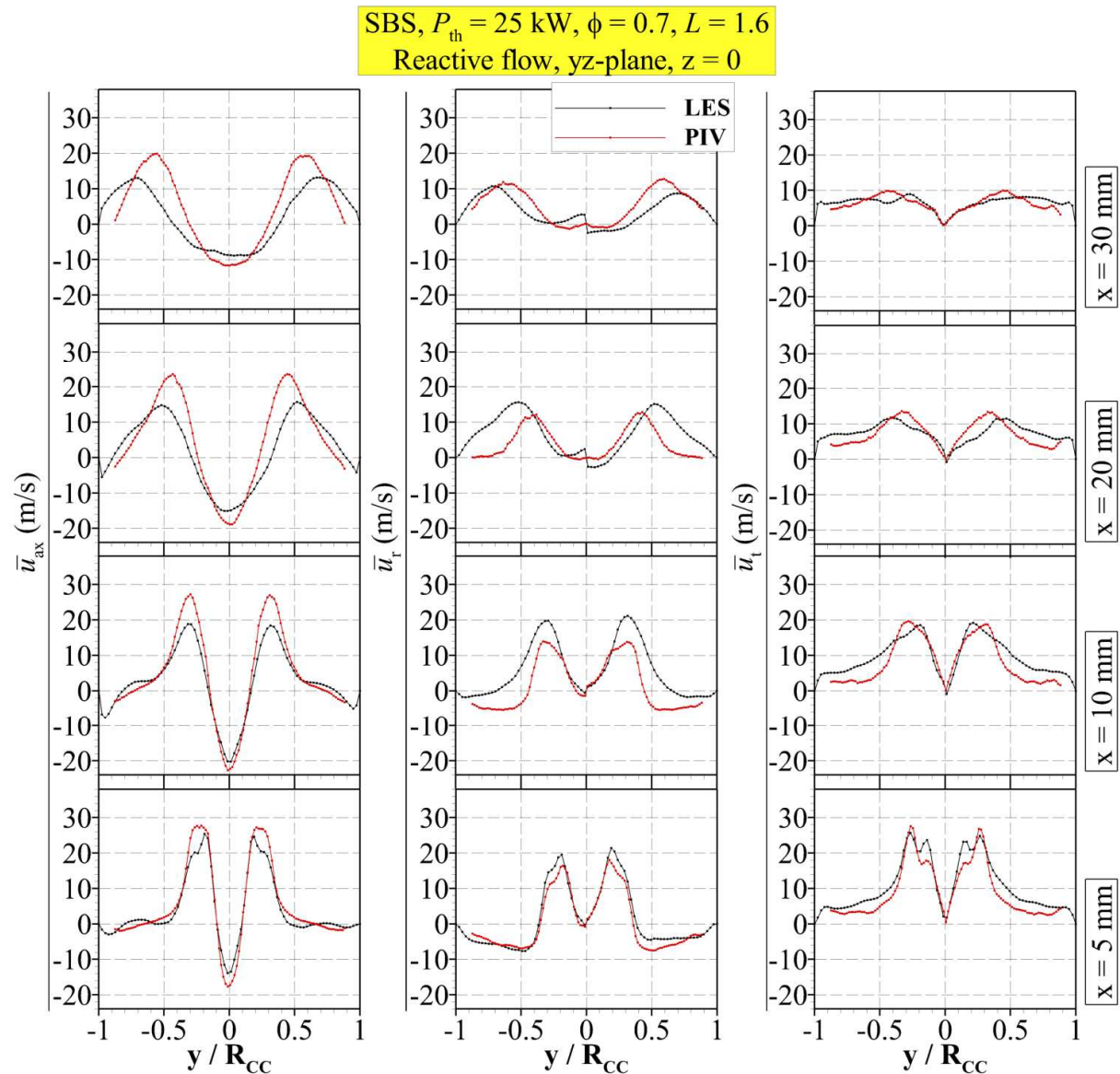


**Figure 5.30.** SBS,  $P_{th} = 25 \text{ kW}$ ,  $\phi = 0.7$ ,  $L = 1.6$ : Time-averaged velocity profiles in the reactive flow at different axial distances to the nozzle in the LES and the experiment

However, some deviations between the simulation and the experiment are visible. Noteworthy are the higher radial velocities in the LES at  $x = 10$  mm and 20 mm. In addition, the angle of the swirl jet predicted by the LES exceeds the one observed in the PIV measurements, which is visible at  $x = 20$  mm and  $x = 30$  mm as well as in the contour plot of the axial velocity in Figure 5.31. The LES seems to overestimate the radial transport of angular momentum. It is possible that the reason for the observed deviation between the LES and the PIV is caused by the increased turbulence level in the LES near the nozzle outlet. This was also observed for the non-reacting flow. The location of the maximum values of the RMS velocity fluctuations of the LES and the PIV measurements are very similar, but the calculated maximum values are more than 100 % higher in the LES than in the experiment (Figure 5.32). The increased turbulence intensity in the LES possibly increases the radial transport of angular momentum, which results in a more wall-bounded flow field than in the experiment.

**SBS,  $P_{th} = 25$  kW,  $\phi = 0.7$ ,  $L = 1.6$**   
**Reactive flow, yz-plane,  $z = 0$**

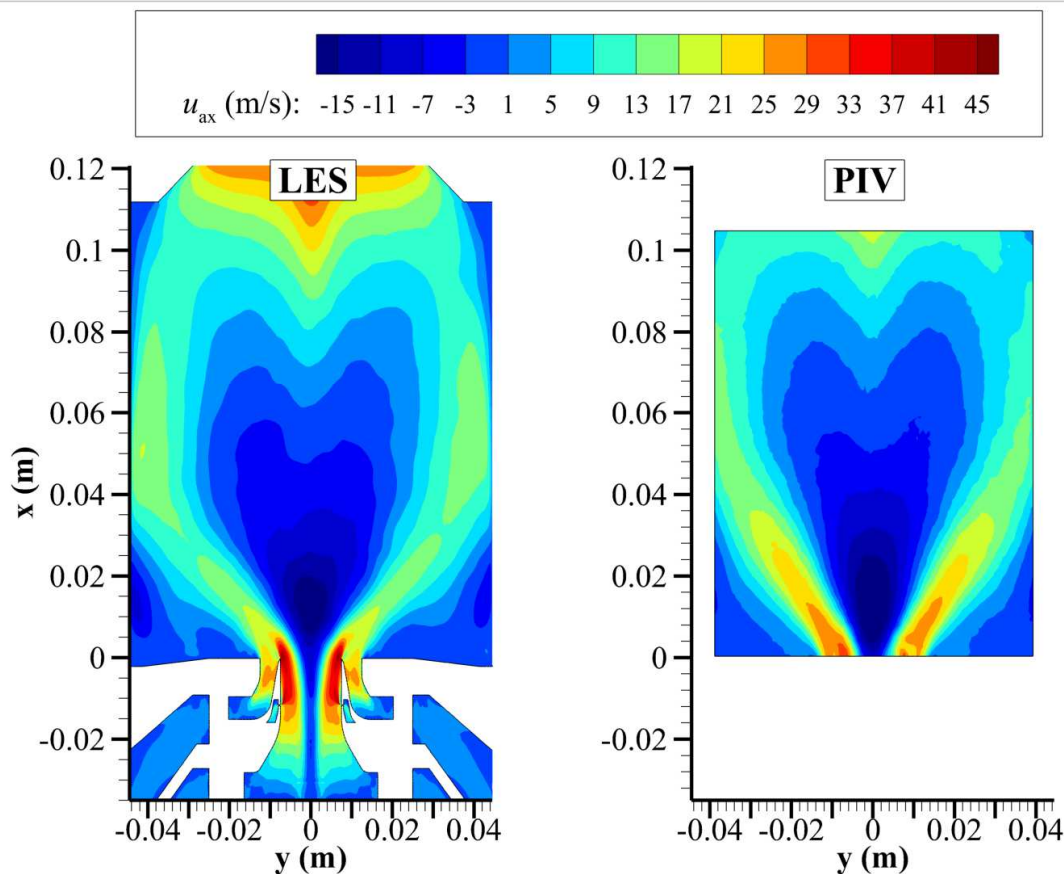


**Figure 5.31. SBS,  $P_{th} = 25$  kW,  $\phi = 0.7$ ,  $L = 1.6$ : Contour plots of the time-averaged axial velocity in the reactive flow in the LES and the experiment**

The velocity fluctuations are highly dependent on the intensity level of the combustion dynamics, and more intense pressure oscillations normally lead to increased velocity fluctuations. Therefore the intensity of the unsteady heat release of the flame has a major

influence on the velocity fluctuations in the experiment and the LES. Therefore different amplitudes of unstable modes in the PIV measurements and the LES may contribute to the observed deviation. It is also possible that the LES is not statistically converged, considering the computed time period of ca. 0.12 s. This can lead to deviations of the mean and the RMS values between the LES and the experiment, where recording times of about 1 s are common. In addition, as outlined in the discussion of the non-reactive flow, the inlet BCs do not consider possible damping effects of the perforated plates, which can result in increased velocity fluctuations. This is discussed in more detail in the next but one section, where spectra of heat release, velocity and pressure oscillations are analysed.

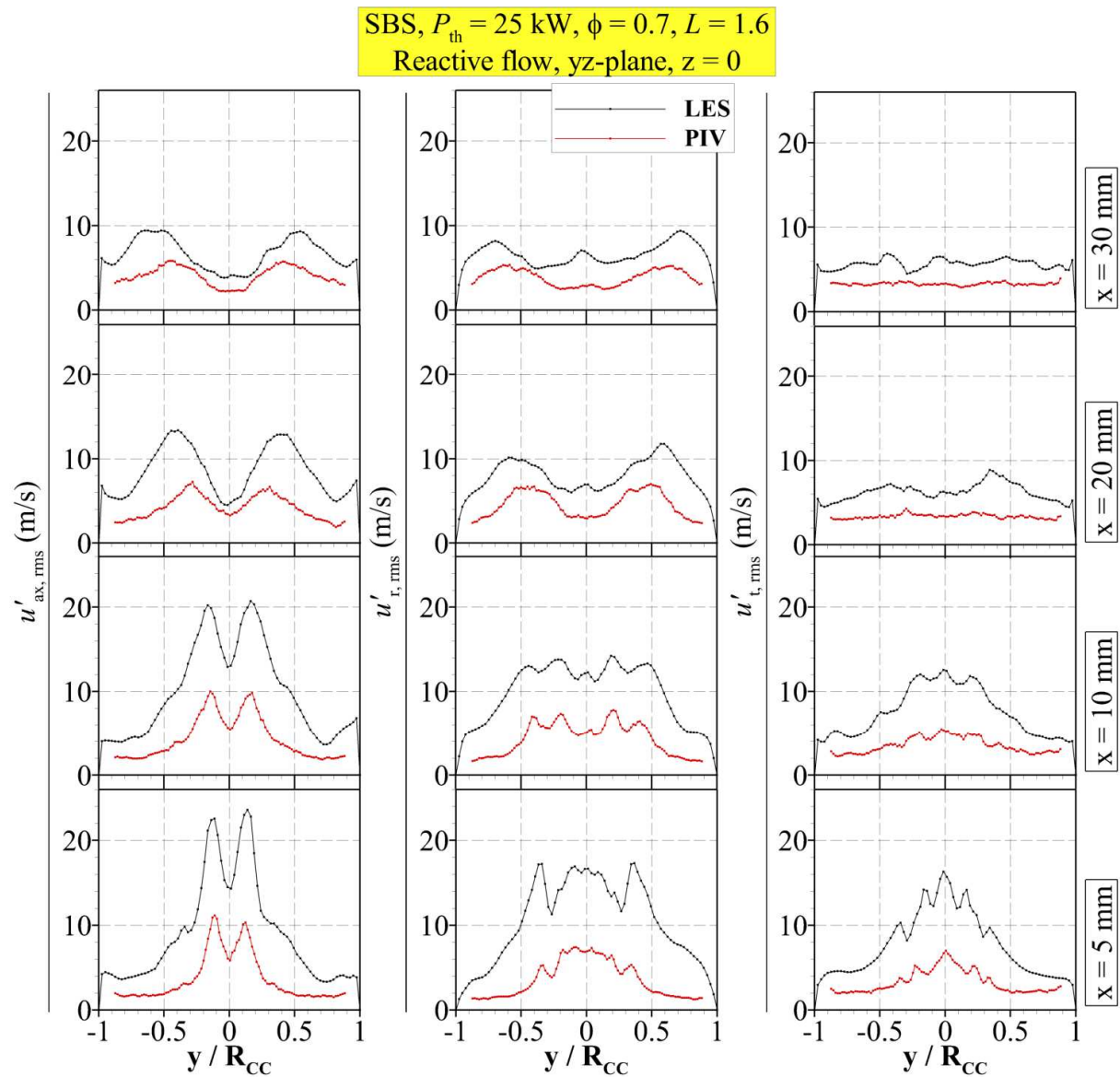


**Figure 5.32.** SBS,  $P_{th} = 25$  kW,  $\phi = 0.7$ ,  $L = 1.6$ : RMS velocity fluctuations in the reactive flow at different axial distances to the nozzle in the LES and the experiment

### Mean fields of Mixture fraction, Temperature and Heat release

Figure 5.33 shows the average temperature and heat release distributions in the combustion chamber. The maximum calculated temperatures are in the range of 1900 K and are located inside the IRZ. The IRZ and the ORZs stabilize the flame by recirculating burnt gases, as indicated by the high temperatures in these areas. The high mean reaction rates near the nozzle outlet on the burner axis are induced by stoichiometric mixture fractions. The flame shape and the distribution of the main reaction zones resembles the mean OH\*-intensity (Figure 5.34).

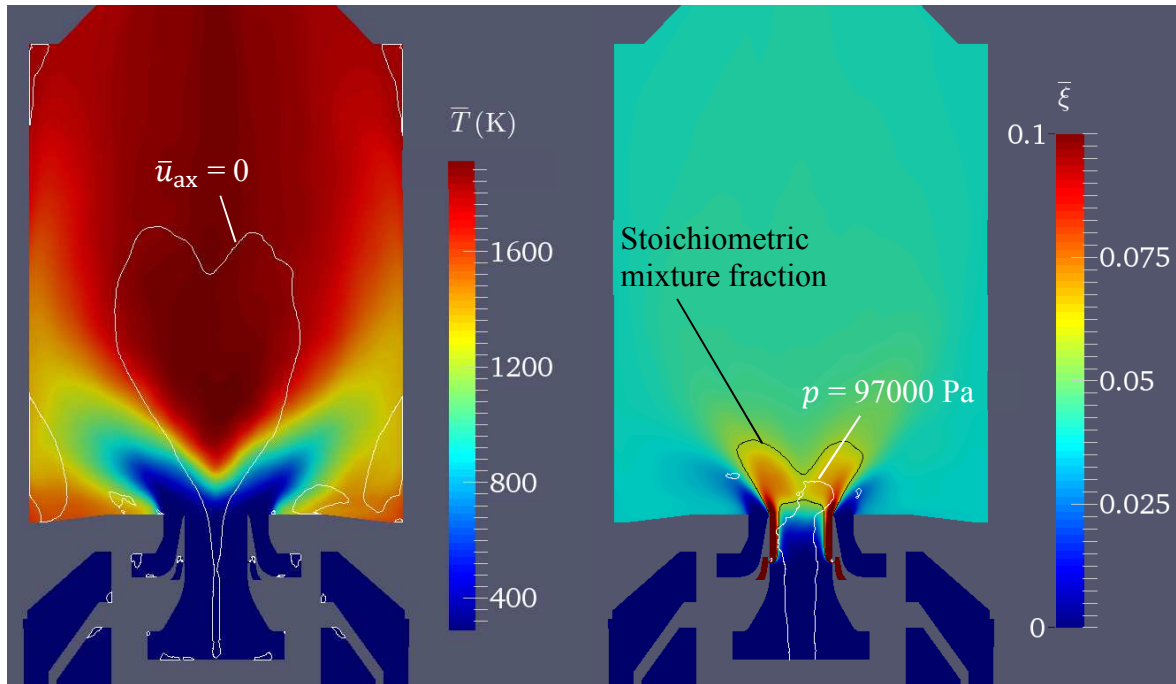


**Figure 5.33.** SBS,  $P_{th} = 25$  kW,  $\phi = 0.7$ ,  $L = 1.6$ : Mean temperature field in the combustion chamber (l.h.s.); Mean heat release field (r.h.s.)

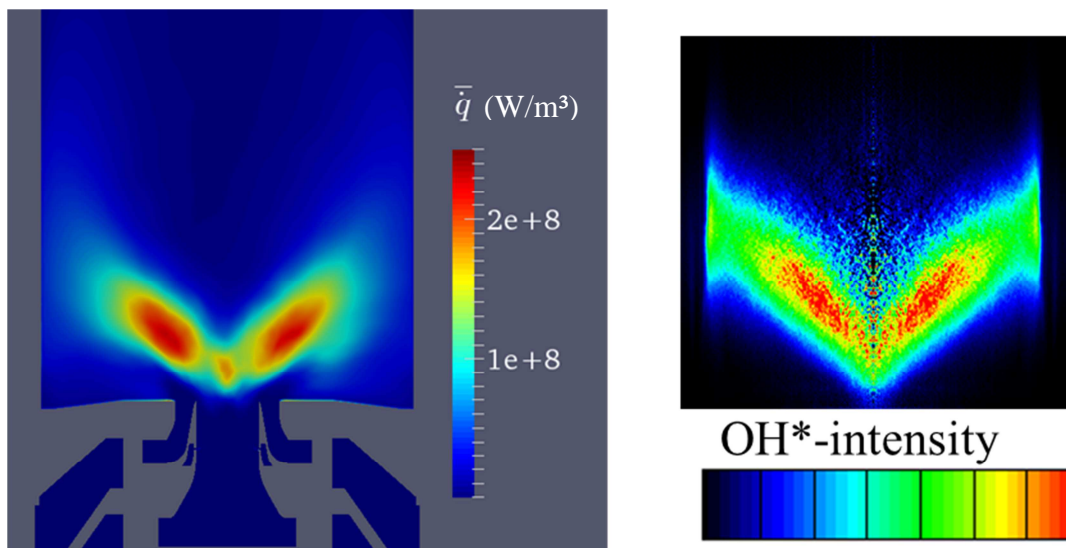


**Figure 5.34.** SBS,  $P_{th} = 25$  kW,  $\phi = 0.7$ ,  $L = 1.6$ : Mean mixture fraction in the combustion chamber

### Pressure, Velocity and Heat Release Oscillations

At first, it should be investigated whether or not the LES is able to reproduce the combustion dynamics of the flame pulsation which was observed in the experiment. Figure 5.35 shows both the measured and the calculated spectra of the pressure oscillations in the combustion chambers.

The spectra show a partial agreement between experiment and simulation, as the dominant frequencies at 320 Hz, 570 Hz, 700 Hz and 800 Hz in the measured spectrum are reproduced by the LES. However, the peak frequency in the LES constitutes around 480 Hz and therefore does not match with the measured peak frequency, which is  $\sim 400$  Hz. In addition, several peaks show higher amplitudes in the LES. As mentioned in the discussion of the results for the non-reactive flow, this may be induced by the pressure BC at the inlets which lack the frequency-dependent attenuation of the perforate plates installed in the real combustor.

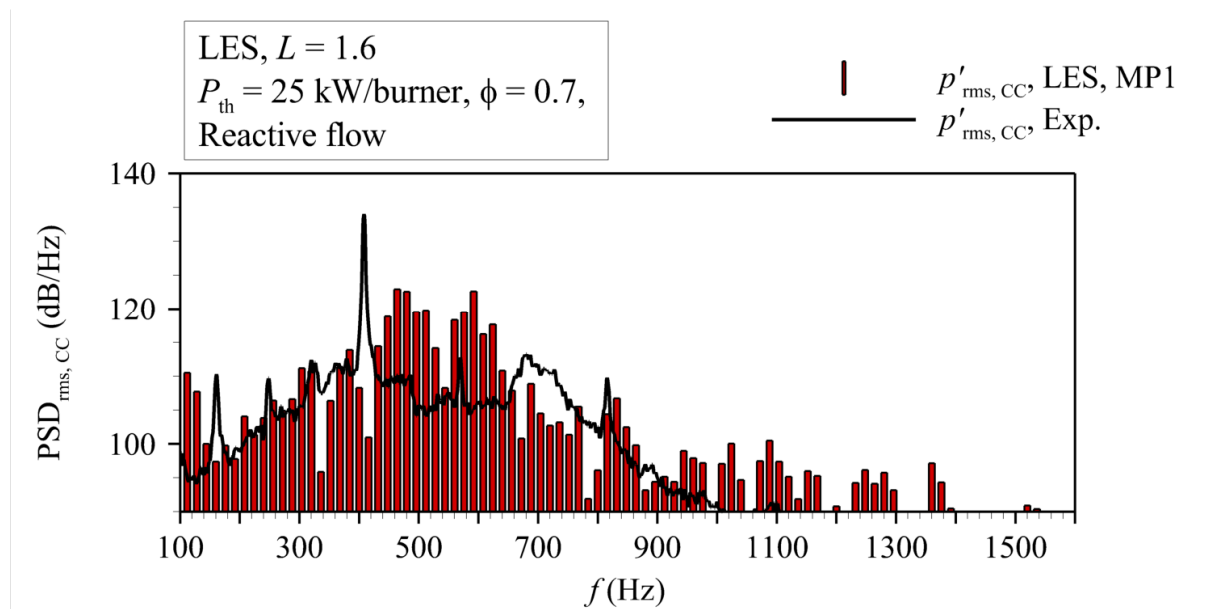


**Figure 5.35. SBS,  $P_{th} = 25$  kW,  $\phi = 0.7$ ,  $L = 1.6$ : Measured and calculated spectrum of the pressure oscillations in the combustion chamber**

Comparing the spectra of the OH\*-intensity and the heat release oscillations calculated by the LES, one can observe that the normalized heat release oscillations are significantly smaller than the OH\*-intensity oscillations (Figure 5.36). However, several peaks in the spectra match, for example at  $\sim 380$  Hz and  $\sim 570$  Hz. There are several possible reasons for the deviation between heat release and OH\*-intensity oscillations. First, as discussed in 4.2.2, the OH\*-intensity oscillations are most likely associated with heat release oscillations as well as equivalence ratio oscillations, since the flame is not perfectly premixed. In addition, if the oscillation in the LES at  $\sim 380$  Hz corresponds to the oscillation of the 400-Hz mode observed in the experiment, then the 400 Hz-Mode apparently does not reach similar amplitudes in terms of heat release and pressure oscillations.

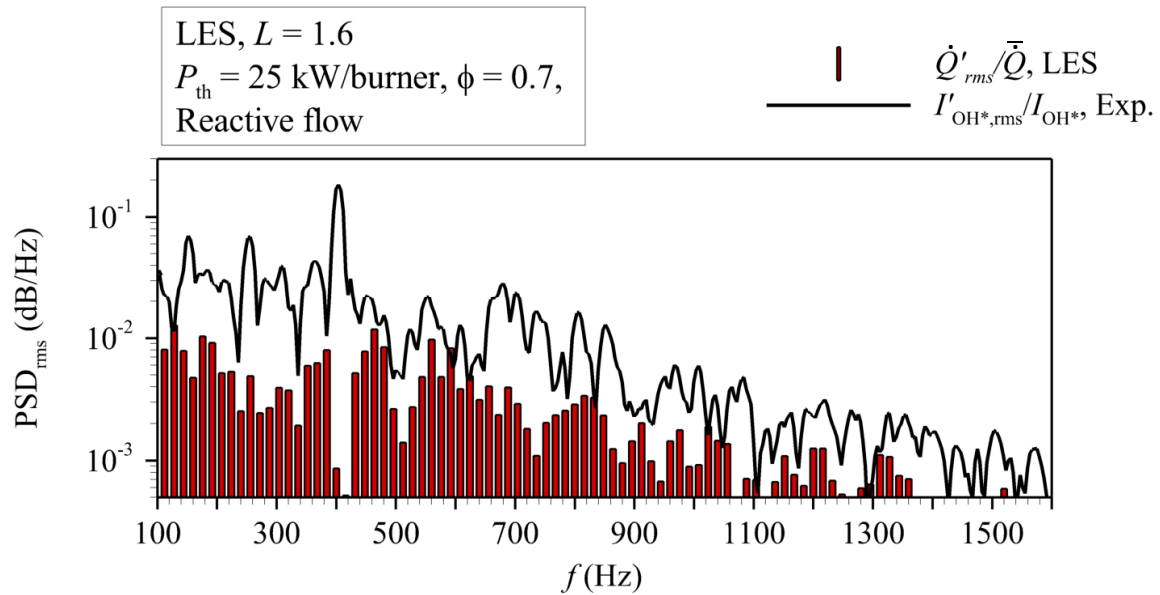


**Figure 5.36. SBS,  $P_{th} = 25 \text{ kW}$ ,  $\phi = 0.7$ ,  $L = 1.6$ :  $\text{OH}^*$ -intensity spectrum of the high-speed  $\text{OH}^*$ -recordings and heat release oscillations computed by the LES**

Figure 5.37(a) shows the time series plot of the heat release calculated by the LES. The plotted time does not correspond to the overall computing time. Starting with the cold flow solution, the LES was run for about 0.01 s (physical time) in order to wait for the initial disturbances to settle down and the flame to spread inside the combustion chamber. Another 0.01 s was computed in order to wait for the reactive flow to generate instabilities. The plot demonstrates the discussed problem when performing self-excited LES (see 3.4.2) of combustion instabilities. A lot of interfering frequencies are visible and it is not clear, whether or when the system will tune to one specific oscillation when the simulation is continued. However, the presence of several modes in the LES complies with the experiment.

More distinct periodic fluctuations of the heat release are visible at the end of the time series plot. This is also illustrated by the plot in Figure 5.37(b), which shows the sequence marked with the dashed rectangle in Figure 5.37(a). In addition to the heat release oscillations, the pressure oscillations at MP1 are plotted. At the beginning of the sequence, pressure and heat release are in phase, which leads to augmented pressure and heat release oscillations. Starting at around 0.082 s, the phase between the pressure and heat release oscillation starts to grow again, and the amplitudes of pressure and heat release oscillation start to diminish. It appears that several modes in the heat release fluctuations are interfering, which leads to temporary in-phase oscillations of heat release and pressure. Whether or not the temporary in-phase oscillations of heat release and pressure take place periodically could only be determined by additional computing. The spectra of the sequences of the pressure and heat release are shown in Figure 5.38. Two major modes for pressure and heat release are observed in the range of 400 Hz and 570 Hz. The 570-Hz mode is much more dominant compared to the mode at 400 Hz, and features significantly higher amplitudes in the LES than in the experiment.

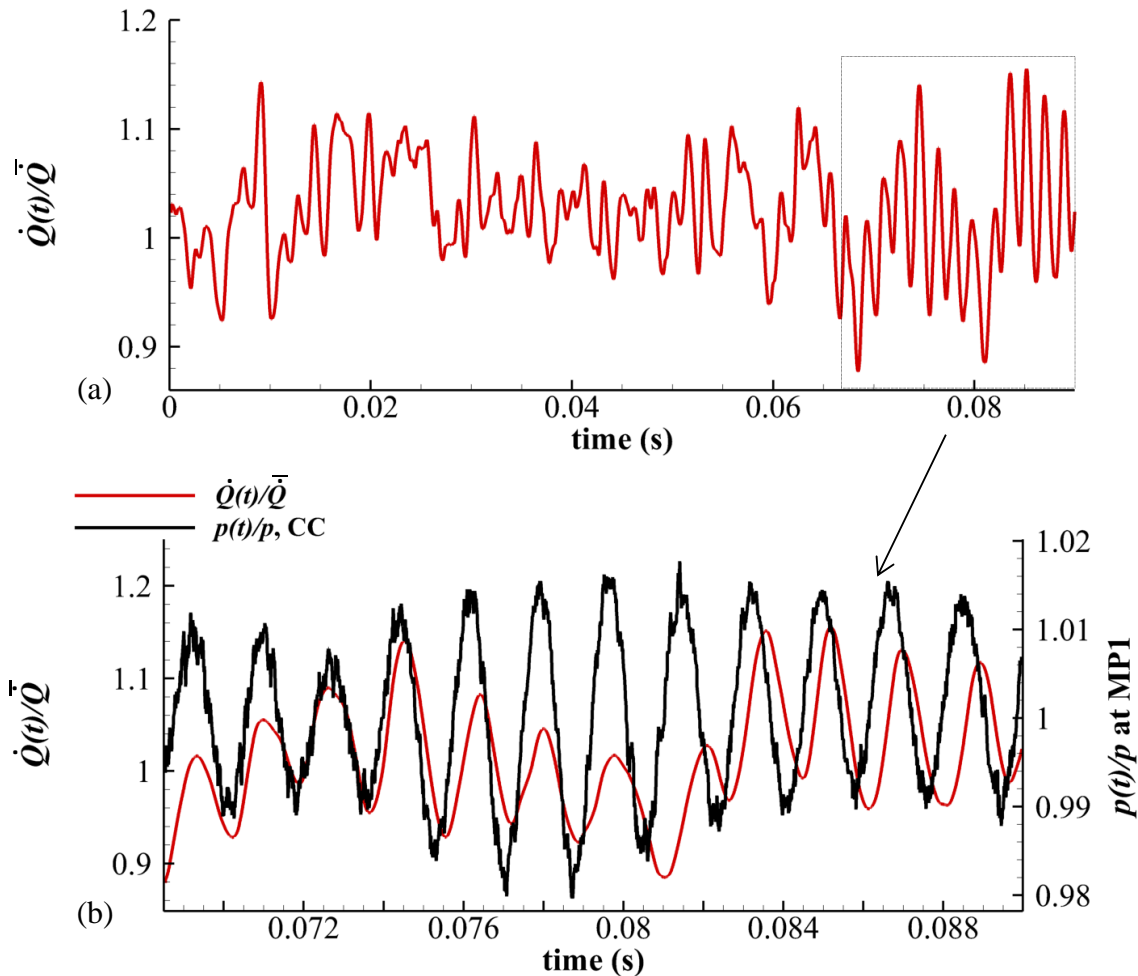


**Figure 5.37. SBS,  $P_{th} = 25$  kW,  $\phi = 0.7$ ,  $L = 1.6$ : (a) Time series plot of computed heat release; (b) Sequence of computed heat release and pressure oscillations**

Therefore, the mode at 570 Hz represents the major unstable mode predicted by the LES. The time series of the mass flow rates at the swirler inlets, the fuel mass flow rate at the nozzle outlet and the heat release shown in Figure 5.39 illustrate the mechanism which drives the instability. Since heat release and pressure in the combustion chamber oscillate almost in phase, the increasing heat release results in an even further increase in the combustion chamber pressure. The oscillating combustion chamber pressure results in oscillations of the air and fuel mass flow rates inside the nozzle, which in turn modulate the heat release. The oscillations of the mass flow rates show relatively constant frequencies around 570 Hz.

The instantaneous image of the heat release in Figure 5.40 shows ring vortices which form inside the combustion chamber. Due to the intense mass flow rate oscillation, the fuel-air-mixture entering the combustion chamber is periodically accelerated and catches up with the slower fuel-air-mixture inside the combustion chamber. The flow deflects in the radial direction and forms the observed toroidal vortices. The coupling of the heat release oscillation with the intense pressure oscillation in the inner plenum is the mechanism which leads to the unstable mode. The contour plot of the RMS pressure fluctuations indicates the presence of a standing half-wave in the inner plenum. This is confirmed by the pressure spectrum at MP4 in

the inner plenum (Figure 5.41). The amplitude of this resonance significantly exceeds the measured amplitude. The deviation may again be explained by the different acoustic impedances of the inlet BC in the LES and the perforated plate installed in the real combustor and is possibly also the reason for the different frequencies of the ring vortex formation in the LES and the experiment.

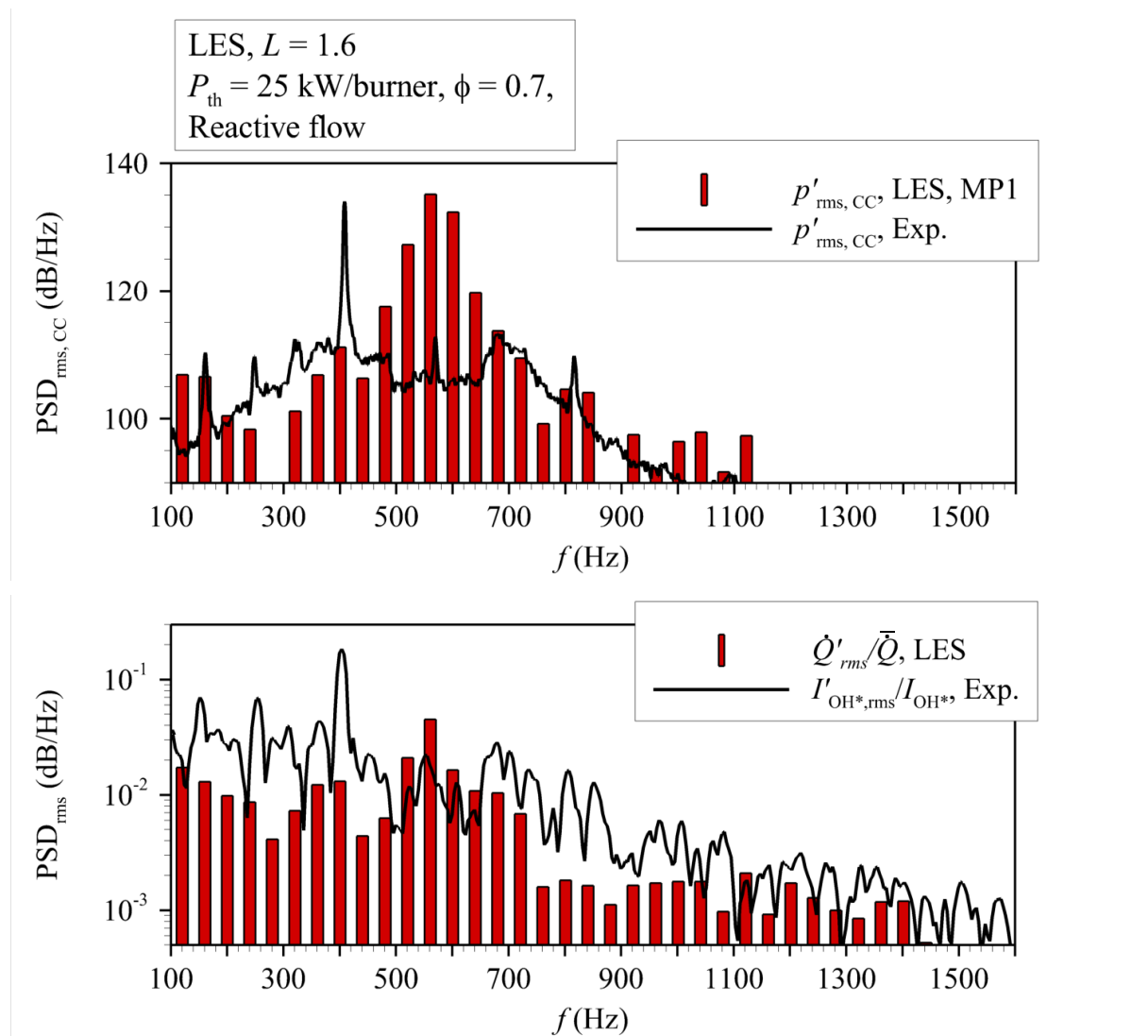


**Figure 5.38.** SBS,  $P_{\text{th}} = 25 \text{ kW}$ ,  $\phi = 0.7$ ,  $L = 1.6$ : Spectra of the time sequence of computed pressure und heat release oscillations shown Figure 5.37(b)

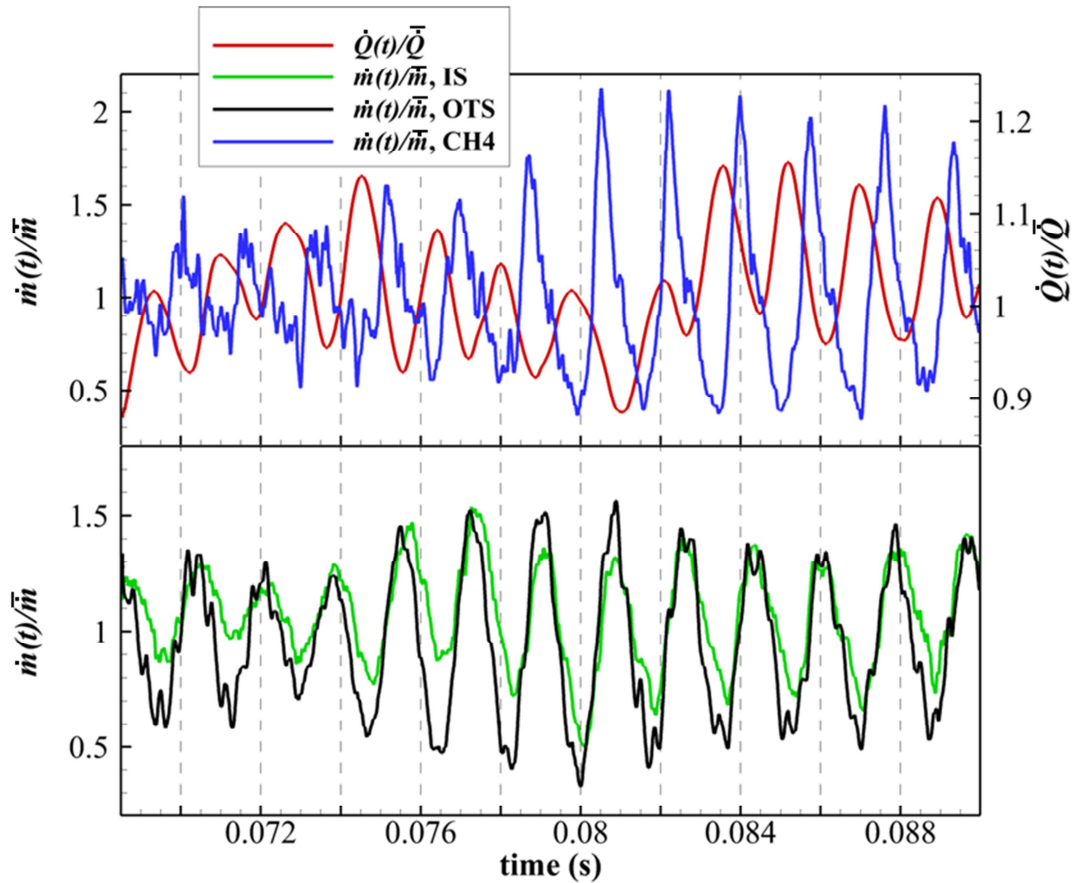


Figure 5.39. SBS,  $P_{th} = 25$  kW,  $\phi = 0.7$ ,  $L = 1.6$ : Computed time series of mass flow rates at the inlets of the inner (IS) and outer (OTS) swirler, fuel mass flow rate at the nozzle outlet and heat release

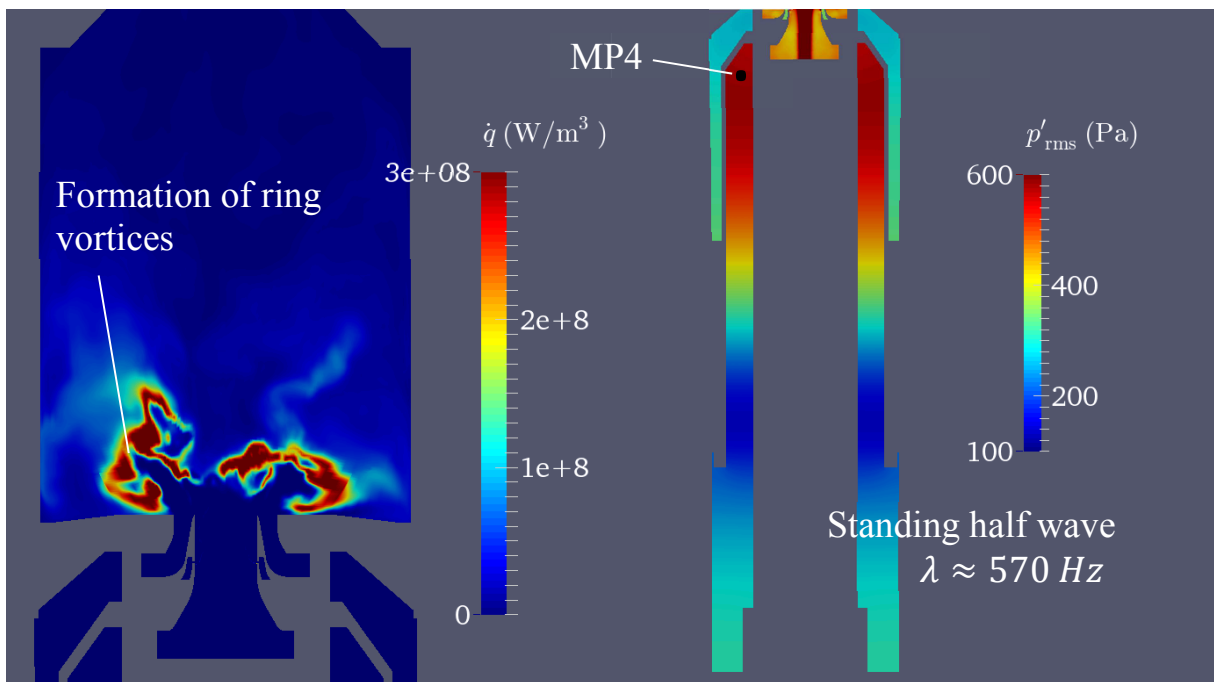


Figure 5.40. SBS,  $P_{th} = 25$  kW,  $\phi = 0.7$ ,  $L = 1.6$ : Ring vortex formation in the combustion chamber (l.h.s.); standing half wave in the inner plenum (IP) (r.h.s.)

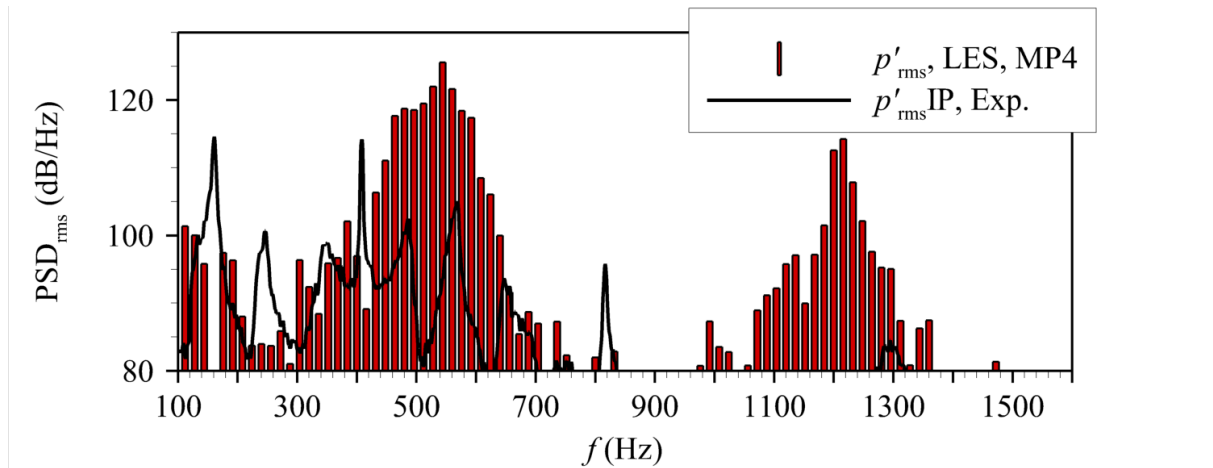


Figure 5.41. SBS,  $P_{th} = 25$  kW,  $\phi = 0.7$ ,  $L = 1.6$ : Measured and computed pressure spectra in the inner plenum (IP)

### 5.3.2.2 LES Single-Burner Setup, $P_{th} = 30$ kW, $\phi = 0.85$ , $L = 1.6$

#### Comparison of the Calculated Velocity Fields with the PIV Measurements

As discussed in 5.3.1.2, the LES of the non-reactive flow for  $P_{th} = 30$  kW,  $\phi = 0.85$  shows a much better agreement to the experimental results than the LES for  $P_{th} = 25$  kW,  $\phi = 0.7$ . As shown in Figure 5.42 and Figure 5.43, this is also the case for the LESs of the reactive flows.

SBS,  $P_{th} = 30$  kW,  $\phi = 0.85$ ,  $L = 1.6$   
Reactive flow, yz-plane,  $z = 0$

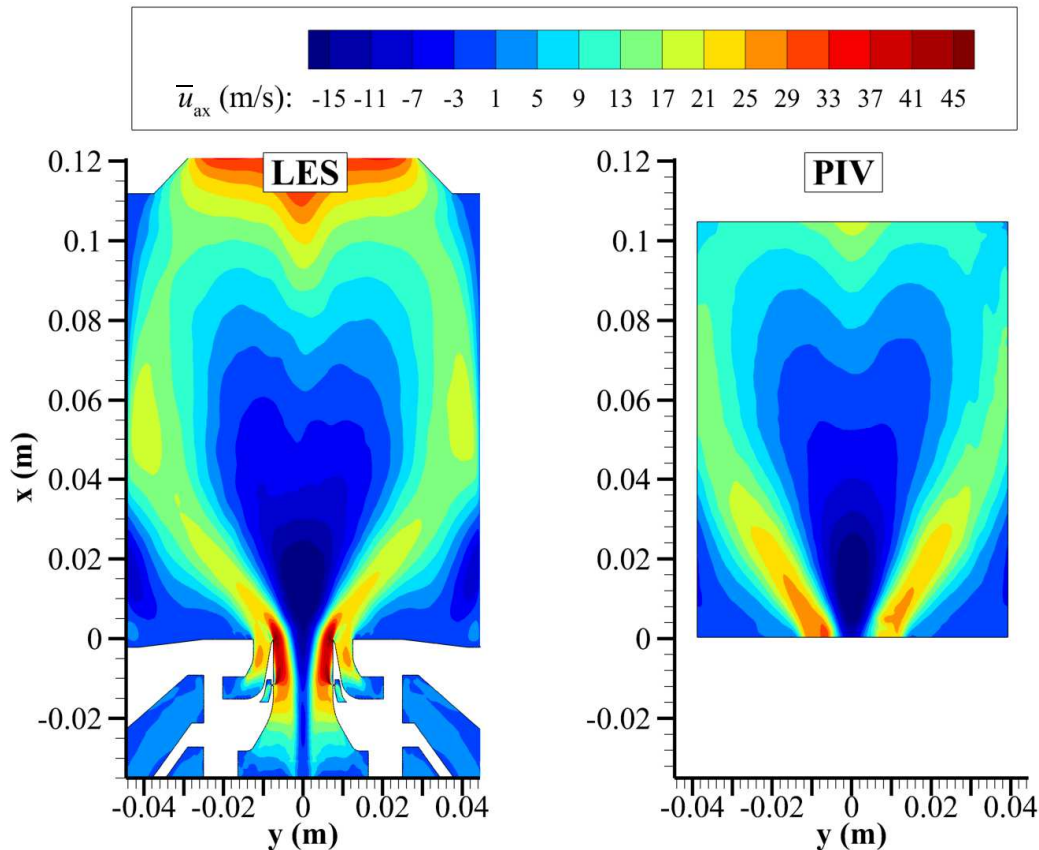
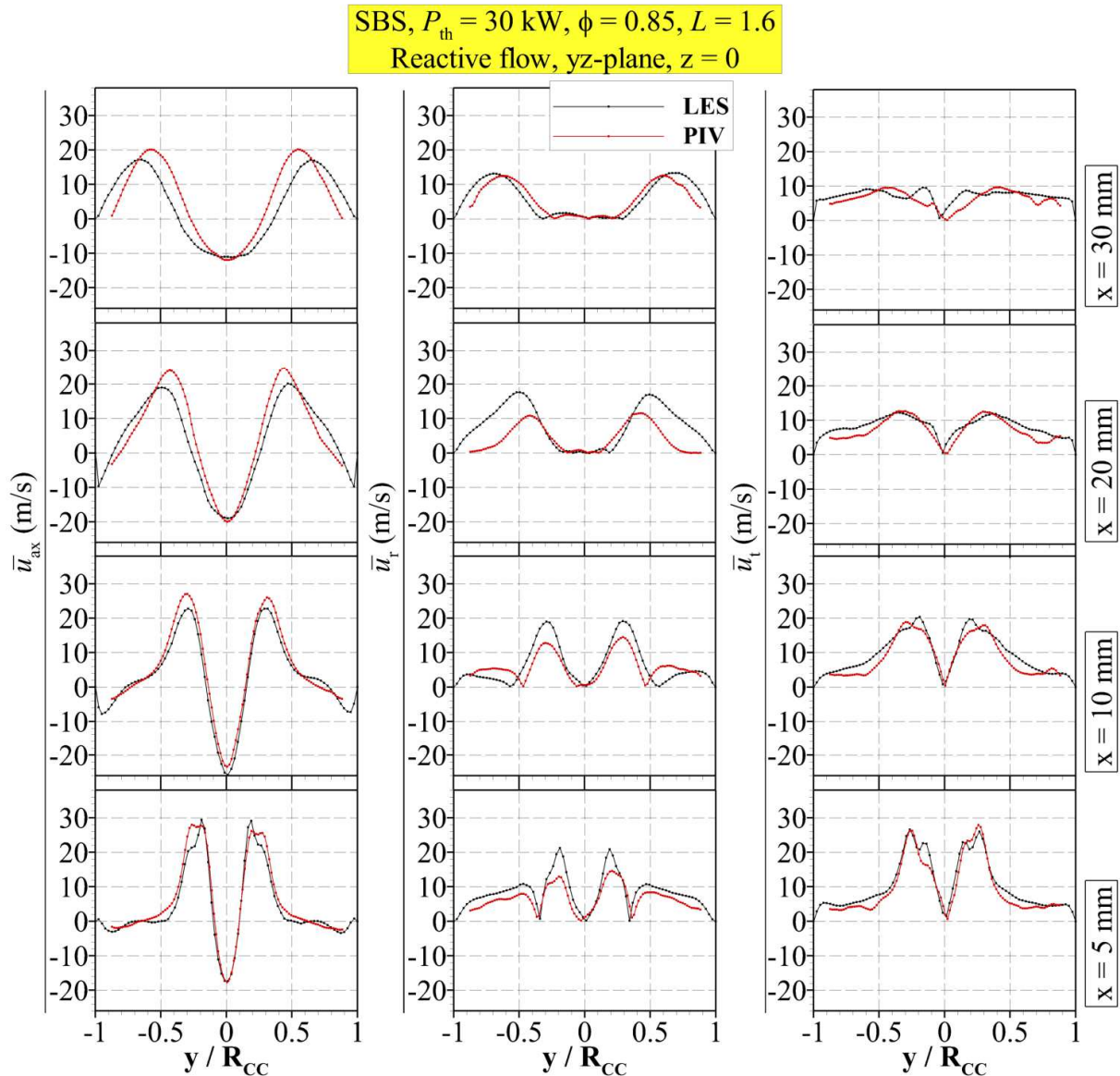


Figure 5.42. SBS,  $P_{th} = 30$  kW,  $\phi = 0.85$ ,  $L = 1.6$ : Contour plots of the time-averaged axial velocity in the reactive flow in the LES and the experiment

### 5.3 Numerical Results

Deviations between the LES and the experiment are observed regarding the jet angle of the swirl jet, which is wider in the LES. This complies with the higher radial velocities in the LES that cause an increased transport of angular momentum to higher radiuses, as illustrated by the velocity profiles of the tangential velocity. Also the calculated mean velocities and the RMS values of the velocity fluctuations show results that are similar to the results obtained by the PIV measurements (Figure 5.44). However, higher velocity fluctuations are observed in the LES, possibly induced by the inlet BCs, calculation time and different unstable modes, as discussed in the previous section.



**Figure 5.43. SBS,  $P_{th} = 30 \text{ kW}$ ,  $\phi = 0.85$ ,  $L = 1.6$ : Time-averaged velocity profiles in the reactive flow at different axial distances to the nozzle in the LES and the experiment**

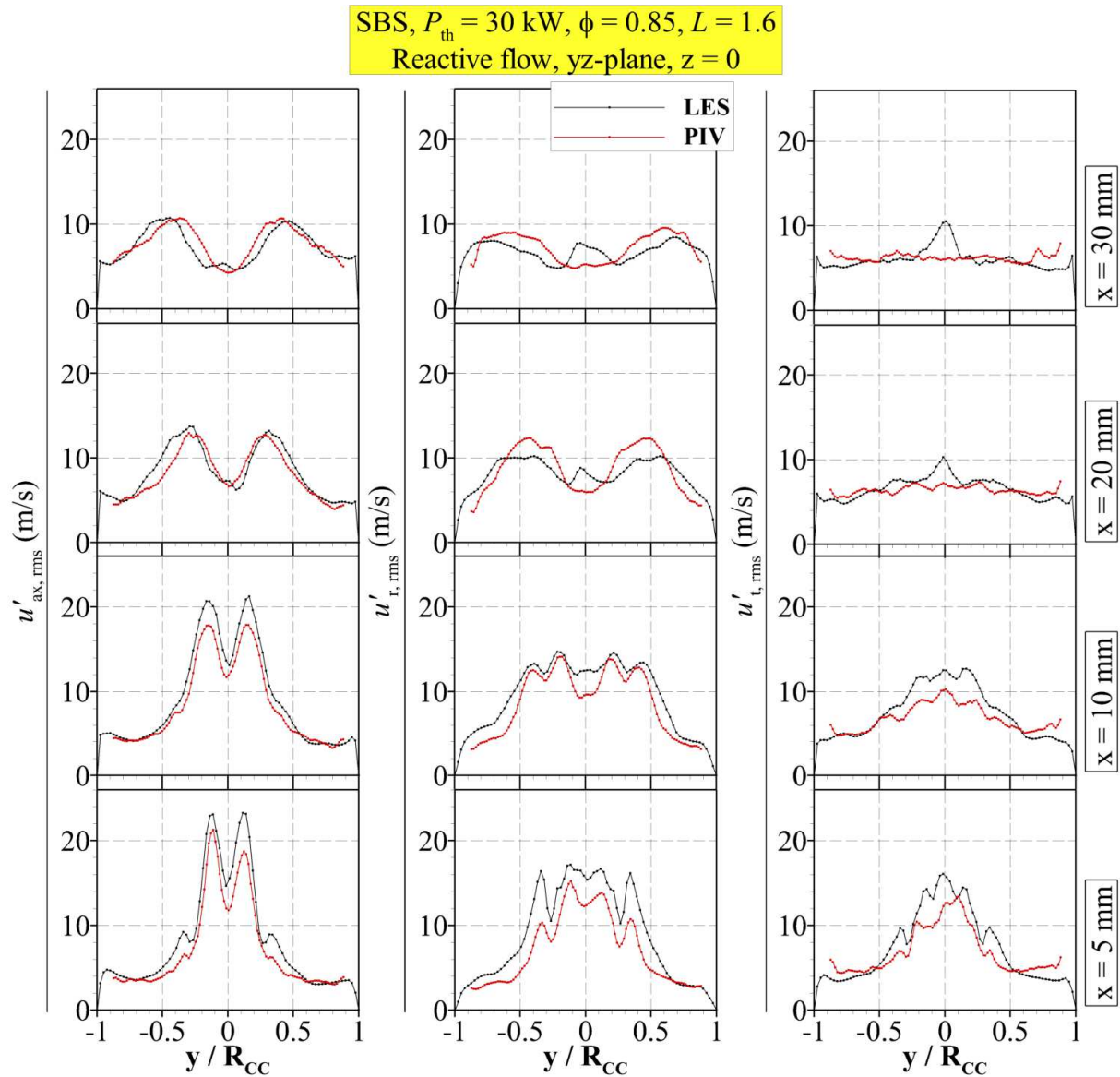
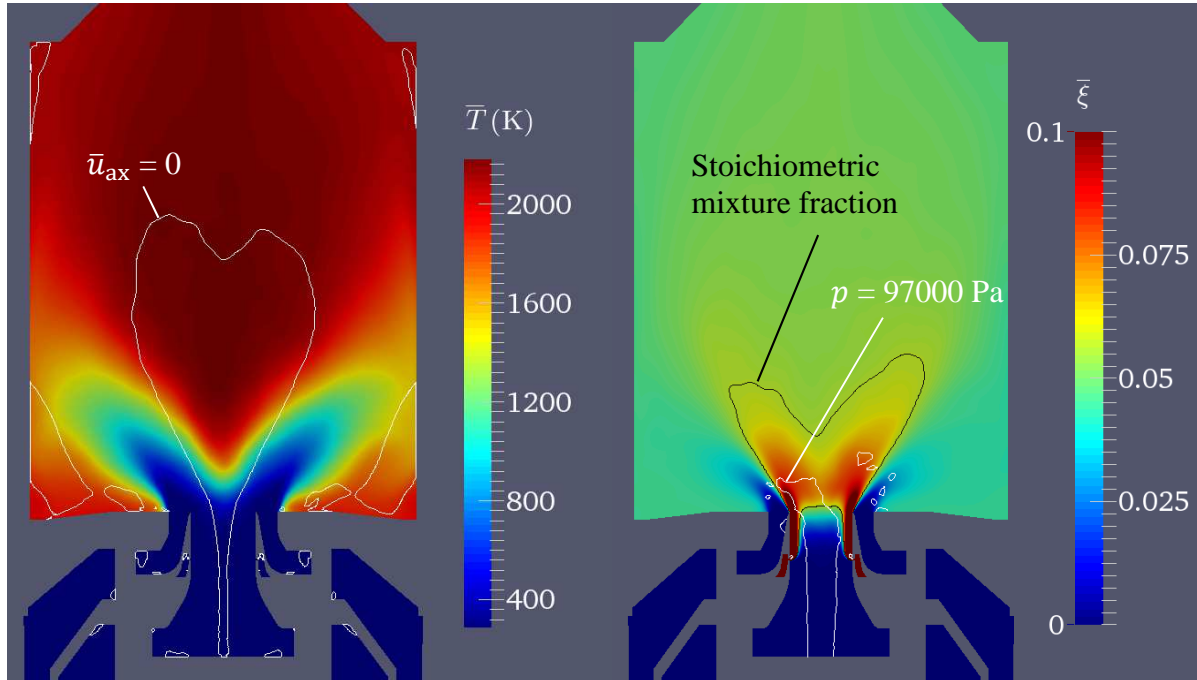


**Figure 5.44. SBS,  $P_{th} = 30$  kW,  $\phi = 0.85$ ,  $L = 1.6$ : RMS velocity fluctuations in the reactive flow at different axial distances to the nozzle in the LES and the experiment**

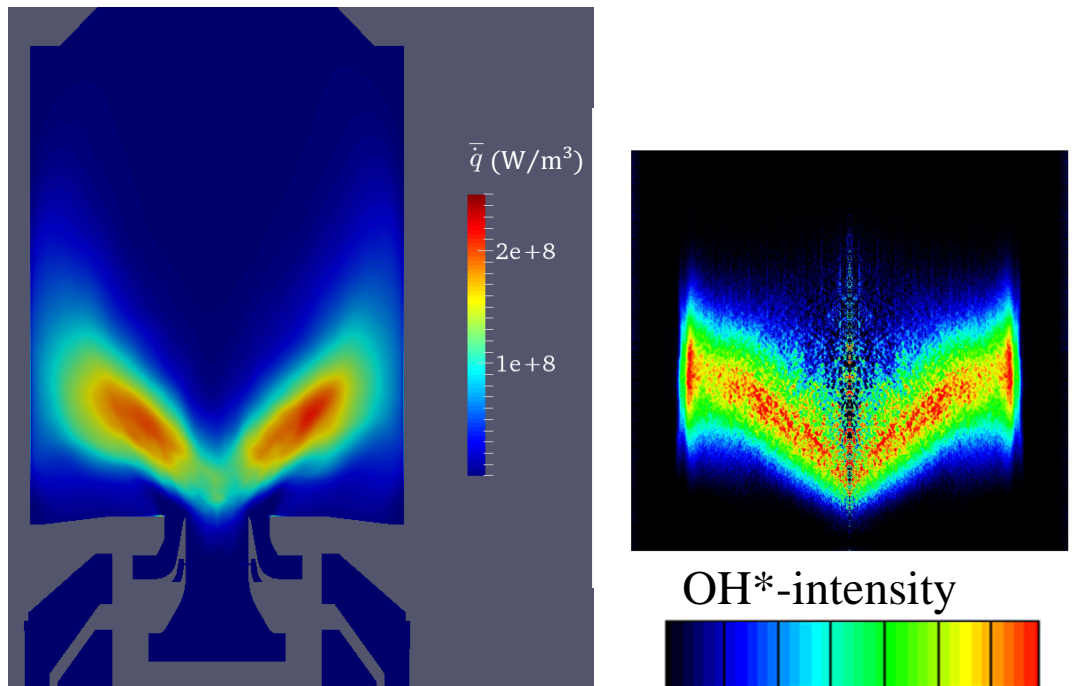
#### *Mean fields of Temperature, Heat Release and Mixture Fraction*

Figure 5.45 shows the results for the mean temperature, heat release and mixture fraction. The highest temperatures of around 2200 K are located in the IRZ. The increased fuel flow results in higher maximum temperatures compared to the OP  $P_{th} = 25$  kW,  $\phi = 0.7$ . The high temperatures of  $\sim 2000$  K in the ORZ are caused by the recirculation of burned gases. The isoline of the stoichiometric mixture fraction is located further upstream than at  $P_{th} = 25$  kW,  $\phi = 0.7$ , which is expected due to the increased fuel flow rate. The PVC is visualized by the isoline at 97000 Pa. It also strongly affects the mixing process in the reactive flow, but breaks down at smaller axial distances to the nozzle than in the non-reactive flow.

The contour plot of the mean heat release rate shows that the flame stabilizes close to the nozzle exit. The comparison with the recorded OH\*-chemiluminescence indicates a good agreement between simulation and experiment in terms of mean flame position and mean flame shape (Figure 5.46).



**Figure 5.45. SBS,  $P_{th} = 30$  kW,  $\phi = 0.85$ ,  $L = 1.6$ : Mean fields of temperature and mixture fraction**



**Figure 5.46. SBS,  $P_{th} = 30$  kW,  $\phi = 0.85$ ,  $L = 1.6$ : Calculated mean heat release in the LES (l.h.s.) and Abel-transformed mean OH\*-chemiluminescence (r.h.s.)**

*Pressure, Velocity and Heat Release Oscillations*

Figure 5.47(a) compares the computed and measured pressure oscillations in the combustion chamber. It is observed that the unstable mode predicted by the LES differs from the experiment.

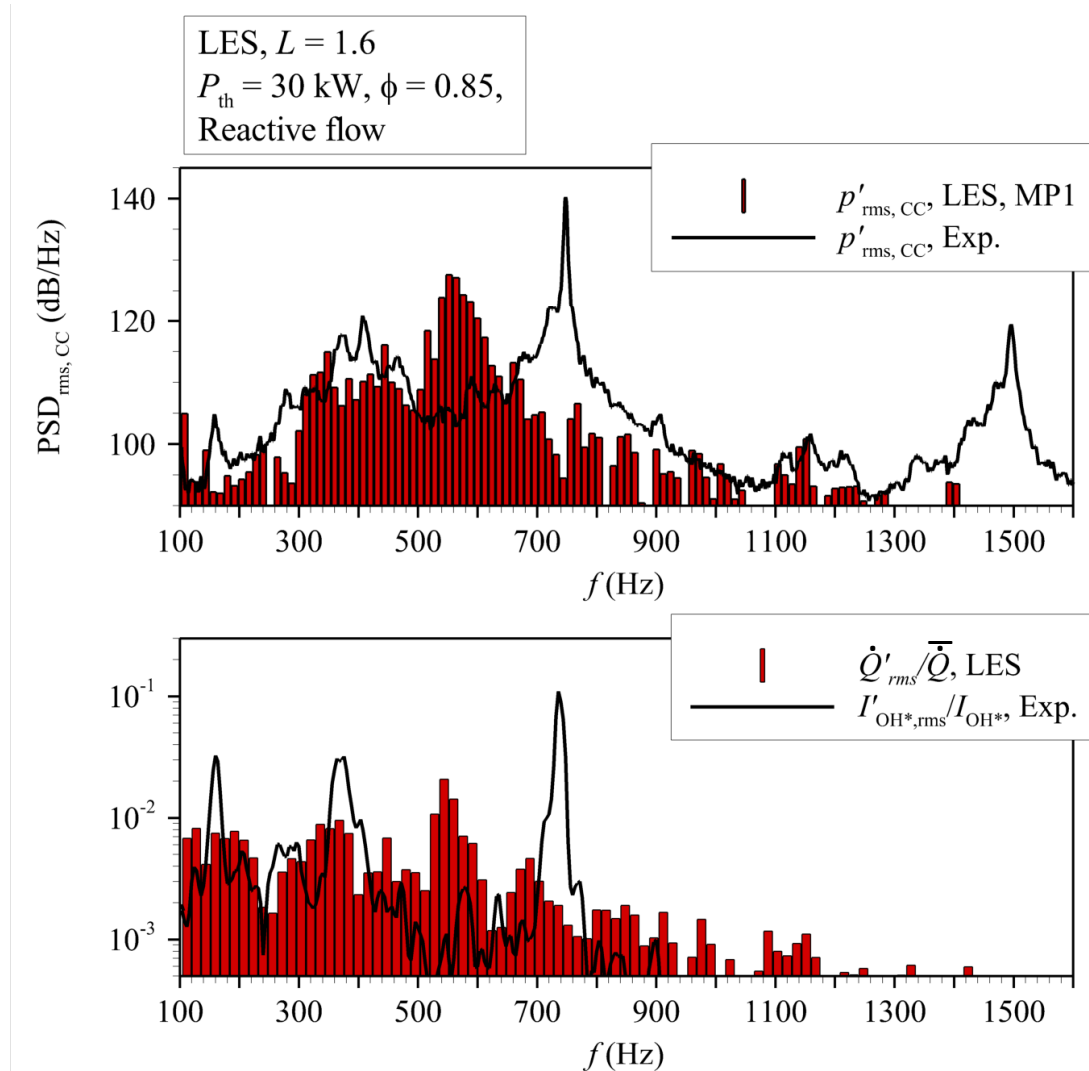


**Figure 5.47. SBS,  $P_{th} = 30$  kW,  $\phi = 0.85$ ,  $L = 1.6$ : (a) Computed spectrum of the pressure oscillations in the combustion chamber (CC) in the LES at MP1 and measured pressure spectrum; (b) Heat release oscillations in the LES and OH\*-intensity oscillations**

Similar to the LES of OP  $P_{th} = 25$  kW,  $\phi = 0.7$ , the peak amplitude is found at around 570 Hz, whereas in the experiment the 750-Hz mode is the dominant pressure oscillation, as illustrated in the discussion of the experimental results. A dominant pressure mode around 750 Hz is also found in the spectrum of the LES, but with significantly lower amplitudes. A peak in the range of the dominant mode predicted by the LES can also be observed in the measured spectrum, but at much lower amplitudes. Figure 5.47(b) illustrates that the unstable mode in the LES is caused by the coupling between the unsteady heat release and the pressure mode at 570 Hz. Figure 5.48 shows that heat release and pressure oscillate temporarily in

phase which amplifies the instability, but the system does not reach a “stable” limit cycle with constant amplitudes of pressure and heat release, at least not in the simulated period of time of around 0.12 s. Instead, the amplitudes temporarily decrease and increase again, which indicates that pressure and heat release are only temporarily in phase. This is also visible at the end of the sequence shown in Figure 5.48.

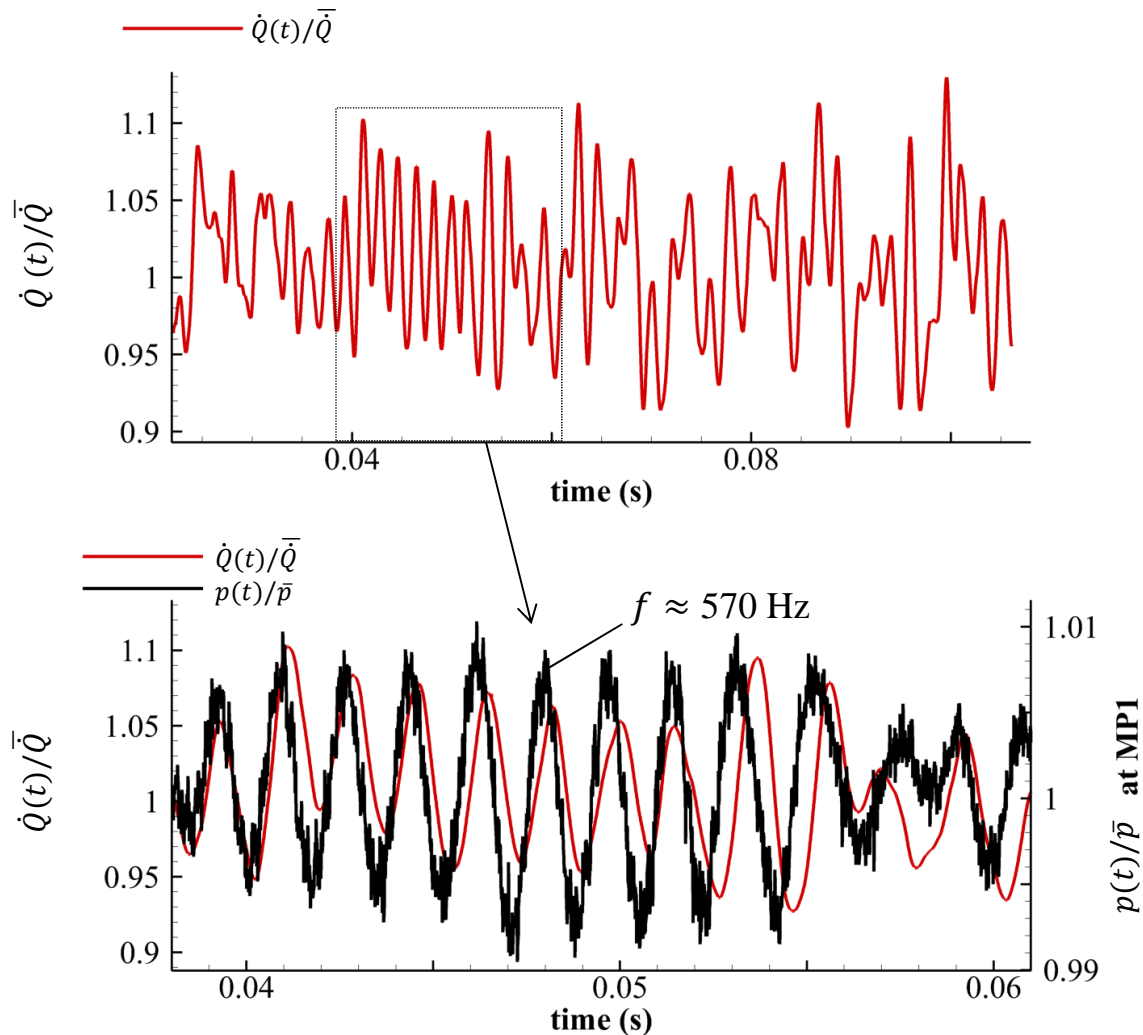


**Figure 5.48.** SBS,  $P_{\text{th}} = 30$  kW,  $\phi = 0.85$ ,  $L = 1.6$ : Pressure and heat release oscillation in the LES

The instability is driven by oscillations of the mass flow rate, as indicated by the oscillations of the mass flows in the plenums and the fuel flow rate at the nozzle outlet (Figure 5.49). The heat release periodically oscillates with a phase angle of around  $180^\circ$  to the flow rate oscillations. The heat release simultaneously increases with the pressure, which causes the pressure to rise even more. The oscillating pressure drop between the plenums and the combustion chamber modulates the flow rate of the air-fuel mixture into the combustion chamber, which in turn modulates the heat release.

Similar to the LES of the OP  $P_{\text{th}} = 25$  kW,  $\phi = 0.7$ , the strong pressure oscillation at  $\sim 570$  Hz is caused by a standing half-wave that forms in the inner plenum. As a consequence, the

spectrum of the pressure oscillations in the inner plenum shows the maximum amplitudes in this frequency range (Figure 5.50). The amplitude of the oscillation significantly exceeds the one in the experiment. As discussed in the previous sections, this is most likely induced by the different acoustic impedances of the inlet in the LES and the perforated plate located at the position of the numerical inlet in the real combustor. Figure 5.51 illustrates the pressure oscillation in the inner plenum.

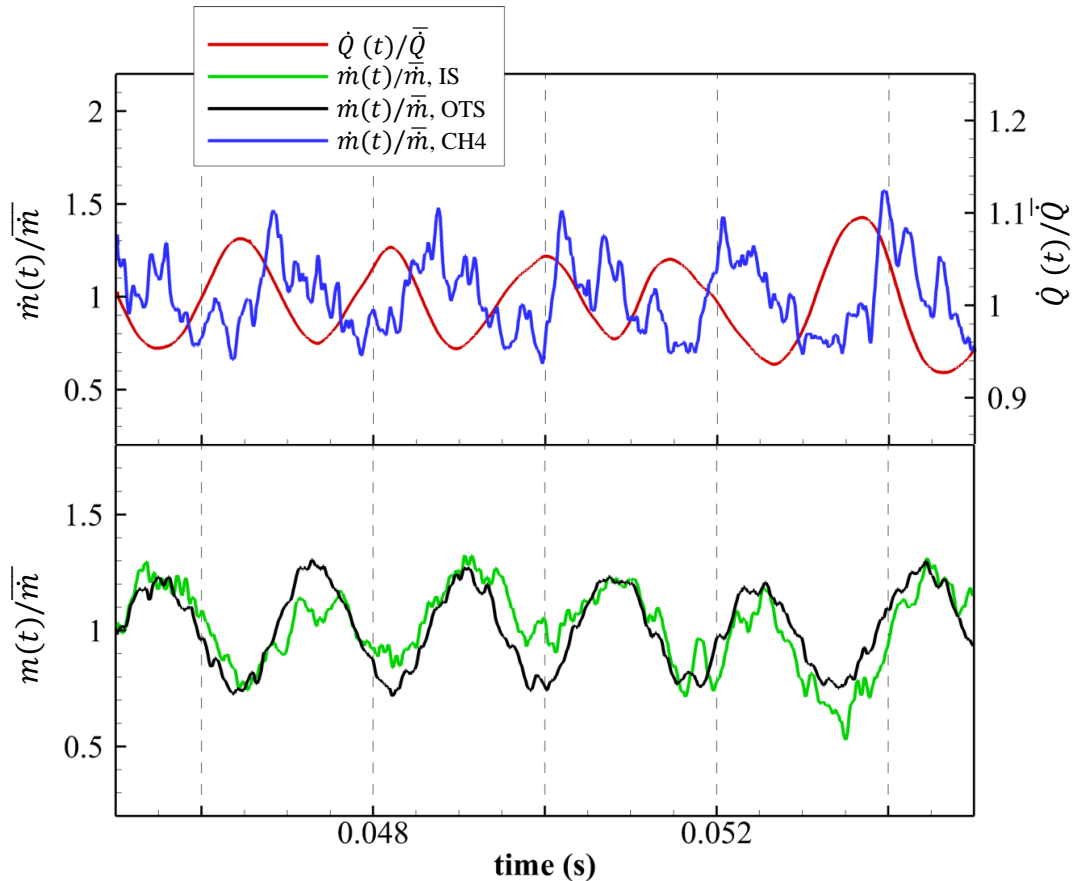


Figure 5.49. SBS,  $P_{th} = 30$  kW,  $\phi = 0.85$ ,  $L = 1.6$ : Oscillations of fuel and air mass flow rates and heat release in the LES

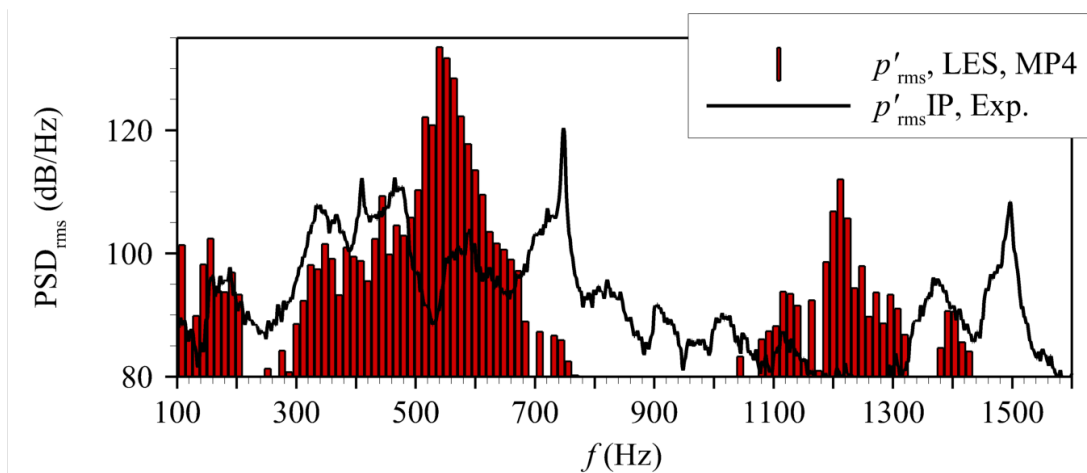
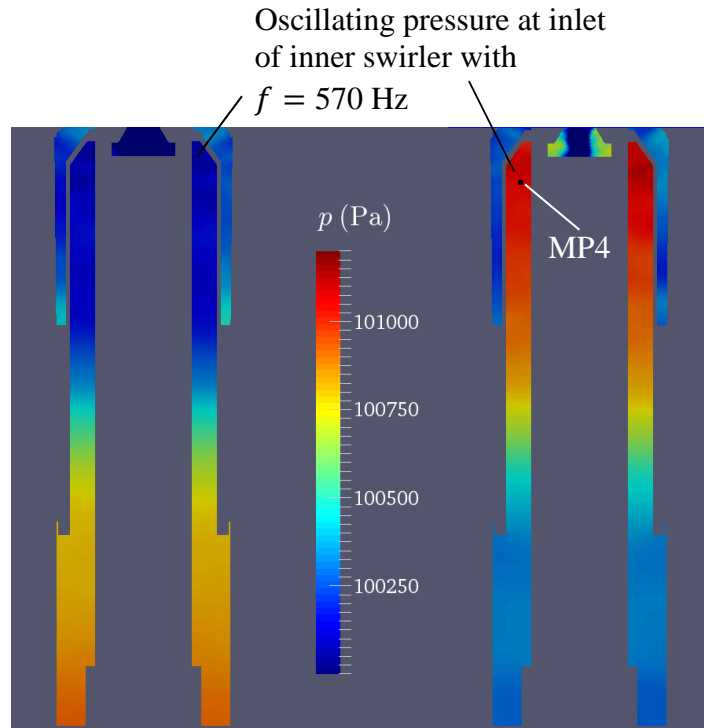
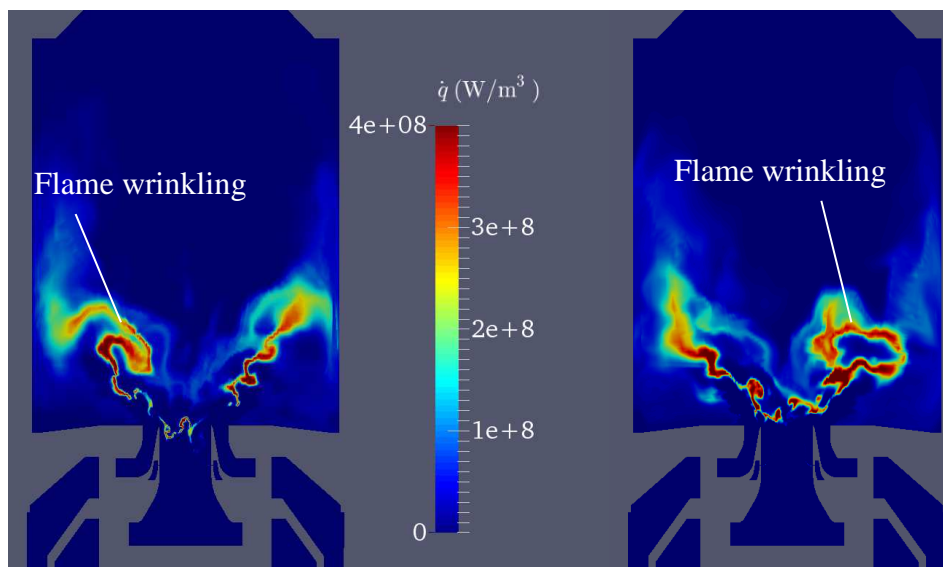


Figure 5.50. SBS,  $P_{th} = 30$  kW,  $\phi = 0.85$ ,  $L = 1.6$ : Comparison of the pressure oscillations in the inner plenum in the LES and the experiment



**Figure 5.51. SBS,  $P_{th} = 30$  kW,  $\phi = 0.85$ ,  $L = 1.6$ : Oscillating pressure in the inner plenum at  $f = 570$  Hz**

In contrast to the previously discussed OP  $P_{th} = 25$  kW,  $\phi = 0.7$ , the oscillation of the flow rate at 570 Hz does not lead to the formation of ring vortices. The simulation shows an unsteady wrinkling of the flame, which increases the flame surface and therefore the heat release (Figure 5.52). The wrinkling is caused by instabilities in the shear layers of the swirl flow, similar to Kelvin-Helmholtz instabilities.



**Figure 5.52. SBS,  $P_{th} = 30$  kW,  $\phi = 0.85$ ,  $L = 1.6$ : Flame wrinkling and the formation of flame pockets observed in the LES**

### 5.3.2.3 LES Multiple-Burner Setup 2, $P_{th} = 30 \text{ kW/burner}$ , $\phi = 0.85$ , $L = 1.6$ ,

#### Comparison of the Flow Fields in the SBS and the MBS2

Figure 5.53 compares the mean velocity profiles at different axial positions in the SBS and the MBS2. In contrast to the flow fields in the non-reactive flow, the flow fields in the reactive flow are very similar in the SBS and the MBS2. As expected, differences are observed around  $y/R_{CC} = 1$ , where the combustion chambers of the single-burners are connected in the MBS2 and a wall is located in the SBS. In this region, the tangential velocities are higher than in the SBS at equal radiuses.

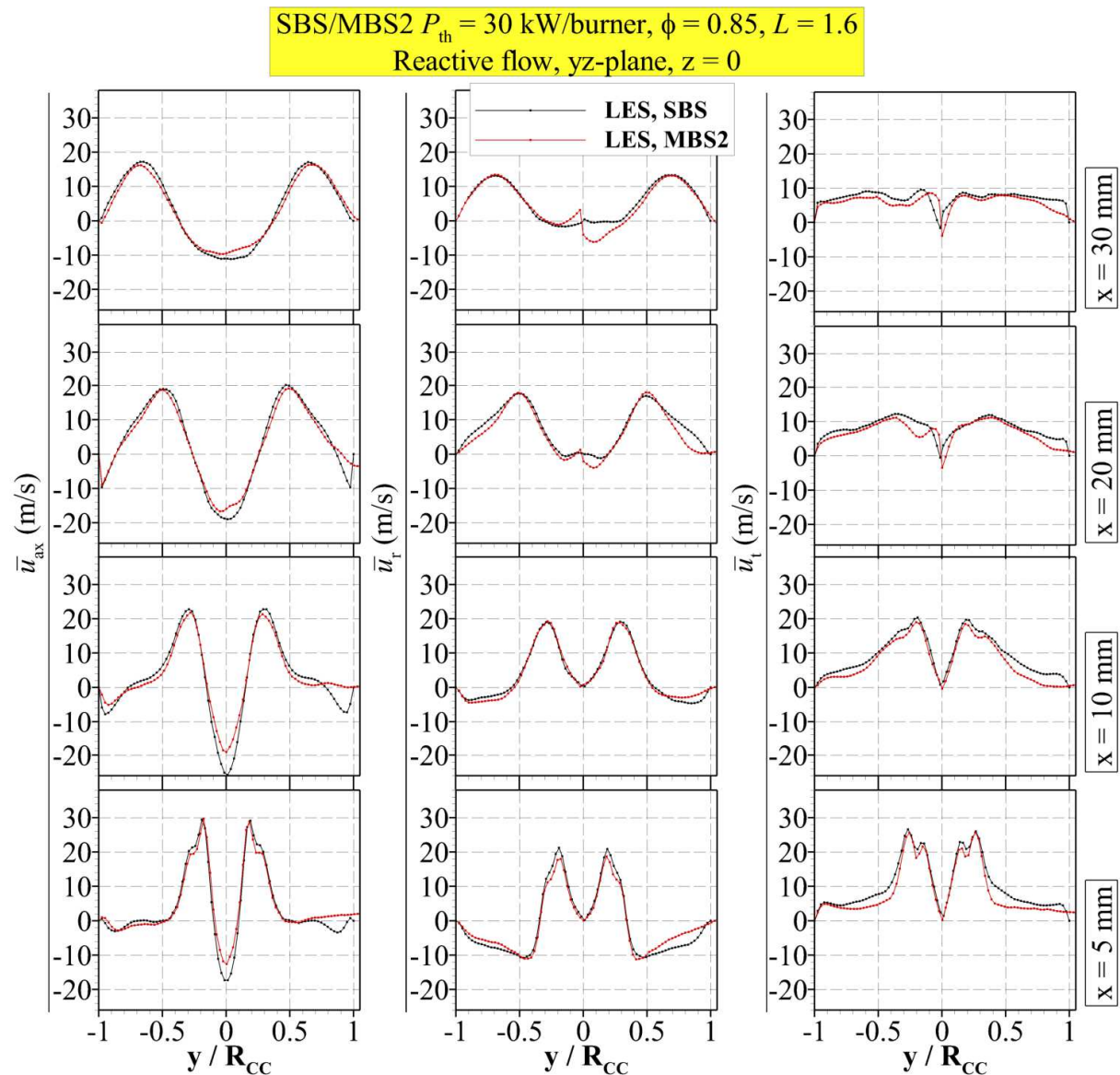


**Figure 5.53. SBS, MBS2,  $P_{th} = 30 \text{ kW/burner}$ ,  $\phi = 0.85$ ,  $L = 1.6$ : Time-averaged velocity profiles in the reactive flow**

The profile of the MBS2 clearly illustrates the influence of the adjacent swirl jets in the reactive flow. In contrast to the earlier findings for the non-reactive case, in the reactive flow the setup of co-rotating swirl jets seems to decrease the swirl intensity. This may be the reason why the maximum negative axial velocities in the IRZ are greater in the SBS than in the MBS2, especially near the nozzle outlet.

Further downstream, the value of the maximum negative axial velocity in the MBS2 exceeds the one in the SBS, as shown in Figure 5.54. This is most likely induced by the missing side walls in the MBS2 which results in different flow fields in the SBS and the MBS2, as indicated by the axial velocity profile at  $x = 50, 60$  mm. The IRZ is longer and slightly wider in the MBS2, as illustrated in the contour plots of the axial velocity in Figure 5.55. Similar to the non-reactive case, a combined recirculation zone can be observed between the adjacent burners in the MBS2.

The RMS velocity fluctuations in Figure 5.56 show that the fluctuations in the SBS exceed the ones in the MBS2, apart from the interface region of the swirl flows. In particular, the velocity fluctuations in the radial direction are more intense in the MBS2. However, the overall characteristics of the velocity fluctuations are similar in both combustor setups.

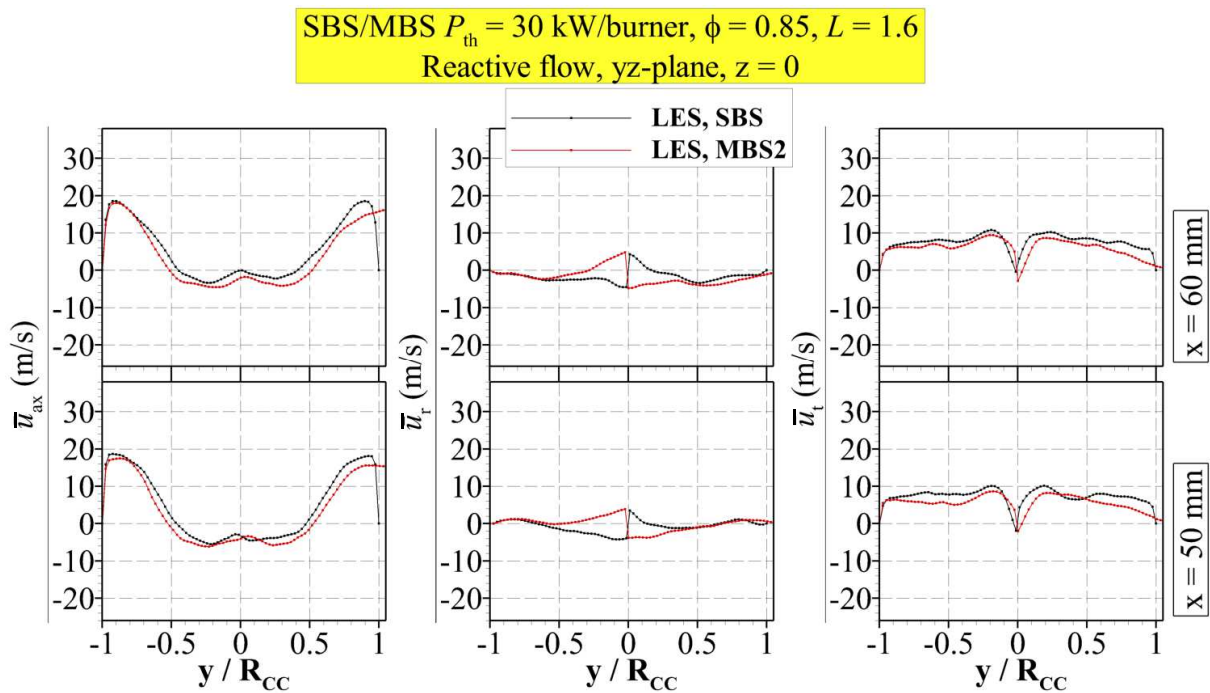


**Figure 5.54. SBS, MBS2,  $P_{th} = 30$  kW/burner,  $\phi = 0.85$ ,  $L = 1.6$ : Time-averaged velocity profiles in the reactive flow**

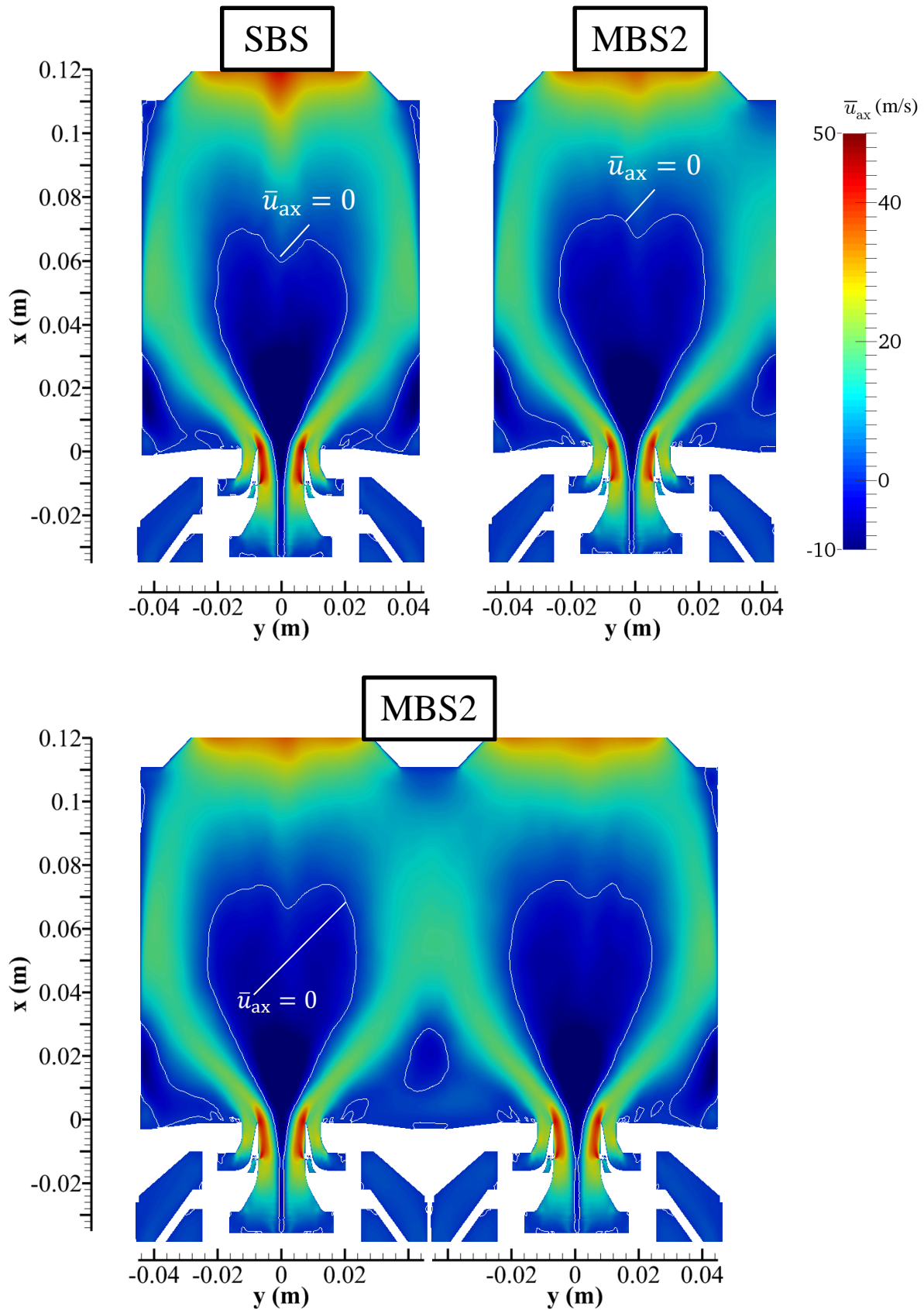


**Figure 5.55.** SBS, MBS2,  $P_{th} = 30$  kW/burner,  $\phi = 0.85$ ,  $L = 1.6$ : Axial velocities and recirculation zones in the reactive flow in the SBS and the MBS2

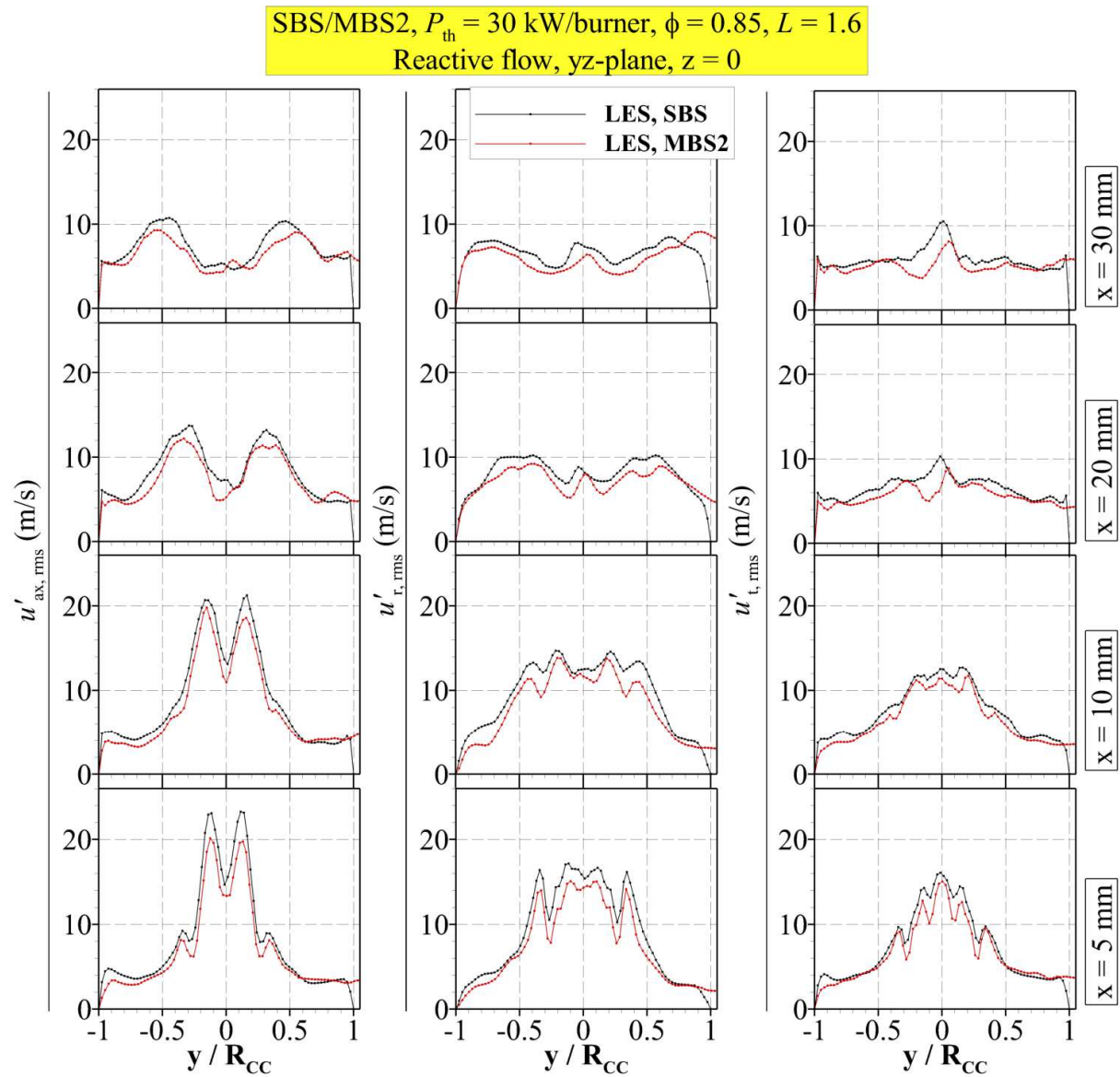


**Figure 5.56. SBS, MBS2,  $P_{th} = 30$  kW/burner,  $\phi = 0.85$ ,  $L = 1.6$ : RMS velocity fluctuations in the reactive flow in the SBS and the MBS2 at  $P_{th} = 30$  kW/burner,  $\phi = 0.85$ ,  $L = 1.6$**

#### *Mean fields of Mixture fraction, Temperature and Heat release*

Figure 5.57 and Figure 5.58 show the time-averaged mixture fraction and temperature fields in the MBS2. The mixing in the radial direction seems to be less intense in the flow region between the swirl jets, as indicated by the isoline of the stoichiometric mixture fraction. The PVC is indicated by the isoline at  $p = 99600$  Pa. Similar to the findings for the reactive flow in the SBS, the PVC strongly affects the mixing in the vicinity of the nozzle outlet, but breaks down at smaller axial distances to the nozzle than in the non-reactive flow. The maximum temperatures constitute around 2230 K and are located in the IRZ, close to the isoline of the stoichiometric mixture fraction. The maximum temperatures found in the ORZs are smaller than in the SBS and have values around 1700 K. Figure 5.59 shows the mean heat release in the MBS2 and compares it to the mean heat release in the SBS. The MBS2 shows higher

maximum heat release rates. The reaction zone is more dispersed in the SBS and the reaction also takes place in proximity to the ORZ. As a result, the unsteady recirculation of burned gases into the ORZ takes place more frequently in the SBS which explains the lower temperatures in the MBS2 in these flow regions.

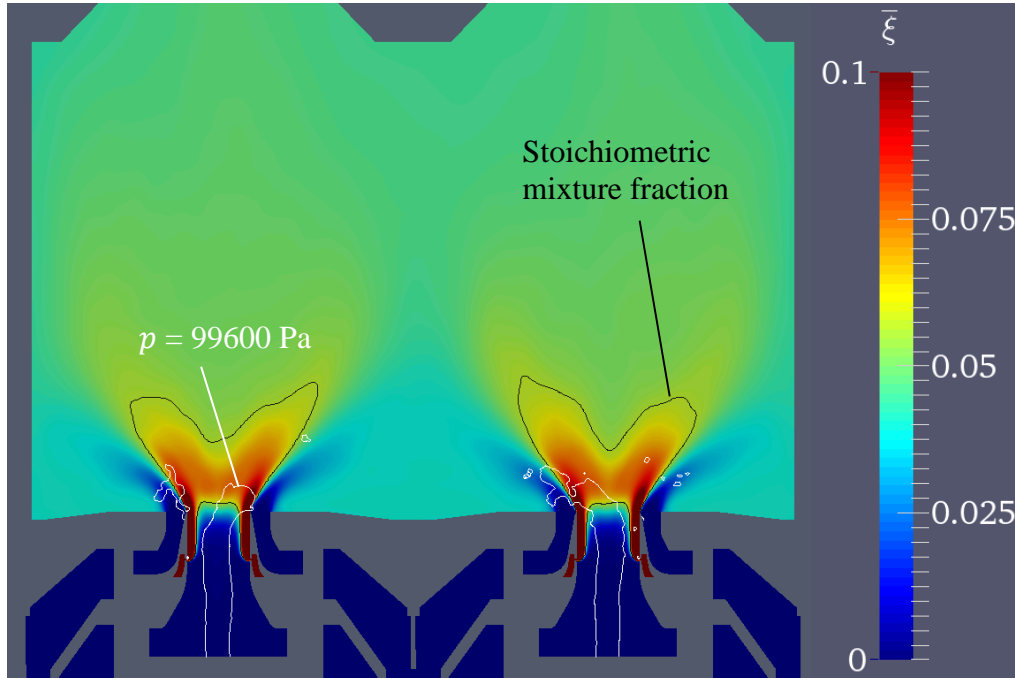


Figure 5.57. MBS2,  $P_{th} = 30$  kW/burner,  $\phi = 0.85$ ,  $L = 1.6$ : Mean mixture fraction and PVC at  $p = 99600$  Pa

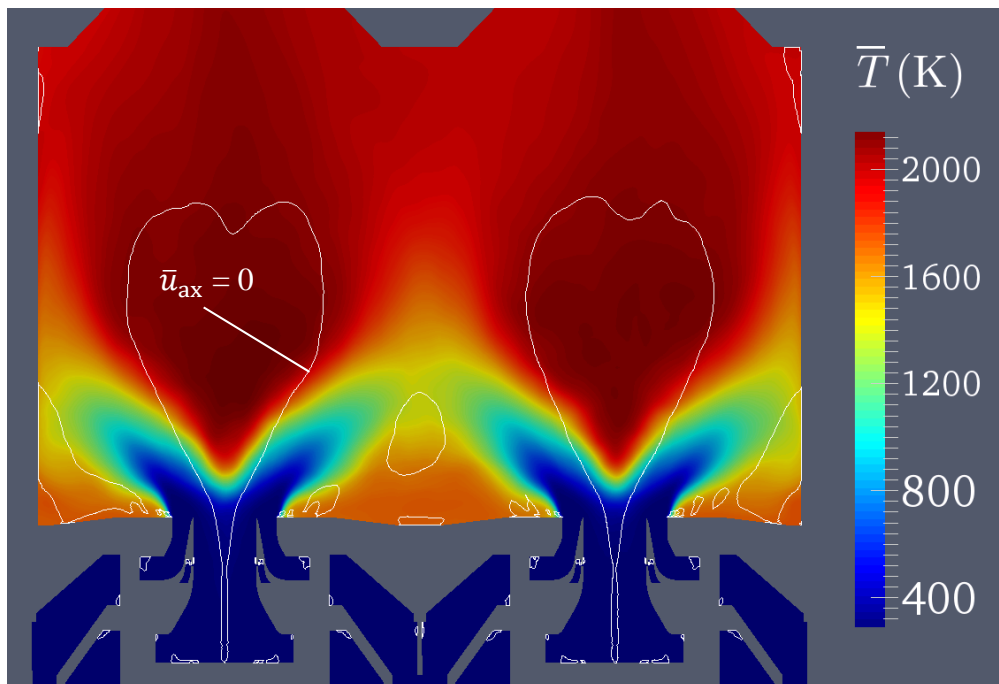


Figure 5.58. MBS2,  $P_{th} = 30$  kW/burner,  $\phi = 0.85$ ,  $L = 1.6$ : Mean temperature and IRZ (indicated by the isoline at  $\bar{u}_{ax} = 0$ )

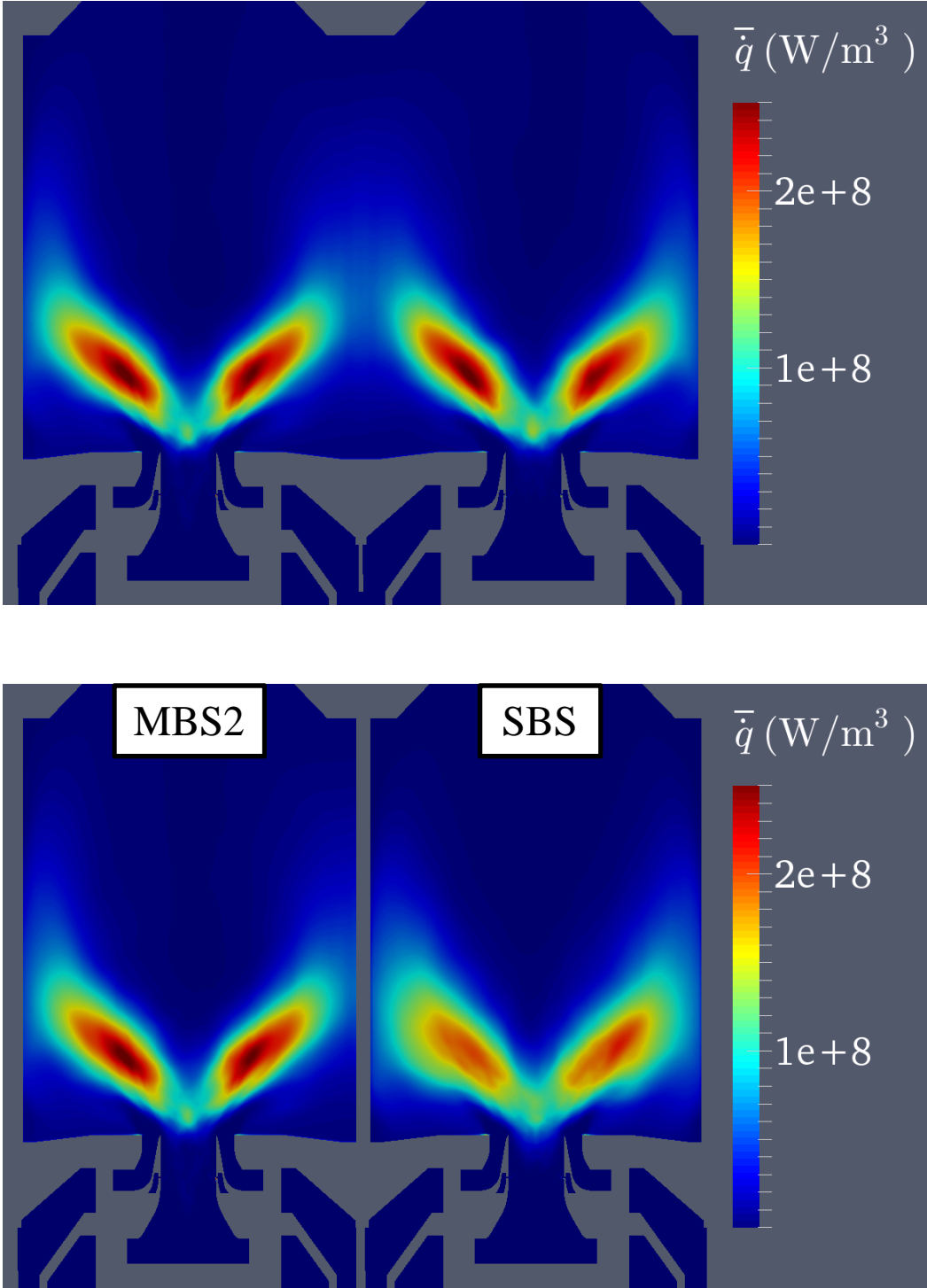
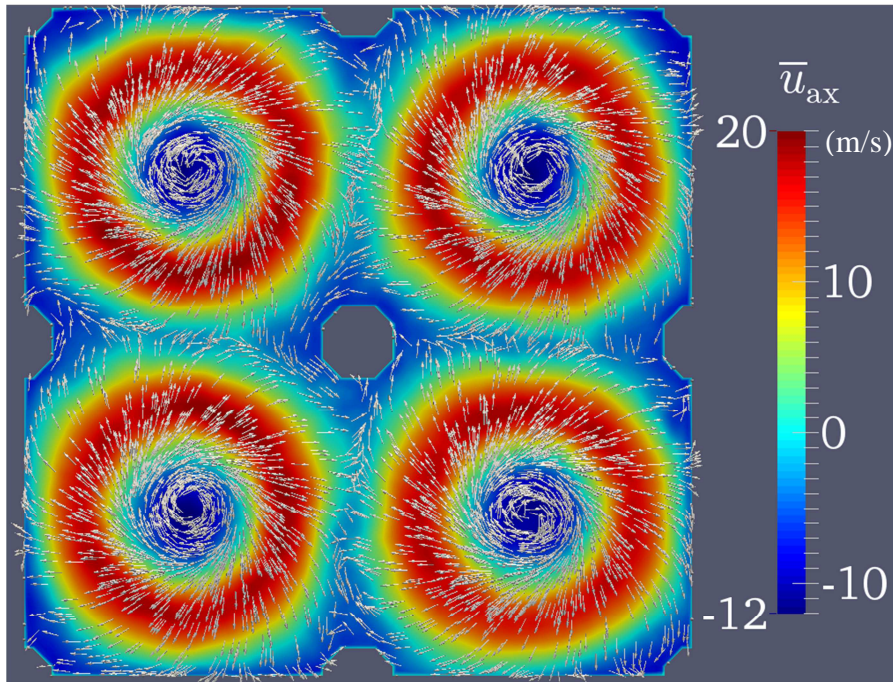


Figure 5.59. MBS2,  $P_{th} = 30$  kW/burner,  $\phi = 0.85$ ,  $L = 1.6$ : Mean heat release in the MBS2 and the SBS

Figure 5.60 shows the vectors of the velocity components in the  $yx$ -plane at  $x = 0.03$  m. Similar to the non-reactive case, the co-rotating swirl jets induce a secondary flow in the centre of the combustion chamber which rotates in the reverse direction.



**Figure 5.60. MBS2,  $P_{th} = 30$  kW/burner,  $\phi = 0.85$ ,  $L = 1.6$ : Vectors of the velocity components in the  $yz$ -plane at  $x = 0.03$  in the reactive flow**

#### *Pressure, Velocity and Heat Release Oscillation*

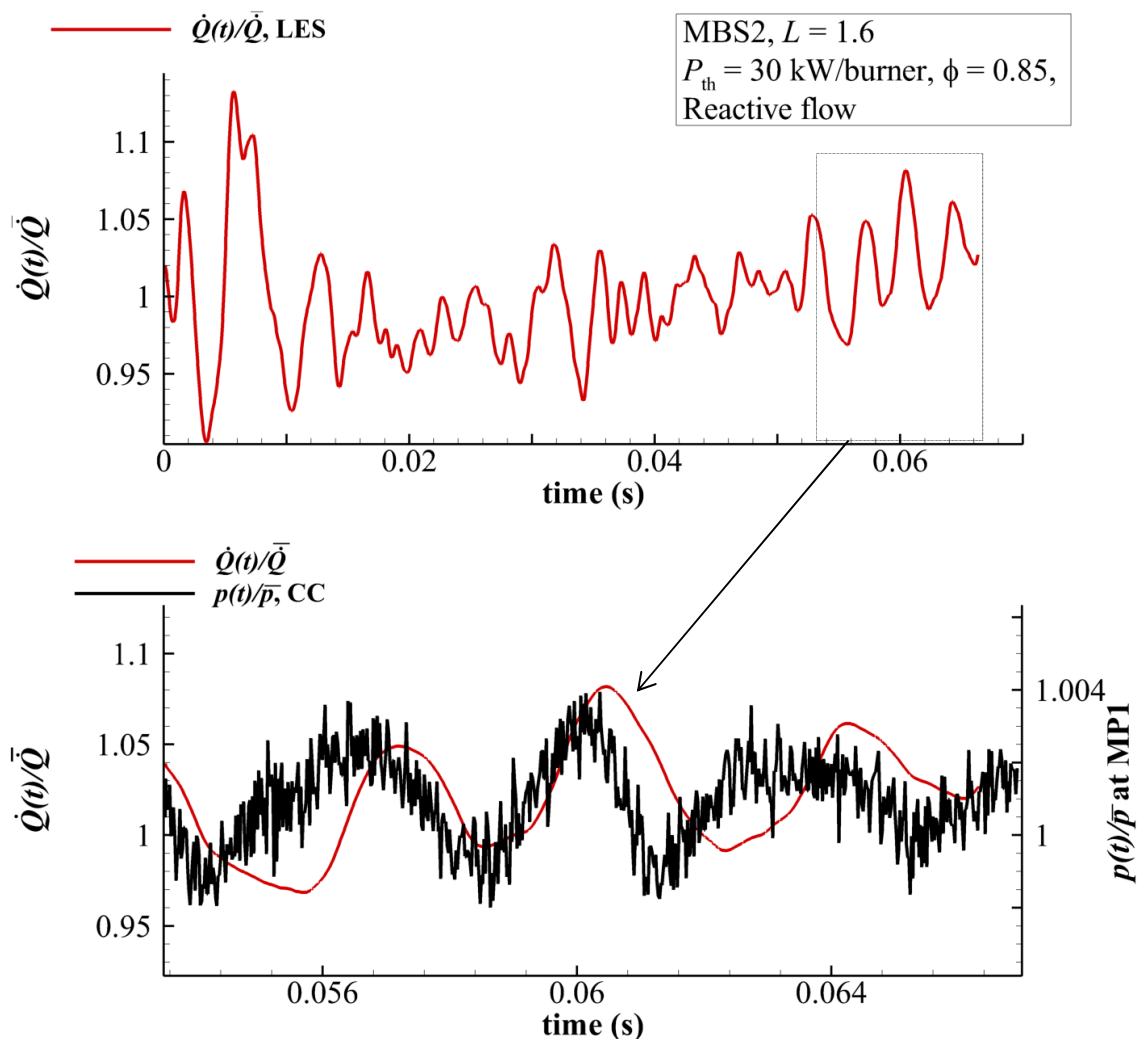
Figure 5.61 shows the computed heat release in the LES of the MBS2. Oscillations of the heat release are clearly visible, but the amplitude and the frequency of the oscillations vary over time. Pressure and heat release are only temporarily in phase. As a consequence, no unstable mode develops in the simulated period of time. In the experiment, the 400-Hz mode is clearly the dominant mode of the pressure and OH\*-intensity oscillations, whereas the LES shows several modes with equivalent amplitudes for pressure and heat release (Figure 5.62). A peak is also observed at around 400 Hz, but for the case it represents the oscillation corresponding to the 400-Hz mode observed in the experiment, it features significantly lower amplitudes.

Figure 5.63 shows that the dominant pressure mode in the inner plenum in the MBS2 is in the frequency range around 540 Hz. A similar mode was found in the inner plenum for the cases of the SBS. Similar to the SBS, the pressure oscillation leads to oscillations of the flow rate of the air-fuel mixture at the nozzle outlet, as indicated by the spectrum of the overall fuel mass flow rate at the nozzle outlet in Figure 5.64. However, the spectrum of the heat release oscillations reveals that the multiple-burner flame exhibits a stronger response to the flow rate perturbations in the frequency range of 150-400 Hz. In contrast to the flame in the SBS, it does not couple with the dominant mode at 540 Hz. The oscillations of the heat release are

induced by unsteady flame wrinkling due to the interaction of the flame with vortices in the shear layer of the swirl flow, as illustrated in Figure 5.65.

One possible reason for the deviation of the LES from the experiment may again be reasoned by the different acoustic impedances of the numerical inlets and the perforated plate installed in the real combustor. The amplitude of the mode at 540 Hz exceeds the amplitude observed in the experiment (Figure 5.63) and therefore alters the acoustics in the inner plenum compared to the experiment. In this way, it may prevent the amplification of one of the other modes to which the flame shows a stronger response.

Another reason for the deviation between the experiment and the LES may be the computation time. In the experiment, the multiple-burners oscillate in phase, but they may require a certain amount of time in order to tune to one frequency. Of course, this does not pose a problem in the experiment, but represents a big issue in the LES, due to its high demand of computational effort.



**Figure 5.61. MBS2,  $P_{th} = 30$  kW/burner,  $\phi = 0.85$ ,  $L = 1.6$ : Pressure and heat release oscillation in the LES of the MBS2**

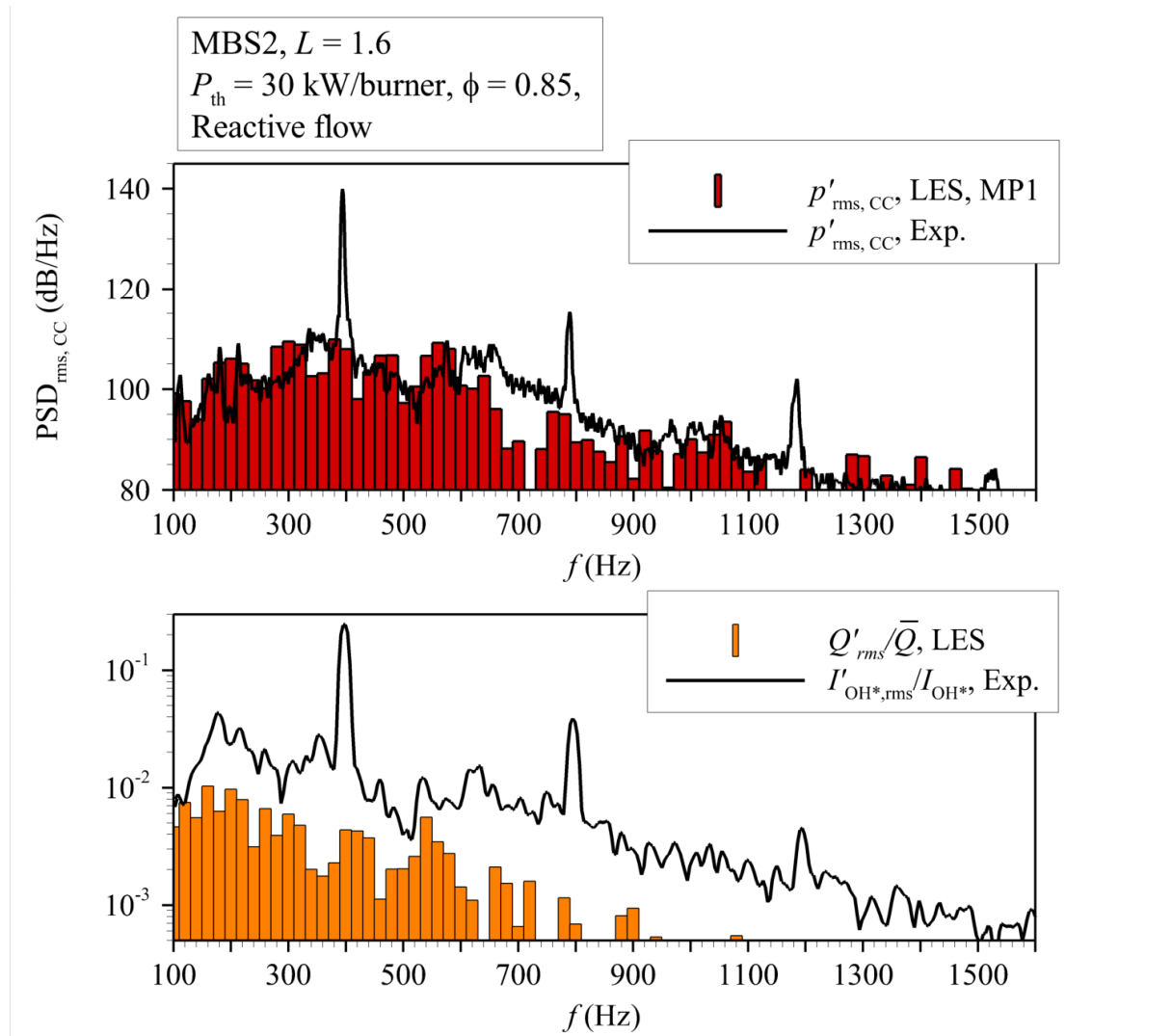


**Figure 5.62. MBS2,  $P_{th} = 30$  kW/burner,  $\phi = 0.85$ ,  $L = 1.6$ : Pressure and heat release oscillations in the LES in comparison to pressure and OH\*-intensity oscillations in the experiment**

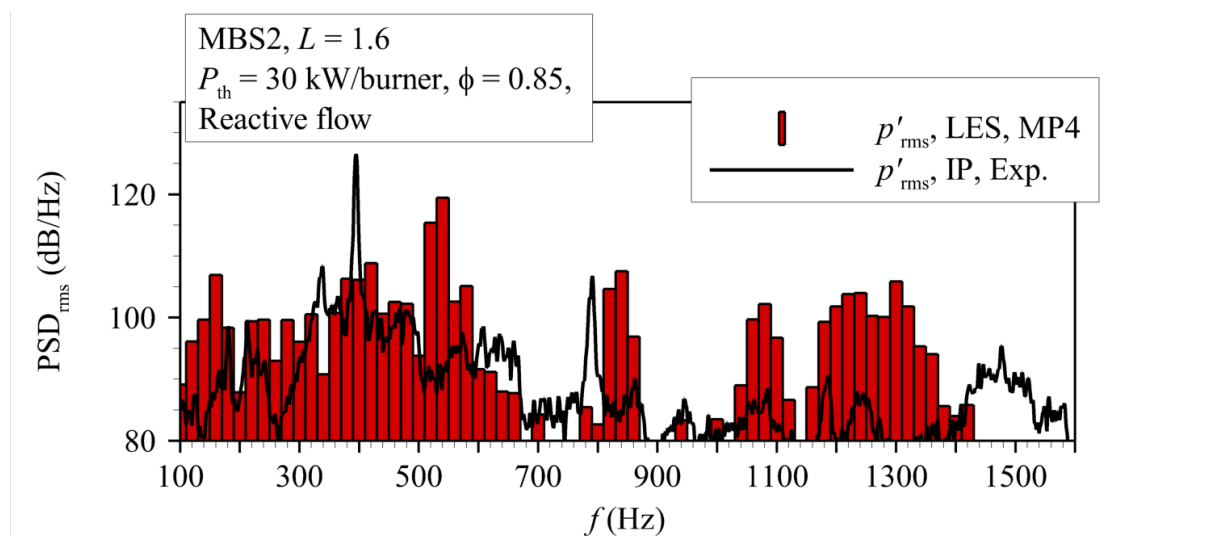


**Figure 5.63. MBS2,  $P_{th} = 30$  kW/burner,  $\phi = 0.85$ ,  $L = 1.6$ : Pressure oscillations in the inner plenum in the LES of the MBS2**

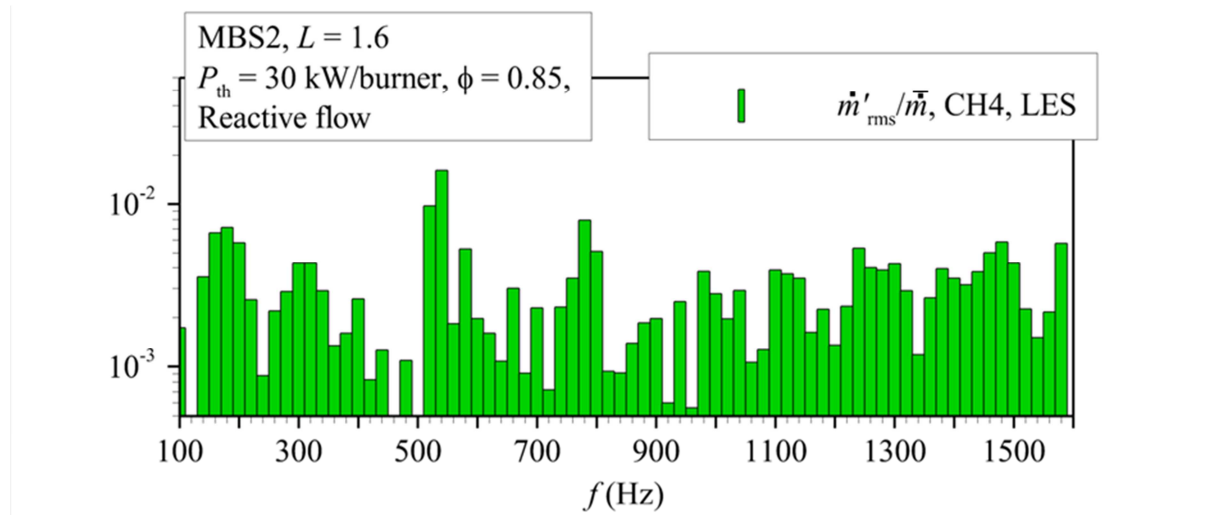


**Figure 5.64. MBS2,  $P_{th} = 30$  kW/burner,  $\phi = 0.85$ ,  $L = 1.6$ : Oscillations of the overall fuel mass flow rate at the outlet of the IS in the LES of MBS2**

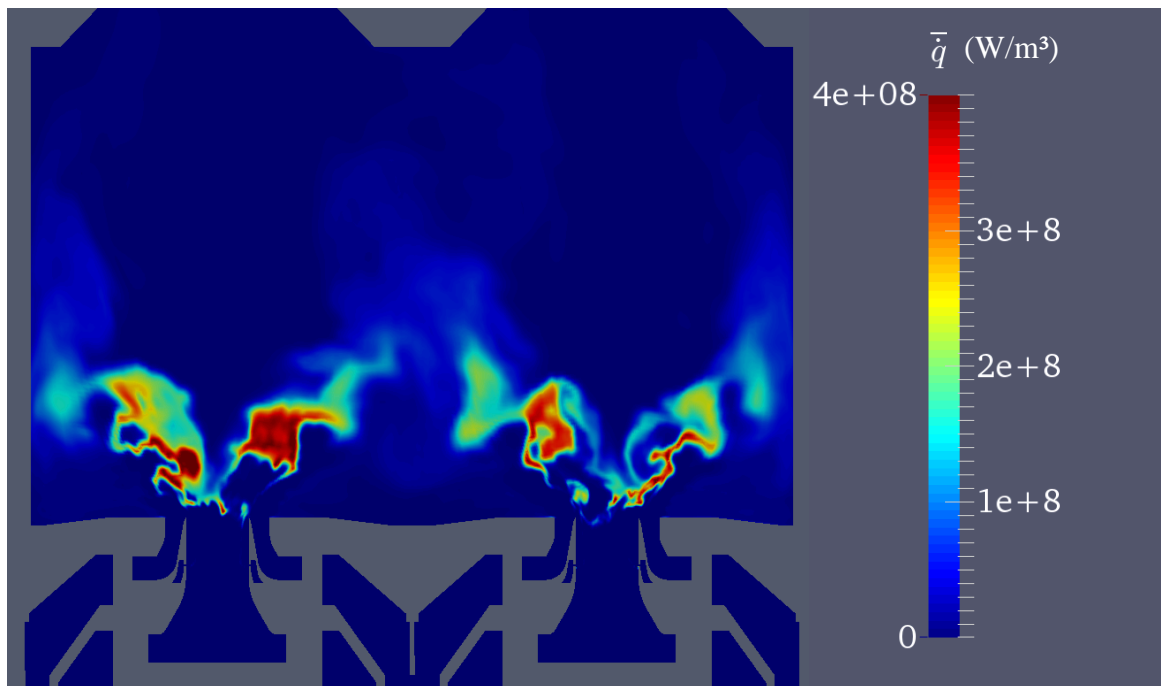


**Figure 5.65. MBS2,  $P_{th} = 30$  kW/burner,  $\phi = 0.85$ ,  $L = 1.6$ : Flame wrinkling due to vortices in the MBS2**

#### *Mean Recirculation Rates in the SBS and the MBS2 in the Reactive Flow*

The mass flow recirculation rates are often considered to be a measure for the stability of the flame, since the recirculation of burned gases ensures the ignition of the fresh gases entering the combustion chamber. The mass flow recirculation rates also affect the characteristic time scales of the flame and therefore affect its thermoacoustic response to pressure and velocity perturbations.

Figure 5.66 shows the mean recirculation rates and the angular momentum flux in the reactive flow at  $P_{th} = 30$  kW/burner,  $\phi = 0.85$ ,  $L = 1.6$ .

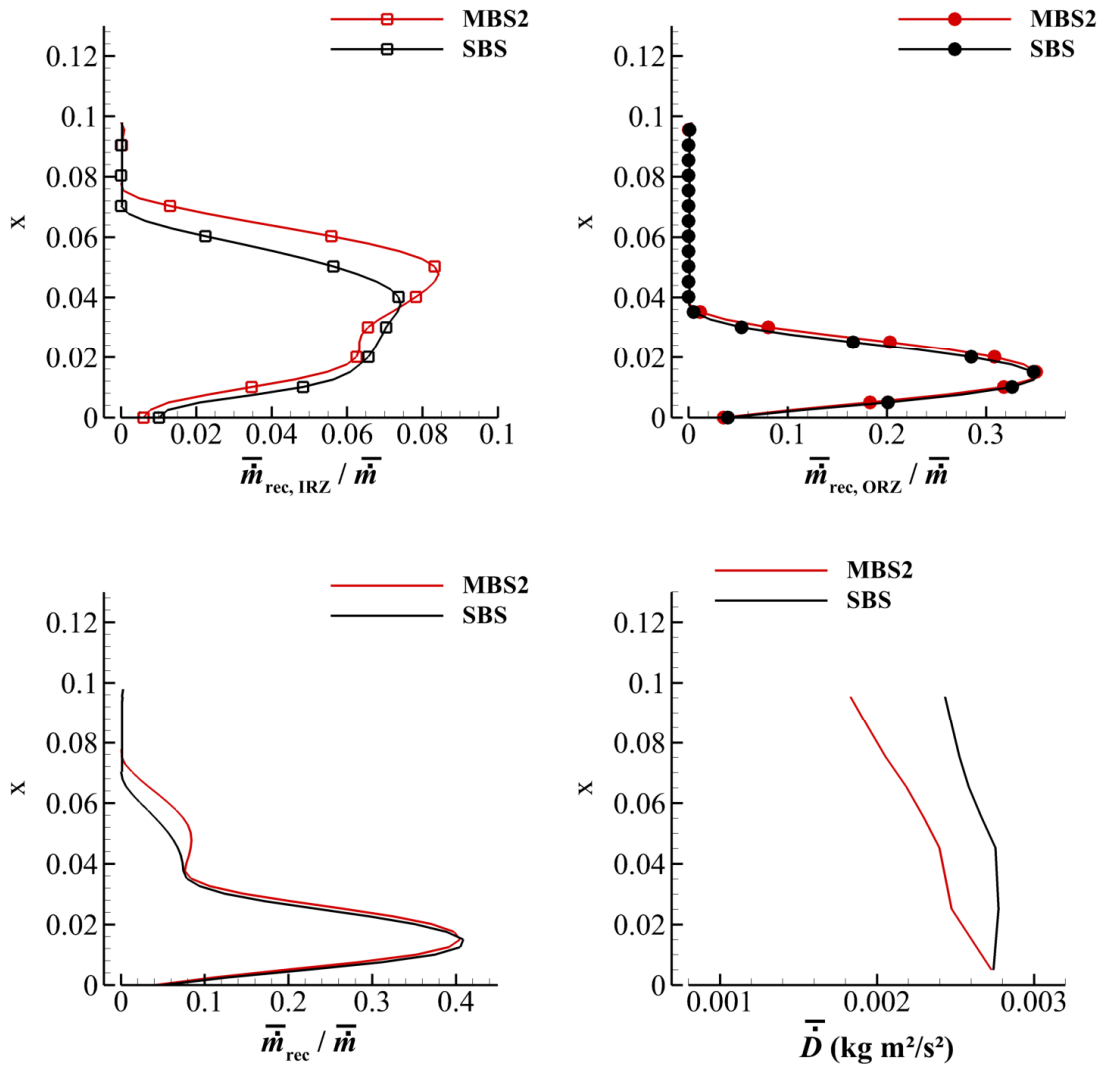


**Figure 5.66. SBS and the MBS2 at  $P_{th} = 30$  kW/burner,  $\phi = 0.85$ ,  $L = 1.6$ : Mean recirculation rates and angular momentum flux in the reactive flow**

As indicated by the results for the mean velocities, the flow characteristics in the MBS2 and the SBS are much more similar in the reactive case than in the non-reactive case. The most significant difference is represented by the higher recirculation rates in the IRZ in the SBS up to  $x = 0.04$  m, which complies with the observations made for the mean axial velocities. The outer recirculation rates are almost equal and exceed the ones in the IRZ. As a result, the overall mass flow recirculation rates are also very similar in both combustor setups. The slightly decreased inner recirculation rate may be induced by the reduced swirl intensity in the MBS2 near the nozzle exit. As pointed out in the discussions of the experimental results in 4.5.5, this may be the result of the effect described by Hirsch et al. in [27]. Due to the exchange of angular momentum between the co-rotating swirl flows, the swirl intensity of the mass flow recirculated in the ORZ is reduced which in turn results in a decrease in the overall effective swirl number.

### 5.3.2.4 Estimation of the Convective Time Delay in the LES

The convective time delay represents a characteristic time scale of the flame, as discussed in 3.4.1. In order to further characterise the simulated turbulent flames in the SBS and the MBS2, the convective time delay was estimated using the streamlines of the mean flow field. The streamlines correspond to the velocity components in the  $xy$ -plane (parallel to the combustion chamber wall) on a slice with the base point located on the burner axis. The streamlines start in the inner swirler 11 mm ( $x = -0.011$  m) upstream to the nozzle exit, next to the location of the fuel jets. Figure 5.67 illustrates that the streamlines pass through the main reaction zone, as indicated by the contours of the mean reaction rate.

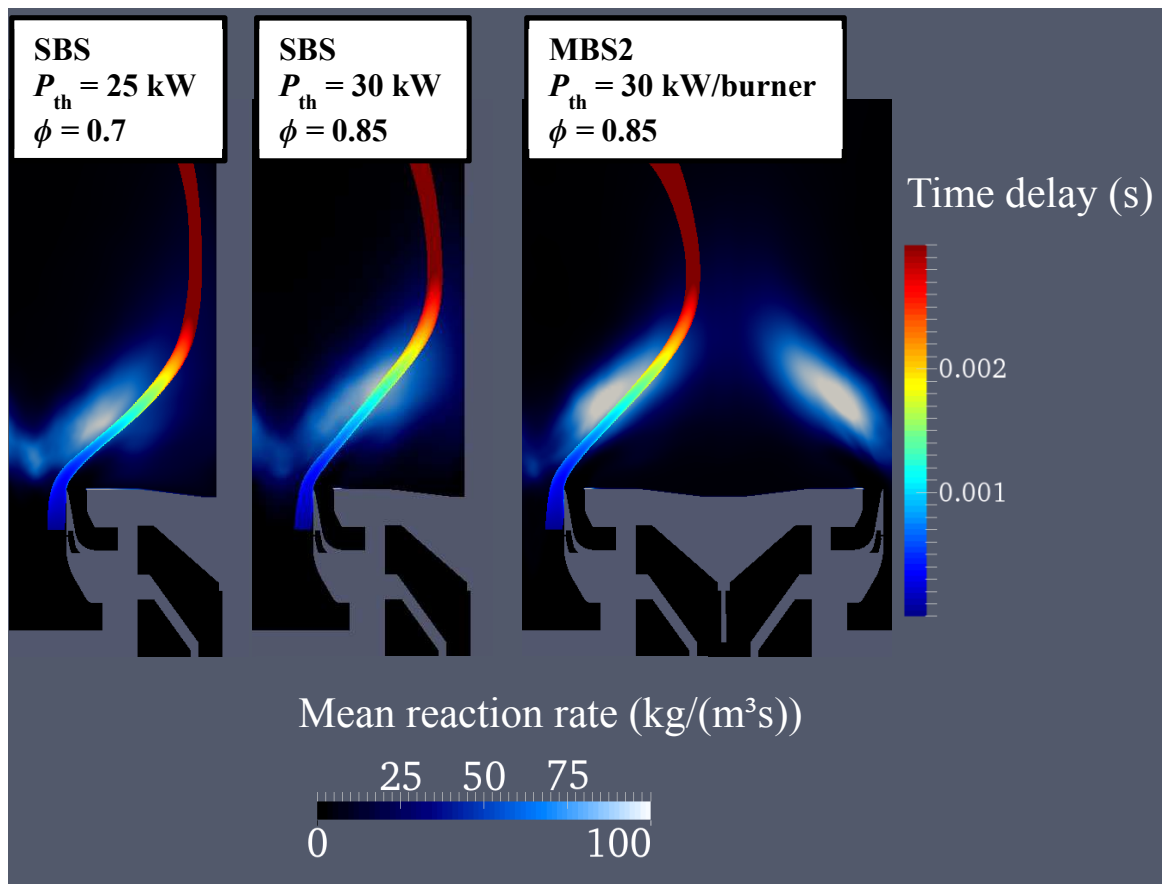


**Figure 5.67. Streamlines used for the estimation of the convective time delay**

From the streamlines, the points were extracted which show mean reaction rates in the range of 80-100 % of the maximum mean reaction rate. The relative frequencies of the determined convective time lags are plotted in Figure 5.68 for the SBS and the MBS2 at  $P_{th} = 30$  kW/burner,  $\phi = 0.85$  and in Figure 5.69 for the SBS at  $P_{th} = 25$  kW,  $\phi = 0.7$ .

It is clearly visible that in the SBS at  $P_{th} = 30$  kW,  $\phi = 0.85$ , a fluid particle or a perturbation reaches the flame front with a significantly smaller minimum time delay of  $\sim 0.0007$  s than in the MBS2 at  $P_{th} = 30$  kW/burner,  $\phi = 0.85$  ( $\sim 0.001$  s). Also the time delays with the maximum relative frequencies, which may be interpreted as the characteristic convective time

delay, are higher in the MBS2 than in the SBS. In the MBS2, they are observed at  $\sim 0.0014$  s and at  $\sim 0.00125$  s in the SBS.

Figure 5.69 shows that the characteristic time delay at  $P_{th} = 25$  kW,  $\phi = 0.7$  in the SBS is similar to  $P_{th} = 30$  kW,  $\phi = 0.85$ . Apparently, the flow characteristics are similar for both OPs, which may be expected as the air flows are approximately equal. The distribution of the time delay appears to be narrower at  $P_{th} = 25$  kW,  $\phi = 0.7$ . This is possibly induced by the decreased fuel flow rate, which in turn results in a smaller length of the main reaction zone, as indicated in Figure 5.68.

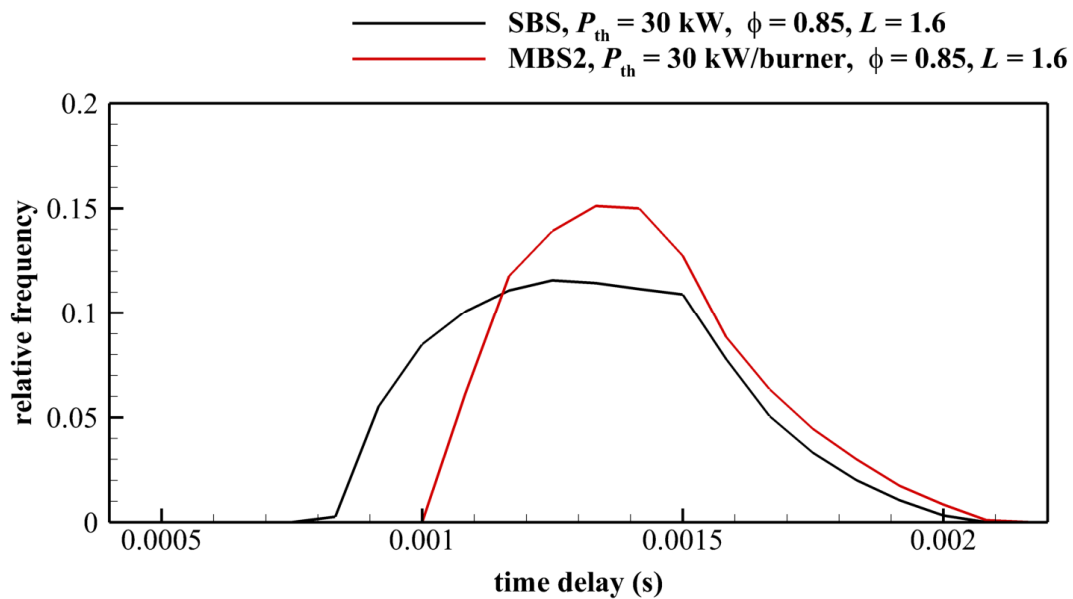


**Figure 5.68.** Relative frequency of the time lag in the SBS and the MBS2 at  $P_{th} = 30$  kW/burner,  $\phi = 0.85$  and in the SBS at  $P_{th} = 25$  kW,  $\phi = 0.7$

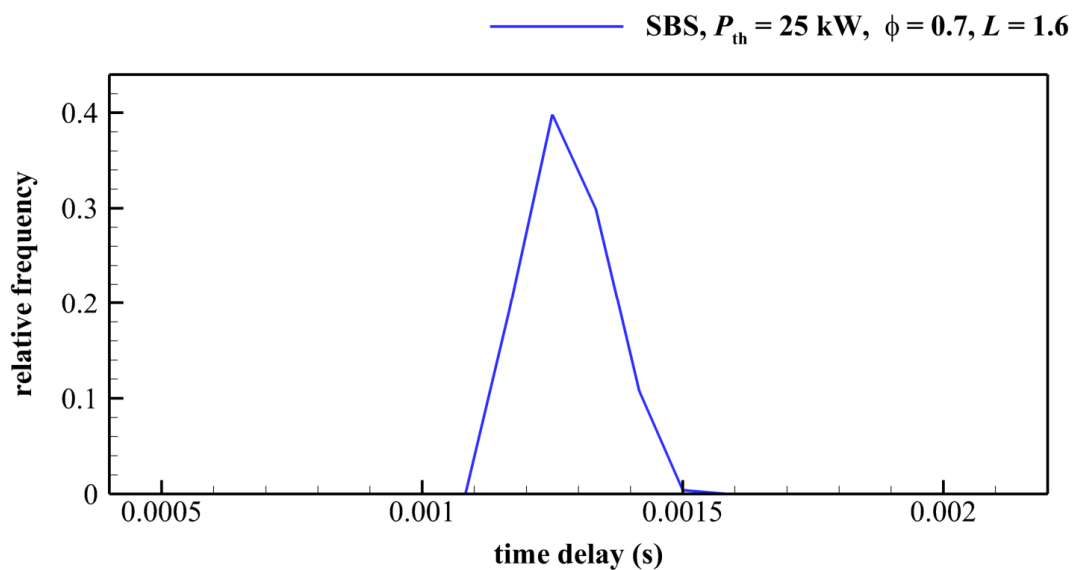


**Figure 5.69.** Relative frequency of the time lag in the SBS at  $P_{th} = 25$  kW,  $\phi = 0.7$

The discussed results for the convective time delay can only be interpreted as an approximation for the characteristic time delay. However, the tendency is very clear and may explain why the flame in the MBS2 shows a stronger response to lower frequencies than the flames in the SBS. As discussed in section 3.4.1, a certain phase of the flame response to a velocity or equivalence ratio perturbation is needed for the generation of unstable modes. In the MBS2, the flame response already shows the necessary phase at lower frequencies than in the SBS, due to the increased characteristic convective time delay.

### **5.4 Concluding Remarks for the Discussion of the Numerical Results**

The results of the LESs in this chapter show that the main characteristics of the mean flow fields are captured by the performed simulations. Since the numerical results of the mean flow fields in the SBS show a good agreement with the PIV results, it is likely that the characteristic features of the mean flow field in the MBS2 are reproduced by the simulation.

The non-reactive flows in the SBS show similar flow fields and the observed differences are attributed to the higher fuel flow rate. Significant differences were found between the non-reactive flow fields in the SBS and the MBS2. Despite the missing side walls, the MBS2 shows a much wider IRZ and features the characteristics of a wall-bounded flow. In contrast, the flow field in the SBS resembles the one of a free jet and attaches the walls further downstream than the swirl flow in the MBS2. This was also reported by Sangl for the isothermal flow in a multiple-burner arrangement [149].

It has been shown that the application of adequate acoustic boundaries is crucial for the correct prediction of combustion instabilities. The frequencies of the predicted unstable modes in the LESs of the SBSs deviate from the frequencies of the unstable modes observed in the experiment. A possible explanation is given by the different acoustic impedances of the numerical inlets and the perforated plates installed at the corresponding locations in the experiment. Due to the fully reflecting inlet BC in the inner plenum, a standing wave with high pressure amplitudes and a frequency of around 570 Hz forms inside the inner plenum and dominates the pressure oscillations. The flames in the LESs show a temporary coupling with this oscillation; the feedback loop of the mode is closed by an in-phase oscillation of combustion chamber pressure and heat release, which in turn modulates the oscillation of the flow rate of fuel and air. Although the frequencies of the unstable modes are different in the experiment and the LES, the driving mechanism appears to be similar. Therefore, it can be stated that the LESs of the SBS also identify oscillations of the air and fuel flow rates as the main driving mechanisms of the unstable modes in the SBS and therefore comply with the findings in the experiments.

In the simulation of the MBS2, no dominant mode was observed in the simulated time period. It is assumed that one major reason for this behaviour is that in the combustion systems with multiple flames it takes a certain amount of time before the system has tuned to one specific

frequency. The results of the LES of the MBS2 also revealed that the flame shows a stronger response to frequencies in the low-frequency range ( $< 400$  Hz) than the flames in the SBS. As a consequence, the flame does not couple with perturbations caused by the dominant pressure oscillation at 540 Hz in the inner plenum that was found to be an equivalent oscillation to the oscillation of the pressure in the inner plenum of the SBS at 570 Hz.

In order to further characterise the simulated turbulent flames, the characteristic convective time delay in all flames was estimated. It was found that the convective time delay in the MBS2 exceeds the one in the SBS for the investigated OPs. However, the characteristic time delay may vary with the operating conditions and for a global analysis, it would be necessary to analyse more OPs. On the other hand, the results comply with the assumptions made in the discussion of the experiments. In the MBS2, it is more likely that an unstable mode in the low-frequency range with frequencies  $< 400$  Hz is excited. The increased characteristic convective time delay in the MBS2 leads to an increase of the frequency-dependent phase angle of the flame response to low-frequency velocity disturbances compared to the SBS. As a consequence, the phase angle of the flame response which is necessary for the generation of instabilities is already reached at lower frequencies than in the SBS.

The different time delays are most likely induced by differences in the flow fields of the SBS and the MBS2. In contrast to the non-reactive case, the flow fields in the SBS and the MBS2 at  $P_{th} = 30$  kW/burner,  $\phi = 0.85$  are quite similar. However, higher mass flow recirculation rates near the nozzle outlet are observed in the IRZ in the SBS. This possibly leads to the smaller axial distance between the main reaction zone and the nozzle exit in the SBS and the therefore reduced characteristic convective time delay. In the MBS2, the reduction of the mass flow recirculation in the IRZ may be induced by the reduction of the angular momentum in the shear layers of the adjacent swirl jets. As a result, the mass flow recirculated in the ORZ of the MBS2 carries less angular momentum than in the SBS, which leads to a reduced swirl intensity in the MBS2, as discussed in [27].



## 6. Summary and Conclusions

The present thesis focuses on the investigations of the influence of multiple-burner arrangements on combustion instabilities in technical combustion systems. For this purpose, a modular combustor was designed and manufactured, which can be operated in single- as well as different multiple-burner setups. The combustor is operated under atmospheric conditions, using natural gas as fuel. A double-concentric swirl nozzle is employed for flame stabilization. A special feature of the combustor is that the swirlers employ separate air inlets which allows for varying the ratio of the mass flows through the swirlers. In this way, the theoretical swirl number can be altered and different flame characteristics can be achieved.

The combustor was operated in single-burner setup (SBS) and two multiple-burner setups (MBSs). In the first MBS (MBS1), the single-burners are linearly arranged. In the second MBS (MBS2), the single burners are arranged in an “annular” arrangement. Experimental and numerical investigations were performed to analyse the combustion instabilities in the combustor.

In the experiments, microphone measurements of pressure oscillations in the plenums and the combustion chamber were carried out and high-speed OH\*-imaging was applied to monitor the heat release of the flame. The focus of the experimental investigations was to identify the operation parameters which lead to unstable conditions in the combustor. It was found that unstable modes are more likely to develop at a thermal power of  $P_{th} > 25$  kW in the SBS and  $P_{th} > 27.5$  kW/burner in the MBSs. Several unstable modes were identified in the low-frequency range of 100-300 Hz and one major combustor mode in the range of 400 Hz. While these modes are found in all combustor setups, the mode found in the frequency range of 750 Hz is only present in the SBS. This complies with the overall observed tendency regarding the frequencies of the unstable modes. Low-frequency modes in the range of 100-300 Hz are found much more frequently in the MBSs. It was concluded that the observed differences in the thermoacoustic behaviour are induced by differences in the flow field between the SBS and the MBSs which are induced by the multiple-burner arrangement. The exchange of momentum between the co-rotating swirl jets lead to lower the swirl intensity in the MBSs. Based on the findings reported in earlier studies, it was concluded that the decreased swirl intensity in the MBSs leads to an increased characteristic time delay between a pressure/velocity perturbation and the flame response. As a consequence, a phase angle of the flame response which is sufficient to generate unstable combustor conditions is reached at lower frequencies in the MBSs than in the SBS. Low-frequency modes are observed even more frequently in the MBS2 than in the MBS1. It was reasoned that the reduction of the swirl intensity may be even more significant in the MBS2, as all swirl jet have two adjacent swirl jets. The OH\*-intensity recordings revealed that the formation of ring vortex structures plays a major part in driving the unstable modes. The formation of the ring vortex structures is

induced by strong mass flow oscillations, which are modulated by in-phase oscillations of the pressure and the heat release in the combustion chamber.

The numerical investigations focused on the investigations of the major combustor modes in the frequency range of 400 Hz and 750 Hz, which were observed in the experiments. At first, the results of the non-reactive flows were discussed, in order to investigate possible influences on the mixing process. The results of the mean flow fields for the SBS were validated by the comparison to experimental data of PIV measurements provided by DLR Stuttgart.

A good agreement was found with the PIV measurements, especially for the OP  $L = 1.6$ ,  $P_{th} = 30$  kW,  $\phi = 0.85$ . The results for the non-reactive cases for the operating conditions  $L = 1.6$ ,  $P_{th} = 30$  kW,  $\phi = 0.85$  in the SBS and the MBS2 were compared, indicating significant differences in the flow field characteristics which are induced by the adjacent swirl jets. Despite the missing side walls, the MBS2 shows a flow field which resembles a wall bounded flow and the flow field in the SBS shows the characteristics of a free jet.

The simulations of the reactive flow in the SBS were also compared to PIV data provided by the DLR Stuttgart. The LESs were able to capture the main characteristics of the mean reactive flow and show reasonable results. However, the importance of adequate acoustic boundaries for the correct prediction of the amplitude and frequency of unstable combustor modes was illustrated by the results of the LESs of the reactive flow in the SBS. The unstable modes predicted by the simulations deviate from the frequencies observed in the experiment. Deviations were explained by the different acoustic impedances of the numerical inlets and the perforated plates installed at the corresponding positions in the real combustor. It was concluded that the acoustic impedance of the numerical inlets causes increased amplitudes of the half-wave mode in the inner plenum, which dominates the remaining pressure modes. The flame temporarily couples with this oscillation and augmented pressure and heat release oscillations are generated in the simulations. Nevertheless, the results of the LESs comply with the assumptions made in the discussion of the experiments, indicating that flow rate oscillations of the fuel-air mixture, modulated by in-phase oscillations of the heat release and combustion chamber pressure, are the main driving mechanisms for the unstable modes in the investigated combustor.

The LES of the reactive flow in the MBS2 does not show an unstable mode. It was concluded that one possible reason for this behaviour is given by the fact that the multiple flames need a certain amount of time to tune to one specific oscillation. Waiting several seconds does not pose a problem in the experimental investigations, but is beyond available computational capacities for LES. However, the simulation illustrates that the multiple-burner flame shows a stronger response to low-frequency perturbations than the flames in the SBS, which complies with the findings from the experiment. A possible explanation is given by an increased characteristic convective time delay in the MBSs, which was derived by the analysis of

streamlines in the mean flow field. It was concluded that the different convective time scales are induced by different flow characteristics in the reactive flow of the SBS and the MBS2. The mean flow fields are much more similar in the reactive case than in the non-reactive case, but the SBS shows higher recirculation rates in the IRZ, which may be the reason for the smaller distance between the main reaction zone and the nozzle outlet in the SBS. Therefore the results for the flow field characteristics in the reactive case show a contrasting behaviour to the non-reactive case, which illustrates the major impact of the flame on the flow field in the combustion chamber.

As a consequence, it can be stated that single-burner experiments can only partially reproduce the thermoacoustic response characteristics of multiple-burner flames. It has to be considered that even in the absence of large-scale flame-flame interactions significant differences between single-burner and multiple-burner setups may occur regarding the thermoacoustic stability of the combustor, due the interactions of the flow fields and their indirect influence on the flame characteristics. This non-linear behaviour makes it complicated to obtain an adequate prediction of the combustor stability with models derived from single-burner analysis.

The results of the LESs performed within the scope of this work confirm that LES is a very useful method when dealing with unsteady combustor dynamics. Compressible LES captures most of the acoustic field and also large scale coherent structures and hydrodynamic instabilities. Therefore, with LES it is possible to calculate broadband combustion noise and to predict or investigate driving mechanisms for combustion instabilities, such as acoustic eigenmodes and large-scale flame-vortex interactions. Thus, LES is a suitable tool to investigate the combustion dynamics of multiple-burner arrangements. The results of the LES of the multiple-burner setup demonstrate that LES is capable of providing the necessary insight into the complex flow and flame interactions that may allow for extension of existing modelling approaches for combustion instabilities so that they are capable of predicting the combustion dynamics of multiple-burners from single-burner analysis.

However, the results also demonstrate that applying adequate acoustic boundaries is indispensable when performing compressible LES with the purpose of predicting combustion instabilities. In addition, self-excited LESs of combustion instabilities may require long computation times which can pose a huge problem. As consequence, it may be advantageous to apply acoustic forcing in order to investigate complex multiple-burner systems, as limit cycle oscillations may be reached with less computation time.



## Bibliography

- [1] International Energy Outlook 2013, Washington, DC, 2013.
- [2] J. Le Conte, *Philosophical Magazine* HP, 235 (1858).
- [3] *Curiosities of Sound. (Concluded.)*, *Watson's Art Journal*. (1868).
- [4] J.T.R. DAVISON, *Music in medicine*, *The Lancet*. 154 (1899) 1159–1162.
- [5] J.W.S. Rayleigh, *The Explanation of Certain Acoustical Phenomena*, *Nature*. 18 (1878) 319–321.
- [6] T.C. Lieuwen, B.T. Zinn, *Combustion Instabilities: Basic Concepts*, in: T.C. Lieuwen, V. Yang (Eds.), *Combustion Instabilities in Gas Turbine Engines : Operational Experience , Fundamental Mechanisms and Modeling*, 2005: pp. 3–24.
- [7] F. Nicoud, T. Poinsot, *Thermoacoustic Instabilities: Should the Rayleigh Criterion be Extended to Include Entropy Changes?*, *Combustion and Flame*. 142 (2005) 153–159. doi:10.1016/j.combustflame.2005.02.013.
- [8] C.O. Paschereit, W. Weisenstein, E. Gutmark, *Control of Thermoacoustic Instabilities and Emissions in an Industrial Type Gas-Turbine Combustor*, *Symposium International On Combustion*. 2 (1998) 25.
- [9] S. Tachibana, L. Zimmer, Y. Kurosawa, K. Suzuki, *Active Control of Combustion Oscillations in a Lean Premixed Combustor by Secondary Fuel Injection Coupling with Chemiluminescence Imaging Technique*, *Proceedings of the Combustion Institute*. 31 (2007) 3225–3233.
- [10] S. Barbosa, M. de La Cruz Garcia, S. Ducruix, B. Labegorre, F. Lacas, *Control of Combustion Instabilities by Local Injection of Hydrogen*, *Proceedings of the Combustion Institute*. 31 (2007) 3207–3214. doi:10.1016/j.proci.2006.07.085.
- [11] B. Schuermans, *Modeling and Control of Thermoacoustic Instabilities*, *Docteur ès sciences*, École polytechnique fédérale de Lausanne, 2003.
- [12] D. Guyot, C.O. Paschereit, S. Raghu, *Active Combustion Control Using a Fluidic Oscillator for Asymmetric Fuel Flow Modulation*, *International Journal of Flow Control*. 1 (2009) 155–166.
- [13] N. Tran, S. Ducruix, T. Schuller, *Damping Combustion Instabilities with Perforates at the Premixer Inlet of a Swirled Burner*, *Proceedings of the Combustion Institute*. 32 (2009) 2917–2924. doi:10.1016/j.proci.2008.06.123.
- [14] M.R. Bothien, N. Noiray, B. Schuermans, *A Novel Damping Device for Broadband Attenuation of Low-Frequency Combustion Pulsations in Gas Turbines*, in: *Proceedings of ASME Turbo Expo 2012*, ASME, Copenhagen, Denmark, 2012: pp. 1–11.
- [15] C. Kulsheimer, H. Büchner, *Combustion Dynamics of Turbulent Swirling Flames*, *Combustion and Flame*. 84 (2002) 70–84.

- [16] M. Lohrmann, H. Büchner, N. Zarzalis, W. Krebs, Flame Transfer Function Characteristics of Swirl Flames for Gas Turbine Applications, in: ASME Turbo Expo 2003, Collocated with the 2003 International Joint Power Generation Conference, ASME, Atlanta, Georgia, USA, 2003: pp. 109–118.
- [17] B. Schuermans, D. Guyot, C.O. Paschereit, F. Guethe, D. Pennell, Thermoacoustic Modeling of a Gas Turbine Using Transfer Functions Measured Under Full Engine Pressure, *Journal of Engineering for Gas Turbines and Power*. 132 (2010) 111503.
- [18] P. Palies, T. Schuller, D. Durox, L.Y.M. Gicquel, S. Candel, Acoustically Perturbed Turbulent Premixed Swirling Flames, *Physics of Fluids*. 23 (2011) 037101. doi:10.1063/1.3553276.
- [19] D. Durox, T. Schuller, N. Noiray, S. Candel, Experimental Analysis of Nonlinear Flame Transfer Functions for Different Flame Geometries, *Proceedings of the Combustion Institute*. 32 (2009) 1391–1398. doi:10.1016/j.proci.2008.06.204.
- [20] D. Durox, J.P. Moeck, J.-F. Bourgooin, P. Morenton, M. Viallon, T. Schuller, et al., Flame Dynamics of a Variable Swirl Number System and Instability Control, *Combustion and Flame*. 160 (2013) 1729–1742. doi:10.1016/j.combustflame.2013.03.004.
- [21] W. Krebs, P. Flohr, B. Prade, S. Hoffmann, Thermoacoustic Stability Chart for High-Intensity Gas Turbine Combustion Systems, *Combustion Science and Technology*. 174 (2002) 99–128. doi:10.1080/00102200208984089.
- [22] P. Palies, D. Durox, T. Schuller, S. Candel, Nonlinear Combustion Instability Analysis Based on the Flame Describing Function Applied to Turbulent Premixed Swirling Flames, *Combustion and Flame*. 158 (2011) 1980–1991. doi:10.1016/j.combustflame.2011.02.012.
- [23] J. Kopitz, A. Huber, T. Sattelmayer, W. Polifke, Thermoacoustic Stability Analysis of an Annular Combustion Chamber With Acoustic Low Order Modeling and Validation Against Experiment, in: ASME Turbo Expo 2005: Power for Land, Sea and Air, ASME, 2005: pp. 583–593. doi:10.1115/GT2005-68797.
- [24] A.P. Dowling, S.R. Stow, Acoustic Analysis of Gas Turbine Combustors, *Journal of Propulsion and Power*. 19 (2003) 751–764. doi:10.2514/2.6192.
- [25] I. Hernández, G. Staffelbach, T. Poinso, J.C. Román Casado, J.B.W. Kok, LES and Acoustic Analysis of Thermo-Acoustic Instabilities in a Partially Premixed Model Combustor, *Comptes Rendus Mécanique*. 341 (2013) 121–130. doi:10.1016/j.crme.2012.11.003.
- [26] D. Laera, G. Campa, S.M. Camporeale, E. Bertolotto, S. Rizzo, F. Bonzani, et al., Modelling of Thermoacoustic Combustion Instabilities Phenomena: Application to an Experimental Test Rig, *Energy Procedia*. 45 (2014) 1392–1401. doi:10.1016/j.egypro.2014.01.146.
- [27] D. Fanaca, P.R. Alemela, C. Hirsch, T. Sattelmayer, B. Schuermans, Comparison of the Flow Fields of a Swirl Stabilised Premixed Burner in an Annular and a Single Burner Combustion Chamber, *Journal of Engineering for Gas Turbines and Power*. 132 (2010) 071502. doi:10.1115/GT2009-59884.
- [28] N. a. Worth, J.R. Dawson, Modal Dynamics of Self-Excited Azimuthal Instabilities in an Annular Combustion Chamber, *Combustion and Flame*. 160 (2013) 2476–2489. doi:10.1016/j.combustflame.2013.04.031.

- [29] N. a. Worth, J.R. Dawson, Self-excited circumferential instabilities in a model annular gas turbine combustor: Global flame dynamics, in: Proceedings of the Combustion Institute, The Combustion Institute, 2013: pp. 3127–3134. doi:10.1016/j.proci.2012.05.061.
- [30] F. Durst, Grundlagen der Strömungsmechanik, Springer, Berlin, 2006.
- [31] H. Oertel, Prandtl-Führer durch die Strömungslehre, Springer Vieweg, 2012.
- [32] H. Herwig, Strömungsmechanik, Vieweg+Teubner, Wiesbaden, 2008.
- [33] T. Poinso, D. Veynante, Theoretical and numerical combustion, 2005.
- [34] L.F. Richardson, Weather prediction by numerical process, University Press, Cambridge, 1922.
- [35] S. Pope, Turbulent flows, Cambridge University Press, Cambridge, 2000.
- [36] A. Kolmogorov, The local structure of turbulence in incompressible viscous fluid for very large Reynolds numbers, in: Proceedings of the USSR Academy of Sciences 30, 1941: pp. 299–303.
- [37] A. Kolmogorov, Dissipation of Energy in the Locally Isotropic Turbulence, in: Proceedings of the USSR Academy of Sciences 32, 1941: pp. 16–18.
- [38] J. Boussinesq, Théorie de l'écoulement tourbillonnant et tumultueux des liquides dans les lits rectilignes a grande section, Paris, Gauthier-Villars et Fils. (1897).
- [39] W.P. Jones, B. Launder, The prediction of laminarization with a 2-equation model of turbulence, International Journal of Heat and Mass Transfer. (1972) 301.
- [40] B. Launder, B. Sharma, Application of the energy-dissipation model of turbulence to the calculation of flow near a spinning disc, Letters in Heat and Mass Transfer. I (1974) 131–137.
- [41] S. Pope, A more general effective-viscosity hypothesis, Journal of Fluid Mechanics. 72 (1975) 331–340.
- [42] K. Hanjalic, B. Launder, Sensitizing the dissipation equation to irrotational strains, Journal of Fluids Engineering. 102 (1980) 34–40.
- [43] D. Wilcox, Multiscale model for turbulent flows, AIAA Journal. 26 (1988) 1311–1320. doi:10.2514/3.10042.
- [44] J. Froehlich, Large Eddy Simulation turbulenter Stroemungen, Teubner, 2006.
- [45] J. Smagorinsky, General Circulation Experiments with the Primitive Equations, Monthly Weather Review. 91 (1963). doi:10.1126/science.27.693.594.
- [46] A. Yoshizawa, Statistical theory for compressible turbulent shear flows, with the application to subgrid modeling, Physics of Fluids. 29 (1986) 2152. doi:10.1063/1.865552.
- [47] M. Germano, U. Piomelli, P. Moin, W.H. Cabot, A dynamic subgrid-scale eddy viscosity model, Physics of Fluids A: Fluid Dynamics. 3 (1991) 1760. doi:10.1063/1.857955.
- [48] S. Arrhenius, Über die Reaktionsgeschwindigkeit bei der Inversion von Rohrzucker durch Säuren, Zeitschrift Für Physikalische Chemie. (1889).

- [49] J. Warnatz, U. Maas, R.W. Dibble, *Verbrennung*, Springer, Berlin, Heidelberg, 1997.
- [50] N. Peters, Length scales in laminar and turbulent flames, *Numerical Approaches to Combustion modeling*(A 92-16977 04-25). Washington, DC, American Institute of Aeronautics and Astronautics, Inc. (1991) 155–182.
- [51] N. Peters, *Turbulent combustion*, Cambridge university press, Cambridge, 2000.
- [52] J. Göttgens, F. Mauss, N. Peters, Analytic approximations of burning velocities and flame thicknesses of lean hydrogen, methane, ethylene, ethane, acetylene, and propane flames, *Symposium (International) on Combustion*. (1992) 129–135.
- [53] Y. Zeldovich, D. Frank-Kamenetskii, A theory of thermal propagation of flame, *Zh. Fiz. Khim.* (1938).
- [54] N. Peters, Kinetic foundation of thermal flame theory, *Advances in Combustion Science: In Honor of Ya. B. Zel'dovich*(A 97-24531 05-25), Reston, VA, American Institute of Aeronautics and Astronautics, Inc.(*Progress in Astronautics and Aeronautics*. 173 (1997) 73–91).
- [55] N. Peters, Local quenching due to flame stretch and non-premixed turbulent combustion, *Combustion Science and Technology*. (1983).
- [56] N. Peters, Laminar diffusion flamelet models in non-premixed turbulent combustion, *Progress in Energy and Combustion Science*. (1984).
- [57] G. Damköhler, Der Einfluß der Turbulenz auf die Flammgeschwindigkeit in Gasgemischen, *Zeitschrift Für Elektrochemie Und Angewandte Physikalische Chemie*. 46 (1940) 601–626.
- [58] R. Abdel-Gayed, D. Bradley, Lewis number effects on turbulent burning velocity, in: *Symposium (International) on Combustion*, 1985: pp. 505–512.
- [59] R. Borghi, Turbulent combustion modelling, *Progress in Energy and Combustion Science*. 14 (1988) 245–292.
- [60] P. Maier, *Untersuchung turbulenter, isothermer Drallfreistrahlen und turbulenter Drallflammen*, Universität Karlsruhe, 1967.
- [61] W. Leuckel, Swirl Intensities, Swirl Types and Energy Losses of Different Swirl Generating Devices, Doc Nr. G , International Flame Research Foundation, Ijmuiden, 1967.
- [62] N.M. Kerr, D. Fraser, Swirl, Part 1: Effect on Axisymmetrical Turbulent Jets, *Journal of the Institute of Fuel*. 38 (1965) 519–526.
- [63] G.P. Smith, D.M. Golden, M. Frenklach, N.W. Moriarty, B. Eiteneer, M. Goldenberg, et al., [http://www.me.berkeley.edu/gri\\_mech/](http://www.me.berkeley.edu/gri_mech/), (n.d.).
- [64] V. Zimont, A. Lipatnikov, A numerical model of premixed turbulent combustion of gases, *Chemical Physics Reports*. (1995).
- [65] H.-P. Schmid, P. Habisreuther, W. Leuckel, A model for calculating heat release in premixed turbulent flames, *Combustion and Flame*. 113 (1998) 79–91.

- [66] H.-P. Schmid, Ein Verbrennungsmodell zur Beschreibung der Wärmefreisetzung von vorgemischten turbulenten Flammen, Karlsruhe, 1995.
- [67] P. Habisreuther, Untersuchungen zur Bildung von thermischen Stickoxid in Turbulenten Drallflammen, Universität Karlsruhe (TH), 2002.
- [68] P.A. Libby, F.A. Williams, eds., Turbulent reacting flows, Academic, London, 1984.
- [69] U. Maas, S.B. Pope, Simplifying chemical kinetics: Intrinsic low-dimensional manifolds in composition space, *Combustion and Flame*. 88 (1992) 239–264. doi:10.1016/0010-2180(92)90034-M.
- [70] F. Zhang, Numerical Modeling of Noise Emissions caused by Turbulent Combustion, 2014.
- [71] H.-P. Schmid, Ein Verbrennungsmodell zur Beschreibung der Wärmefreisetzung von vorgemischten turbulenten Flammen, Karlsruhe, 1995.
- [72] R. Kee, J. Miller, T. Jefferson, CHEMKIN: A general-purpose, problem-independent, transportable, FORTRAN chemical kinetics code package, (1980).
- [73] C. Bender, F. Zhang, P. Habisreuther, H. Bockhorn, Measurement and Simulation of Combustion Noise emitted from Swirl Burners, in: A. Schwarz, J. Janicka (Eds.), *Combustion Noise (DFG Research Unit 486). Fluid Mechanics and Its Applications*, Springer Berlin Heidelberg, Berlin, Heidelberg, 2009: pp. 33–62. doi:10.1007/978-3-642-02038-4.
- [74] F. Zhang, P. Habisreuther, M. Hettel, H. Bockhorn, Numerical computation of combustion induced noise using compressible LES and hybrid CFD/CAA methods, *Acta Acustica United with Acustica*. 98 (2012) 120–134. doi:10.3813/AAA.918498.
- [75] F. Zhang, P. Habisreuther, H. Bockhorn, H. Nawroth, C.O. Paschereit, On Prediction of Combustion Generated Noise with the Turbulent Heat Release Rate, *Acta Acustica United with Acustica*. 99 (2013) 940–951. doi:10.3813/AAA.918673.
- [76] F. Zhang, P. Habisreuther, M. Hettel, H. Bockhorn, Modelling of a Premixed Swirl-stabilized Flame Using a Turbulent Flame Speed Closure Model in LES, *Flow, Turbulence and Combustion*. 82 (2008) 537–551. doi:10.1007/s10494-008-9175-x.
- [77] F. Zhang, P. Habisreuther, M. Hettel, H. Bockhorn, Numerical Investigations of the Noise Sources Generated in a Swirl Stabilized Flame, 95 (2009) 1–10.
- [78] F. Zhang, P. Habisreuther, M. Hettel, H. Bockhorn, Application of a Unified TFC Model to Numerical Simulation of a Turbulent Non-Premixed Flame, in: *Proceedings of the 8th International ERCOFTAC Symposium on Engineering Turbulence Modelling and Measurements - ETMM8*, Marseille, France, 2011: pp. 681–686.
- [79] M. Lighthill, On Sound Generated Aerodynamically. I. General theory, *Proceedings of the Royal Society of London. Series A. Mathematical and Physical Sciences*. 211 (1952) 564–587.
- [80] W. Strahle, On combustion generated noise, 7th Propulsion Joint Specialist Conference. (1971). doi:10.2514/6.1971-735.
- [81] T.P. Bui, W. Schröder, M. Meinke, Numerical analysis of the acoustic field of reacting flows via acoustic perturbation equations, *Computers & Fluids*. 37 (2008) 1157–1169. doi:10.1016/j.compfluid.2007.10.014.

- [82] C.F. Silva, M. Leyko, F. Nicoud, S. Moreau, Assessment of combustion noise in a premixed swirled combustor via Large-Eddy Simulation, *Computers & Fluids*. 78 (2013) 1–9. doi:10.1016/j.compfluid.2010.09.034.
- [83] F. Flemming, a. Sadiki, J. Janicka, Investigation of combustion noise using a LES/CAA hybrid approach, *Proceedings of the Combustion Institute*. 31 (2007) 3189–3196. doi:10.1016/j.proci.2006.07.060.
- [84] C. Hirsch, J. Wäsle, A. Winkler, T. Sattelmayer, A spectral model for the sound pressure from turbulent premixed combustion, in: *Proceedings of the Combustion Institute, 2007*: pp. 1435–1441. doi:10.1016/j.proci.2006.07.154.
- [85] K. Smith, J. Blust, Combustion instabilities in industrial gas turbines: Solar turbines' experience, *Progress in Astronautics and Aeronautics*. (2005) 29–41.
- [86] J. Sewell, P. Sobieski, C. Beers, Application of continuous Combustion Dynamics Monitoring on large industrial gas turbines, *Proceedings of ASME Turbo Expo 2004, Power for Land, Sea and Air*. (2004) 1–9.
- [87] J.W.S. Rayleigh, *The Theory of Sound*, 2 (1945).
- [88] A.A. Putnam, *Combustion-driven oscillations in industry*, American Elsevier Publishing Company. (1971).
- [89] B. Zinn, T. Lieuwen, *Combustion instabilities: Basic concepts*, *Progress in Astronautics and Aeronautics*. (2005).
- [90] L. Crocco, S.-I. Cheng, High frequency combustion instability in rockets with distributed combustion, *Symposium (International) on Combustion*. 4 (1953) 865–880.
- [91] B.T. Zinn, E.A. Powell, Nonlinear combustion instability in liquid-propellant rocket engines, *Symposium (International) on Combustion*. 13 (1971) 491–503. doi:10.1016/S0082-0784(71)80051-6.
- [92] J. Cohen, W. Proscia, J. DeLaat, Characterization and control of aeroengine combustion instability: Pratt & Whitney and NASA experience, *Progress in Astronautics and Aeronautics*. (2005).
- [93] T. Scarinci, Combustion instability and its passive control: Rolls-Royce aeroderivative engine experience, in: *Progress in Astronautics and Aeronautics, 2005*.
- [94] J. Hermann, S. Hoffmann, Implementation of active control in a full-scale gas-turbine combustor, *Progress in Astronautics and Aeronautics*. (2005).
- [95] J. Keller, Thermoacoustic oscillations in combustion chambers of gas turbines, *AIAA Journal*. 33 (1995).
- [96] S. Ducruix, T. Schuller, D. Durox, S. Candel, Combustion instability mechanisms in premixed combustors, *Progress in Astronautics and Aeronautics*. (2005).
- [97] D.W. Kendrick, T.J. Anderson, W.A. Sowa, T.S. Snyder, Acoustic sensitivities of lean-premixed fuel injectors in a single nozzle rig, *Journal of Engineering for Gas Turbines and Power*. 121 (1999) 429–436.

- [98] W. Meier, P. Weigand, X. Duan, R. Giezendannerthoben, Detailed characterization of the dynamics of thermoacoustic pulsations in a lean premixed swirl flame, *Combustion and Flame*. 150 (2007) 2–26. doi:10.1016/j.combustflame.2007.04.002.
- [99] S. Hermeth, G. Staffelbach, L.Y.M. Gicquel, T. Poinsot, LES evaluation of the effects of equivalence ratio fluctuations on the dynamic flame response in a real gas turbine combustion chamber, *Proceedings of the Combustion Institute*. 34 (2013) 3165–3173. doi:10.1016/j.proci.2012.07.013.
- [100] T. Lieuwen, B.T. Zinn, The role of equivalence ratio oscillations in driving combustion instabilities in low NO<sub>x</sub> gas turbines, *Symposium (International) on Combustion*. 27 (1998) 1809–1816. doi:10.1016/S0082-0784(98)80022-2.
- [101] M. Delacruzgarca, E. Mastorakos, a Dowling, Investigations on the self-excited oscillations in a kerosene spray flame, *Combustion and Flame*. 156 (2009) 374–384. doi:10.1016/j.combustflame.2008.11.018.
- [102] S. Candel, *Combustion dynamics and control: Progress and challenges*, *Proceedings of the Combustion Institute*. 29 (2002) 1–28. doi:10.1016/S1540-7489(02)80007-4.
- [103] H. Büchner, *Strömungs-und Verbrennungsinstabilitäten in technischen Verbrennungssystemen*, Universität Karlsruhe (TH), 2001.
- [104] N. Syred, J. Beer, *Combustion in swirling flows: a review*, *Combustion and Flame*. (1974).
- [105] N. Syred, A. Gupta, J. Beer, Temperature and density gradient changes arising with the precessing vortex core and vortex breakdown in swirl burners, *Symposium (International) on Combustion*. (1975).
- [106] N. Syred, W. Fick, T. O’Doherty, a. J. Griffiths, The Effect of the Precessing Vortex Core on Combustion in a Swirl Burner, *Combustion Science and Technology*. 125 (1997) 139–157. doi:10.1080/00102209708935657.
- [107] N. Syred, A Review of Oscillation Mechanisms and the Role of the Precessing Vortex Core (PVC) in Swirl Combustion Systems, *Progress in Energy and Combustion Science*. 32 (2006) 93–161. doi:10.1016/j.pecs.2005.10.002.
- [108] J. Eckstein, E. Freitag, C. Hirsch, T. Sattelmayer, Experimental Study on the Role of Entropy Waves in Low-Frequency Oscillations in a RQL Combustor, *Journal of Engineering for Gas Turbines and Power*. 128 (2006) 264. doi:10.1115/1.2132379.
- [109] K.-U. Schildmacher, a. Hoffmann, L. Selle, R. Koch, C. Schulz, H.-J. Bauer, et al., Unsteady flame and flow field interaction of a premixed model gas turbine burner, *Proceedings of the Combustion Institute*. 31 (2007) 3197–3205. doi:10.1016/j.proci.2006.07.081.
- [110] S.M. Candel, Combustion instabilities coupled by pressure waves and their active control, *Symposium (International) on Combustion*. 24 (1992) 1277–1296. doi:10.1016/S0082-0784(06)80150-5.
- [111] S. Forster, U. Michel, I. Röhle, *Optimierung der passiven und aktiven Dämpfung von thermoakustischen Schwingungen*, Berlin, 2005.
- [112] K.H. Yu, *Active Control of Engine Dynamics : Fundamentals and Fluid Dynamics – Experiments 1 . Active Control Classification*, (2001) 14–18.

- [113] M.R. Bothien, J.P. Moeck, C. Oliver Paschereit, Active control of the acoustic boundary conditions of combustion test rigs, *Journal of Sound and Vibration*. 318 (2008) 678–701. doi:10.1016/j.jsv.2008.04.046.
- [114] C.O. Paschereit, W. Weisenstein, E. Gutmark, Control of thermoacoustic instabilities and emissions in an industrial-type gas-turbine combustor, in: *Symposium (International) on Combustion*, 1998: pp. 1817–1824.
- [115] C.O. Paschereit, B. Schuermans, W. Polifke, O. Mattson, Measurement of transfer matrices and source terms of premixed flames, *Journal of Engineering for Gas Turbines and Power*. 124 (2002) 239–247.
- [116] D. Durox, T. Schuller, S. Candel, Combustion dynamics of inverted conical flames, *Proceedings of the Combustion Institute*. 30 (2005) 1717–1724. doi:10.1016/j.proci.2004.08.067.
- [117] A. Dowling, Nonlinear self-excited oscillations of a ducted flame, *Journal of Fluid Mechanics*. 346 (1997) 271–290.
- [118] L. Crocco, Research on combustion instability in liquid propellant rockets, *Symposium (International) on Combustion*. 12 (1969) 85–99. doi:10.1016/S0082-0784(69)80394-2.
- [119] M. Lohrmann, H. Büchner, N. Zarzalis, W. Krebs, Flame Transfer Function Characteristics of Swirl Flames for Gas Turbine Applications, in: *ASME Turbo Expo 2003, Collocated with the 2003 International Joint Power Generation Conference*, ASME, Atlanta, Georgia, USA, 2003.
- [120] W. Polifke, a. Poncet, C.O. Paschereit, K. Döbbeling, Reconstruction of Acoustic Transfer Matrices By Instationary Computational Fluid Dynamics, *Journal of Sound and Vibration*. 245 (2001) 483–510. doi:10.1006/jsvi.2001.3594.
- [121] G. Staffelbach, L.Y.M. Gicquel, G. Boudier, T. Poinso, Large Eddy Simulation of Self Excited Azimuthal Modes in Annular Combustors, *Proceedings of the Combustion Institute*. 32 (2009) 2909–2916.
- [122] H. Krediet, Prediction of limit cycle pressure oscillations in gas turbine combustion systems using the flame describing function, Twente, 2012.
- [123] L.Y.M. Gicquel, G. Staffelbach, T. Poinso, Large Eddy Simulations of gaseous flames in gas turbine combustion chambers, *Progress in Energy and Combustion Science*. 38 (2012) 782–817. doi:10.1016/j.pecs.2012.04.004.
- [124] B. Franzelli, E. Riber, L.Y.M. Gicquel, T. Poinso, Large Eddy Simulation of combustion instabilities in a lean partially premixed swirled flame, *Combustion and Flame*. 159 (2012) 621–637. doi:10.1016/j.combustflame.2011.08.004.
- [125] P. Wolf, G. Staffelbach, L.Y.M. Gicquel, J.-D. Müller, T. Poinso, Acoustic and Large Eddy Simulation studies of azimuthal modes in annular combustion chambers, *Combustion and Flame*. 159 (2012) 3398–3413. doi:10.1016/j.combustflame.2012.06.016.
- [126] R. Garby, L. Selle, T. Poinso, Large-Eddy Simulation of combustion instabilities in a variable-length combustor, *Comptes Rendus Mécanique*. 341 (2013) 220–229. doi:10.1016/j.crme.2012.10.020.

- [127] L. Selle, Compressible large eddy simulation of turbulent combustion in complex geometry on unstructured meshes, *Combustion and Flame*. 137 (2004) 489–505.  
doi:10.1016/j.combustflame.2004.03.008.
- [128] S. Menon, W.-H. Jou, Large-Eddy Simulations of Combustion Instability in an Axisymmetric Ramjet Combustor, *Combustion Science and Technology*. 75 (1991) 53–72.  
doi:10.1080/00102209108924078.
- [129] C. Fureby, Large eddy simulation modelling of combustion for propulsion applications., *Philosophical Transactions. Series A, Mathematical, Physical, and Engineering Sciences*. 367 (2009) 2957–69. doi:10.1098/rsta.2008.0271.
- [130] B.E. Motheau, L. Selle, Y. Mery, T. Poinso, A mixed acoustic-entropy combustion instability in a realistic gas turbine, (2012) 449–458.
- [131] T. Lieuwen, *Unsteady combustor physics*, Cambridge University Press, Cambridge, 2012.
- [132] S. Mendez, J.D. Eldredge, Acoustic modeling of perforated plates with bias flow for Large-Eddy Simulations, *Journal of Computational Physics*. 228 (2009) 4757–4772.  
doi:10.1016/j.jcp.2009.03.026.
- [133] T. Kathrotia, U. Riedel, A. Seipel, K. Moshhammer, A. Brockhinke, Experimental and numerical study of chemiluminescent species in low-pressure flames, *Appl Phys B*. 107 (2012) 571–584.
- [134] B. Schuermans, F. Guethé, W. Mohr, Optical Transfer Function Measurements for Technically Premixed Flames, *Journal of Engineering for Gas Turbines and Power*. 132 (2010) 081501.  
doi:10.1115/1.3124663.
- [135] M. Lauer, T. Sattelmayer, On the adequacy of chemiluminescence as a measure for heat release in turbulent flames with mixture gradients, *Journal of Engineering for Gas Turbines and Power*. 132 (2010).
- [136] A.M. Steinberg, C.M. Arndt, W. Meier, Parametric Study of Vortex Structures and their Dynamics in Swirl-Stabilized Combustion, *Proceedings of the Combustion Institute*. 34 (2013) 3117–3125. doi:10.1016/j.proci.2012.05.015.
- [137] M. Stöhr, R. Sadanandan, W. Meier, Experimental study of unsteady flame structures of an oscillating swirl flame in a gas turbine model combustor, in: *Proceedings of the Combustion Institute*, 2009: pp. 2925–2932. doi:10.1016/j.proci.2008.05.086.
- [138] K. Schildmacher, R. Koch, S. Wittig, Experimental investigations of the temporal air-fuel mixing fluctuations and cold flow instabilities of a premixing gas turbine burner, *Journal of Engineering for Gas Turbines and Power*. 127 (2005) 295–300.
- [139] M. Lohrmann, *Die Bedeutung flammeninterner Verzugszeiten für die Entstehung selbsterregter Verbrennungsinstabilitäten*, Karlsruhe, 2006.
- [140] D. Durox, J.P. Moeck, J.-F. Bourgoignie, P. Morenton, M. Viallon, T. Schuller, et al., Flame Dynamics of a Variable Swirl Number System and Instability Control, *Combustion and Flame*. 160 (2013) 1729–1742. doi:10.1016/j.combustflame.2013.03.004.
- [141] M.W.M. Thring, Combustion oscillations in industrial combustion chambers, *Symposium (International) on Combustion*. 12 (1969) 163–168.

- [142] Y. Fu, J. Cai, S.-M. Jeng, H. Mongia, Confinement Effects on the Swirling Flow of a Counter-Rotating Swirl Cup, in: Proceedings of GT2005 ASME Turbo Expo 2005: Power for Land, Sea and Air., ASME, Nevada, 2005: pp. 469–478. doi:10.1115/GT2005-68622.
- [143] J. Ferziger, M. Perić, Computational methods for fluid dynamics, 3rd ed., Springer, Berlin, Heidelberg, New York, 2002.
- [144] M. Schäfer, Computational Engineering – Introduction to Numerical Methods, Springer Berlin Heidelberg, 2006.
- [145] T. Poinso, S. Lelef, Boundary conditions for direct simulations of compressible viscous flows, Journal of Computational Physics. (1992).
- [146] F. Dynamics, F. Peng, A. Mechanics, Numerical Modelling of Diesel Spray Injection , Turbulence Interaction and Combustion, 2008.
- [147] E. Gullaud, S. Mendez, C. Sensiau, F. Nicoud, T. Poinso, Effect of multiperforated plates on the acoustic modes in combustors, Comptes Rendus Mécanique. 337 (2009) 406–414. doi:10.1016/j.crme.2009.06.020.
- [148] D. Spalding, A single formula for the law of the wall, Journal of Applied Mechanics. 28 (1961) 455–458.
- [149] J. Sangl, Erhöhung der Brennstoffflexibilität von Vormischbrennern durch Beeinflussung der Wirbeldynamik, München, 2011.